MODELLING AND IDENTIFICATION OF INDUSTRIAL ROBOTS INCLUDING DRIVE AND JOINT FLEXIBILITIES

Toon Hardeman

Netherlands Institute
for Metals Research

The research described in this thesis was carried out in the framework of the Strategic Research Programme of the Netherlands Institute for Metal Research (www.nimr.nl).

Modelling and Identification of Industrial Robots
including Drive and Joint Flexibilities
Hardeman, Toon
ISBN 978-90-365-2621-0

Printed by PrintPartners Ipskamp.

MODELLING AND IDENTIFICATION OF INDUSTRIAL ROBOTS INCLUDING DRIVE AND JOINT FLEXIBILITIES

PROEFSCHRIFT

ter verkrijging van
de graad van doctor aan de Universiteit Twente,
op gezag van de rector magnificus,
prof. dr. W.H.M. Zijm,
volgens besluit van het College voor Promoties
in het openbaar te verdedigen
op vrijdag 1 februari 2008 om 15.00 uur

door

Toon Hardeman
geboren op 1 maart 1979
te Strijen

Dit proefschrift is goedgekeurd door
prof.dr.ir. J.B. Jonker, promotor
dr.ir. R.G.K.M. Aarts, assistent-promotor

Voorwoord

Dit proefschrift zou niet tot stand zijn gekomen zonder de hulp van vele anderen. Bij deze wil ik dan ook iedereen bedanken die mij de afgelopen jaren heeft geholpen tijdens mijn promotie.

Een speciale dank gaat uit naar mijn promotor Ben Jonker en assistent-promotor Ronald Aarts. Naast de inspirerende vakinhoudelijke discussies wil ik hen vooral bedanken voor het geduld dat zij hebben opgebracht en de tijd die zij hebben gestoken in het becommentariëren en corrigeren van mijn teksten.

Een naam die zeker ook niet mag ontbreken, is mijn voorganger Rob Waiboer. Zonder de basis die hij heeft gelegd, was ik nooit zover gekomen. Verder wil ik ook graag mijn projectgenoot Wouter Hakvoort bedanken voor de goede samenwerking gedurende dit traject. Ook een dank aan de studenten die delen van dit onderzoek met veel enthousiasme hebben uitgevoerd, namelijk Herman Battjes, Chris Nieuwenhuis, Ivo Scheringa en Marcel Scholts.

Alle jaren ben ik met veel plezier naar mijn werk gegaan. Naast het uitdagende onderzoek kwam dit vooral door de leuke groep collega's. De vele conversaties tijdens de koffie, de jaarlijkse BBQ, de verjaardagen van en de stapuitjes met collega's, maar ook de kritische blik op opstellingen en onderzoek van elkaar, hebben een positieve bijdrage geleverd aan de totstandkoming van dit proefschrift. Dank daarvoor. A special thanks goes to Dimitrios for improving my English conversation skills, but also for acting as a target for stress balls during the coffee breaks, giving me a warm welcome each morning and of course the supply of 'gangmakers'.

Een belangrijke bijdrage aan de leuke tijd die ik hier in Enschede heb gehad, kan worden toegeschreven aan het Musica Silvestra Orkest. De vele concerten op stoere locaties in binnen- en buitenland, de honderden repetities en alle gezelligheid eromheen zijn voor mij zeer waardevol geweest. Een dank gaat ook uit naar de (oud-)leden van het onafhankelijk dispuut WAZIG, met wie ik de afgelopen jaren vele gezellige borrels, uitjes en mooie feestjes heb mogen meemaken.

Ook wil ik graag mijn ouders en (schoon)familie bedanken voor de interesse die zij altijd getoond hebben in mijn werk op de UT. Het vertrouwen van mijn ouders in mijn kunnen heeft in grote mate bijgedragen aan de totstandkoming van dit proefschrift. Hierbij hielden de interesse voor de wetenschap van mijn vader en de nuchtere kijk van mijn moeder, elkaar mooi in evenwicht.

Tot slot wil ik vooral Suzanne bedanken, met wie ik al mijn frustraties over niet werkende simulaties, mijn euforie over een nieuwe formule en mijn desillusies over een vastgelopen onderzoek altijd kon delen.

Toon Hardeman

Enschede, januari 2008

Contents

Summary

The applicability of industrial robots is restricted by their tip accuracy, in particular for applications in which a tool needs to track a trajectory at high speed. Flexibility in the drives and joints of these manipulators is an important cause for their limited accuracy. The flexibilities will cause vibration of the robot tip along the desired trajectory and deflection due to gravity. The goal of this thesis is to develop modelling and identification techniques for industrial robots that include the effects of joint and drive flexibilities, aiming at the prediction of the tip motion. The developed modelling and identification techniques are applied on a Stäubli RX90B industrial robot.

Static measurements have shown that the dominant flexibilities of this robot are located both in the drives and joints. The links are assumed to be rigid. A nonlinear finite element formulation is used to derive the equations of motion, including both types of flexibilities. The simulation model includes the mass and inertias of the arms and drives, damping of the flexible joints, joint friction and the stiffness of a gravity compensating spring. Furthermore a model of the industrial CS8 motion controller is included.

The nonlinear finite element formulation is extended with a new lumped mass formulation. In this formulation for each rigid beam element, representing a robot link, a rigid body is defined with equivalent mass and rotational inertia properties. Furthermore, a vector is defined that describes the centre of mass of this rigid body with respect to one of the element nodes. This vector, which is not included in the original element mass formulation, enables a parameter linear description for the equations of motion. As a result, the nonlinear finite element formulation is suitable for linear parameter identification techniques.

A linear least squares parameter identification technique is developed to identify the dynamic parameters of the robot model. This method provides accurate parameter estimates that are suitable for realistic robot simulations, provided that the model structure is correct and all degrees of freedom are known accurately. In this work it has been attempted to measure the relative motion between two links with a Krypton Rodym 6D camera system. Unfortunately, it appeared that the measurement setup is not sufficiently accurate for measuring the small flexible deformations in combination with the large joint motion.

An alternative parameter identification method is developed, which requires only motor position and motor torque or current data. This inverse eigenvalue parameter identification method is based on the work of Hovland et al. (2001), for which some important improvements are proposed. Firstly, the requirement to switch off the feedback controllers is avoided by using Multiple Input Multiple Output identification experiments. Secondly, a frequency domain system identification technique is proposed to extract the required (anti-)resonance frequencies accurately from experimental data. The original work does not provide any method for this. Thirdly, it is shown that although only drive flexibilities can be identified, the new method can be applied to robots with both joint and drive flexibilities.

The undamped (anti-)resonance frequencies of the robot are extracted from a common denominator matrix polynomial that is estimated using frequency domain system identification techniques. Accurate identification of such a matrix polynomial requires a correct description of the robot dynamics and the experimental conditions. Therefore, the nonlinear distortions arising from the nonlinear robot dynamics are included in a linear errors in variables stochastic framework. To exclude the nonlinearities of the controller in the estimation of the noise covariances, a new reference signal is proposed for the mapping of the input and output signals of several experiments to a common input signal.

An experimental analysis shows that the number of modes that can be extracted from experimental data is in agreement with the number of modes of the proposed robot model. Furthermore, the estimated accuracy of the dynamic parameters as a result of measurement noise and nonlinear distortions is very reasonable. The current analysis is limited to the estimation of the inertia and stiffness of the drives and the mass matrix of the corresponding rigidified system. Estimating the other dynamic parameters requires an experimental setup that is able to measure the small elastic joint deformations accurately. More research is needed to develop such a setup. Nevertheless, the results obtained so far demonstrate the abilities of the proposed method to estimate several dynamic parameters of a flexible robot model using only the limited and noisy data that is available in an industrial robot setup.

Samenvatting

De toepasbaarheid van industriële robots wordt beperkt door hun nauwkeurigheid, in het bijzonder voor applicaties waarbij met hoge snelheid een traject moet worden gevolgd. Een belangrijke oorzaak van deze beperkte nauwkeurigheid is flexibiliteit in de aandrijving en in de scharnieren van deze manipulatoren. Deze flexibiliteiten veroorzaken trillingen van de robot langs het gewenste pad en doorbuiging ten gevolge van de zwaartekracht. Dit onderzoek tracht modellering- en identificatietechnieken te ontwikkelen voor flexibele industriële robots, met als doel het voorspellen van de beweging van de robot en zijn gereedschap. De ontwikkelde modellerings- en identificatietechnieken zijn toegepast op een Stäubli RX90B industriële robot.

Statische metingen hebben laten zien dat de dominante stijfheden van deze robot zich bevinden in zowel de aandrijving als de scharnieren. De robotarmen worden verondersteld star te zijn. Een niet-lineaire eindige elementen methode is gebruikt voor het opstellen van de bewegingsvergelijkingen van deze robot, inclusief een beschrijving van beide flexibiliteiten. Het simulatiemodel beschrijft de massa's en traagheden van de armen en de aandrijving, de demping van de elastische scharnieren, de wrijving in de scharnieren en de stijfheid van een zwaartekracht compenserende veer. Daarnaast is een model van de industriële CS8 motion controller opgenomen.

De niet-lineaire eindige elementen formulering is gedurende dit onderzoek uitgebreid met een nieuwe geconcentreerde massa formulering. In deze formulering wordt voor iedere robotarm, welke is beschreven middels een star balk element, een star lichaam gedefinieerd met equivalente massa en traagheidseigenschappen. Daarnaast wordt een vector gedefinieerd, die het massamiddelpunt van een arm beschrijft ten opzichte van één van de knooppunten van het balk element. Deze vector, welke in de oorspronkelijke formulering niet was opgenomen, maakt een beschrijving mogelijk van de bewegingsvergelijkingen in een parameter lineaire vorm.

Met behulp van deze formulering is een lineaire kleinste kwadraten parameter identificatie methode ontwikkeld. Deze methode geeft nauwkeurige schattingen van de dynamische parameters van het flexibele robot model, welke gebruikt kunnen worden voor realistische simulaties, vooropgesteld dat alle vrijheidsgraden nauwkeurig bekend zijn. In dit werk is getracht de relatieve

beweging tussen twee armen te meten met behulp van een Krypton Rodym 6D camera systeem. Helaas blijkt dit systeem te onnauwkeurig voor het meten van de kleine elastische deformaties in combinatie met grote scharnier rotaties.

Een alternatieve parameter identificatie methode is ontwikkeld, welke alleen gebruikmaakt van gemeten motorposities en motorkoppels of motorstromen. Deze inverse eigenwaarde parameter identificatie methode is gebaseerd op het werk van Hovland et al. (2001), echter zijn een aantal belangrijke verbeteringen aangebracht. Ten eerste is de eis voor het uitschakelen van de motion controller opgeheven door gebruik te maken van Multiple Input Multiple Output identificatie experimenten. Ten tweede zijn frequentie domein systeem identificatie technieken toegepast voor het schatten van de benodigde (anti-)resonantie frequenties uit experimentele data. In het originele werk ontbreekt hiervoor een methode. Ten derde is aangetoond dat hoewel alleen aandrijf flexibiliteiten kunnen worden geschat, de methode toepasbaar is voor robots met flexibiliteiten in zowel de aandrijving als de scharnieren.

De ongedempte (anti-)resonantie frequenties van de robot worden geschat uit een overdrachtsfunctie matrix met een gezamenlijk noemer polynoom. De overdrachtsfuncties worden geschat middels frequentie domein systeem identificatie technieken. Het nauwkeurig schatten van een dergelijk model vereist een correcte beschrijving van de robot dynamica en de experimentele condities. Daarom zijn de verstoringen afkomstig van de niet-lineaire robot dynamica toegevoegd aan een lineair errors in variables framework. Voor het uitsluiten van de niet-lineariteiten afkomstig van de motion controller in de schatting van de covariantie van de totale meetruis, is een nieuwe methode ontwikkeld. In deze methode wordt de daadwerkelijk gemeten input in plaats van het meestal gebruikte externe excitatie signaal gebruikt als referentie signaal voor het projecteren van de in- en uitgangssignalen van verschillende experimenten op een gezamenlijk ingangssignaal.

Een experimentele analyse laat zien dat het aantal eigenfrequenties dat kan worden geschat uit experimentele data in overeenstemming is met het aantal eigenfrequenties van het ontwikkelde robot model. Bovendien is de nauwkeurigheid van de geschatte parameters als gevolg van meetruis en niet-lineaire verstoringen redelijk. De huidige analyse beperkt zich tot het schatten van de traag- en stijfheid van de aandrijvingen en de massa matrix van het corresponderende starre robot model. Het schatten van de overige parameters vereist een meetopstelling die in staat is om de kleine elastische deformaties van de scharnieren nauwkeurig te meten. Meer onderzoek is nodig voor het ontwikkelen van een dergelijke opstelling. Desalniettemin geven de huidige resultaten een goede indicatie van de mogelijkheden van de ontwikkelde methode voor het schatten van meerdere dynamische parameters van een elastisch robot model, wanneer slechts gebruik gemaakt wordt van de beperkte en vaak verruiste signalen die beschikbaar zijn in een industriële robot.

List of symbols

Latin symbols

a_r	denominator coefficient of transfer function
$A(s)$	denominator polynomial of transfer function
$\mathbf{A}$	regression matrix
$b_{j,k,r}$	nominator coefficients transfer function
$\mathbf{B}(s)$	nominator matrix polynomial of transfer function
$\mathbf{B}^{(u)}$	input matrix
$c^{(a)}$	velocity constant friction model
$c_j^{(v)}$	viscous friction coefficient of joint j
$\mathbf{C}$	covariance matrix
$\mathbf{C}(s)$	linear feedback controller
$\mathbf{C}_0$	velocity sensitivity matrix
$\boldsymbol{d}^{[k+1]}$	vector of structural damping parameters of element $k+1$
$\mathcal{D}$	vector with deformation functions
$\mathbf{D}$	structural damping matrix
$\mathbf{D}_0$	linearised damping matrix
$\boldsymbol{e}$	vector of deformation modes
$e^{(c)}$	calculable deformation of gravity compensating spring
$\boldsymbol{e}^{(m)}$	vector of drive angles
$\boldsymbol{f}$	vector of nodal forces
$\boldsymbol{f}^{(c)}$	vector of gravitational forces
$\boldsymbol{f}^{(in)}$	vector of inertia forces
$\boldsymbol{f}^{(p)}$	vector of external forces acting on the body
$\boldsymbol{f}^{(r)}$	vector of external nodal forces exclusive inertia and gravitational forces
$\mathcal{F}$	vector of geometric transfer functions
$\mathbf{F}$	friction matrix
$\mathbf{F}_0$	linearised friction matrix
$\boldsymbol{g}$	gravitation field
$\mathbf{G}_0$	geometric stiffening matrix

$\mathbf{H}(s)$	transfer function matrix
$\mathbf{H}(j\omega)$	multivariable frequency response function
i_j	motor current of joint j
$\mathbf{J}$	Jacobian matrix / derivative of weighted residual $\boldsymbol{\epsilon}$
$J^{[k](a)}$	drive inertia of element k
$\mathbf{J}^{[k]}$	rotational inertia matrix of lumped body k
$k^{(c)}$	stiffness gravity compensating spring
$\boldsymbol{k}^{[k+1]}$	vector of drive and joint stiffness of element $k+1$
$k_j^{(a)}$	motor constant of joint j
$\mathbf{K}$	stiffness matrix
$\mathbf{K}_0$	linearised stiffness matrix
$\mathbf{K}^{(H)}$	proportional gain matrix of transferfunction
l	rank of a matrix
$\boldsymbol{l}$	relative position vector
$m^{[k]}$	mass of lumped body k
$\mathbf{M}$	mass matrix
n_j	gear ratio of joint j
$n_{\bar{x}}, n_{\bar{y}}, n_{\bar{z}}$	orthogonal triads
$N^{(e)}$	number of deformation mode parameters associated with large relative displacements and rotations
$N^{(em)}$	number of drive rotations
$N^{(\epsilon)}$	number of deformation mode parameters associated with small elastic deformations
$N^{(\epsilon m)}$	number of joint and drive deformations
$N^{(f)}$	number of frequencies
$N^{(m)}$	number of periods
$N^{(o)}$	number of phase realisations
$N^{(p)}$	number of dynamic parameters
$N^{(q)}$	number of generalised coordinates
$N^{(r)}$	number of generalised rigid-body modes
$N^{(t)}$	number of time steps
$N^{(u)}$	number of inputs
$N^{(y)}$	number of outputs
$\mathbf{N}_0$	dynamic stiffening matrix
$\mathbf{O}^{(ff)}$	feed-forward matrix, in which each column corresponds to one experiment
p_r	r^{th} pole of transfer function
$\boldsymbol{p}$	vector of dynamic parameters
$\boldsymbol{p}^{(E)}$	vector of dynamic parameters projected on the essential parameter space
$\boldsymbol{p}^{(l)}$	vector of lumped mass parameters

$\mathbf{P}^{(0)}$	true linear time-invariant multi-variable system
$\mathbf{P}^{(B)}$	bias error of linear time-invariant multi-variable system
$\mathbf{P}^{(R)}$	related linear time-invariant multi-variable system
$\mathbf{P}(s)$	linear time-invariant multi-variable system
$\boldsymbol{q}$	vector of generalised coordinates
$\boldsymbol{r}$	vector of reference joint positions
$R_j^{(\epsilon)}$	correlation of residual ϵ_j
$\mathbf{R}$	rotation matrix
$\boldsymbol{s}^{[k]}$	vector defining the centre of mass of the lumped body k
t_n	n^{th} time step
$\mathbf{T}$	coordinate transformation matrix
$\mathbf{T}^{(p)}$	coordinate transformation matrix for markers in set p
$\boldsymbol{U}$ / $\boldsymbol{u}$	vector of measured inputs
$\boldsymbol{U}^{(v)}$ / $\boldsymbol{u}^{(v)}$	vector of stochastic input noise
$\boldsymbol{U}^{(0)}$ / $\boldsymbol{u}^{(0)}$	vector of true input
$\mathbf{U}$	matrix with input vectors / left singular matrix
$\boldsymbol{v}^{(c)}$	vector of controller noise
$\boldsymbol{v}^{(p)}$	translation vector for markers in set p
$\boldsymbol{v}^{(p)}$	vector of process noise
$V^{(IWLS)}$	objective function iterated weighted least squares estimation
$V^{(ML)}$	objective function maximum likelihood estimation
$\mathbf{V}$	right singular matrix
w	weighting coefficient of the iterated weighted least squares method
$\mathbf{W}$	weighting matrix
$\boldsymbol{x}$	vector of nodal coordinates
$\boldsymbol{x}^{[i](p)}$	position vector marker i in set p
$\boldsymbol{y}$	measurement vector
$\boldsymbol{Y}$ / $\boldsymbol{y}$	vector of measured outputs
$\boldsymbol{Y}^{(0)}$ / $\boldsymbol{y}^{(0)}$	vector of true output
$\boldsymbol{Y}^{(NL)}$	vector of outputs nonlinear model
$\boldsymbol{Y}^{(s)}$	vector of stochastic nonlinear output distorsions
$\boldsymbol{Y}^{(v)}$ / $\boldsymbol{y}^{(v)}$	vector of stochastic output noise
$z_{j,k,r}$	zeros of transfer function matrix
$\boldsymbol{Z}$	measurement vector
$\boldsymbol{Z}^{(s)}$	vector of stochastic nonlinear distorsions
$\boldsymbol{Z}^{(v)}$	vector of stochastic noise
$\boldsymbol{Z}^{(0)}$	vector of true input and output data

Greek symbols

$\alpha_{j,k}$	scalar in a Multivariable Frequency Response Function
$\delta_j^{(a)}$	Stribeck velocity power of joint j
$\delta_j^{(v)}$	viscous friction power of joint j
$\boldsymbol{\epsilon}$	vector with elastic deformations / weighted residual
$\boldsymbol{\epsilon}^{(m)}$	vector of independent joint and drive deformations
$\boldsymbol{\epsilon}^{(1m)}$	vector of independent drive deformations
$\boldsymbol{\epsilon}^{(2m)}$,$\boldsymbol{\epsilon}^{(3m)}$	vector of independent joint deformations
ζ	relative damping coefficient
θ_j	rotation of joint j
$\boldsymbol{\theta}^{(m)}$	vector of joint angles
$\dot{\theta}_j^{(s)}$	Stribeck velocity of joint j
$\boldsymbol{\lambda}$	vector of Euler parameters
$\boldsymbol{\Lambda}$,$\boldsymbol{\Lambda}'$	3×4 Euler transformation matrices
$\boldsymbol{\nu}^{[r]}$	eigenvector
$\mathbf{N}$	eigenvector matrix
$\boldsymbol{\rho}$	residual
$\boldsymbol{\sigma}$	stress vector / singular value
$\sigma^{(c0)}$	pre-stress in gravity compensating spring
$\sigma^{(ec)}$	stress in gravity compensating spring
$\boldsymbol{\sigma}^{(d)}$	global stress vector of structural damping
$\boldsymbol{\sigma}^{(em)}$	global stress vector that is dual to $\mathbf{e}^{(m)}$
$\boldsymbol{\sigma}^{(k)}$	global stress vector of structural stiffness
$\boldsymbol{\sigma}^{(\epsilon m)}$	global stress vector that is dual to $\boldsymbol{\epsilon}^{(m)}$
$\boldsymbol{\Sigma}$	singular value matrix
$\tau_j^{(a,0)}$	asperity friction torque of joint j
$\tau_j^{(f)}$	friction torque of joint j
$\tau_j^{(ff)}$	feed-forward torque of joint j
$\tau_j^{(f,s)}$	sliding friction torque of joint j
$\tau_j^{(a)}$	driving torque of joint j
$\boldsymbol{\Upsilon}$	input selection matrix
$\mu_{j,k}^{[r]}$	anti-resonance frequencies
ϕ	angle
$\boldsymbol{\Phi}$	system matrix
$\bar{\boldsymbol{\Phi}}$	reduced system matrix
$\omega^{[r]}$	resonance frequency
$\boldsymbol{\omega}$	angular velocity / angular frequency
$\boldsymbol{\Omega}$	resonance frequency matrix

List of conventions

$\mathcal{C}$	complex number
$\mathcal{R}$	real number
$\mathcal{E}\{\}$	expected value
D	differential operator
d	derivative
∂	partial derivative
δ	virtual infinitesimal variation
^{H}	Hermitian transpose: complex conjugate matrix transpose
^{T}	matrix transpose
$\dot{}$	time derivative
$\tilde{}$	defines a skew symmetric matrix of a vector, see equation (3.24)
$<,>$	scalar product
$\hat{}$	estimation
$\frown$	see equation (3.52)
subscript	index
superscript	power
[superscript]	index: element [k] / experiment [m] / phase realisation [o]
(superscript)	name
italic	scalar
italic bold	vector
CAPITAL BOLD	matrix
CAPITAL	Fourier transform

List of abbreviations

DOF	Degrees Of Freedom
EV	Errors in Variables
JCS	Stäubli Combined Joint
LED	Light Emitting Diode
LTI	Linear Time Invariant
LTV	Linear Time Varying
MFRF	Multivariable Frequency Response Function
PID	Proportional, Integrating and Derivative
SISO	Single Input Single Output
SIMO	Single Input Multiple Output
MIMO	Multiple Input Multiple Output
ML	Maximum Likelihood

Chapter 1

Introduction

The applicability of industrial robots is restricted by the tip accuracy, in particulary for applications in which industrial robots need to track a trajectory at high speed. An example of such an application is robotised laser welding. During laser welding, products are welded with a focussed high power laser beam. The manipulator has to move the focus of the high-power laser beam along the weld seam. Typically, an accuracy of about 0.1 mm is required at speeds higher than 50 mm/s. At these speeds, the accuracy of industrial robots is often insufficient for the laser welding task.

The accuracy of industrial robots is limited by several aspects, e.g. manufacturing tolerances, joint friction, drive nonlinearities and tracking errors of the feedback controller. In addition, flexibilities in the drives and joints of these robot manipulators significantly limit their accuracy. Because of these flexibilities, the robot tip will vibrate along the desired trajectory and deflects due to gravitational forces. These flexibilities not only limit the accuracy but also the dynamic performance, since flexibilities in the manipulator decrease the maximum bandwidth of feedback controllers.

A realistic model of the dynamic behaviour of a robot would offer the possibility of accurately predicting its tip position. Tip predictions can be used for off-line programming to decide whether or not a robot can perform a task within the required tolerance, which would otherwise require costly machine time for tests on production facilities. A realistic model can also be used to develop an advanced model-based robot controller, that will drive the robot more accurately. For example, Iterative Learning Control can increase the tip accuracy almost to the level of repeatability, provided that a sufficiently accurate dynamical model of the robot is available.

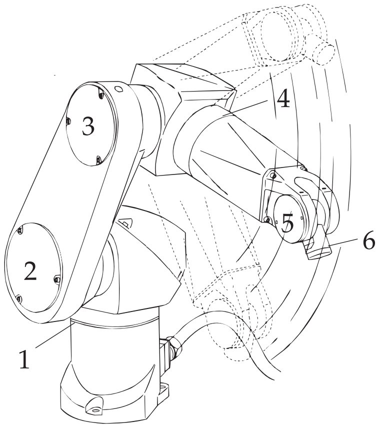

Figure 1.1: Depiction of the Stäubli RX90B industrial robot.

1.1 Problem statement

The previous examples show the need for accurate dynamical models of industrial robots. For cases in which the flexibilities can be ignored, the rigid modelling and identification of industrial robot manipulators is an area that has been explored more or less in its entirety and standard techniques described in textbooks exist, see Kozlowski (1998); Khalil and Dombre (2002). However, for cases in which flexibility does play a role, the modelling and especially the identification of industrial robots is still an active research area. The goal of this work is related to this:

The development of modelling and identification techniques that include the effects of flexibilities, aiming at the prediction of the tip motion of industrial robots.

The modelling and identification techniques developed in this thesis will be applied on a Stäubli RX90B industrial robot. A depiction of this six degree of freedom robot is given in figure 1.1. To predict the tip motion during welding, Waiboer (2007) developed a realistic closed-loop simulation model of the Stäubli RX90B robot. This model includes a finite element description of the rigid body dynamics, an accurate description of the joint friction and a model of the industrial motion controller.

To improve the accuracy of this simulation model, the dominant flexibilities of the robot manipulator should be included in the model. Measurements performed on the Stäubli RX90B, which will be explained in section 4.1, showed that the dominant stiffness of this robot is located in both the drives and the joints. A finite stiffness in the bearings of a joint results in a bending stiffness of the joint perpendicular to the rotation axis of the joint. This stiffness will be called *joint stiffness*. The torsional stiffness of the drive system, due to a finite stiffness of axes and gears, will be called *drive stiffness*.

1.2 Contributions

As will be demonstrated in chapter 2, no standard techniques are available for the modelling and identification of industrial robots containing joint and drive flexibilities. The modelling and identification techniques proposed in this thesis make use of results from several research areas, such as flexible multibody dynamics, inverse eigenvalue problems and system identification. In this thesis some contributions have been made to these research areas, which can be summarised as follows:

- To identify the dynamic parameters of nonlinear finite element models (Jonker and Meijaard (1990)), a new lumped mass formulation is developed, which is linear with regard to the dynamic parameters. Since with this formulation the number of elements can be reduced, it also has advantages for simulation.

- Static measurements have shown that the joint and drive flexibility of the Stäubli RX90B are of the same order of magnitude. A model is developed which includes both flexibilities.

- A linear least squares identification method is developed to identify the dynamic parameters of the robot model, including mass and stiffness parameters. Simulations show that this method yields an accurate model of the robot, provided that all degrees of freedom (the large joint rotations and the small elastic deformations) can be measured.

- An alternative parameter identification method is developed, which requires only motor encoder and motor current data. This inverse eigenvalue parameter identification method is based on the work of Hovland et al. (2001). Using their method it is required that the feedback controllers are switched off. Furthermore, the extraction of the eigenvalues from experimental data is unspecified and their models include only drive flexibilities. The first requirement is made redundant by using Multiple Input Multiple Output (MIMO) closed-loop identification experiments. Frequency domain system identification techniques are proposed to extract the required eigenvalues frequencies from experimental data. In addition, it is shown that although only drive flexibilities can be identified, the new method can be applied to robots with both joint and drive flexibilities.

- The norms of the eigenvectors of an eigenvalue problem can be chosen arbitrary. To solve the inverse eigenvalue problem the eigenvectors are normalised with respect to the mass matrix. By using this mass normalisation, an sofar implicitly defined scaling factor in the Multivariable Frequency Response Function (MFRF) of a mechanical system is proven to be an element of the inverse mass matrix. Furthermore, relations for the amplitude of the MFRF at infinitely high and low frequencies are derived using this mass normalisation of the eigenvectors.

- Accurate identification of a MFRF from experimental data requires an appropriate description of the model structure and the noise conditions. Therefore, the influence of nonlinear distortions arising from robot nonlinearities are included in a linear errors in variables stochastic framework. To exclude the nonlinearities of the controller in the estimation of the noise covariances, a new reference signal is proposed for the mapping of the input and output signals of several experiments to a common input signal.

- The identification of a transfer function matrix from experimental robot data requires more functionality than implemented in available frequency domain system identification toolboxes. Therefore, a new toolbox is developed which includes this functionality, namely: starting the estimation with a user defined initial model, adding parameter constraints, using a pole-zero parametrisation of a common denominator transfer function matrix, and using symmetric input and output relations.

1.3 Outline of this thesis

Chapter 2 presents a literature overview of robot modelling and identification techniques. Chapter 3 presents the proposed model of the Stäubli RX90B industrial robot. The equations of motion are written in forms suitable for simulation and parameter identification. Chapter 4 presents the identification of the joint and drive stiffnesses using static measurements. Furthermore, a linear least squares parameter identification technique is presented, which is able to identify the dynamic parameters provided that the full robot motion can be measured sufficiently accurately. In chapter 5, an inverse eigenvalue technique is presented to identify the dynamic parameters of the drives using only motor encoder and motor current measurements. Chapter 6 presents a frequency domain system identification technique to estimate the eigenvalues needed for this identification technique. The theory is illustrated with numerical simulations and experimental measurements of the StäubliRX90B industrial robot. Chapter 7 discusses the conclusions from preceding chapters and presents recommendations for further research.

Chapter 2

State of the art

An overview of the available techniques to model and identify robot manipulators is given in this chapter.

Outline

First, a literature overview of the modelling of flexible robots is presented. Next, a literature overview of the techniques to identify the dynamic parameters of these models will be given.

2.1 Modelling of flexible robots

A vast amount of literature on the modelling of flexible robot manipulators is available. First, an overview of the techniques to describe robots with joint stiffness will be given. In section 1.1, joint stiffness is defined as the bending stiffness of a joint perpendicular to the rotation axis of the joint, arising from a finite stiffness of the joint bearings. Next, an overview regarding the modelling of drive flexibilities will be given. The presented approaches will be discussed in the section 2.1.3.

2.1.1 Joint stiffness

Several formulations are proposed to model flexible joint manipulators as a serial chain composed of rigid bodies and joints (Jain and Rodriguez (1993); Khalil (2000); Swain and Morris (2003)). Each joint describes either a large joint rotation or a small flexible deformation, see figure 2.1.

Khalil (2000) presents a recursive dynamic model for flexible joint robots, which is an extension of the recursive Newton-Euler method for rigid serial robots, described in the textbooks of Kozlowski (1998); Khalil and Dombre (2002). In general, recursive Newton-Euler methods are efficient in terms of

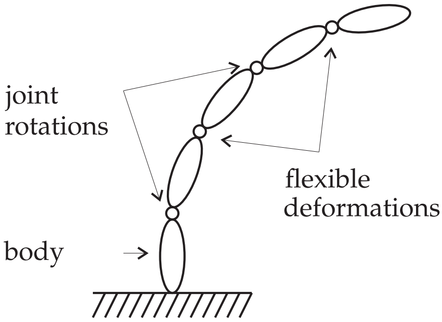

Figure 2.1: Schematic representation of a robot model with joint flexibilities

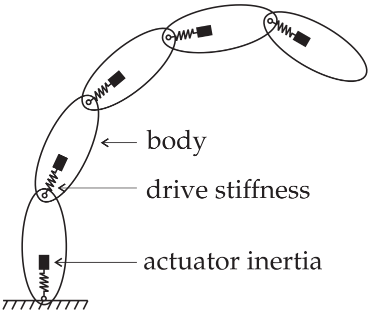

Figure 2.2: Schematic representation of a joint with drive flexibility

the number of mathematical operations. The (modified) Denavit-Hartenberg notation is used to describe the relative position and orientation of two succeeding bodies. This formulation is used for describing both the large joint rotations and the flexible deformations. The algorithms for the forward and inverse dynamic problems consist of three recursive loops. Within these loops, the joint accelerations or joint torques are computed as functions of the positions and velocities of the links and actuators.

In addition, Jain and Rodriguez (1993) present a recursive Newton-Euler algorithm to compute the inverse dynamics of flexible joint robots. The model is based on the concept of the decomposition of the manipulator into an active and a passive manipulator system. The active system is related to the large joint rotations and the passive system is related to the flexible motion. Then, the respective independent motions are superimposed to represent the complete system. The presented algorithm is a combination of the existing inverse and forward recursive algorithms for rigid manipulators.

Swain and Morris (2003) state that the inherent assumption of linear separability of a flexible manipulator into its active and passive subsystems to formulate the model may not represent the true dynamic model of the original manipulator system. A new formulation is presented without the need for this assumption. In both references the kinematics of the manipulator model are described with spatial operator algebra, see Rodriguez et al. (1991).

2.1.2 Drive stiffness

In control literature, flexible robot manipulators are usually modelled using lumped elasticities in the robot drives. In this case, each drive system is modelled as a one degree of freedom mass-spring-damper system. The spring and damper are located between the actuator inertia and the inertia representing the link. The inertia and mass properties of the links are usually modelled by rigid bodies. Figure 2.2 shows a schematic representation of a joint with drive flexibility. To facilitate readability, the damper has been omitted.

The drive model is based on two assumptions regarding dynamic coupling between the actuators and the links (Spong (1987)). First, it is assumed that the kinetic energy of the rotor is due only to its own rotation. Equivalently, the motion of the rotor is a pure rotation with respect to an inertial frame. The gyroscopic interactions between the actuator and the links are neglected. Second, it is assumed that the rotor/gear inertia is symmetric with regard to the rotor axis of rotation so that the gravitational potential of the system and also the velocity of the rotor centre of mass are both independent of the rotor position. In general, these two assumptions hold true for robots with high gear ratios. As a result the actuator inertia of these robots can be modelled by a one degree of freedom rotational inertia. A different approach is presented by Ochier et al. (1995) and Mata et al. (2005). In their work the actuator is modelled as a rigid body instead of a rotational inertia only.

2.1.3 Discussion

The modelling of robots with elasticity in both the drives *and* the joints has not received much attention so far. The models presented above either have flexibilities in the joints or in the drives. However, for realistic dynamic simulations of the Stäubli RX90B, the effects of both joint and drive flexibilities should be included in the model. No suitable model is available from the above quoted literature and hence it has been developed within the scope of this work.

The basic principles of mechanics can be used to derive a model describing the equations of motion for this specific robot. According to Miro and White (2002), several authors have published articles showing that for any given manipulator, customised closed form dynamic formulations are more efficient than the best of the general schemes. However, the loss of generality makes it less attractive for this work.

The finite element method (FEM) presented by Jonker (1989) is able to incorporate both flexibilities in a dynamic robot model using a so-called hinge element (Geradin et al. (1986)). The key point in this finite element formulation is the specification of a set of deformation parameters that are invariant under rigid body motion (Besseling (1982)). Using this formulation, Waiboer (2007) presented a model of the Stäubli RX90B robot, describing the rigid body dynamics. Because both type of flexibilities can be incorporated, it is also a promising formulation for the flexible model as will be shown in chapter 3.

2.2 Parameter identification for robot models

Accurate knowledge of the model parameters is important for obtaining a reliable and accurate dynamic robot model. Determination of these parameters from CAD data may not yield a complete representation because it may not include dynamic effects like joint friction, joint and drive elasticity and masses introduced by additional equipment. Experimental parameter identification using the assembled robot may be the only reliable method to determine accurate values for the parameters.

Regarding rigid models standard techniques are available for the identification of the robot parameters, as outlined below. An extension to flexible models is not straightforward and will be discussed separately.

2.2.1 Parameter identification for rigid robot models

A general overview of the parameter identification methods for rigid robots can be found in textbooks like Kozlowski (1998); Khalil and Dombre (2002). Experimental robot identification techniques estimate dynamic robot parameters based on motion and force/torque data that are measured during robot motions along optimised trajectories (Armstrong (1989); Swevers et al. (1996)). Most of these techniques are based on the fact that the dynamic robot model can be written as a linear set of equations with the dynamic parameters as unknowns. A formulation such as this allows the use of linear estimation techniques that find the optimal parameter set in a global sense.

However, not all parameters can be identified using these techniques since some of the parameters do not affect the dynamic response or affect the dynamic response in linear combinations with other parameters. The null space is defined as the parameter space containing parameter combinations that do not affect the dynamic response. Gautier and Khalil (1990) and Mayeda et al. (1990) present a set of rules based on the topology of the manipulator system to group the dependent inertia parameters and to form a minimal set of parameters that uniquely determine the dynamic response of the robot. In addition, numerical techniques like the QR decomposition used by Khalil and Dombre (2002) or the Singular Value Decomposition as described in the work of Shome et al. (1998) can be used to find the set of minimal or base parameters. In general the base parameter set obtained from a linear parameter fit is not guaranteed to be a physically meaningful solution. Waiboer et al. (2005a) suggest that the identified parameters become more physically convincing by choosing the null space in such a way that the estimated parameters match a priori given values in least squares sense. This requires an a priori estimation of the parameter values and a sufficiently accurate description of the null space, neither of which are trivial, in general. Mata et al. (2005) force a physical feasible solution by adding nonlinear constraints to the optimisation problem.

However, adding nonlinear constraints to a linear problem gives a nonlinear optimisation problem for which it is hard to find the global minimum.

Optimisation of the excitation trajectory by minimising the influence of measurement noise is necessary to guarantee sufficient excitation of all parameters. Armstrong (1989) and Gautier and Khalil (1992) propose criteria for finding optimal trajectories when using a least squares identification method. Since the sensitivity of a least squares solution to measurement noise depends on the condition number of the regression matrix, they used the value of the condition number as a criterion for finding the optimal excitation trajectories. Swevers et al. (1996) and Olsen and Petersen (2001) present an experimental estimation technique using maximum likelihood estimation to solve the noise problem. With regard to the excitation trajectories, it is advantageous for them to be periodic, which enables averaging of measurements in order to reduce stochastic measurements noise. In addition, controlling the frequency contents of the excitation is needed to avoid excitation of vibrations due to flexibilities. Therefore, Swevers et al. (1996) and Olsen and Petersen (2001) advice the use of harmonic excitation trajectories.

2.2.2 Parameter identification for flexible models

The linear least squares identification procedure used for the identification of rigid robot models assumes that the position signal of all degrees of freedom are known or can be measured. If the position of all degrees of freedom including the corresponding velocities and accelerations are known, the dynamic model can be written as a linear set of equations with the dynamic parameters as unknowns. For industrial robots, usually only motor position and torque data is available. Therefore, measurements from additional degrees of freedom arising from flexibilities are not readily available and consequently the linear least squares technique cannot be used for flexible robot models. Several authors suggest the application of additional sensors to measure the elastic deformations, e.g. acceleration sensors (Pham et al. (2002)), link position and/or velocity sensors (Tsaprounis and Aspragathos (2000), Huang (2003)) or torque sensors (Albu-Schäffer and Hirzinger (2001)). First, an overview of identification techniques using these additional sensors will be given. Next, an overview of approaches without the need to apply additional sensors will be given. This section will conclude with a discussion of the presented approaches.

Identification using additional sensors

Pham et al. (2002) present an identification method for the dynamical parameters of simple mechanical systems with lumped elasticity. The parameters are estimated by using the solution of a weighted least squares system of an overdetermined system that is linear with regard to a minimal set of parameters and obtained by sampling the dynamic model along a trajectory. Two different cases are considered regarding the types of measurements available for identification. In the first case, it is assumed that measurements for the motor and the load position are available. In the second case, it is assumed that measurements for the motor position and the load acceleration are available. Instead of the reconstruction of the load position by integration of the measured acceleration, they suggest differentiating the dynamic equations twice. However, problems arise for non-continuous terms like joint friction. The use of a so-called chirp signal as excitation signal should reduce the influence of the dynamic behaviour, which is represented by these non-differentiable terms, on the measured data.

Tsaprounis and Aspragathos (2000) suggest the use of both position and velocity signals to build an adaptive tracking controller for robots with drive elasticity. The adaptive estimator identifies the parameters of both the flexible and the rigid subsystems; the drive stiffness is assumed to be known. Huang (2003) presents an adaptive observer for identifying the parameters of a single-link flexible drive manipulator, using the position and velocity measurements of the joint and drive. The motor inertia must be known a priori. In both references, only simulation results are presented.

Alici and Shirinzadeh (2005) performed static identification experiments to identify the drive stiffness of a Motoman SK120 industrial robot. They applied a force to the tip using a cable-pulley system and deadweights. A force/torque tip sensor measured the applied load. The resulting tip displacement was measured using a laser tracking system. Based on measured tip data, the drive stiffness values for three joints were identified.

Albu-Schäffer and Hirzinger (2001) performed identification experiments on a 7 DOF experimental robot with position sensors on both the motors and the links. The torque responsible for the elastic deformation of the transmission system was measured with an additional torque sensor. The robot links were modelled rigid and only drive flexibilities were present. The rigid body dynamic parameters were estimated from 3D CAD data. The joint friction parameters and motor constants were identified using a linear least squares estimation. The friction was identified independent of the other parameters by choosing a trajectory that only excites the friction parameters, namely a saw tooth profile for the joint position with different constant velocities. The stiffness and damping parameters were obtained from an impulse response generated by abruptly stopping the motors by closing the brakes. The resulting vibrational motion was recorded on the torque sensors. To improve the accuracy of the estimations the dynamic parameters were identified before assembly in a dedicated test bed.

Identification without additional sensors

From a practical point of view, the application of additional sensors for identification is not preferred. Adding additional internal sensors to industrial robots is expensive or even impossible. Therefore, several authors propose methods that only require motor torque and motor position signals. An overview of these methods will be given below.

Instead of measuring the elastic deformations with additional sensors, they can be solved from the equations of motion as a function of the unknown parameters. In general, this yields dynamic equations which are nonlinear in the dynamic parameters. As a result, nonlinear optimisation techniques such as those presented by Wernholt and Gunnarsson (2005) and Hakvoort (2004) are required to estimate the parameters. As stated by Albu-Schäffer and Hirzinger (2001), these techniques suffer from the fact that local minima are often obtained, in which case the estimated parameters are very different from the real physical parameters. For this approach to succeed initial parameter values are required that are sufficiently accurate.

In the approach proposed by Pham et al. (2001), only the position and torque data from the motors is used to identify a robot model with drive flexibilities. A nonlinear combination of the original parameters is identified using the linear least squares solution of an overdetermined linear system, obtained from sampling the dynamic model along a trajectory. Afterwards, the original parameters are extracted from the identified nonlinear combinations. In order to write the system in a parameter linear form, gravitation forces and Coulomb joint friction are removed from the dynamic equations. To minimise the influence of joint friction and gravity on the measurements obtained from excitation experiments, the authors proposed the tracking of a chirp signal.

Hovland et al. (1999) presented an approach for the identification of the drive flexibilities for industrial robots. The proposed method assumes that the parameters concerning the rigid-body dynamics are known a priori, including the motor inertia. During an identification experiment, the motor positions and motor torques are measured and the motor velocities and accelerations are computed off-line using Fourier techniques. The equations of motion are transformed to the frequency domain in a form linear in the unknown parameter vector, containing the stiffness and damping parameters of the joints. The parameter vector is estimated by using the weighted least squares solution of an overdetermined system obtained from sampling the transformed equations of motion along the measured trajectory. The authors present experimental results for an industrial ABB robot.

Some of the robot identification methods presented in literature originate from model updating techniques used for finite element models, Berglund and Hovland (2000); Hovland et al. (2001). For updating finite element models, it is usually impossible to measure all degrees of freedom. The number of degrees of freedom is usually very large and the number of measurements is limited. So, a lack of sensors is commonly present. A good overview of the possibilities of so-called model updating techniques is given in textbooks written by Gladwell (1986); Friswell and Mottershead (1995) and Ewins (2000). According to Ewins (2000), it is convenient to group the model updating techniques into two groups: direct matrix methods, which are those methods in which individual elements in the mass and stiffness matrices are adjusted directly from the comparison between test data and the initial model; and indirect, physical property adjustment methods, in which changes are made to specific physical or elemental properties in the model. Probably for historical reasons, a lot of techniques use measured modal data as input, often extracted from frequency response functions. Another group of algorithms uses the frequency response function directly.

Berglund and Hovland (2000) presented a direct method using modal data to identify the dynamic parameters of a mass-spring-damper equivalent of any order using only the motor position and motor torque. The identification method was applied to one joint of an industrial ABB robot. At first, a friction model is identified by moving a robot joint at low speeds without excitation of the flexibilities. The friction model is used to remove the friction effects from measured torque data before the other parameters are estimated.

Secondly, the stiffness and mass parameters are identified using a measured frequency response function describing the dynamic behaviour from motor torque to motor acceleration. At this stage it is assumed that the damping is small and may be neglected. The peaks and valleys in the frequency response function correspond to the resonance and anti-resonance frequencies of the system. By using the Lanczos algorithm (Gladwell (1986)), the system matrix of a generalised eigenvalue problem can be reconstructed from the eigenvalues and the first coordinate of the eigenvectors. The eigenvalues correspond to the resonance frequencies of the frequency response function. The first coordinates of the eigenvectors are computed from the measured resonance and anti-resonance frequencies. A serial connected mass-spring model has a diagonal mass matrix and a symmetric three-diagonal stiffness matrix. This special structure is exploited to extract the stiffness and mass parameters from the system matrix. The mass parameters can be computed up to a scale factor. The low frequency amplitude of the frequency response function corresponds to the sum of all masses and can be used to compute the scale factor.

Thirdly, the damper coefficients are identified by minimising the difference between the heights of the measured and modelled anti-resonance peaks in a least squares sense using a nonlinear optimisation method.

In Hovland et al. (2001) the method is extended to the identification of multiple joints of a robot. The robot model contains drive flexibilities and coupled dynamics between the joints. Because of the inertia coupling, the reduced mass matrix has off-diagonal terms and the standard Lanczos algorithm cannot be applied. Instead, a partial identification is performed with the first step of the

Lanczos algorithm and iteratively the order of the system is reduced. The coupled inertia terms in the mass matrix are identified from the low-frequency behaviour of the cross-excited frequency response functions. The method requires that for all joints a proportional controller is active and can be switched off during the excitation of a specific joint.

In the frequency response methods a measured frequency response is directly compared with the response of an analytical model, without the use of eigenvalue and eigenvector data. Examples of the frequency response technique are given by Imregun et al. (1995b,a) and Modak et al. (2002). The methods update physical parameters for finite element models, so they belong to the indirect updating methods.

In general, the modal updating techniques only update linear models. Industrial robots show nonlinear position and velocity dependent dynamics. Chen and Beale (2003) present a method to combine identified linear models at different operation points into one nonlinear physical parameterised model.

System identification theory gives several algorithms to estimate higher order state space or transfer function models from a limited number of in- and outputs, for example using prediction error methods or subspace techniques. Applications in the field of flexible robot identification are presented below.

Östring et al. (2003) present a grey-box identification of a physically parameterised three-mass model of an industrial robot. The model is based on the first joint of an ABB IRB 1400 robot. The identified model is a time invariant state space model with a pre-defined model structure. The estimates of the moments of inertia and spring stiffness, obtained using different data sets, are almost equal, while the estimates of the friction and damping coefficients fluctuate considerably.

Wernholt and Gunnarsson (2005) use a nonlinear grey-box identification to identify an industrial robot. A three-step identification procedure is proposed in which parameters for rigid body dynamics, friction and flexibilities can be identified using measurements on the motor axes only. In the first step, an initial estimate of the rigid body and friction parameters is performed using standard linear regression techniques. In the second step, an initial estimation of the flexibilities using the method devised by Hovland et al. (2001) is proposed. In the third step, the parameters of a nonlinear physical parameterised grey-box model are identified directly in time domain using the System Identification Toolbox of MATLAB.

In addition, black box state space models have been considered in literature for the estimation of mass, stiffness and damping matrices. De Angelis et al. (2002) present a methodology to identify the mass stiffness and inertia parameters for a general linear second order system from identified state-space matrices. The minimum requirement for the proposed methodology is that all of the degrees of freedom should contain either a sensor or an actuator, with at least one co-located sensor-actuator pair. In the work of Lus et al. (2003)

it is shown that if a system is insufficiently instrumented with sensors and actuators, it is still possible to create reduced order mass-damping-stiffness models that incorporate measured and unmeasured degrees of freedom.

Adaptive observers estimate both states and unknown parameters. The work of Tsaprounis and Aspragathos (2000) and Huang (2003) has already been discussed. Both references assume that the position and velocity of the motors and the links can be measured. Östring and Gunnarsson (2004) show an approach for the identification of three dynamic parameters of a single link flexible robot model, with only measurements on the motor axis. The total amount of parameters that can be updated is limited, because some information about the system is required to update the states and parameters in the observer. In general, there is no restriction as to which parameters can be updated. The paper shows experimental results for an industrial ABB robot. For this robot the motor constant, the link inertias and the viscous friction coefficient are estimated.

Discussion

Many of the references previously mentioned present only simulation examples or show results for self designed experimental robots. Only a few references show experimental results for industrial robots (Berglund and Hovland (2000); Hovland et al. (2001); Östring et al. (2003); Östring and Gunnarsson (2004); Wernholt and Gunnarsson (2005)). The identified models of Berglund and Hovland (2000); Östring et al. (2003); Östring and Gunnarsson (2004) are restricted to linear models of only one joint. Hovland et al. (2001); Wernholt and Gunnarsson (2005) identified models with several joints but their models contain only drive flexibilities. Furthermore many of the presented techniques require some a priori knowledge of the system. The drive stiffness, the motor inertia or the inertia parameters of the links, for instance, are assumed to be known. The accuracy of these assumed parameters may be limited and fixing one parameter to a wrong value will ruin the fit for the other parameters. Therefore, using a priori data should only be allowed if these parameters are known with sufficient accuracy.

From the presented overview it can be concluded that there is still a need for better identification techniques to estimate the dynamic parameters of industrial robots containing joint and drive flexibilities. This work is, to a large extent, devoted to this need. Some of the previously mentioned approaches provide a starting point to tackle the identification problem. Basically, two approaches are selected as the promising techniques of this thesis.

The first technique addressed in this thesis is the linear least squares technique using additional sensors to measure the elastic deformations. Although measuring all degrees of freedom with external sensors can be quite complicated or even impossible, the use of a linear least squares technique has several advantages as compared to nonlinear methods. Most important is that the global minimum can always be found even without initial values.

The second technique investigated in this thesis is the one presented by Hovland et al. (2001). Although an extension is required for joint stiffness, a global solution can also be found for the parameters without the requirement of initial values. The method is based on frequency domain data, offering the possibility to interpret intermediate results and provide insight in the model structure.

Chapter 3

Robot modelling

A nonlinear finite element method, as described by Jonker (1990), is used to derive the equations of motion for the Stäubli RX90B robot. In this method, the equations of motion are derived using Lagrange's form of Jourdain's principle. The SPACAR computer programme, based on this finite element formulation, has been developed (Jonker and Meijaard (1990)) for the dynamic analysis and simulation of (elastic) mechanisms that can be assembled from basic components, including beams, hinges, sliders, springs and dampers. The programme also allows the analytic generation of locally linearised models around a nominal trajectory (Jonker (1991); Meijaard (1991)). Interfaces for simulation and control system design with MATLAB and SIMULINK have been developed by Jonker and Aarts (1998). In this work, the finite element formulation is extended with a new lumped mass formulation, suitable for dynamic parameter identification (Hardeman et al. (2006)).

In this formulation for each rigid beam element, representing a robot link, a rigid body is defined with equivalent mass and rotational inertia properties. Furthermore, a vector is defined that describes the centre of mass of this rigid body with respect to one of the element nodes. This vector, which is not included in the original element mass formulation, enables a parameter linear description for the equations of motion. As a result, the nonlinear finite element formulation is suitable for linear least squares parameter identification techniques. Furthermore the number of elements can be reduced, because no additional elements are required to describe the centre of mass outside the link axis.

Accurate prediction of the robot's tip motion requires that all dominant dynamic behaviour is included in the model. Waiboer (2007) developed a rigid model of the Stäubli RX90B robot using the nonlinear finite element formalism. His model includes an accurate tribological-based model of the joint friction. In this work the model is extended to include joint and drive flexibilities (Hardeman et al. (2005)).

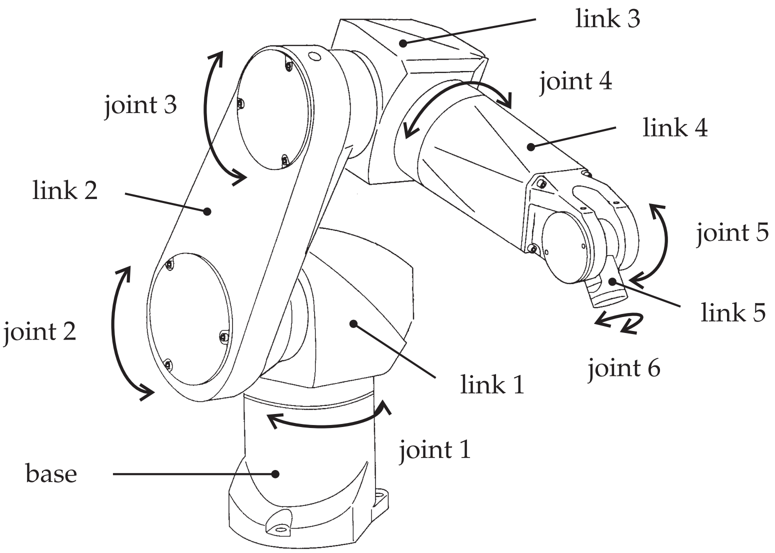

Figure 3.1: The Stäubli RX90B six axis industrial robot

Outline

This chapter starts with a description of the Stäubli RX90B industrial robot manipulator and its motion controller. Section 3.2 describes the kinematics of the manipulator, including the proposed joint assembly, and serves as an introduction to the nonlinear finite element method. The dynamic analysis of the manipulator is presented in section 3.3. An outlook on the use of the results obtained in this chapter is presented in section 3.4.

3.1 The Stäubli RX90B industrial robot

The Stäubli RX90B industrial robot is illustrated in figure 3.1. The mechanical manipulator arm of this robot consists of stiff and lightweight robot links that are interconnected by means of six revolute joints. The manipulator arm also includes a gravity compensating spring mounted inside link 2, which balances the unloaded arm.

The first four joints are equipped with a so-called JCS (Stäubli Combined Joint), which is a sophisticated assembly that includes both a cycloidal transmission and the joint bearing support (Gerat (1994)). The cycloidal transmission is driven by a servo motor via a helical gear pair, see figure 3.2. The construction of the JCS results in a high gear ratio of the driving system, namely

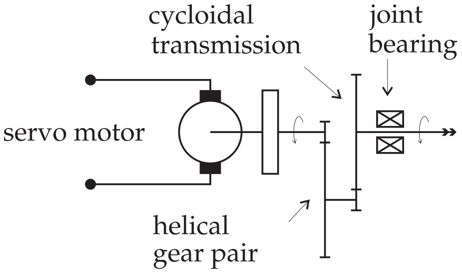

Figure 3.2: Schematic representation of the transmission inside the joint assembly, picture from Waiboer et al. (2005b)

in the order of 1:100. The last two joints in the robot's wrist are driven via a worm and wheel gear.

The servo motors are brushless three-phase servo motors. The three phase currents are replaced by one equivalent DC current, denoted by i_j, in which index j corresponds to the joint number. The motor constant, denoted by $k_j^{(a)}$, is assumed to be constant in the velocity range used for this work. The electrical current i_j supplied by electrical amplifiers is transformed by the servo motor into a torque delivered at the motor axis. From a kinematical point of view it is assumed that the transmission is ideal, i.e. no backlash or other nonlinear kinematic behaviour is present. Subsequently, for a given gear ratio n_j, the driving torque is defined as

$$\tau_j^{(a)} = k_j^{(a)} n_j i_j. \tag{3.1}$$

To prevent backlash, the transmission is highly prestressed. As a result a large part of this driving torque is dissipated by friction forces.

The robot is controlled by an industrial Stäubli CS8 motion controller, see figure 3.3. This controller contains six independent motion controllers, which compute the current commands for digital current amplifiers located inside the CS8 controller. The term independent refers to the fact that every servo motor is equipped with a Single Input Single Output (SISO) controller. The inputs of the motion controller are the joint reference position $\boldsymbol{r}$ and velocity $\dot{\boldsymbol{r}}$, which must be provided at a rate of 250 Hz. Internally these signals are upsampled using a so-called micro-interpolator. In addition, a user defined driving torque feed-forward signal, denoted by $\tau_j^{(ff)}$, can be provided as well. All servo motors are equipped with resolvers that provide the motor position and velocity for the PID (Proportional, Integrating and Derivative) feedback controller. For a more elaborate description of the Stäubli RX90B manipulator and the CS8 motion controller the reader is referred to Waiboer (2007).

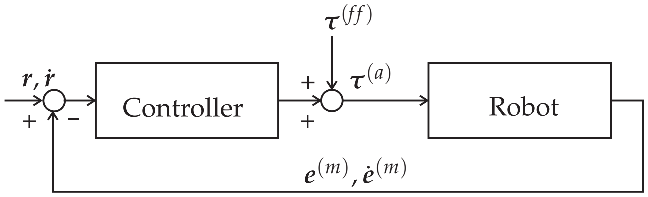

Figure 3.3: Stäubli RX90B robot with CS8 motion controller

3.2 Kinematical analysis

First, an introduction to the used nonlinear finite element method is presented. Second, the kinematics of the proposed flexible joint model are expounded. Third, the so-called geometric transfer functions are introduced.

3.2.1 Finite element representation of robot manipulators

In the presented finite element method a manipulator mechanism is modelled as an assembly of link elements interconnected by joint elements. This is illustrated in figure 3.4, in which the first four joints and links of the Stäubli RX90B robot manipulator are modelled by three different types of elements: the manipulator links are modelled by beam elements, the joints are modelled by two hinge elements each and a truss element is used to model the gravity compensating spring.

The location of each element is described relative to a fixed inertial coordi-

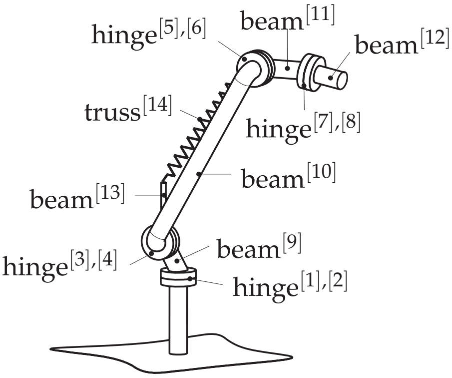

Figure 3.4: Finite element representation of Stäubli RX90B, with the element numbering indicated between the squared brackets.

nate system by a set of nodal coordinates $x_i^{[k]}$. Some coordinates may be the Cartesian coordinates of the end nodes, while others are so-called Euler parameters describing the orientation of orthogonal base vectors or triads rigidly attached to the element nodes. The superscript k between squared brackets is added to show that a specific element k is considered. With respect to some reference configuration of the element, the instantaneous values of the nodal coordinates represent a fixed number of deformation modes for the element. The number of deformation modes is equal to the number of nodal coordinates minus the number of degrees of freedom of the element as a rigid body. The deformation modes are specified by a set of deformation parameters $e_i^{[k]}$, some of which are associated with large relative displacements and rotations between the element nodes, while others describe small elastic deformations of the element and will be denoted by $\epsilon_i^{[k]}$. The components of the vector of deformation parameters $(\boldsymbol{e}^{[k]}, \boldsymbol{\epsilon}^{[k]})$ are expressed as analytical functions of the vector of nodal coordinates $\boldsymbol{x}^{[k]}$. Using this method, we can define a vector function $\boldsymbol{\mathcal{D}}^{[k]}$ for each element k:

$$(\boldsymbol{e}^{[k]}, \boldsymbol{\epsilon}^{[k]}) = \boldsymbol{\mathcal{D}}^{[k]}(\boldsymbol{x}^{[k]}). \tag{3.2}$$

A description of the deformation functions for the beam, truss and hinge elements is presented in appendix A. Up until now, the kinematics of the robot have been described on an element level. The next section describes the kinematics of a joint assembly.

3.2.2 Joint assembly for Stäubli RX90B

Each robot joint j is modelled as a substructure consisting of two hinge elements: a driving hinge element that provides the driving torque and a flexible hinge element, describing the joint and drive flexibilities; see figure 3.5.

Each hinge element has two nodes p and q at the element axis, see figure 3.6. The configuration of the hinge element is determined with two orthogonal triads $(\boldsymbol{n}_{\bar{x}}, \boldsymbol{n}_{\bar{y}}, \boldsymbol{n}_{\bar{z}})$ rigidly attached to the two end nodes. For the hinge element, three deformation functions are defined, namely a large rotation about the element axis denoted by $e_1^{[k]}$ and two small orthogonal bending deformations denoted by $\epsilon_2^{[k]}$ and $\epsilon_3^{[k]}$. For a detailed description of the hinge element the reader is referred to appendix A.

The driving hinge represents the servo motor. The relative rotation $e_1^{[k]}$ of the driving hinge is called the drive angle and is defined as the motor rotation divided by the gear ratio. The flexibilities of the joint are described by the flexible hinge. Therefore, the bending deformations $\epsilon_2^{[k]}$ and $\epsilon_3^{[k]}$ of the driving hinge are prescribed to be zero.

The elastic deformations of the flexible hinge element are assumed to be small and are denoted by $\boldsymbol{\epsilon}^{[k+1]} = (\epsilon_1^{[k+1]}, \epsilon_2^{[k+1]}, \epsilon_3^{[k+1]})$. Deformation $\epsilon_1^{[k+1]}$ is

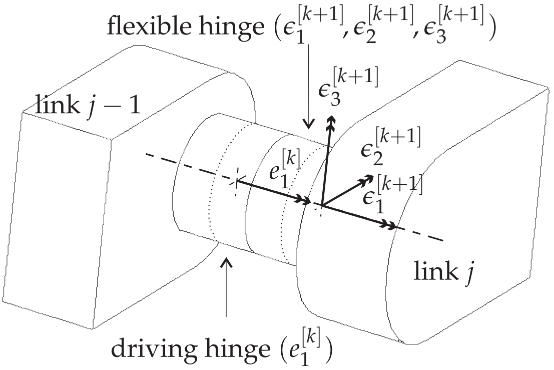

Figure 3.5: Kinematics joint assembly, in which $k = 2j - 1$

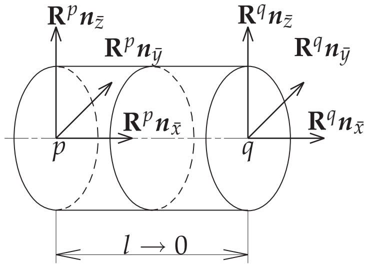

Figure 3.6: Spatial hinge element

called the drive deformation and is used to describe the drive flexibilities. The two orthogonal bending modes $\epsilon_2^{[k+1]}$ and $\epsilon_3^{[k+1]}$ are called the joint deformations and describe the joint flexibilities. The superscript $k+1$ is introduced to distinguish between the driving hinge k and the flexible hinge $k+1$. The joint and element numbering is specified in figures 3.1 and 3.4, respectively. Hence joint number j is related to element index k according to $k = 2j - 1$ for $j = 1, \cdots, 4$.

The total rotation of joint j is called joint angle and is defined by

$$\theta_j = e_1^{[k]} + \epsilon_1^{[k+1]}. \tag{3.3}$$

Differentiation of equation (3.3) with respect to time yields the joint velocity,

$$\dot{\theta}_j = \dot{e}_1^{[k]} + \dot{\epsilon}_1^{[k+1]}. \tag{3.4}$$

3.2.3 Geometric transfer functions

A manipulator model can be built up with finite elements by letting them have nodal points in common. The assemblage of finite elements is realised by defining a vector $\boldsymbol{x}$ of nodal coordinates for the entire manipulator mechanism. The deformation functions of the elements can be described in terms of the components of $\boldsymbol{x}$. These equations can be written as

$$\begin{bmatrix} e_1 \\ \vdots \\ e_{N^{(e)}} \\ \epsilon_{N^{(e)}+1} \\ \vdots \\ \epsilon_{N^{(e)}+N^{(\epsilon)}} \end{bmatrix} = \begin{bmatrix} \mathcal{D}_1(\boldsymbol{x}) \\ \vdots \\ \mathcal{D}_{N^{(e)}}(\boldsymbol{x}) \\ \mathcal{D}_{N^{(e)}+1}(\boldsymbol{x}) \\ \vdots \\ \mathcal{D}_{N^{(e)}+N^{(\epsilon)}}(\boldsymbol{x}) \end{bmatrix}, \tag{3.5}$$

or

$$\begin{bmatrix} \boldsymbol{e} \\ \boldsymbol{\epsilon} \end{bmatrix} = \begin{bmatrix} \mathcal{D}^{(e)}(\boldsymbol{x}) \\ \mathcal{D}^{(\epsilon)}(\boldsymbol{x}) \end{bmatrix}, \tag{3.6}$$

in which $N^{(e)}$ is the total number of deformation parameters of the mechanism associated with large relative displacements and rotations and $N^{(\epsilon)}$ is the total number of small elastic deformations. Kinematic constraints can be introduced by putting conditions on the nodal coordinates $\boldsymbol{x}$ as well as by imposing conditions on the deformation parameters $(\boldsymbol{e}, \boldsymbol{\epsilon})$ which are all assumed to be holonomic.

The motion of manipulator mechanisms is described by relative degrees of freedom, which are the $N^{(em)}$ drive angles denoted by $\boldsymbol{e}^{(m)}$ and the $N^{(\epsilon m)}$ elastic deformation parameters of the flexible hinges denoted by $\boldsymbol{\epsilon}^{(m)}$. The superscript m is used to denote the degrees of freedom. The total number of degrees of freedom denoted by $N^{(q)}$ equals $N^{(q)} = N^{(em)} + N^{(\epsilon m)}$. The degrees of freedom are combined into the vector of relative generalised coordinates

$$\boldsymbol{q} = \begin{bmatrix} \boldsymbol{e}^{(m)} \\ \boldsymbol{\epsilon}^{(m)} \end{bmatrix}. \tag{3.7}$$

The objective of the kinematic analysis is to solve system (3.6) for the vector of generalised coordinates in equation (3.7).

The solution for the vector of nodal coordinates $\boldsymbol{x}$ is expressed by means of geometric transfer function $\boldsymbol{\mathcal{F}}^{(x)}$ as

$$\boldsymbol{x} = \boldsymbol{\mathcal{F}}^{(x)}(\boldsymbol{e}^{(m)}, \boldsymbol{\epsilon}^{(m)}) = \boldsymbol{\mathcal{F}}^{(x)}(\boldsymbol{q}). \tag{3.8}$$

The solution for the dependent deformation coordinate $e^{(c)}$, representing the elongation of the gravity compensating spring, is expressed by

$$e^{(c)} = \mathcal{F}^{(ec)}(\boldsymbol{e}^{(m)}, \boldsymbol{\epsilon}^{(m)}) = \mathcal{F}^{(ec)}(\boldsymbol{q}). \tag{3.9}$$

By differentiating the transfer function $\boldsymbol{\mathcal{F}}^{(x)}$ with respect to time, we obtain the velocity vector

$$\dot{\boldsymbol{x}} = \frac{\partial \boldsymbol{\mathcal{F}}^{(x)}}{\partial \boldsymbol{e}^{(m)}} \dot{\boldsymbol{e}}^{(m)} + \frac{\partial \boldsymbol{\mathcal{F}}^{(x)}}{\partial \boldsymbol{\epsilon}^{(m)}} \dot{\boldsymbol{\epsilon}}^{(m)}. \tag{3.10}$$

Using the differential operator D to represent partial differentiation with respect to the vector of degrees of freedom, we write for equation (3.10)

$$\dot{\boldsymbol{x}} = \mathrm{D}\boldsymbol{\mathcal{F}}^{(x)} \cdot \dot{\boldsymbol{q}}. \tag{3.11}$$

The second time derivative of equation (3.8) yields the nodal accelerations

$$\ddot{\boldsymbol{x}} = (\mathrm{D}^2\boldsymbol{\mathcal{F}}^{(x)} \cdot \dot{\boldsymbol{q}}) \cdot \dot{\boldsymbol{q}} + \mathrm{D}\boldsymbol{\mathcal{F}}^{(x)} \cdot \ddot{\boldsymbol{q}}. \tag{3.12}$$

Differentiation of equation (3.9) with respect to time yields

$$\dot{e}^{(c)} = \mathrm{D}\mathcal{F}^{(ec)} \cdot \dot{\boldsymbol{q}}. \tag{3.13}$$

The geometric transfer functions and their derivatives are determined numerically in an iterative way.

3.3 Dynamical analysis

In the dynamical analysis, forces and torques are related to the robot's position, velocity and acceleration by means of the equations of motion. The equations of motion are derived using Lagrange's form of Jourdain's Principle (Lanczos (1970)). This principle may be defined as follows:

The virtual power of the external forces, inclusive of the inertial forces acting on an element, is equal to the internal virtual power of the element for every velocity distribution.

The external forces denoted by $f_i^{[k]}(\boldsymbol{x}, \dot{\boldsymbol{x}}, t)$, applied at the nodal points, are introduced as dual quantity of the nodal velocities $\dot{x}_i^{[k]}$. The inertia properties of the element are represented by a mass matrix $\mathbf{M}^{[k]}(\boldsymbol{x})$ and a velocity dependent force vector $\boldsymbol{f}^{[k](in)}(\boldsymbol{x}^{[k]}, \dot{\boldsymbol{x}}^{[k]})$. The principle of virtual power for element k can now be formulated as

$$\langle(\boldsymbol{f}^{[k]} - \boldsymbol{f}^{[k](in)} - \mathbf{M}^{[k]}\ddot{\boldsymbol{x}}^{[k]}), \delta\dot{\boldsymbol{x}}^{[k]}\rangle = \langle\sigma^{[k]}, \delta\dot{\boldsymbol{e}}^{[k]}\rangle, \tag{3.14}$$

for all $\delta\dot{\boldsymbol{x}}^{[k]}$ and $\delta\dot{\boldsymbol{e}}^{[k]}$ satisfying

$$\delta\dot{\boldsymbol{e}}^{[k]} = \mathrm{D}\mathcal{D}^{[k]}\delta\dot{\boldsymbol{x}}^{[k]}. \tag{3.15}$$

Equation (3.15) is derived by the differentiation of equation (3.2) with respect to time. The right hand side of equation (3.14) represents the internal virtual power of the element. The components of $\boldsymbol{\sigma}^{[k]}$ represent the dual components of $\dot{\boldsymbol{e}}^{[k]}$ and may be identified as the stress resultant vector for element k.

First, the equations for mass matrix $\mathbf{M}^{[k]}(\boldsymbol{x}^{[k]})$ and the velocity dependent force vector $\boldsymbol{f}^{[k](in)}(\boldsymbol{x}^{[k]}, \dot{\boldsymbol{x}}^{[k]})$ corresponding to a rigid body lumped on one of the nodes of the rigid beam element will be derived. The development of this section follows Jonker (1989). Second, the constitutive equations will be presented for the stress resultants $\boldsymbol{\sigma}^{[k]}$ of the driving and flexible hinges and the gravity compensating spring. Third, the principle of virtual power and the results of the first two sections will be combined yielding an acceleration linear form of the equations of motion in terms of the degrees of freedom $\boldsymbol{q}$. To identify the dynamic parameters of the manipulator an expression of the dynamic equations linear in these parameters will be presented also. Finally, the linearised equations of motion will be presented, which will be used for both simulation and identification.

3.3.1 Lumped mass formulation for a rigid spatial beam element

Since the robot links are assumed to be rigid, their inertia properties can be described by a lumped mass formulation. To derive the corresponding mass matrix $\mathbf{M}^{[k]}(\boldsymbol{x}^{[k]})$ and velocity dependent force vector $\boldsymbol{f}^{[k](in)}(\boldsymbol{x}^{[k]}, \dot{\boldsymbol{x}}^{[k]})$, let us consider a rigid body attached to node p of element k. The centre of mass c of the lumped body is positioned with respect to node p by the position vector $\boldsymbol{s}^{[k](p)}$, see figure 3.7(a). The nodal coordinates $\boldsymbol{x}^{(p)}$ define the origin of the $(\bar{x}, \bar{y}, \bar{z})$ Cartesian coordinate system fixed in the body, relative to the global (inertial) coordinate system (x, y, z). In the initial unrotated state of the body,

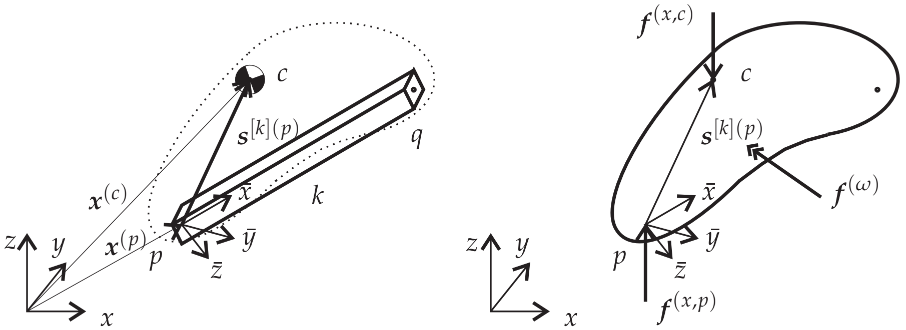

(a) Rigid body at node p of element k (b) Forces acting on lumped body

Figure 3.7: Lumped mass formulation for a rigid beam element

the body-fixed coordinate system $(\bar{x}, \bar{y}, \bar{z})$ coincides with the global coordinate system (x, y, z). The orientation of the body-fixed axes $(\bar{x}, \bar{y}, \bar{z})$ relative to the global coordinate system (x, y, z) is then determined by a rotation matrix $\mathbf{R}^{(p)}$. Note that the orientation is the same for all points of a rigid body. To facilitate notation, the superscript p will be omitted for the position vector $\boldsymbol{s}^{[k](p)}$ and orientation variables in the remainder of this section. The components of the rotation matrix are expressed in terms of four Euler parameters $(\lambda_0, \lambda_1, \lambda_2, \lambda_3)$. According to Nikravesh (1988) the rotation matrix can be written as

$$\mathbf{R} = \begin{bmatrix} \lambda_0^2 + \lambda_1^2 - \lambda_2^2 - \lambda_3^2 & 2(\lambda_1\lambda_2 - \lambda_0\lambda_3) & 2(\lambda_1\lambda_3 + \lambda_0\lambda_2) \\ 2(\lambda_1\lambda_2 + \lambda_0\lambda_3) & \lambda_0^2 - \lambda_1^2 + \lambda_2^2 - \lambda_3^2 & 2(\lambda_2\lambda_3 - \lambda_0\lambda_1) \\ 2(\lambda_1\lambda_3 - \lambda_0\lambda_2) & 2(\lambda_2\lambda_3 + \lambda_0\lambda_1) & \lambda_0^2 - \lambda_1^2 - \lambda_2^2 + \lambda_3^2 \end{bmatrix}. \tag{3.16}$$

By definition the Euler parameters satisfy the constrained equation

$$\lambda_0^2 + \lambda_1^2 + \lambda_2^2 + \lambda_3^2 = 1, \quad \text{or} \quad \boldsymbol{\lambda}^T\boldsymbol{\lambda} = 1. \tag{3.17}$$

The velocity and angular velocity of the body at a given instant of time are determined by the vector $\dot{\boldsymbol{x}}^{(c)}$ representing the velocity of the centre of mass of the body and the vector $\dot{\boldsymbol{\lambda}}$, representing the time derivative of the Euler parameters. Let $\boldsymbol{\omega}$ be the absolute angular velocity of the body, with components $(\omega_x, \omega_y, \omega_z)$ relative to the global coordinate system (x, y, z). The relationship between these components and the time derivative of the Euler parameters is determined by the transformation (Nikravesh (1988))

$$\boldsymbol{\omega} = 2\boldsymbol{\Lambda}\dot{\boldsymbol{\lambda}}, \tag{3.18}$$

in which

$$\boldsymbol{\Lambda} = \begin{bmatrix} -\lambda_1 & \lambda_0 & -\lambda_3 & \lambda_2 \\ -\lambda_2 & \lambda_3 & \lambda_0 & -\lambda_1 \\ -\lambda_3 & -\lambda_2 & \lambda_1 & \lambda_0 \end{bmatrix}. \tag{3.19}$$

Using the identity $\dot{\boldsymbol{\Lambda}}\dot{\boldsymbol{\lambda}} = 0$ (Nikravesh (1988)) a similar expression exists for the absolute angular acceleration, namely

$$\dot{\boldsymbol{\omega}} = 2\boldsymbol{\Lambda}\ddot{\boldsymbol{\lambda}}. \tag{3.20}$$

The time derivatives of the Euler parameters are not independent and must therefore satisfy the constraint equations

$$2\boldsymbol{\lambda}^T\dot{\boldsymbol{\lambda}} = 0 \tag{3.21}$$

and

$$2\dot{\boldsymbol{\lambda}}^T\dot{\boldsymbol{\lambda}} + 2\boldsymbol{\lambda}^T\ddot{\boldsymbol{\lambda}} = 0, \tag{3.22}$$

which are obtained by differentiating equation (3.17) with respect to time.

With the vector $\boldsymbol{\omega}$ the velocity vector $\dot{\boldsymbol{x}}^{(c)}$ of the centre of mass c can be expressed by

$$\dot{\boldsymbol{x}}^{(c)} = \dot{\boldsymbol{x}}^{(p)} + \tilde{\boldsymbol{\omega}}\boldsymbol{s}^{[k]}. \tag{3.23}$$

The tilde operator $\tilde{(.)}$ is used to define a skew symmetric matrix and corresponds to the cross product of two vectors in such a way that

$$\tilde{\boldsymbol{\omega}}\boldsymbol{s}^{[k]} = \boldsymbol{\omega} \times \boldsymbol{s}^{[k]}. \tag{3.24}$$

The operator × denotes the vector outer product, see Nikravesh (1988).

In order to derive the inertial and gravitational forces and torques as dual components of the nodal velocities $\dot{\boldsymbol{x}}^{(p)}$ and $\dot{\boldsymbol{\lambda}}$, we turn to the use of a special case of the principle of virtual power stated earlier. This principle is defined as follows:

The total power applied by external forces and torques, including all inertial forces acting on a body, must be zero for all virtual velocity distributions that are associated with rigid body motion.

Let $\boldsymbol{f}^{(x,c)}$ be the gravity force vector applied to the body's mass centre c, let $\boldsymbol{f}^{(x,p)}$ be an external force vector applied to the body at nodal point p and let $\boldsymbol{f}^{(\omega)}$ be an external torque vector acting on the body, see figure 3.7(b). Then the principle takes the form

$$\begin{aligned}&\langle \boldsymbol{f}^{(x,c)} - \frac{d}{dt}(m^{[k]}\dot{\boldsymbol{x}}^{(c)}), \delta\dot{\boldsymbol{x}}^{(c)}\rangle \\ &\quad + \langle \boldsymbol{f}^{(\omega)} - \frac{d}{dt}(\mathbf{J}^{[k](c)}\boldsymbol{\omega}), \delta\boldsymbol{\omega}\rangle + \langle \boldsymbol{f}^{(x,p)}, \delta\dot{\boldsymbol{x}}^{(p)}\rangle = 0,\end{aligned} \tag{3.25}$$

for all $\delta\dot{\boldsymbol{x}}^{(p)}$, $\delta\dot{\boldsymbol{x}}^{(c)}$ and $\delta\boldsymbol{\omega}$ satisfying

$$\delta\dot{\boldsymbol{x}}^{(c)} = \delta\dot{\boldsymbol{x}}^{(p)} - \tilde{\mathbf{s}}^{[k]}\delta\boldsymbol{\omega}, \tag{3.26}$$

$$\delta\boldsymbol{\omega} = 2\boldsymbol{\Lambda}\delta\dot{\boldsymbol{\lambda}}. \tag{3.27}$$

Here, $m^{[k]}$ and $\mathbf{J}^{[k](c)}$ are the mass and rotational inertia matrix. The latter represents the rotational inertia with respect to the mass centre of the body. The parts $\frac{d}{dt}(m^{[k]}\dot{\boldsymbol{x}}^{(c)})$ and $\frac{d}{dt}(\mathbf{J}^{[k](c)}\boldsymbol{\omega})$ in equation (3.25) arise from the primitive forms of the dynamic equations of Newton and Euler. Assuming the gravitation works in the minus z-direction, the gravity force vector $\boldsymbol{f}^{(x,c)}$ is defined by

$$\boldsymbol{f}^{(x,c)} = m^{[k]}\boldsymbol{g} = m^{[k]}\begin{bmatrix}0\\0\\-g\end{bmatrix}, \tag{3.28}$$

in which g represents the gravitation constant.

In the next part of this section the force components in the first term of equation (3.25) will be converted to force and torque components dual to $\delta\dot{\boldsymbol{x}}^{(p)}$ and $\delta\boldsymbol{\omega}$, respectively. Substitution of equation (3.23) and equation (3.26) in this term gives

$$\begin{aligned}
&\langle \frac{d}{dt}(m^{[k]}\dot{\boldsymbol{x}}^{(c)}), \delta\dot{\boldsymbol{x}}^{(c)} \rangle = \\
&\qquad \langle \frac{d}{dt}(m^{[k]}\dot{\boldsymbol{x}}^{(p)}), \delta\dot{\boldsymbol{x}}^{(p)} \rangle - \langle \tilde{\boldsymbol{s}}^{[k]T}\frac{d}{dt}(m^{[k]}\dot{\boldsymbol{x}}^{(p)}), \delta\boldsymbol{\omega} \rangle \\
&\qquad - \langle \frac{d}{dt}(m^{[k]}\tilde{\boldsymbol{s}}^{[k]}\boldsymbol{\omega}), \delta\dot{\boldsymbol{x}}^{(p)} \rangle + \langle \tilde{\boldsymbol{s}}^{[k]T}\frac{d}{dt}(m^{[k]}\tilde{\boldsymbol{s}}^{[k]}\boldsymbol{\omega}), \delta\boldsymbol{\omega} \rangle. \qquad (3.29)
\end{aligned}$$

Using identity $\tilde{\boldsymbol{a}}^T = -\tilde{\boldsymbol{a}}$ (Nikravesh (1988)) the third term on the right hand side of equation (3.29) can be rewritten to

$$\begin{aligned}
\langle \frac{d}{dt}(m^{[k]}\tilde{\boldsymbol{s}}^{[k]}\boldsymbol{\omega}), \delta\dot{\boldsymbol{x}}^{(p)} \rangle &= \langle m^{[k]}(\dot{\tilde{\boldsymbol{s}}}^{[k]}\boldsymbol{\omega} + \tilde{\boldsymbol{s}}^{[k]}\dot{\boldsymbol{\omega}}), \delta\dot{\boldsymbol{x}}^{(p)} \rangle \\
&= \langle m^{[k]}(\widetilde{\tilde{\boldsymbol{\omega}}\boldsymbol{s}}^{[k]}\boldsymbol{\omega} + \tilde{\boldsymbol{s}}^{[k]}\dot{\boldsymbol{\omega}}), \delta\dot{\boldsymbol{x}}^{(p)} \rangle \\
&= -\langle m^{[k]}(\tilde{\boldsymbol{\omega}}\tilde{\boldsymbol{\omega}}\boldsymbol{s}^{[k]} + \tilde{\boldsymbol{s}}^{[k]T}\dot{\boldsymbol{\omega}}), \delta\dot{\boldsymbol{x}}^{(p)} \rangle. \qquad (3.30)
\end{aligned}$$

Bringing the matrix $\tilde{\boldsymbol{s}}^{[k]T}$ of the fourth right hand side term of equation (3.29) inside the differentiation yields

$$\begin{aligned}
\langle \tilde{\boldsymbol{s}}^{[k]T}\frac{d}{dt}(m^{[k]}\boldsymbol{s}^{\widetilde{[k]}}\boldsymbol{\omega}), \delta\boldsymbol{\omega} \rangle &= -\langle \tilde{\boldsymbol{s}}^{[k]}\frac{d}{dt}(m^{[k]}\boldsymbol{s}^{\widetilde{[k]}}\boldsymbol{\omega}), \delta\boldsymbol{\omega} \rangle \\
&= -\langle \frac{d}{dt}(m^{[k]}\tilde{\boldsymbol{s}}^{[k]}\tilde{\boldsymbol{s}}^{[k]}\boldsymbol{\omega}), \delta\boldsymbol{\omega} \rangle \\
&\qquad + \langle m^{[k]}\dot{\tilde{\boldsymbol{s}}}^{[k]}\tilde{\boldsymbol{s}}^{[k]}\boldsymbol{\omega}, \delta\boldsymbol{\omega} \rangle \\
&= -\langle \frac{d}{dt}(m^{[k]}\tilde{\boldsymbol{s}}^{[k]}\tilde{\boldsymbol{s}}^{[k]}\boldsymbol{\omega}), \delta\boldsymbol{\omega} \rangle. \qquad (3.31)
\end{aligned}$$

In the last step of equation (3.31) the identities $\tilde{\boldsymbol{a}}\boldsymbol{a} = 0$ and $\tilde{\boldsymbol{a}}\boldsymbol{b} = -\tilde{\boldsymbol{b}}\boldsymbol{a}$ (Nikravesh (1988)) are combined to obtain

$$\dot{\tilde{\boldsymbol{s}}}^{[k]}\tilde{\boldsymbol{s}}^{[k]}\boldsymbol{\omega} = -\widetilde{\tilde{\boldsymbol{\omega}}\boldsymbol{s}}^{[k]}\tilde{\boldsymbol{\omega}}\boldsymbol{s}^{[k]} = 0. \qquad (3.32)$$

After substitution of equations (3.18), (3.27) and (3.29)-(3.31) in the virtual power equation (3.25) we obtain the desired formulation in terms of Euler parameters. However, the principle is based on the assumption that the velocity components of the body are independent. Since the time derivatives for the Euler parameters are dependent on constraint equation (3.21), the effect of this condition must be included in the virtual power equation. This can be done by using the Lagrange multiplier technique. After applying the above substitutions in equation (3.25) and adding constraint equation (3.21) we obtain

$$\begin{aligned} &\langle \boldsymbol{f}^{(x,p)} - \frac{d}{dt}(m^{[k]}\dot{\boldsymbol{x}}^{(p)}), \delta\dot{\boldsymbol{x}}^{(p)} \rangle + \langle \boldsymbol{f}^{(\omega)} - \frac{d}{dt}(\mathbf{J}^{[k](p)}\boldsymbol{\omega}), 2\boldsymbol{\Lambda}\delta\dot{\boldsymbol{\lambda}} \rangle \\ &\quad + \langle \boldsymbol{f}^{(x,c)} - m^{[k]}(\tilde{\boldsymbol{\omega}}\tilde{\boldsymbol{\omega}}\boldsymbol{s}^{[k]} + \tilde{\mathbf{s}}^{[k]T}\dot{\boldsymbol{\omega}}), \delta\dot{\boldsymbol{x}}^{(p)} \rangle \\ &\qquad + \langle \tilde{\mathbf{s}}^{[k]}(\boldsymbol{f}^{(x,c)} - \frac{d}{dt}(m^{[k]}\dot{\boldsymbol{x}}^{(p)})), 2\boldsymbol{\Lambda}\delta\dot{\boldsymbol{\lambda}} \rangle - \langle \sigma^{(\lambda)}, 2\boldsymbol{\lambda}^{T}\delta\dot{\boldsymbol{\lambda}} \rangle = 0, \end{aligned} \tag{3.33}$$

for all $\delta\dot{\boldsymbol{x}}^{(p)}$ and $\delta\dot{\boldsymbol{\lambda}}$. The inertia matrix $\mathbf{J}^{[k](p)}$ is defined by

$$\mathbf{J}^{[k](p)} = \mathbf{J}^{[k](c)} - m^{[k]}\tilde{\mathbf{s}}^{[k]}\tilde{\mathbf{s}}^{[k]}, \tag{3.34}$$

which corresponds to the rotational inertia matrix with respect to point p of the body. The scalar $\sigma^{(\lambda)}$ is the Lagrange multiplier associated with the constrained condition (3.21).

Since the virtual velocities $\delta\dot{\boldsymbol{x}}^{(p)}$ and $\delta\dot{\boldsymbol{\lambda}}$ are independent, it follows from equation (3.33) that

$$\boldsymbol{f}^{(x,p)} + \boldsymbol{f}^{(x,c)} - m^{[k]}\ddot{\boldsymbol{x}}^{(p)} - m^{[k]}(\tilde{\boldsymbol{\omega}}\tilde{\boldsymbol{\omega}}\boldsymbol{s}^{[k]} + \tilde{\mathbf{s}}^{[k]T}\dot{\boldsymbol{\omega}}) = 0 \tag{3.35}$$

and with the transpose of the transformations $\boldsymbol{\Lambda}$ and $\boldsymbol{\lambda}^{T}$, we have

$$\boldsymbol{f}^{(\lambda)} - 2\boldsymbol{\Lambda}^{T}\frac{d}{dt}(\mathbf{J}^{[k](p)}\boldsymbol{\Lambda}\dot{\boldsymbol{\lambda}}) + 2\boldsymbol{\Lambda}^{T}\tilde{\mathbf{s}}^{[k]}(\boldsymbol{f}^{(x,c)} - m^{[k]}\ddot{\boldsymbol{x}}^{(p)}) - 2\boldsymbol{\lambda}\sigma^{(\lambda)} = 0. \tag{3.36}$$

The components of the vector $\boldsymbol{f}^{(\lambda)}$ are defined by

$$\boldsymbol{f}^{(\lambda)} = 2\boldsymbol{\Lambda}^{T}\boldsymbol{f}^{(\omega)}. \tag{3.37}$$

These are the four torque components associated with the time derivatives of the Euler parameters.

In general, the components of the inertia matrix $\mathbf{J}^{[k](p)}$ and the position vector $\boldsymbol{s}^{[k]}$, referred to the global coordinate system (x, y, z), change as the body rotates. This dependency may be avoided by referring them to the set of axis $(\bar{x}, \bar{y}, \bar{z})$ fixed in the body. Therefore, we introduce the following coordinate transformations,

$$\mathbf{J}^{[k](p)} = \mathbf{R}\mathbf{J}'^{[k](p)}\mathbf{R}^{T}, \tag{3.38}$$

and

$$\boldsymbol{s}^{[k]} = \mathbf{R}\boldsymbol{s}'^{[k]}. \tag{3.39}$$

in which $\mathbf{J}'^{[k](p)}$ and $\boldsymbol{s}'^{[k]}$ denote the inertia matrix and the position vector with constant components referred to the body fixed coordinate system $(\bar{x}, \bar{y}, \bar{z})$. $\mathbf{R}$

is the rotation matrix, which can be expressed as the result of two successive transformations (Nikravesh (1988)) as

$$\mathbf{R} = 2\boldsymbol{\Lambda}\boldsymbol{\Lambda}'^{T}, \tag{3.40}$$

in which

$$\boldsymbol{\Lambda}' = \begin{bmatrix} -\lambda_1 & \lambda_0 & \lambda_3 & -\lambda_2 \\ -\lambda_2 & -\lambda_3 & \lambda_0 & \lambda_1 \\ -\lambda_3 & \lambda_2 & -\lambda_1 & \lambda_0 \end{bmatrix}. \tag{3.41}$$

Substitution of equations (3.38), (3.39) into equations (3.35), (3.36) yields with the identities (3.18), (3.20),

$$\boldsymbol{f}^{(x,p)} + \boldsymbol{f}^{(x,c)} - m^{[k]}\ddot{\boldsymbol{x}}^{(p)} - 4m^{[k]}(\widetilde{\boldsymbol{\Lambda}\dot{\boldsymbol{\lambda}}}\widetilde{\boldsymbol{\Lambda}\dot{\boldsymbol{\lambda}}}\boldsymbol{s}'^{[k]} + \widetilde{\mathbf{R}\boldsymbol{s}}'^{[k]}T\boldsymbol{\Lambda}\ddot{\boldsymbol{\lambda}}) = 0 \tag{3.42}$$

and

$$\begin{aligned} &\boldsymbol{f}^{(\lambda)} - 4\boldsymbol{\Lambda}^{T}\frac{d}{dt}(\boldsymbol{\Lambda}\boldsymbol{\Lambda}'^{T}\mathbf{J}'^{[k](p)}\boldsymbol{\Lambda}'\boldsymbol{\Lambda}^{T}\boldsymbol{\Lambda}\dot{\boldsymbol{\lambda}}) \\ &\quad + 2\boldsymbol{\Lambda}^{T}\widetilde{\mathbf{R}\boldsymbol{s}'}^{[k]}(\boldsymbol{f}^{(x,c)} - m^{[k]}\ddot{\boldsymbol{x}}^{(p)}) - 2\boldsymbol{\lambda}\sigma^{(\lambda)} = 0. \end{aligned} \tag{3.43}$$

Carrying out the differentiation with respect to time in equation (3.43), see appendix B or Haug (1992), yields

$$\begin{aligned} &\boldsymbol{f}^{(\lambda)} - 8\dot{\boldsymbol{\Lambda}}'^{T}\mathbf{J}'^{[k](p)}\boldsymbol{\Lambda}'\dot{\boldsymbol{\lambda}} - 4\boldsymbol{\Lambda}'^{T}\mathbf{J}'^{[k](p)}\boldsymbol{\Lambda}'\ddot{\boldsymbol{\lambda}} \\ &\quad + 2\boldsymbol{\Lambda}^{T}\widetilde{\mathbf{R}\boldsymbol{s}'}^{[k]}\boldsymbol{f}^{(x,c)} - 2\boldsymbol{\Lambda}^{T}\widetilde{\mathbf{R}\boldsymbol{s}'}^{[k]}m^{[k]}\ddot{\boldsymbol{x}}^{(p)} - 2\boldsymbol{\lambda}\sigma^{(\lambda)} = 0. \end{aligned} \tag{3.44}$$

In matrix form, equations (3.42), (3.44) and the constraint equation (3.22) may be combined as

$$\begin{bmatrix} \mathbf{M}_{xx}^{[k]} & \mathbf{M}_{x\lambda}^{[k]} & \mathbf{0} \\ \mathbf{M}_{\lambda x}^{[k]} & \mathbf{M}_{\lambda\lambda}^{[k]} & 2\boldsymbol{\lambda} \\ \mathbf{0} & 2\boldsymbol{\lambda}^{T} & \mathbf{0} \end{bmatrix} \begin{bmatrix} \ddot{\boldsymbol{x}}^{(p)} \\ \ddot{\boldsymbol{\lambda}} \\ \sigma^{(\lambda)} \end{bmatrix} + \boldsymbol{f}^{[k](in)} - \boldsymbol{f}^{[k](c)} = \boldsymbol{f}^{[k](p)}, \tag{3.45}$$

in which

$$\mathbf{M}_{xx}^{[k]} = m^{[k]}\mathbf{I}, \tag{3.46a}$$

$$\mathbf{M}_{x\lambda}^{[k]} = 2m^{[k]}\widetilde{\mathbf{R}\boldsymbol{s}'}^{[k]T}\boldsymbol{\Lambda}, \tag{3.46b}$$

$$\mathbf{M}_{\lambda x}^{[k]} = 2\boldsymbol{\Lambda}^{T}\widetilde{\mathbf{R}\boldsymbol{s}'}^{[k]}m^{[k]}, \tag{3.46c}$$

$$\mathbf{M}_{\lambda\lambda}^{[k]} = 4\boldsymbol{\Lambda}'^{T}\mathbf{J}'^{[k](p)}\boldsymbol{\Lambda}', \tag{3.46d}$$

$$\boldsymbol{f}^{[k](in)} = \begin{bmatrix} 4m^{[k]}\widetilde{\boldsymbol{\Lambda}\dot{\boldsymbol{\lambda}}}\widetilde{\boldsymbol{\Lambda}\dot{\boldsymbol{\lambda}}}\mathbf{R}\boldsymbol{s}'^{[k]} \\ 8\dot{\boldsymbol{\Lambda}}'^{T}\mathbf{J}'^{[k](p)}\boldsymbol{\Lambda}'\dot{\boldsymbol{\lambda}} \\ 2\dot{\boldsymbol{\lambda}}^{T}\dot{\boldsymbol{\lambda}} \end{bmatrix}, \tag{3.46e}$$

$$\boldsymbol{f}^{[k](c)} = \begin{bmatrix} \boldsymbol{f}^{(x,c)} \\ 2\boldsymbol{\Lambda}^{T}\widetilde{\mathbf{R}\boldsymbol{s}'}^{[k]}\boldsymbol{f}^{(x,c)} \\ \mathbf{0} \end{bmatrix}, \tag{3.46f}$$

$$\boldsymbol{f}^{[k](p)} = \begin{bmatrix} \boldsymbol{f}^{(x,p)} \\ \boldsymbol{f}^{(\lambda)} \\ \mathbf{0} \end{bmatrix}. \tag{3.46g}$$

Matrix $\mathbf{M}^{[k]}$ represents the element mass matrix corresponding to a rigid body k that is attached to node p by a vector $\boldsymbol{s}'^{[k]}$. Vectors $\boldsymbol{f}^{[k](in)}$ and $\boldsymbol{f}^{[k](c)}$ represent the corresponding velocity dependent inertial nodal forces and the gravitational nodal forces, respectively.

Equation (3.45) describes the motion of the body in a form which is linear in the accelerations. This equation can also be written in a parameter linear form

$$\boldsymbol{\Phi}^{[k]}\boldsymbol{p}^{[k](l)} = \boldsymbol{f}^{[k](p)}, \tag{3.47}$$

or,

$$\begin{bmatrix} \boldsymbol{\Phi}_{xm}^{[k]} & \boldsymbol{\Phi}_{xs}^{[k]} & \mathbf{0} \\ \mathbf{0} & \boldsymbol{\Phi}_{\lambda s}^{[k]} & \boldsymbol{\Phi}_{\lambda l}^{[k]} \end{bmatrix} \begin{bmatrix} m^{[k]} \\ m^{[k]}\boldsymbol{s}'^{[k]} \\ \boldsymbol{l}^{[k]} \end{bmatrix} = \boldsymbol{f}^{[k](p)}, \tag{3.48}$$

in which

$$\boldsymbol{\Phi}_{xm}^{[k]} = \ddot{\boldsymbol{x}}^{(p)} - \boldsymbol{g}, \tag{3.49a}$$

$$\boldsymbol{\Phi}_{xs}^{[k]} = 2(\widetilde{\boldsymbol{\Lambda}\ddot{\boldsymbol{\lambda}}} + 2\widetilde{\boldsymbol{\Lambda}\dot{\boldsymbol{\lambda}}}\widetilde{\boldsymbol{\Lambda}\dot{\boldsymbol{\lambda}}})\mathbf{R}, \tag{3.49b}$$

$$\boldsymbol{\Phi}_{\lambda s}^{[k]} = 2\boldsymbol{\Lambda}^{T}(\tilde{\boldsymbol{g}} - \tilde{\ddot{\boldsymbol{x}}}^{(p)})\mathbf{R}, \tag{3.49c}$$

$$\boldsymbol{\Phi}_{\lambda l}^{[k]} = 4\boldsymbol{\Lambda}'^{T}\widehat{\boldsymbol{\Lambda}'\ddot{\boldsymbol{\lambda}}} + 8\dot{\boldsymbol{\Lambda}}'^{T}\widehat{\boldsymbol{\Lambda}'\dot{\boldsymbol{\lambda}}}, \tag{3.49d}$$

$$\boldsymbol{f}^{[k](p)} = \begin{bmatrix} \boldsymbol{f}^{(x,p)} \\ 2\boldsymbol{\Lambda}^{T}\boldsymbol{f}^{(\omega)} \end{bmatrix} \tag{3.49e}$$

and

$$\boldsymbol{p}^{[k](l)} = \begin{bmatrix} m^{[k]} \\ m^{[k]}\boldsymbol{s}'^{[k]} \\ \boldsymbol{l}^{[k]} \end{bmatrix}. \tag{3.50}$$

Here, $\boldsymbol{l}^{[k]}$ consist of the entries of the inertia matrix $\mathbf{J}'^{[k](p)}$, namely $\boldsymbol{l}^{[k]}$ is defined as

$$\boldsymbol{l}^{[k]} = [J'^{[k](p)}_{xx}, J'^{[k](p)}_{yy}, J'^{[k](p)}_{zz}, J'^{[k](p)}_{xy}, J'^{[k](p)}_{xz}, J'^{[k](p)}_{yz}]^T \tag{3.51}$$

and operator $\widehat{(.)}$ is defined as

$$\widehat{\boldsymbol{a}} = \begin{bmatrix} a_x & 0 & 0 & a_y & a_z & 0 \\ 0 & a_y & 0 & a_x & 0 & a_z \\ 0 & 0 & a_z & 0 & a_x & a_y \end{bmatrix}. \tag{3.52}$$

The equations of motion for a lumped mass attached to one of the nodes of the spatial beam element in acceleration linear form, equation (3.45), and in parameter linear form, equation (3.47), will be used for simulation and identification, respectively. The assembly of the beam elements including the contributions of the lumped masses will be discussed in section 3.3.3

3.3.2 Constitutive equations

This section describes the constitutive equations for the joints and the gravity compensating spring. First, the existing joint friction model for a rigid Stäubli RX90B will be introduced. Then this model will be extended for a flexible joint. Next, the constitutive equations for the driving hinge and the flexible hinge will be presented. Finally, the constitutive equation for the gravity compensating spring will be given.

Friction model for a rigid joint

Several models are proposed to describe the friction characteristics for industrial robots. An overview of the proposed models can be found in Armstrong-Hélouvry (1991); Armstrong-Hélouvry et al. (1994); Olsen et al. (1998). More recently, Waiboer et al. (2005b) analysed viscous friction and friction caused by asperity contacts inside gears and the prestressed roller bearings of industrial robots and, in particular, the Stäubli RX90B robot. This tribological based friction model accurately describes the friction behaviour in the full velocity range with a minimal and physically sound parametrisation. First, an overview of this model will be given. Next this friction model, which was original developed for a rigid drive so $\boldsymbol{\epsilon}^{[k+1]} \equiv \mathbf{0}$, is adapted for a flexible joint.

According to Waiboer et al. (2005b) the sliding friction model for joint $j = 1, \cdots, 4$ is described by:

$$\tau_j^{(f,s)}(\dot{\theta}_j) = \underbrace{\tau_j^{(a,0)} e^{-\left(\frac{|\dot{\theta}_j|}{\dot{\theta}_j^{(s)}}\right)^{\delta_j^{(a)}}}}_{\text{asperity part}} + \underbrace{c_j^{(v)} |\dot{\theta}_j|^{(1-\delta_j^{(v)})}}_{\text{viscous part}}, \tag{3.53}$$

in which $|\dot{\theta}_j|$ denotes the absolute value of the joint velocity. Note that for a rigid transmission the joint velocity $\dot{\theta}_j$ is equal to the drive velocity $\dot{e}_1^{[k]}$. For each joint j, there are five parameters: the static asperity friction torque $\tau_j^{(a,0)}$, the Stribeck velocity $\dot{\theta}_j^{(s)}$, the Stribeck velocity power $\delta_j^{(a)}$, the viscous friction coefficient $c_j^{(v)}$ and the viscous friction power $\delta_j^{(v)}$. Waiboer et al. (2005b) estimated the values of these parameters by dedicated identification experiments. The parameters $\tau_j^{(a,0)}$ and $c_j^{(v)}$ are strongly temperature dependent, so they can change over time, whereas the other parameters are considered constant. The reader is referred to Waiboer et al. (2005b) for further explanation about this friction model.

The sliding friction model presented in equation (3.53) assumes a positive joint velocity. For negative velocities, the sign of the friction torque should be reversed. For joint velocities equal to zero the sliding friction model is undefined and around velocity reversals the asperity function model shows a discontinuity. During forward simulation a smoothed version of equation (3.53) is used

$$\tau_j^{(f)}(\dot{\theta}_j) = \frac{2}{\pi} \arctan(c^{(a)} \dot{\theta}_j) \tau_j^{(f,s)}(\dot{\theta}_j). \tag{3.54}$$

The constant $c^{(a)}$ should be chosen sufficiently high. More sophisticated models exist to describe the velocity reversals, see for example Dahl (1977) and Canudas De Wit et al. (1995). However, these are beyond the scope of this work.

Friction model for a flexible joint

Next the joint friction model of equation (3.53) will be adapted for the flexible joint. Most of the asperity contacts show up in the pre-stressed joint bearings. In both the flexible and rigid joint the corresponding sliding velocity is defined by the joint velocity $\dot{\theta}_j$, which describes the relative velocity between two links, see equation (3.4) and figure 3.5 on page 22. Therefore the asperity part of equation (3.53) is applicable for the flexible model as well.

The origin of the viscous part is less evident. There are contributions from several components in the joint with sliding velocities governed by $\dot{e}_1^{[k]}$ as well as by $\dot{\theta}_j$. Therefore the viscous friction model of equation (3.53) should be split up into two parts: one describing the viscous friction torque on the motor side as a function of $\dot{e}_1^{[k]}$ and one describing the viscous friction on the link side as a function of $\dot{\theta}_j$. However, accurate identification of these two parts requires independent measurements of the corresponding friction torques and velocities. In case of the Stäubli RX90B only the drive velocity $\dot{e}_1^{[k]}$ and the external driving torque $\tau_j^{(a)}$ can be measured accurately. Therefore it is very hard to identify the two viscous friction parts independently. In stead of splitting the viscous friction into two ill identifiable parts, it is preferred to keep them combined in one viscous contribution as a function of one velocity for which the joint velocity $\dot{\theta}_j$ is taken. This simplification is justifiable since the difference between $\dot{e}_1^{[k]}$ and $\dot{\theta}_j$ has a negligible influence on the viscous friction torque $\tau_j^{(f,s)}$. As a result equation (3.53) is applicable to the flexible joint as well.

The friction torque $\tau_j^{(f)}(\dot{\theta}_j)$ should describe a torque between two links depending on joint velocity $\dot{\theta}_j$. In the joint assembly of figure 3.5 on page 22 this torque is not easily included as there is not a single element connecting both links. The joint assembly could be extended with an additional hinge element, that describes this torque and the corresponding joint angle θ_j. Instead, the friction torque $\tau_j^{(f)}(\dot{\theta}_j)$ will be included in the constitutive equations of both the driving and flexible hinge. In section 3.3.3 on page 40 it will be shown that both implementations are dynamical equivalent, which means that the friction power dissipated in the two hinges is equal to the friction power that would have been dissipated if an additional hinge element was used. The constitutive equations of the driving and flexible hinge will be presented below.

Constitutive equation driving hinge

In equation (3.1), page 19, $\tau_j^{(a)}$ is defined as the external driving torque of joint j. Part of this torque is dissipated by the joint friction torque $\tau_j^{(f)}(\dot{\theta}_j)$. As shown by Spong (1987) and discussed in section 2.1.2, the inertia properties of the driving system for robots with high transmission ratios may be described by a single rotational inertia. This rotational inertia is called drive inertia and is incorporated into the finite element model by adding a rotational inertia $J^{[k](a)}$ to the deformation $e_1^{[k]}$ of the driving hinge. For the torsional stress resultant $\sigma_1^{[k]}$ of the driving hinge k this yields

$$\sigma_1^{[k]} = -(\tau^{[k](a)} - \tau^{[k](f)} - J^{[k](a)}\ddot{e}_1^{[k]}), \tag{3.55}$$

in which

$$\tau^{[k](f)} = \tau_j^{(f)}(\dot{\theta}_j), \tag{3.56}$$

$$\tau^{[k](a)} = \tau_j^{(a)} \tag{3.57}$$

and $k = 2j - 1$. The first minus sign on the right hand side of equation (3.55) is the result of different sign conventions for the stress resultant $\sigma_1^{[k]}$ and the driving torque $\tau^{[k](a)}$.

Constitutive equations flexible hinge

For the flexible hinge, the torsion moment $\sigma_1^{[k+1]}$ and the two bending moments $\sigma_2^{[k+1]}$, $\sigma_3^{[k+1]}$ are linearly related to the deformations $\epsilon^{[k+1]}$ and their time derivatives $\dot{\epsilon}^{[k+1]}$. Furthermore, the joint friction torque $\tau_j^{(f)}$ is included in the torsion moment $\sigma_1^{[k+1]}$ as well, yielding

$$\sigma_1^{[k+1]} = k_1^{[k+1]}\epsilon_1^{[k+1]} + d_1^{[k+1]}\dot{\epsilon}_1^{[k+1]} + \tau^{[k+1](f)}, \tag{3.58}$$

in which

$$\tau^{[k+1](f)} = \tau_j^{(f)}(\dot{\theta}_j), \qquad (k = 2j - 1) \tag{3.59}$$

and

$$\sigma_i^{[k+1]} = k_i^{[k+1]}\epsilon_i^{[k+1]} + d_i^{[k+1]}\dot{\epsilon}_i^{[k+1]}, \tag{3.60}$$

for $i = 2, 3$. Parameter $k_1^{[k+1]}$ represents the drive stiffness and $k_i^{[k+1]}$ for $i = 2, 3$ represents the joint stiffness. The parameter $d_i^{[k+1]}$ for $i = 1, 2, 3$ describes viscous damping. Figure 3.8 depicts the dynamical model that is described by the constitutive equations of driving and flexible hinge.

Constitutive equation gravity compensating spring

The normal force in the gravity compensating spring, denoted by $\sigma^{(ec)}$, is linearly related to the deformation $e^{(c)}$ by a spring stiffness $k^{(c)}$ and an additional pre-stress $\sigma^{(c0)}$, giving the constitutive equation

$$\sigma^{(ec)} = k^{(c)}e^{(c)} + \sigma^{(c0)}, \tag{3.61}$$

in which $e^{(c)}$ is defined by equation (3.9).

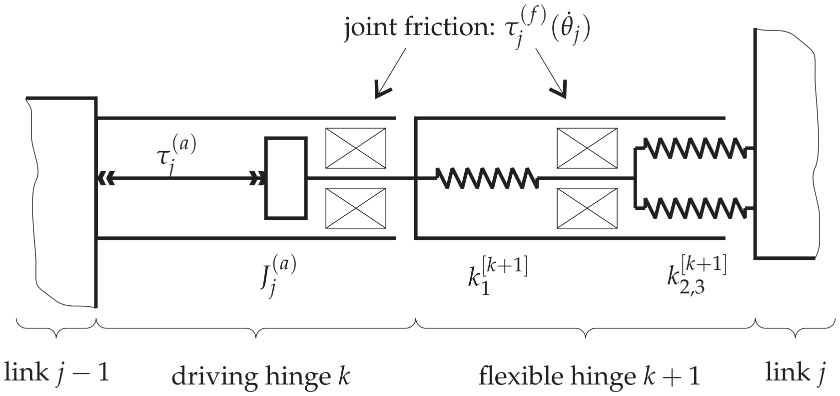

Figure 3.8: Dynamical model of joint j. To improve the visibility the dampers $d_i^{[k+1]}$*, that are modelled in parallel with the springs* $k_i^{[k+1]}$*, are omitted in this figure.*

3.3.3 Equations of motion in acceleration linear form

Let $\mathbf{M}(\boldsymbol{x})$ be the global mass matrix and $\boldsymbol{f}(\boldsymbol{x}, \dot{\boldsymbol{x}}, t)$ the vector of external nodal forces, including gravitational forces and velocity dependent inertia forces $\boldsymbol{f}^{(in)}(\boldsymbol{x}, \dot{\boldsymbol{x}}, t)$ obtained by assembling the inertia contributions of the lumped bodies of the links, see equation (3.45). Let vectors $\boldsymbol{\sigma}^{(em)}$ and $\boldsymbol{\sigma}^{(\epsilon m)}$ represent the vectors of stress resultants dual to drive velocity $\dot{\boldsymbol{e}}^{(m)}$ and the time derivatives of the elastic deformations $\dot{\boldsymbol{\epsilon}}^{(m)}$, as defined by equations (3.55), (3.58) and (3.60). Furthermore, let $\sigma^{(ec)}$ represent the stress resultant in the gravity compensating spring dual to $\dot{e}^{(c)}$. According to the principle of virtual power for the external forces $\boldsymbol{f}$, the inertial forces $\mathbf{M}\ddot{\boldsymbol{x}}$ and the internal stress vectors $\boldsymbol{\sigma}^{(em)}$, $\boldsymbol{\sigma}^{(\epsilon m)}$ and $\sigma^{(ec)}$, we obtain

$$\langle(\boldsymbol{f} - \mathbf{M}\ddot{\boldsymbol{x}}), \delta\dot{\boldsymbol{x}}\rangle = \langle\boldsymbol{\sigma}^{(em)}, \delta\dot{\boldsymbol{e}}^{(m)}\rangle + \langle\boldsymbol{\sigma}^{(\epsilon m)}, \delta\dot{\boldsymbol{\epsilon}}^{(m)}\rangle + \langle\sigma^{(ec)}, \delta\dot{e}^{(c)}\rangle, \tag{3.62}$$

for all virtual velocities $\delta\dot{\boldsymbol{x}}, \delta\dot{\boldsymbol{e}}^{(m)}, \delta\dot{\boldsymbol{\epsilon}}^{(m)}$ and $\delta\dot{e}^{(c)}$, which satisfy the instantaneous kinematic constraints (3.10) and (3.13), respectively.

Equations of motion in terms of the generalised coordinates q

Substitution of kinematic relations (3.10), (3.12) and (3.13) in virtual power equation (3.62) yields the reduced equations of motion

$$\begin{aligned}&\begin{bmatrix}\breve{\mathbf{M}}_{ee} & \breve{\mathbf{M}}_{e\epsilon}\\ \breve{\mathbf{M}}_{\epsilon e} & \breve{\mathbf{M}}_{\epsilon\epsilon}\end{bmatrix}\begin{bmatrix}\ddot{\boldsymbol{e}}^{(m)}\\ \ddot{\boldsymbol{\epsilon}}^{(m)}\end{bmatrix}\\ &\quad+\begin{bmatrix}\mathrm{D}_{e^m}\boldsymbol{\mathcal{F}}^{(x)T}\\ \mathrm{D}_{\epsilon^m}\boldsymbol{\mathcal{F}}^{(x)T}\end{bmatrix}\left[\mathbf{M}(\mathrm{D}^2\boldsymbol{\mathcal{F}}^{(x)}\cdot(\dot{\boldsymbol{e}}^{(m)},\dot{\boldsymbol{\epsilon}}^{(m)}))\cdot(\dot{\boldsymbol{e}}^{(m)},\dot{\boldsymbol{\epsilon}}^{(m)})-\boldsymbol{f}\right]\\ &\quad+\begin{bmatrix}\mathrm{D}_{e^m}\boldsymbol{\mathcal{F}}^{(ec)T}\\ \mathrm{D}_{\epsilon^m}\boldsymbol{\mathcal{F}}^{(ec)T}\end{bmatrix}\sigma^{(ec)}=-\begin{bmatrix}\boldsymbol{\sigma}^{(em)}\\ \boldsymbol{\sigma}^{(\epsilon m)}\end{bmatrix},\end{aligned}\tag{3.63}$$

with the reduced system mass matrices

$$\begin{aligned}\breve{\mathbf{M}}_{ee}&=\mathrm{D}_{e^m}\boldsymbol{\mathcal{F}}^{(x)T}\mathbf{M}\mathrm{D}_{e^m}\boldsymbol{\mathcal{F}}^{(x)}, & \breve{\mathbf{M}}_{e\epsilon}&=\mathrm{D}_{e^m}\boldsymbol{\mathcal{F}}^{(x)T}\mathbf{M}\mathrm{D}_{\epsilon^m}\boldsymbol{\mathcal{F}}^{(x)},\\ \breve{\mathbf{M}}_{\epsilon e}&=\mathrm{D}_{\epsilon^m}\boldsymbol{\mathcal{F}}^{(x)T}\mathbf{M}\mathrm{D}_{e^m}\boldsymbol{\mathcal{F}}^{(x)}, & \breve{\mathbf{M}}_{\epsilon\epsilon}&=\mathrm{D}_{\epsilon^m}\boldsymbol{\mathcal{F}}^{(x)T}\mathbf{M}\mathrm{D}_{\epsilon^m}\boldsymbol{\mathcal{F}}^{(x)}.\end{aligned}\tag{3.64}$$

Matrix $\breve{\mathbf{M}}_{ee}$ represents the reduced system mass matrix of the links corresponding to drive angles $\boldsymbol{e}^{(m)}$. The matrices $\breve{\mathbf{M}}_{e\epsilon}$ and $\breve{\mathbf{M}}_{\epsilon e}$ represent the dynamic coupling between the gross rigid motion and the flexible deformation of the joints.

Substitution of the constitutive equations (3.55), (3.58) and (3.60) for stress resultants $\boldsymbol{\sigma}^{(em)}$ and $\boldsymbol{\sigma}^{(\epsilon m)}$ and equation (3.61) for stress resultant $\sigma^{(ec)}$ into the reduced equations of motion (3.63) yields

$$\bar{\mathbf{M}}\ddot{\boldsymbol{q}}+\mathrm{D}\boldsymbol{\mathcal{F}}^{(x)T}[\mathbf{M}(\mathrm{D}^2\mathcal{F}\cdot\dot{\boldsymbol{q}})\cdot\dot{\boldsymbol{q}}-\boldsymbol{f}]+\boldsymbol{\sigma}^{(d)}+\boldsymbol{\sigma}^{(s)}+\mathbf{F}\boldsymbol{\tau}^{(f)}=\mathbf{B}^{(u)}\boldsymbol{\tau}^{(a)}.\tag{3.65}$$

The reduced system mass matrix $\bar{\mathbf{M}}$ is defined by including the drive inertias into the reduced mass matrix of links $\breve{\mathbf{M}}$, yielding

$$\begin{aligned}\bar{\mathbf{M}}_{ee}&=\breve{\mathbf{M}}_{ee}+\mathrm{diag}(\boldsymbol{J}^{(a)}), & \bar{\mathbf{M}}_{e\epsilon}&=\breve{\mathbf{M}}_{e\epsilon},\\ \bar{\mathbf{M}}_{\epsilon e}&=\breve{\mathbf{M}}_{\epsilon e}, & \bar{\mathbf{M}}_{\epsilon\epsilon}&=\breve{\mathbf{M}}_{\epsilon\epsilon},\end{aligned}\tag{3.66}$$

in which $\boldsymbol{J}^{(a)}$ is the vector with drive inertias. Vector $\boldsymbol{\sigma}^{(d)}$ describes the viscous damping and is defined by

$$\boldsymbol{\sigma}^{(d)}=\mathbf{D}\dot{\boldsymbol{q}},\tag{3.67}$$

in which

$$\mathbf{D}=\begin{bmatrix}\mathbf{0} & \mathbf{0}\\ \mathbf{0} & \mathbf{D}_{\epsilon\epsilon}\end{bmatrix}.\tag{3.68}$$

Diagonal damping matrix $\mathbf{D}_{\epsilon\epsilon}$ is assembled from the viscous damping parameters of the flexible hinge elements. Vector $\boldsymbol{\sigma}^{(s)}$ represents the stresses arising from structural flexibilities and is defined by

$$\boldsymbol{\sigma}^{(s)}=\mathbf{K}\boldsymbol{q}+\mathrm{D}\mathcal{F}^{(ec)T}(k^{(c)}\mathcal{F}^{(ec)}+\sigma^{(ec0)}),\tag{3.69}$$

in which

$$\mathbf{K} = \begin{bmatrix} \mathbf{0} & \mathbf{0} \\ \mathbf{0} & \mathbf{K}_{\epsilon\epsilon} \end{bmatrix}. \tag{3.70}$$

Matrix $\mathbf{K}_{\epsilon\epsilon}$ is a diagonal structural stiffness matrix assembled from the joint and drive flexibilities of the flexible hinge elements. Vector $\boldsymbol{\tau}^{(f)}$ is assembled from the nonlinear joint friction torques presented in equation (3.54) and $\mathbf{F}$ is a $N^{(q)} \times N^{(em)}$ matrix defined by

$$\mathbf{F} = \begin{bmatrix} \mathbf{I} \\ \mathbf{I} \\ \mathbf{0} \end{bmatrix}, \tag{3.71}$$

in which $\mathbf{I}$ is an $N^{(em)} \times N^{(em)}$ identity matrix. Matrix $\mathbf{B}^{(u)}$ is the $N^{(q)} \times N^{(em)}$ input matrix defined by

$$\mathbf{B}^{(u)} = \begin{bmatrix} \mathbf{I} \\ \mathbf{0} \end{bmatrix}. \tag{3.72}$$

Equations of motion in terms of generalised coordinates $\breve{q}$

The reduced equations of motion will be derived for a new set of generalised coordinates that is denoted by $\breve{\boldsymbol{q}}$ and defined as

$$\breve{\boldsymbol{q}} = \begin{bmatrix} \boldsymbol{e}^{(m)} \\ \boldsymbol{\theta}^{(m)} \\ \boldsymbol{\epsilon}^{(2m)} \\ \boldsymbol{\epsilon}^{(3m)} \end{bmatrix}. \tag{3.73}$$

Vectors $\boldsymbol{\epsilon}^{(2m)}$ and $\boldsymbol{\epsilon}^{(3m)}$ contain the joint flexibilities $\epsilon_2^{[k+1]}$ and $\epsilon_3^{[k+1]}$, respectively. The relation between the vectors $\boldsymbol{q}$ and $\breve{\boldsymbol{q}}$ is given by

$$\boldsymbol{q} = \begin{bmatrix} \boldsymbol{e}^{(m)} \\ \boldsymbol{\epsilon}^{(1m)} \\ \boldsymbol{\epsilon}^{(2m)} \\ \boldsymbol{\epsilon}^{(3m)} \end{bmatrix} = \begin{bmatrix} \mathbf{I} & \mathbf{0} & \mathbf{0} & \mathbf{0} \\ -\mathbf{I} & \mathbf{I} & \mathbf{0} & \mathbf{0} \\ \mathbf{0} & \mathbf{0} & \mathbf{I} & \mathbf{0} \\ \mathbf{0} & \mathbf{0} & \mathbf{0} & \mathbf{I} \end{bmatrix} \begin{bmatrix} \boldsymbol{e}^{(m)} \\ \boldsymbol{\theta}^{(m)} \\ \boldsymbol{\epsilon}^{(2m)} \\ \boldsymbol{\epsilon}^{(3m)} \end{bmatrix} = \mathbf{T}\breve{\boldsymbol{q}}, \tag{3.74}$$

in which $\boldsymbol{\epsilon}^{(1m)}$ is a vector containing the drive flexibilities $\epsilon_1^{[k+1]}$. Substitution of this relation into the reduced equations of motion (3.65) yields

$$\begin{aligned} &\mathbf{T}^T\bar{\mathbf{M}}\mathbf{T}\ddot{\breve{\boldsymbol{q}}} + \mathbf{T}^T\mathrm{D}\boldsymbol{\mathcal{F}}^{(x)T}[\mathbf{M}(\mathrm{D}^2\mathcal{F}^{(x)} \cdot \mathbf{T}\dot{\breve{\boldsymbol{q}}}) \cdot \mathbf{T}\dot{\breve{\boldsymbol{q}}} - \boldsymbol{f}] \\ &\quad + \mathbf{T}^T\boldsymbol{\sigma}^{(d)} + \mathbf{T}^T\boldsymbol{\sigma}^{(s)} + \mathbf{T}^T\mathbf{F}\boldsymbol{\tau}^{(f)} = \mathbf{T}^T\mathbf{B}^{(u)}\boldsymbol{\tau}^{(a)}. \end{aligned} \tag{3.75}$$

In the presented joint model, the rotation axes described by the deformation parameters $e_1^{[k]}$ and $\epsilon_1^{[k+1]}$ have the same the spatial orientation with respect to the fixed inertia coordinate system, yielding

$$\mathrm{D}_{e^m}\boldsymbol{\mathcal{F}}^{(x)} = \mathrm{D}_{\epsilon_1^m}\boldsymbol{\mathcal{F}}^{(x)}. \tag{3.76}$$

Substitution of this relation into the reduced mass matrix of equation (3.75) yields

$$\bar{\mathbf{M}}_{ee} - \mathrm{diag}(\boldsymbol{J}^{(a)}) = \bar{\mathbf{M}}_{e\epsilon_1} = \bar{\mathbf{M}}_{\epsilon_1 e} = \bar{\mathbf{M}}_{\epsilon_1\epsilon_1}, \tag{3.77a}$$

$$\bar{\mathbf{M}}_{e\epsilon_2} = \bar{\mathbf{M}}_{\epsilon_1\epsilon_2} = \bar{\mathbf{M}}^T_{\epsilon_2 e} = \bar{\mathbf{M}}^T_{\epsilon_2\epsilon_1}, \tag{3.77b}$$

$$\bar{\mathbf{M}}_{e\epsilon_3} = \bar{\mathbf{M}}_{\epsilon_1\epsilon_3} = \bar{\mathbf{M}}^T_{\epsilon_3 e} = \bar{\mathbf{M}}^T_{\epsilon_3\epsilon_1}, \tag{3.77c}$$

in which the reduced mass matrix $\bar{\mathbf{M}}$ is partitioned according to

$$\bar{\mathbf{M}} = \begin{bmatrix} \bar{\mathbf{M}}_{ee} & \bar{\mathbf{M}}_{e\epsilon_1} & \bar{\mathbf{M}}_{e\epsilon_2} & \bar{\mathbf{M}}_{e\epsilon_3} \\ \bar{\mathbf{M}}_{\epsilon_1 e} & \bar{\mathbf{M}}_{\epsilon_1\epsilon_1} & \bar{\mathbf{M}}_{\epsilon_1\epsilon_2} & \bar{\mathbf{M}}_{\epsilon_1\epsilon_3} \\ \bar{\mathbf{M}}_{\epsilon_2 e} & \bar{\mathbf{M}}_{\epsilon_2\epsilon_1} & \bar{\mathbf{M}}_{\epsilon_2\epsilon_2} & \bar{\mathbf{M}}_{\epsilon_2\epsilon_3} \\ \bar{\mathbf{M}}_{\epsilon_3 e} & \bar{\mathbf{M}}_{\epsilon_3\epsilon_1} & \bar{\mathbf{M}}_{\epsilon_3\epsilon_2} & \bar{\mathbf{M}}_{\epsilon_3\epsilon_3} \end{bmatrix}. \tag{3.78}$$

Substitution of relation (3.77) into the reduced mass matrix of equation (3.75) yields

$$\mathbf{T}^T\bar{\mathbf{M}}\mathbf{T} = \begin{bmatrix} \mathrm{diag}(\boldsymbol{J}^{(a)}) & \mathbf{0} & \mathbf{0} & \mathbf{0} \\ \mathbf{0} & \bar{\mathbf{M}}_{\theta\theta} & \bar{\mathbf{M}}_{\theta\epsilon_2} & \bar{\mathbf{M}}_{\theta\epsilon_3} \\ \mathbf{0} & \bar{\mathbf{M}}_{\epsilon_2\theta} & \bar{\mathbf{M}}_{\epsilon_2\epsilon_2} & \bar{\mathbf{M}}_{\epsilon_2\epsilon_3} \\ \mathbf{0} & \bar{\mathbf{M}}_{\epsilon_3\theta} & \bar{\mathbf{M}}_{\epsilon_3\epsilon_2} & \bar{\mathbf{M}}_{\epsilon_3\epsilon_3} \end{bmatrix}, \tag{3.79}$$

in which

$$\bar{\mathbf{M}}_{\theta\theta} = \bar{\mathbf{M}}_{\epsilon_1\epsilon_1} = \check{\mathbf{M}}_{ee}, \tag{3.80a}$$

$$\bar{\mathbf{M}}_{\theta_1\epsilon_1} = \bar{\mathbf{M}}_{\epsilon_1\epsilon_2} = \bar{\mathbf{M}}^T_{\epsilon_1\theta_1} = \bar{\mathbf{M}}^T_{\epsilon_2\epsilon_1}, \tag{3.80b}$$

$$\bar{\mathbf{M}}_{\theta_1\epsilon_2} = \bar{\mathbf{M}}_{\epsilon_1\epsilon_3} = \bar{\mathbf{M}}^T_{\epsilon_2\theta_1} = \bar{\mathbf{M}}^T_{\epsilon_3\epsilon_1}. \tag{3.80c}$$

From equation (3.79) it can be seen that the applied coordinate transformation results in a simpler reduced mass matrix without coupling terms between the drive angles $\boldsymbol{e}^{(m)}$ and the other degrees of freedom. This dynamical coupling is taken care of by the damping and stiffness matrices. Carrying out the calculations for equation (3.75) yields

$$\mathbf{T}^T\mathbf{D}\mathbf{T} = \begin{bmatrix} \mathbf{D}_{\epsilon_1\epsilon_1} & -\mathbf{D}_{\epsilon_1\epsilon_1} & \mathbf{0} & \mathbf{0} \\ -\mathbf{D}_{\epsilon_1\epsilon_1} & \mathbf{D}_{\epsilon_1\epsilon_1} & \mathbf{0} & \mathbf{0} \\ \mathbf{0} & \mathbf{0} & \mathbf{D}_{\epsilon_2\epsilon_2} & \mathbf{0} \\ \mathbf{0} & \mathbf{0} & \mathbf{0} & \mathbf{D}_{\epsilon_3\epsilon_3} \end{bmatrix}, \tag{3.81}$$

$$\mathbf{T}^T\mathbf{K}\mathbf{T} = \begin{bmatrix} \mathbf{K}_{\epsilon_1\epsilon_1} & -\mathbf{K}_{\epsilon_1\epsilon_1} & \mathbf{0} & \mathbf{0} \\ -\mathbf{K}_{\epsilon_1\epsilon_1} & \mathbf{K}_{\epsilon_1\epsilon_1} & \mathbf{0} & \mathbf{0} \\ \mathbf{0} & \mathbf{0} & \mathbf{K}_{\epsilon_2\epsilon_2} & \mathbf{0} \\ \mathbf{0} & \mathbf{0} & \mathbf{0} & \mathbf{K}_{\epsilon_3\epsilon_3} \end{bmatrix} \tag{3.82}$$

and

$$\mathbf{T}^T\mathbf{F} = \begin{bmatrix} \mathbf{0} \\ \mathbf{I} \\ \mathbf{0} \\ \mathbf{0} \end{bmatrix}. \tag{3.83}$$

The partitioning of the matrices is equal to the one used for the reduced system mass matrix, see equation (3.78). Equation (3.83) demonstrates the statement of section 3.3.2, namely that the two joint friction torques $\tau^{[k](f)}$ and $\tau^{[k+1](f)}$ that are described by the constitutive equations for the driving and flexible hinge, equation (3.55) and (3.58) respectively, are dynamical equivalent to a single joint friction torque $\tau_j^{(f)}$ dual to the joint velocity $\dot{\theta}_j$, provided that $\tau^{[k](f)} = \tau^{[k+1](f)} = \tau_j^{(f)}$ for $k = 2j - 1$.

The equations of motion presented in this section are written in an acceleration linear form. The equations can also be written linear to the physical parameters. This will be the topic of the next section.

3.3.4 Equation of motion in parameter linear form

For the identification of the unknown dynamic parameters, the equations of motion will be written in a parameter linear form by using the result of equation (3.47). Let $\mathbf{\Phi}(\boldsymbol{x}, \dot{\boldsymbol{x}}, \ddot{\boldsymbol{x}})$ be the global system matrix obtained by assembling the lumped matrices $\mathbf{\Phi}^{[k]}$ and let $\boldsymbol{p}^{(l)}$ be the corresponding parameter vector. Substitution into equation (3.62) yields

$$\langle (\boldsymbol{f}^{(r)} - \mathbf{\Phi}\boldsymbol{p}^{(l)}), \delta\dot{\boldsymbol{x}} \rangle = \langle \boldsymbol{\sigma}^{(em)}, \delta\dot{\boldsymbol{e}}^{(m)} \rangle + \langle \boldsymbol{\sigma}^{(\epsilon m)}, \delta\dot{\boldsymbol{\epsilon}}^{(m)} \rangle + \langle \boldsymbol{\sigma}^{(ec)}, \delta\dot{\boldsymbol{e}}^{(c)} \rangle, \tag{3.84}$$

in which $\boldsymbol{f}^{(r)}$ is the external force vector exclusive the inertia and gravitational forces, which are already included in the term $\mathbf{\Phi}\boldsymbol{p}^{(l)}$. This must hold true for all velocities $\delta\dot{\boldsymbol{x}}$ satisfying the instantaneous kinematic constrains (3.10) and velocity $\delta\dot{e}^{(c)}$ that should satisfy equation (3.13). Note that for most applications $\boldsymbol{f}^{(r)}$ consists of only the support forces of the base, for which the dual virtual velocities have to be zero. Consequently, the contribution of these forces to the virtual power of the manipulator is zero and therefore their contribution can be omitted. Substitution of equations (3.10,3.55) and (3.60) into equation (3.84) yields

$$\bar{\mathbf{\Phi}}(\boldsymbol{q}, \dot{\boldsymbol{q}}, \ddot{\boldsymbol{q}})\boldsymbol{p} = \begin{bmatrix} \boldsymbol{\tau}^{(a)} \\ \mathbf{0} \end{bmatrix}, \tag{3.85}$$

in which

$$
\begin{aligned}
\bar{\boldsymbol{\Phi}} = \Bigg[& \begin{matrix} \mathrm{D}_{e^m}\boldsymbol{\mathcal{F}}^{(x)T}\boldsymbol{\Phi} & \operatorname{diag}(\ddot{\boldsymbol{e}}^{(m)}) \\ \mathrm{D}_{\epsilon^m}\boldsymbol{\mathcal{F}}^{(x)T}\boldsymbol{\Phi} & \mathbf{0} \end{matrix} \qquad \cdots \\
& \begin{matrix} \operatorname{diag}(e^{(\dot{\boldsymbol{\theta}}^{(m)}/\dot{\boldsymbol{\theta}}^{(s)})^{\delta^{(a)}}}) & \operatorname{diag}(\dot{\boldsymbol{\theta}}^{(m)\ (1-\delta^{(v)})}) \\ \operatorname{diag}(e^{(\dot{\boldsymbol{\theta}}^{(m)}/\dot{\boldsymbol{\theta}}^{(s)})^{\delta^{(a)}}}) & \operatorname{diag}(\dot{\boldsymbol{\theta}}^{(m)\ (1-\delta^{(v)})}) \end{matrix} \qquad \cdots \\
& \begin{matrix} \mathbf{0} & \mathbf{0} & \mathrm{D}_{e^m}\boldsymbol{\mathcal{F}}^{(ec)T}\dot{e}^{(c)} & \mathrm{D}_{e^m}\boldsymbol{\mathcal{F}}^{(ec)T} \\ \operatorname{diag}(\dot{\boldsymbol{\epsilon}}^{(m)}) & \operatorname{diag}(\boldsymbol{\epsilon}^{(m)}) & \mathrm{D}_{\epsilon^m}\boldsymbol{\mathcal{F}}^{(ec)T}\dot{e}^{(c)} & \mathrm{D}_{\epsilon^m}\boldsymbol{\mathcal{F}}^{(ec)T} \end{matrix} \Bigg]
\end{aligned}
\tag{3.86}
$$

and parameter vector $\boldsymbol{p}$ is defined as

$$
\boldsymbol{p} = (\boldsymbol{p}^{(l)}, \boldsymbol{J}^{(a)}, \boldsymbol{\tau}^{(a,0)}, \boldsymbol{c}^{(v)}, \boldsymbol{d}, \boldsymbol{k}, k^{(c)}, \sigma^{(c0)}). \tag{3.87}
$$

Vectors $\boldsymbol{J}^{(a)}, \boldsymbol{\tau}^{(a,0)}, \boldsymbol{c}^{(v)}, \boldsymbol{k}, \boldsymbol{d}$ represent the parameter vectors containing drive inertias, static asperity friction, viscous friction, stiffness and structural damping coefficients, respectively. Note that it is assumed that the parameters $\dot{\theta}_j^{(s)}$, $\delta_j^{(a)}$ and $\delta_j^{(v)}$ in the friction model are known from previous experiments, see e.g. Waiboer (2007)

To analyse the response of the robot manipulator to harmonic inputs, but also to reduce simulation time, the nonlinear equations of motion will be linearised around a predefined trajectory.

3.3.5 Linearised equations of motion

Given the nonlinear equations of motion in equation (3.65), now consider small perturbations around a predefined nominal trajectory $(\boldsymbol{q}_0, \dot{\boldsymbol{q}}_0, \ddot{\boldsymbol{q}}_0)$ in such a way that the actual variables are of the form

$$
\begin{aligned}
&\boldsymbol{q} = \boldsymbol{q}_0 + \delta\boldsymbol{q}, \\
&\dot{\boldsymbol{q}} = \dot{\boldsymbol{q}}_0 + \delta\dot{\boldsymbol{q}}, \\
&\ddot{\boldsymbol{q}} = \ddot{\boldsymbol{q}}_0 + \delta\ddot{\boldsymbol{q}}, \\
&\boldsymbol{\tau}^{(a)} = \boldsymbol{\tau}_0^{(a)} + \delta\boldsymbol{\tau}^{(a)}.
\end{aligned}
\tag{3.88}
$$

The prefix δ denotes a perturbation and should not be confused with the virtual velocities in equation (3.62). A symbol subscripted with 0 is evaluated along the nominal trajectory. Expanding equations (3.8) and (3.11) in their Taylor series expansions and disregarding second and higher order terms results in the linear approximations

$$
\begin{aligned}
&\delta\boldsymbol{x} = \mathrm{D}\boldsymbol{\mathcal{F}}_0\delta\boldsymbol{q}, \\
&\delta\dot{\boldsymbol{x}} = \mathrm{D}\boldsymbol{\mathcal{F}}_0\delta\dot{\boldsymbol{q}} + (\mathrm{D}^2\boldsymbol{\mathcal{F}}_0 \cdot \dot{\boldsymbol{q}}_0) \cdot \delta\dot{\boldsymbol{q}}.
\end{aligned}
\tag{3.89}
$$

Linearisation of the reduced equations of motion (3.65) around the nominal trajectory $(\boldsymbol{q}_0, \dot{\boldsymbol{q}}_0, \ddot{\boldsymbol{q}}_0)$ results (Jonker (1991)) in

$$\bar{\mathbf{M}}_0 \delta\ddot{\boldsymbol{q}} + (\mathbf{D}_0 + \mathbf{C}_0 + \mathbf{F}_0)\delta\dot{\boldsymbol{q}} + (\mathbf{K}_0 + \mathbf{G}_0 + \mathbf{N}_0)\delta\boldsymbol{q} = \mathbf{B}^{(u)}\delta\boldsymbol{\tau}^{(a)}. \tag{3.90}$$

Matrix $\bar{\mathbf{M}}_0$ is the system mass matrix as in equation (3.65). Matrix $\mathbf{D}_0$ is the structural damping matrix as in equation (3.68). Matrix $\mathbf{C}_0$ is the velocity sensitivity matrix. Matrix $\mathbf{F}_0$ is the linearised friction matrix and $\mathbf{K}_0$ denotes the structural stiffness matrix. $\mathbf{G}_0$ and $\mathbf{N}_0$ are the geometric stiffening matrix and the dynamic stiffening matrix, respectively. Matrices $\bar{\mathbf{M}}_0$, $\mathbf{D}_0$, $\mathbf{F}_0$, $\mathbf{K}_0$ and $\mathbf{G}_0$ are symmetric, whereas matrices $\mathbf{C}_0$ and $\mathbf{N}_0$ are not. These matrices are calculated (Jonker (1991)) by

$$\begin{aligned}
\mathbf{C}_0 &= \mathrm{D}\boldsymbol{\mathcal{F}}_0^T[\mathrm{D}_{\dot{x}}\boldsymbol{f}^{(in)}\mathrm{D}\boldsymbol{\mathcal{F}}_0 + 2\mathbf{M}_0\mathrm{D}^2\boldsymbol{\mathcal{F}}_0 \cdot \dot{\boldsymbol{q}}_0],\\
\mathbf{K}_0 &= \mathbf{K} + \mathrm{D}\mathcal{F}_0^{(ec)T} k^{(c)} \mathrm{D}\mathcal{F}_0^{(ec)},\\
\mathbf{G}_0 &= -\mathrm{D}^2\boldsymbol{\mathcal{F}}_0^T \cdot (\boldsymbol{f} - \mathbf{M}_0\ddot{\boldsymbol{x}}_0),\\
\mathbf{N}_0 &= \mathrm{D}\boldsymbol{\mathcal{F}}_0^T[(-\mathrm{D}_x\boldsymbol{f}^{(in)} + \mathrm{D}_x\mathbf{M}_0\ddot{\boldsymbol{x}}_0)\mathrm{D}\boldsymbol{\mathcal{F}}_0\\
&\qquad + \mathbf{M}_0(\mathrm{D}^2\boldsymbol{\mathcal{F}}_0 \cdot \ddot{\boldsymbol{q}}_0 + (\mathrm{D}^3\boldsymbol{\mathcal{F}}_0 \cdot \dot{\boldsymbol{q}}_0) \cdot \dot{\boldsymbol{q}}_0) + \mathrm{D}_{\dot{x}}\boldsymbol{f}^{(in)}\mathrm{D}^2\boldsymbol{\mathcal{F}}_0 \cdot \dot{\boldsymbol{q}}_0].
\end{aligned} \tag{3.91}$$

The linearised friction matrix $\mathbf{F}_0$ is a diagonal matrix obtained by linearisation of equation (3.54) yielding

$$\mathbf{F}_0 = \begin{bmatrix} \mathrm{diag}(\bar{\boldsymbol{\tau}}^{(f)}) & \mathbf{0} & \mathbf{0} & \mathbf{0} \\ \mathbf{0} & \mathrm{diag}(\bar{\boldsymbol{\tau}}^{(f)}) & \mathbf{0} & \mathbf{0} \\ \mathbf{0} & \mathbf{0} & \mathbf{0} & \mathbf{0} \\ \mathbf{0} & \mathbf{0} & \mathbf{0} & \mathbf{0} \end{bmatrix}, \tag{3.92}$$

in which the vector with linearised joint friction torques $\bar{\boldsymbol{\tau}}^{(f)}$ is defined by

$$\bar{\tau}_j^{(f)} = \frac{2}{\pi}\arctan(c^{(a)}\dot{\theta}_{0,j})\bar{\tau}_j^{(f,s)} + \frac{2}{\pi}\frac{c^{(a)}}{1 + (c^{(a)}\dot{\theta}_{0,j})^2}\tau_j^{(f,s)} \tag{3.93}$$

and

$$\bar{\tau}_j^{(f,s)} = \tau_j^{(a)}\frac{\delta_j^{(a)}}{\dot{\theta}_j^{(s)}}\left(\frac{|\dot{\theta}_{0,j}|}{\dot{\theta}_j^{(s)}}\right)^{(\delta_j^{(a)}-1)} e^{\left(\frac{|\dot{\theta}_{0,j}|}{\dot{\theta}_j^{(s)}}\right)^{\delta_j^{(a)}}} + c_j^{(v)}(1 - \delta_j^{(v)})|\dot{\theta}_{0,j}|^{(-\delta_j^{(v)})}, \tag{3.94}$$

which are both functions of the nominal joint rotation $\dot{\boldsymbol{\theta}}_0 = \dot{\boldsymbol{e}}_0^{(m)} + \dot{\boldsymbol{\epsilon}}_0^{(1m)}$. Note that all the matrix coefficients of equation (3.90) can vary over time, since they depend on the nominal position, velocity and acceleration of the manipulator.

3.4 Discussion

A variety of representations for the equations of motion have been presented in this chapter. The most general form is that of the nonlinear equations of motion presented in section 3.3.3. This representation is implemented in the computer program SPACAR, which is used for the dynamic simulations of the robot manipulator. Furthermore the so called perturbation method (Jonker and Aarts (2001)) is used for simulations. In this method the vibrational motion of the manipulator is modelled as a first-order perturbation of the nominal rigid link motion. For that purpose, the nonlinear flexible dynamic model is split into two parts. A rigidified nonlinear system describes the nominal rigid link motion of the manipulator and the linearised equations of motion presented in section 3.3.5 describe the vibrational motion of the manipulator. The perturbation method is implemented in SPACAR as well.

The next chapter presents a linear identification technique which can be used to identify the unknown dynamic parameters of the presented robot model from experimental data. This method makes extensive use of the parameter linear formulation presented in section 3.3.4. In chapter 5, an inverse eigenvalue method will be presented to identify the dynamic parameters of the joints. The inverse eigenvalue problem is related to the linearised equations of motion that are presented in section 3.3.5. In addition the manipulator's response to harmonic driving torques is directly related to the linearised equations of motion. The identification of this response will be the topic of chapter 6.

Chapter 4

Linear identification methods

The unknown dynamic parameters of the robot model presented in chapter 3 need to be identified from experimental data. An overview of linear identification methods is presented in this chapter.

Outline

Section 4.1 presents a static identification method which can be used to identify the stiffness parameters of the drives and joints. In section 4.2, a linear least squares identification method will be presented for the identification of all dynamic parameters.

4.1 Stiffness measurements on the Stäubli RX90B

The stiffness parameters of the robot model presented in the previous chapter are estimated using static stiffness measurements. An overview of the setup is shown in figure 4.1. Using a rope, a pulley and combinations of deadweights, a force is applied to the tip of the robot. The deadweights, in a range of 0-19 kg, are suspended to the free end of the cable. The force on the tip of the robot acts as a moment on the joints. By changing the configuration of the robot and the pulley, the joints are loaded with moments in different directions.

By measuring the relative change in orientation between two succeeding links, the deformation of the joint in between is measured. The orientations of the links are measured using a Krypton Rodym 6D camera system. This system measures the 3D position of up to six markers. A description of this system is given in appendix C. The accuracy of the camera system in a plane parallel to the camera is higher than perpendicular to this plane. Therefore, most of the measurements are done in this 2D space. Four markers are used to measure one elastic deformation, see the example in figure 4.1. A marker is mounted on both ends of a link. The two markers on each link define a line. The change

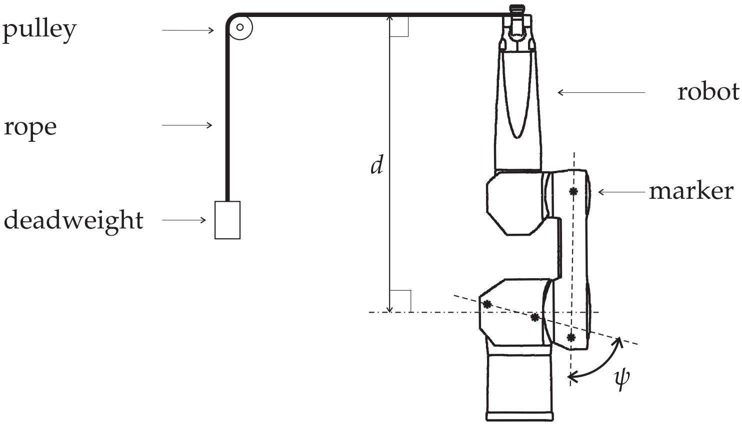

Figure 4.1: Setup to measure the joint stiffness of the Stäubli RX90B at joint 2.

of angle between two lines is the elastic deformation. In figure 4.1 this angle is denoted by the symbol ψ.

To measure the drive stiffness of the joints, the robot controller is switched on. During a measurement the integrating action of the feedback controller keeps the motor at a predefined location, also when an external moment is applied. This has been verified by measuring the motor rotation with resolvers installed on the servo motors.

Starting from an unloaded configuration the force on the tip is increased in 7 discrete steps and then the force is decreased until the system is unloaded again. From the geometry of the robot, the perpendicular distance d between the rotation point of the joint and the applied force is known, see figure 4.1 for an explanation. This distance is used to compute the moment that the force on the tip applies to the joint under consideration.

Figure 4.2 presents the results for the drive and joint flexibilities of joints 1-3. For the joint flexibilities of joint 3 only data with increasing moments is available. It is assumed that the joint stiffnesses, corresponding to deformations $\epsilon_2^{[k+1]}$ and $\epsilon_3^{[k+1]}$, are equal. This is a reasonable assumption for the first four joints, because the joints including the bearings are rotation symmetric.

Using linear regression techniques a straight line is fit through the measured data. The line is included in figure 4.2. The line is estimated as a function of the applied load. The reason for this is that the measurement accuracy of the applied loads is expected to be higher than the measurement accuracy of the elastic deformations. The measured marker displacement for each loading step is about 0.1 mm and the specified 95% reliability interval for a calibrated camera system is ±0.014 mm for measurements in the x,y-plane (2 times the standard deviation presented in table C.2). This accuracy is specified for measure-

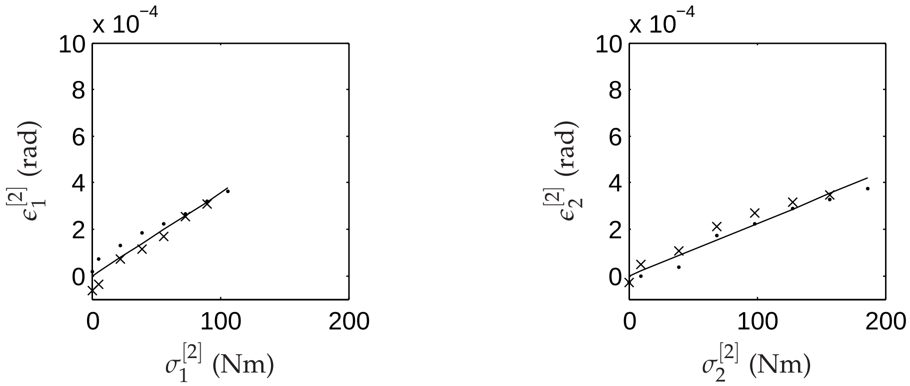

(a) Drive stiffness joint 1 (b) Joint stiffness joint 1

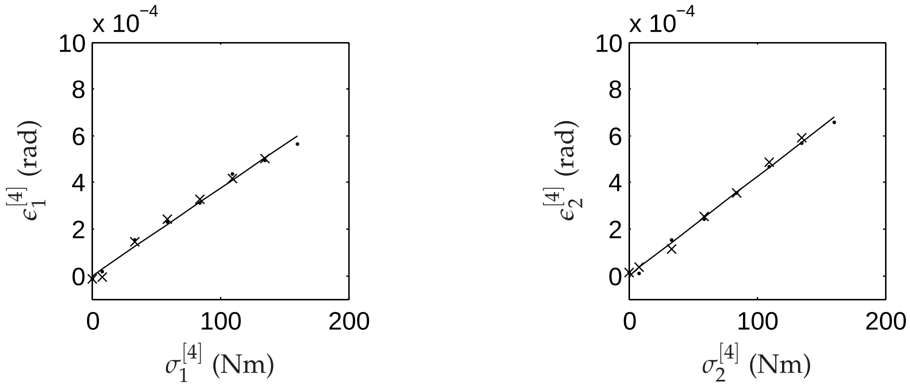

(c) Drive stiffness joint 2 (d) Joint stiffness joint 2

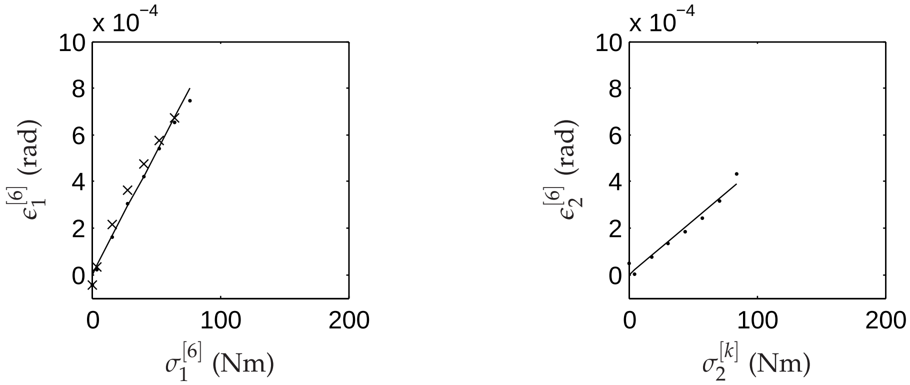

(e) Drive stiffness joint 3 (f) Joint stiffness joint 3

Figure 4.2: Measured drive and joint deformation as a function of the moments applied to the corresponding joint. The measurements with increasing load are denoted by (·), the measurements with decreasing load by (×). The line (—) is estimated using linear regression.

joint number	drive stiffness	joint stiffness	Unit
1	$k_1^{[2]} = 2.8 \times 10^5$	$k_{2,3}^{[2]} = 4.4 \times 10^5$	N m rad^{-1}
2	$k_1^{[4]} = 2.7 \times 10^5$	$k_{2,3}^{[4]} = 2.4 \times 10^5$	N m rad^{-1}
3	$k_1^{[6]} = 1.0 \times 10^5$	$k_{2,3}^{[6]} = 2.1 \times 10^5$	N m rad^{-1}
4	$k_1^{[8]} = 0.9 \times 10^5$	$k_{2,3}^{[8]} = 1.6 \times 10^5$	N m rad^{-1}

Table 4.1: Stiffness parameter estimated from static identification experiments

ments over a measurement volume of 1 m^3. In reality, the displacements are within a few mm, so the actual accuracy should be better. However, Scheringa (2006) demonstrated that the measurement system is no longer within its accuracy specifications. Overall, it is expected that it is reasonable to assume a measurement accuracy of ±0.014 mm for these experiments. The distance between the 2 markers on each link varies between 442 mm and 735 mm. By taking an average value of 500 mm, the 95% reliability interval of the angle measurements is given by: $\pm\arctan(2 \cdot 0.014/500) = 0.6 \times 10^{-4}$ rad. The drive stiffness of joints 1 and 4 are measured in the x,z-plane, giving a 95% reliability interval of $\pm 3 \times 10^{-4}$ rad.

Figures 4.2(b) and 4.2(e) show that the deformations measured with increasing load are smaller than the ones measured with decreasing load. This behaviour indicates that some hysteresis is present. However, the measurements of the drive flexibility of joint 1, see figure 4.2(a), show the opposite behaviour. It is unclear whether the hysteresis is actually present or if this behaviour is caused by measurement errors. The 95% reliability interval of the angle measurements predict variations of this order, but in that case a more stochastic error behaviour is expected. Another explanation would be drift on the camera measurements due to ambient temperature fluctuations or friction in the pulley, for example.

Although the accuracy is limited, the data can be used for a rough estimation of the unknown stiffness parameters. Namely, the inverses of the slopes of the estimated lines correspond to the stiffness parameters. The estimated values can be found in table 4.1. The table shows that the drive and joint stiffness are of the same order of magnitude. This confirms the statement in section 1.1 that both drive and joint flexibility should be included in the model.

4.2 Linear least squares identification of model parameters

A linear least squares identification method is proposed to identify the dynamic parameters of the model presented in chapter 3. First, an overview of the identification method is presented. The method is then demonstrated with a simulation example. Finally, the complications that showed up during the experimental validation of this method are discussed.

4.2.1 Linear least squares method

The dynamic parameters of the robot are estimated using the parameter linear formulation of the equations of motion presented in section 3.3.4. The robot is moved along a prescribed trajectory while the driving torques $\hat{\boldsymbol{\tau}}^{(a)}$ and all $N^{(q)}$ degrees of freedom $\hat{\boldsymbol{q}}$ are measured at time steps t_n for $n = 1, \cdots, N^{(t)}$. The symbol $(\hat{\cdot})$ is added to express that measured quantities are estimations and not necessarily the true values. Besides the positions $\hat{\boldsymbol{q}}$ also the velocities $\hat{\dot{\boldsymbol{q}}}$ and accelerations $\hat{\ddot{\boldsymbol{q}}}$ should be known. They are computed afterwards by numerical differentiation of the positions $\hat{\boldsymbol{q}}$. Let regression matrix $\mathbf{A}$ and measurement vector $\boldsymbol{y}$ be obtained by sampling the system matrix $\bar{\boldsymbol{\Phi}}(t_n)$ (defined in equation (3.86)) and the driving torques $\hat{\boldsymbol{\tau}}^{(a)}(t_n)$ along the measured trajectory $(\hat{\boldsymbol{q}}, \hat{\dot{\boldsymbol{q}}}, \hat{\ddot{\boldsymbol{q}}})$, this yields

$$\boldsymbol{y} = \begin{bmatrix} \hat{\boldsymbol{\tau}}^{(a)}(t_1) \\ \mathbf{0} \\ \vdots \\ \hat{\boldsymbol{\tau}}^{(a)}(t_{N^{(t)}}) \\ \mathbf{0} \end{bmatrix}, \quad \mathbf{A} = \begin{bmatrix} \bar{\boldsymbol{\Phi}}(\hat{\boldsymbol{q}}(t_1), \hat{\dot{\boldsymbol{q}}}(t_1), \hat{\ddot{\boldsymbol{q}}}(t_1)) \\ \vdots \\ \bar{\boldsymbol{\Phi}}(\hat{\boldsymbol{q}}(t_{N^{(t)}}), \hat{\dot{\boldsymbol{q}}}(t_{N^{(t)}}), \hat{\ddot{\boldsymbol{q}}}(t_{N^{(t)}})) \end{bmatrix}. \tag{4.1}$$

The dynamic parameter vector $\boldsymbol{p}$, defined in equation (3.87), the measurement vector $\boldsymbol{y}$ and the regression matrix $\mathbf{A}$ are related as

$$\boldsymbol{y} = \mathbf{A}\boldsymbol{p} + \boldsymbol{\rho}, \tag{4.2}$$

in which the vector $\boldsymbol{\rho}$ represents the residual torques arising from measurement noise and model errors. The dynamic parameters are found by solving the linear least squares problem

$$\hat{\boldsymbol{p}} = \arg\min_{\boldsymbol{p}} ||\boldsymbol{y} - \mathbf{A}\boldsymbol{p}||^2. \tag{4.3}$$

According to Strang (1976) the regression matrix $\mathbf{A}$ can be decomposed using a singular value decomposition as

$$\mathbf{A} = \mathbf{U}\boldsymbol{\Sigma}\mathbf{V}^T, \tag{4.4}$$

in which

$$\boldsymbol{\Sigma} = \begin{bmatrix} \mathbf{S} & \mathbf{0} \\ \mathbf{0} & \mathbf{0} \end{bmatrix}, \quad \mathbf{S} = \mathrm{diag}(\sigma_1, \sigma_2, \cdots, \sigma_l). \tag{4.5}$$

The integer l corresponds to the rank of matrix $\mathbf{A}$, which equals the number of non-zero singular values σ_i. The matrices $\mathbf{U}$ and $\mathbf{V}$ are orthogonal matrices that are written as $\mathbf{U} = [\mathbf{U}_1, \mathbf{U}_2]$ and $\mathbf{V} = [\mathbf{V}_1, \mathbf{V}_2]$, in which

$$\begin{aligned} \mathbf{U}_1 &= [\boldsymbol{u}_1, \boldsymbol{u}_2, \cdots, \boldsymbol{u}_l], \quad & \mathbf{U}_2 &= [\boldsymbol{u}_{l+1}, \boldsymbol{u}_{l+2}, \cdots, \boldsymbol{u}_{N^{(t)} \times N^{(q)}}], \\ \mathbf{V}_1 &= [\boldsymbol{v}_1, \boldsymbol{v}_2, \cdots, \boldsymbol{v}_l], \quad & \mathbf{V}_2 &= [\boldsymbol{v}_{l+1}, \boldsymbol{v}_{l+2}, \cdots, \boldsymbol{v}_{N^{(p)}}]. \end{aligned} \tag{4.6}$$

Using the singular value decomposition, a solution of the linear least squares problem (4.3) can be found as

$$\hat{\boldsymbol{p}}^{(E)} = \mathbf{V}_1 \mathbf{S}^{-1} \mathbf{U}_1^T \boldsymbol{y}, \tag{4.7}$$

in which $\mathbf{S}^{-1} = \mathrm{diag}(1/\sigma_1, 1/\sigma_2, \cdots, 1/\sigma_l)$; see e.g. Shome et al. (1998).

Not all parameters of the vector $\boldsymbol{p}$ can be identified uniquely, since some of them do not affect the dynamic response at all or affect the dynamic response only in linear combinations with other parameters. The essential parameter space of $\mathbf{A}$ is the smallest subspace that contains the solution of equation (4.3). The dimension of this subspace, denoted by the number l, is equal to the rank of matrix $\mathbf{A}$. The vectors $\boldsymbol{v}_1, \boldsymbol{v}_2, \cdots, \boldsymbol{v}_l$, i.e. the submatrix $\mathbf{V}_1$, provide an orthogonal basis for the essential parameter space. The estimated parameter vector, presented in equation (4.7), is a linear combination of the columns of $\mathbf{V}_1$. Therefore, this estimated parameter vector lies in the essential parameter space. Of course it is not a unique solution of equation (4.3) because any linear combinations of columns of V_2 can be added to this solution without affecting the residual vector $\boldsymbol{\rho}$. To compare two parameter vectors it is therefore not meaningful to compare the individual parameters in each vector. Yet two parameter vectors describe systems with identical physical behaviour if their projection into the essential parameter space is identical. E.g. the estimated parameter vector in equation (4.7) can be compared to an arbitrary vector like the actual or physical parameter vector $\boldsymbol{p}$ when the latter is also projected into the essential parameter space, i.e.

$$\boldsymbol{p}^{(E)} = \mathbf{V}_1 \mathbf{V}_1^T \boldsymbol{p}, \tag{4.8}$$

in which $\boldsymbol{p}^{(E)}$ denotes the vector $\boldsymbol{p}$ projected onto the essential parameter space. Note that in the equations of motion (3.85) the values of all parameters from the vector $\boldsymbol{p}$ can be replaced by the corresponding values for the parameters in vector $\boldsymbol{p}^{(E)}$ without changing the computed torques $\boldsymbol{\tau}^{(a)}$, even though these parameters in $\boldsymbol{p}^{(E)}$ may have unphysical values like negative masses.

Mathematically the rank of matrix $\mathbf{A}$ only depends on the model structure. In practice the size of the parameters, the excitation signal and the amount of measurement noise also influence the number of parameters that can be identified uniquely and reliably. If the contribution of a parameter to the response of the robot for a given excitation is smaller than the amount of measurement noise, then that parameter cannot be identified reliably. To incorporate a priori

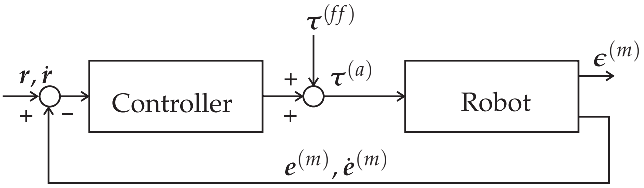

Figure 4.3: Closed-loop system

known information about accuracies or uncertainties of $\mathbf{A}$ and $\boldsymbol{y}$ in the optimisation, Lawson and Hanson (1974) describe a left multiplication of regression matrix $\mathbf{A}$ and measurement vector $\boldsymbol{y}$ by a weighting matrix $\mathbf{W}^{(L)}$. In addition, a right multiplication of matrix $\mathbf{A}$ with a scaling matrix $\mathbf{W}^{(R)}$ is presented. This matrix $\mathbf{W}^{(R)}$ is used to include a priori information about parameter vector $\boldsymbol{p}$ in the estimation problem.

The effect of a parameter on the dynamic response of the robot can only be measured if the trajectory is sufficiently exciting for the considered parameter. Keeping the experimental limitations in mind, the following approach is suggested. Parameters related to position dependent behaviour such as gravitation can only be identified if the measurement data is obtained from sufficiently distinguishable robot configurations. Therefore, the robot is programmed to follow a trajectory $\boldsymbol{r}$ along various configurations in its work space. For stability and safety reasons, the experiments are carried out in closed-loop. Problems arise regarding the identifiability of the dynamic parameters of the flexible joints because the controller is designed to damp out the vibrations of the robot. Therefore, during the trajectory the driving torques are perturbed with feed-forward torques $\boldsymbol{\tau}^{(ff)}$ having a frequency spectrum beyond the bandwidth of the closed-loop system; see figure 4.3. Details about the reference trajectory $\boldsymbol{r}$ and the feed-forward torques $\boldsymbol{\tau}^{(ff)}$ will be presented in next section.

4.2.2 Simulation example

The identification method will be demonstrated with simulated responses of the four link manipulator model presented in figure 3.4, page 20. The parameters of the robot model are adopted from the industrial Stäubli RX90B robot. The mass and inertia parameters, including the drive inertias, are obtained from CAD data. The last two joints are replaced by a single rotational inertia of 0.05 kg m^2, which has been added to $J'^{[4](p)}_{zz}$ of link 4. Numerical values for the stiffness and prestress of the gravity compensating spring in link 2 are provided by the manufacturer. The joint friction model and parameters are based on the work of Waiboer (2007), see section 3.3.2. For the stiffness parameters the results of section 4.1, table 4.1 have been used. No a priori values for the damping parameters are known. Their numerical values are set to 0.1% of the stiffness parameters to avoid the occurrence of undamped vibrational modes. An overview of the used parameters can be found in table D.1 on page 139.

The nonlinear manipulator model is implemented in the simulation package SPACAR. For the simulations the nonlinear SPASIM routine has been used, operating under MATLAB SIMULINK. The ODE23t numerical integration scheme is selected, with an absolute and relative accuracy set to 1e-7. This integration scheme is suitable for moderate stiff problems and is free of numerical damping. The dynamic responses are computed in the closed-loop configuration of figure 4.3 with a model of the real digital Stäubli CS8 motion controller.

The reference trajectory $\boldsymbol{r}$ is described by the second harmonic (joints 1 and 3) and third harmonic (joints 2 and 4) of a sine function with a period of 4.096 s and an amplitude and offset of $\frac{1}{4}\pi$. Therefore, the reference signals for the joint positions vary between 0 and $\frac{1}{2}\pi$. The feed-forward torques are described by a multi-sine signal containing 72 equally spaced frequencies ranging from 1 to 110 Hz. The real CS8 motion controller can log several signals at 250 Hz. In the simulation model the data is sampled at 4 kHz. To mimic the real controller and to prevent aliasing the data is resampled to 250 Hz using a digital lowpass filter. It has been found that without this lowpass filter the estimation is inaccurate because of aliasing effects.

The velocities and accelerations are obtained by means of numerical differentiation of the position signals using an eighth order central difference scheme given by Khan and Ohba (2003). In a simulation the true velocities and accelerations are easily accessible, but with the real robot only position data is available. To mimic the experimental conditions as much as possible the numerical differentiation procedure is included in this simulation example as well.

From the simulated responses, the regression matrix $\mathbf{A}$ and the measurement vector $\boldsymbol{y}$ are constructed. The parameter vector $\boldsymbol{p}$ contains 78 parameters, namely the stiffness and prestress of the gravity compensating spring, 10 inertia parameters $\boldsymbol{p}^{[k](l)}$ for each link, and 1 drive inertia, 2 friction parameters ($\tau_j^{(a,0)}$ and $c_j^{(v)}$), 3 stiffness and 3 damping parameters for each joint. The scaling matrix $W^{(R)}$ is used to divide each column by an initial estimation of the corresponding parameter value. It is expected that all measurements have equal uncertainty, therefore weighting matrix $W^{(L)}$ has not been used.

Using a singular value decomposition for the regression matrix, the essential parameter vector $\hat{\boldsymbol{p}}^{(E)}$ is identified. The solid line in figure 4.4 shows the norm of the residuals in equation (4.3) for an increasing number of singular values that are used to compute this parameter vector. The dashed line in figure 4.4 represents the norm of equation (4.3) for the true parameter vector $\boldsymbol{p}$. This line is also a measure of the noise level in the simulation example. The figure shows that for more than 59 singular values only a negligible extra reduction of the residual is possible. The solid line crosses the dashed line between 58 and 59 singular values. Consequently, the contribution of the parameter

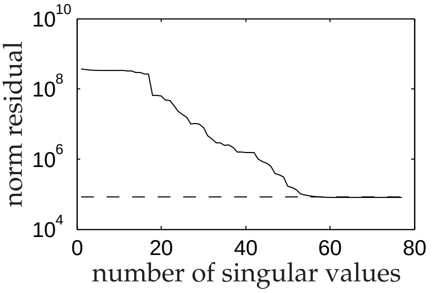

Figure 4.4: Norm of the residuals for an increasing number of singular values (—). The dashed line (- -) represents the norm of the residual for the true parameter vector.

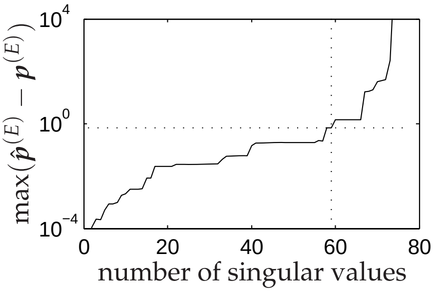

Figure 4.5: Maximum difference between the estimated ($\hat{\boldsymbol{p}}^{(E)}$) and true parameter ($\boldsymbol{p}^{(E)}$) vector in the essential parameter space for an increasing number of singular values.

space spanned by columns 59-78 of the right singular matrix $\mathbf{V}$ to the measured response of the manipulator is smaller than the noise level. Furthermore, the measurement noise will decrease the accuracy of the estimated parameter values for an increased number of singular values. This effect is visualised in figure 4.5, in which the maximum error between the estimated and true parameter vector in the essential parameter space is given for an increasing number of singular values.

Based on the results presented in the last two figures the essential parameter vector will be spanned by the first 59 columns of the right singular matrix $\mathbf{V}$. This number is marked in figure 4.5 by the dotted lines. The estimated parameters are given in table D.1 on page 139. To compare the identified parameters with the original values, both are projected onto the essential parameter space. The difference between both parameter sets arises from measurement noise generated by quantisation effects in the controller, aliasing effects during sampling and numerical differentiation of the position signals. The list of parameters shows that the mass of the first link, denoted by $m^{[1]}$, cannot be identified. The reason for this is that this parameter has no influence on the dynamic response and may be omitted from the model. In addition, the static asperity friction torques $\tau_j^{(a,0)}$ cannot be identified from the data set. These parameters define the sliding friction torque for very low velocities around velocity reversals. The identification trajectory does not contain enough data points in this velocity region to identify these parameters. Although it cannot identified from this data set it has a large influence on forward simulations and may not be omitted in the model. Therefore these parameters should be identified from dedicated friction identification experiments as described by Waiboer (2007).

Furthermore, the parameters $J'^{[3](p)}_{yz}$ and $J'^{[4](p)}_{yz}$ cannot be identified from this data set. For the other parameters a satisfactory estimation is achieved.

As the ultimate goal of this work is to simulate the robot response, not only are the estimated parameters important but also the ability to simulate the robot tip motion. Simulated tip responses of both the original and the identified model are used for the validation of the identified parameters. The identified static asperity friction torques $\tau_j^{(a,0)}$ are replaced by the original values in this simulation.

The robot is programmed to perform a tip motion along a straight line of 1.7 m in the horizontal plane as illustrated in figure 4.6(a) with starting point A and end point B. The joint reference signals are presented in figure 4.6(b). Due to the flexibilities and limited tracking performance of the control system, the robot tip deviates from the programmed straight line. The tip deviations of the model using the original parameters are shown in figures 4.7(a) and 4.7(b) in a vertical and horizontal directions, respectively. The figures show that at start-up for $t = 0$ due to high accelerations in combination with the static asperity friction torque the robot is excited resulting in a small vibration of the robot tip, which damps out during the first half second. Next, at $t = 1$ s, a high acceleration of joint 1 and a change of the sign of the friction torque due to joint velocity reversals of joint 2 and 3 result in a significant deviation of the robot tip. The influence of gravity is clearly recognisable in figure 4.7(a) as well, namely the tip motion first shows a decreasing static deflection from point A towards the middle of the trajectory and subsequently an increasing deflection towards point B.

Figures 4.7(c) and 4.7(d) show the differences in the vertical and horizontal direction of the tip motion simulated with models using the original and the identified parameters. These differences appear to be more than two orders of magnitude smaller than the tip deviations of the original model. Similar results are found when other quantities are compared, e.g. the driving torques. Furthermore, the absolute accuracy of the tip motion is an order of magnitude smaller than the 0.1 mm bound, which is required for laser welding as previously mentioned in section 1.1. Therefore, it can be concluded that there is a good agreement between both models and that the identification technique works for this simulation example.

4.2.3 Experimental approach linear least squares method

To apply the linear identification method to the actual Stäubli RX90B robot, all degrees of freedom should be measured. The drive angles can be computed from measurements of the resolvers attached to the motor shafts. For the elastic deformations, the Krypton camera system is proposed. Unfortunately the dynamic identification involves much more than the static identification of section 4.1. The robot appears to vibrate in a complicated 3D motion even

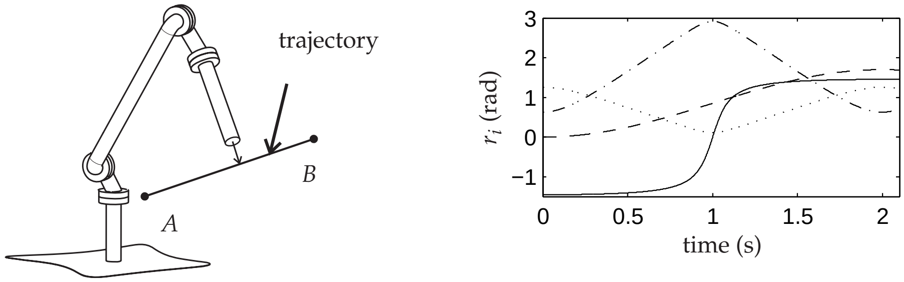

(a) Visualisation

(b) Reference signals: joint 1 (—), joint 2 (· · ·), joint 3 (− ·), joint 4 (− −).

Figure 4.6: Validation trajectory 4 DOF model.

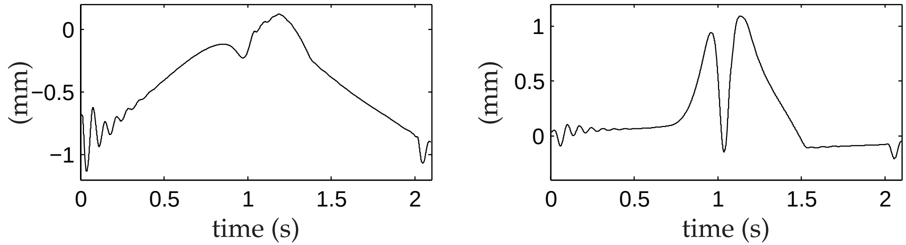

(a) Vertical deviation robot tip original model

(b) Horizontal deviation robot tip original model

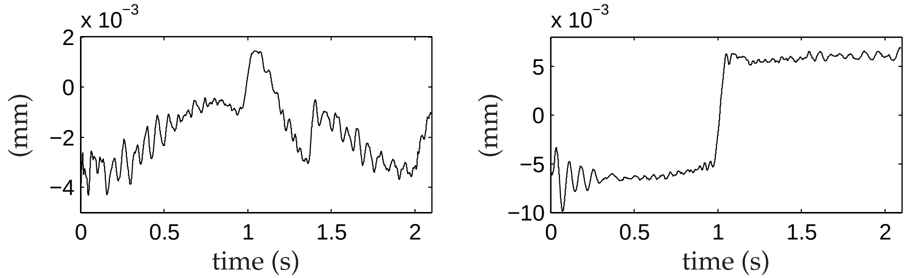

(c) Difference between tip motion of original and identified model in vertical direction

(d) Difference between tip motion of original and identified model in horizontal direction

Figure 4.7: Simulation results validation trajectory 4 DOF model.

if it is excited in one plane. So, instead of measuring only one elastic deformation of one joint, now all deformations of all joints need to be measured synchronously. Therefore another method is required to compute the joint deformations from the camera measurements. First, the developed measurement technique is presented. Then some experimental results including the accuracy of the measurement technique are given. Finally, the use of this measurement technique for the parameter identification of the Stäubli RX90B is discussed.

3D measurement technique for the Krypton camera system

To measure the elastic deformations of one joint, three markers are attached to the links on either side of the joint, see figure 4.8. The position of these markers, denoted by $(\boldsymbol{x}^{[1](p)}, \boldsymbol{x}^{[2](p)}, \boldsymbol{x}^{[3](p)})$ and $(\boldsymbol{x}^{[1](q)}, \boldsymbol{x}^{[2](q)}, \boldsymbol{x}^{[3](q)})$, are expressed in a frame $(\boldsymbol{n}_x, \boldsymbol{n}_y, \boldsymbol{n}_z)$ fixed to the camera. The links are assumed to be rigid, so the position of the three markers on link p can be described with a single transformation $\mathcal{T}^{(p)}(\boldsymbol{\lambda}^{(p)}, \boldsymbol{v}^{(p)})$ with respect to some reference positions of the markers, denoted by $(\boldsymbol{x}^{[1](p,0)}, \boldsymbol{x}^{[2](p,0)}, \boldsymbol{x}^{[3](p,0)})$. The rotational part of this transformation is described by four Euler parameters $\boldsymbol{\lambda}^{(p)}$. The translation is described with a vector $\boldsymbol{v}^{(p)}$. In this way the position of marker i during motion will be described by

$$\begin{bmatrix} x_x^{[i](p)} \\ x_y^{[i](p)} \\ x_z^{[i](p)} \end{bmatrix} = \mathbf{R}(\boldsymbol{\lambda}^{(p)}) \begin{bmatrix} l_x^{[i](p,0)} \\ l_y^{[i](p,0)} \\ l_z^{[i](p,0)} \end{bmatrix} + \begin{bmatrix} v_x^{(p)} \\ v_y^{(p)} \\ v_z^{(p)} \end{bmatrix}, \tag{4.9}$$

in which $\mathbf{R}(\boldsymbol{\lambda}^{(p)})$, also denoted as $\mathbf{R}^{(p)}$, is a rotation matrix. An expression for the rotation matrix in terms of Euler parameters is presented in equation (3.16). In the initial configuration, matrix $\mathbf{R}(\boldsymbol{\lambda}^{(p)})$ is the identity matrix and vector $\boldsymbol{v}^{(p)}$ contains zeros. For each link configuration measurements for all three markers are available, which are mutually related through equation (4.9). This results in a system with 9 equations and 7 unknowns, namely 4 λ-parameters and 3 coordinates of vector $\boldsymbol{v}^{(p)}$. For each new measurement, the transformation parameters $(\boldsymbol{\lambda}^{(p)}, \boldsymbol{v}^{(q)})$ are estimated by solving this overdetermined nonlinear system in a least squares sense. The λ-parameters are not independent, so the solution is further constrained by equation (3.17). This procedure is carried out for the links on either side of the joint.

Next, the elastic deformations of the joints are related to the relative motion between the links on each side of the joint. The deformation functions of the hinge element, equation A.13 on page 130, are used to describe the required deformation parameters in a local reference frame $(\boldsymbol{n}_{\bar{x}}, \boldsymbol{n}_{\bar{y}}, \boldsymbol{n}_{\bar{z}})$ as a function of the estimated λ-parameters. The local reference frame $(\boldsymbol{n}_{\bar{x}}, \boldsymbol{n}_{\bar{y}}, \boldsymbol{n}_{\bar{z}})$ must be specified with respect to the global camera frame. This is done by first calibrating the base frame of the robot with respect to the camera frame. Next, the local

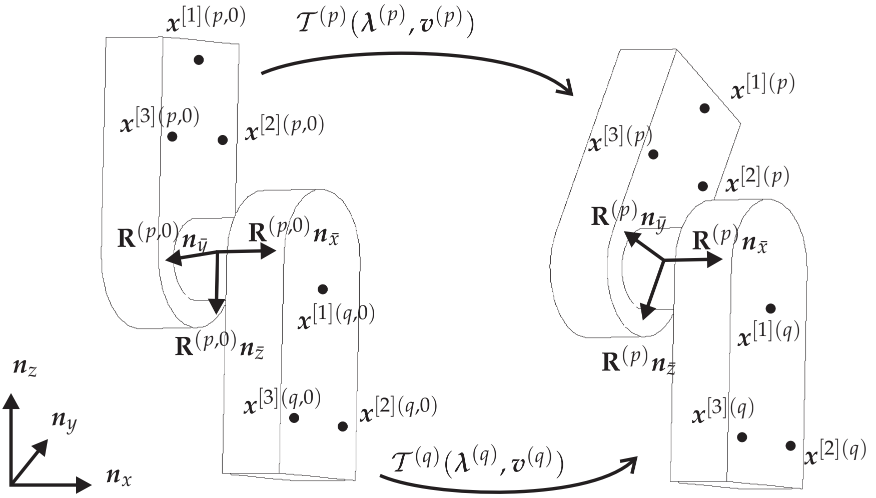

Figure 4.8: Measurement setup with Krypton camera system to measure the joint deformations in 3 directions. The dots represent the markers.

frames are computed from the calibrated base frame and an a priori known kinematical model of the robot. The base frame is calibrated by solving an over-determined set of equations describing the position of measured markers as a function of the base frame and the kinematic model for several robot poses, see Khalil and Dombre (2002). For this calibration a set of three markers is attached to the robot tip. The local reference frame is attached to link p. Therefore it only needs to be specified for the initial configuration. It is important that the local reference frames are defined accurately, because only then do the measured deformations correspond to the deformations of the model.

Results 3D measurement technique

The experimental results of the proposed measurement technique applied to the Stäubli RX90B are presented in this section. During movement of the joints along a specified trajectory $\boldsymbol{r}$, the robot is excited by feed-forward torques $\boldsymbol{\tau}^{(ff)}$. The measured drive angles $\hat{\boldsymbol{e}}^{(m)}$ are presented in figure 4.9(a). All markers should be visible for the camera system throughout the measurement. As a result the trajectory is less exciting than the trajectory presented in section 4.2.2.

The total joint rotations $\hat{\boldsymbol{\theta}}$ and joint deformations $\hat{\boldsymbol{\epsilon}}^{(2m)}$ and $\hat{\boldsymbol{\epsilon}}^{(3m)}$ are estimated from Krypton data using the procedure described above. The drive deformations $\hat{\boldsymbol{\epsilon}}^{(1m)}$ are computed by

$$\hat{\boldsymbol{\epsilon}}^{(1m)} = \hat{\boldsymbol{\theta}}^{(m)} - \hat{\boldsymbol{e}}^{(m)}. \tag{4.10}$$

The results for joint 2 are presented in figure 4.9(b).

As expected, the elastic deformations are much smaller than the drive angle $\hat{e}_2^{(m)}$. This, in combination with relation (4.10), indicates that the proposed measurement technique is able to estimate the large joint motion $\boldsymbol{\theta}^{(m)}$. However, the accuracy of this estimation and in particular that of the elastic deformations $\boldsymbol{\epsilon}^{(m)}$ appeared to be insufficient, for reasons explained below.

First of all, the accuracy of the camera system itself is insufficient for this application. For the stiffness measurements, 2D data could be used. During the dynamic excitation 3D measurements are required and, as specified in appendix C, the accuracy is less for the third dimension. In addition the gross motion of the manipulator required to excite the pose-dependent dynamics has a negative influence on the obtained accuracy, because the accuracy of a measured marker displacement decreases if the total marker displacement increases.

Second, it appeared that insufficient accuracy of the kinematic model and the base calibration resulted in a small orientation mismatch of the local frames $(\bar{x}, \bar{y}, \bar{z})$. Because of this, part of the large joint motions $\boldsymbol{\theta}$ is projected onto the small bending deformations $(\boldsymbol{\epsilon}^{(2m)}, \boldsymbol{\epsilon}^{(3m)})$. For example, the measured deformations $\hat{e}_2^{(2m)}$ and $\hat{e}_2^{(3m)}$ presented in figure 4.9(b), show a low frequency behaviour similar to the large rotations $\theta_1^{(m)}$ and $\theta_2^{(m)}$, presented in figure 4.9(a). As a result, even if the high frequency vibration is measured correctly, a measurement error in the low frequency behaviour will result in an inaccurate least squares fit, as the outcome of the least squares fit is very sensitive to the rather large amplitude of the low frequency trend. Note that specifying a local frame to express the joint deformations is always an issue when measuring the joint deformations. This is not only the case for camera systems but also for other external sensors, especially if the small joint deformations are computed from large and absolute link movements.

4.3 Discussion

The static identification method of section 4.1 is straightforward to apply but only gives the stiffness parameters. The linear least squares parameter identification technique of section 4.2.1 can be used provided that all degrees of freedom can be measured with sufficient accuracy. Unfortunately it appeared that the measurement setup with the Krypton camera system is to inaccurate for these measurements. It is expected that no other measurement system is available in or outside the laboratory that is applicable for this task. Therefore, another method that does not require measuring all deformations will be presented in the following chapters.

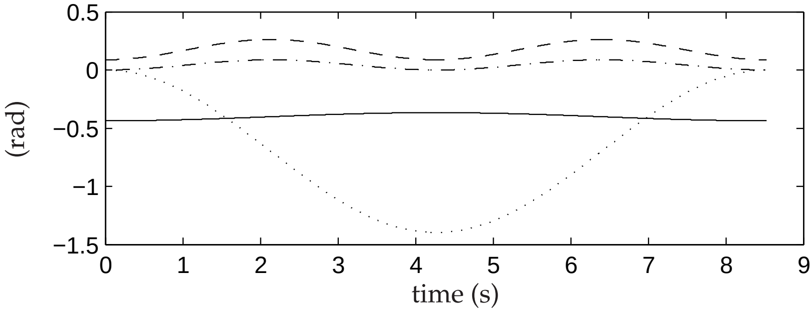

(a) Measured drive angles $e^{(m)}$: joint 1 (—), joint 2 ($\cdots$), joint 3 ($- \cdot$), joint 4 ($- -$).

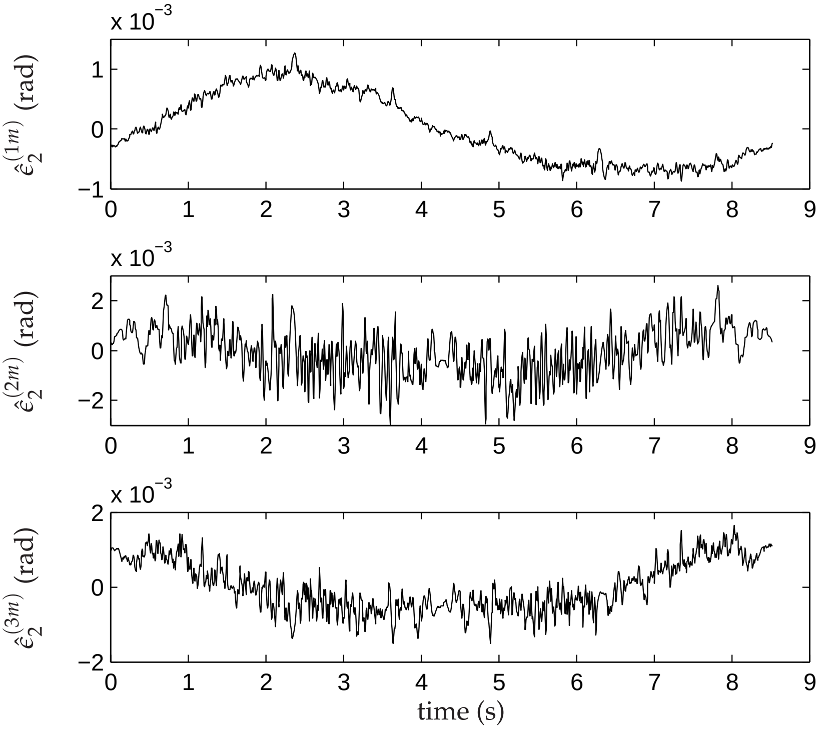

(b) Estimated elastic deformations joint 2.

Figure 4.9: Experimental results 3D Krypton measurements.

Chapter 5

Inverse eigenvalue parameter identification method

To estimate the dynamic parameters of the drive system of the robot model, an identification method is proposed that has its roots in the inverse eigenvalue theory. The method is based on the work of Hovland et al. (2001). In this chapter, some important modifications are proposed.

A first modification is to use Multivariable Frequency Response Functions (MFRF), while in the original method SISO frequency response functions are proposed. As will become clear in chapter 6, the use of MIMO closed-loop measurements cancels the requirement of the original method to switch off the feedback controllers of the excited joints.

A second modification concerns the determination of the (anti-)resonance frequencies that are needed as input for the inverse eigenvalue identification method. Using the original method the extraction of the (anti-)resonance frequencies from an identified MFRF was unspecified. In this work the parametrisation of the MFRF by means of transfer functions is proposed. A transfer function is a mathematical representation of the relationship between the input and output of a linear time invariant system. The inputs and outputs of the robot are defined as the driving torques and drive angles, respectively. The parametrisation of the MFRF by means of transfer functions enables accurate estimation of the required undamped eigenvalues. The transfer functions are identified by frequency domain system identification techniques that will be presented in chapter 6. Although these techniques are quite involved, they enable a thorough validation of the estimated (anti-)resonance frequencies.

Furthermore, the method is applied to a robot containing both drive and joint flexibilities, while originally only drive flexibilities were included. Although the joint flexibilities cannot be identified with this method, it is shown that the presence of joint flexibilities does not influence the estimation of the drive flexibilities.

Outline

Before the inverse eigenvalue problem will be discussed by giving a brief overview of the available literature, the forward eigenvalue problem will be introduced. Next, it will be shown that an appropriate normalisation of the eigenvectors can help to solve the inverse problem. In section 5.4 the relationship between an MFRF and the eigenvalue problem will be presented. In section 5.5 a special type of eigenvectors, namely the rigid-body modes, will be introduced to explain the low frequency amplitude of the MFRF. In section 5.6 the parametrisation of the MFRF using transfer functions is presented. Section 5.7 shows the derivation of the transfer functions from the nonlinear robot model featured in chapter 3. After discussing this general eigenvalue theory, the proposed method to identify the dynamic parameters of the drive system will be presented in section 5.8. The method will be illustrated with a numerical example using the robot model presented in section 4.2.2. Finally, the approach presented in this chapter will be discussed.

5.1 Eigenvalue problem

The development of this section follows Gatti and Ferrari (1999). Let us consider a set of linear second order differential equations in terms of the degrees of freedom $\boldsymbol{q} \in \mathcal{R}^{N^{(q)}}$ excited by an external force vector $\boldsymbol{f} \in \mathcal{R}^{N^{(q)}}$,

$$\tilde{\mathbf{M}}\ddot{\boldsymbol{q}} + \tilde{\mathbf{D}}\dot{\boldsymbol{q}} + \tilde{\mathbf{K}}\boldsymbol{q} = \boldsymbol{f}, \tag{5.1}$$

in which matrices $\tilde{\mathbf{M}}$, $\tilde{\mathbf{D}}$ and $\tilde{\mathbf{K}}$ represent the mass matrix, the damping matrix and the stiffness matrix, respectively.

In the undamped eigenvalue problem we seek solutions for equation (5.1) when no external forces are applied and damping is not present:

$$\tilde{\mathbf{M}}\ddot{\boldsymbol{q}} + \tilde{\mathbf{K}}\boldsymbol{q} = \mathbf{0}. \tag{5.2}$$

Let us seek a particular solution, namely that in which all the coordinates execute synchronous harmonic motion. Mathematically, this type of motion is expressed by

$$\boldsymbol{q} = \boldsymbol{v}e^{-j\omega t}, \tag{5.3}$$

in which $\boldsymbol{v}$ are constant amplitudes and $e^{-j\omega t}$ is a harmonic function of time that is the same for all the coordinates $\boldsymbol{q}$. Substitution of a solution of this type yields

$$(-\omega^2\tilde{\mathbf{M}} + \tilde{\mathbf{K}})\boldsymbol{v}e^{-j\omega t} = \mathbf{0}. \tag{5.4}$$

Let us assume that matrices $\tilde{\mathbf{M}}$ and $\tilde{\mathbf{K}}$ are nonsingular, so that $\tilde{\mathbf{K}}\boldsymbol{v}$ and $\tilde{\mathbf{M}}\boldsymbol{v}$ do not vanish except for the trivial solution $\boldsymbol{v} = \mathbf{0}$. Separating the time-dependent and space-dependent variables yields the *generalised eigenvalue problem* from which follows that (5.4) allows a non-trivial solution $\boldsymbol{\nu}^{[r]}$ so that

$$(\tilde{\mathbf{K}} - \omega^{[r]^2}\tilde{\mathbf{M}})\boldsymbol{\nu}^{[r]} = \mathbf{0}, \tag{5.5}$$

if $\omega^{[r]^2}$ is a root of the algebraic equation

$$\det(\tilde{\mathbf{K}} - \omega^2\tilde{\mathbf{M}}) = 0. \tag{5.6}$$

The eigenvalue equation (5.6) is of degree $N^{(q)}$ in ω^2 and thus possesses $N^{(q)}$ roots $\omega^{[r]^2}$. It can be shown that for symmetric and positive $\tilde{\mathbf{K}}$ and $\tilde{\mathbf{M}}$, scalar $\omega^{[r]^2}$ is a real and positive quantity. To each root $\omega^{[r]^2}$ corresponds a real solution $\boldsymbol{\nu}^{[r]}$, namely the solution of equation (5.5), which is called the eigenvector associated with the eigenvalue $\omega^{[r]^2}$.

5.2 Overview inverse eigenvalue techniques

The inverse eigenvalue problem is defined as follows: construct the mass, stiffness and, if possible, damping matrix according to a modal data set containing their eigenvalues and eigenvectors.

For the undamped eigenvalue problem (5.5) no unique solution is available because the eigenvectors are only unique up to a scalar multiplier. If it is known, for example, that the given set of eigenvectors is normalised with respect to the mass matrix or the mass matrix is known a priori, the mass and stiffness matrices can be reconstructed from the modal data set.

Often only a limited number of coordinates can be measured (or excited) independently. Therefore only a subset of the eigenvector coordinates is available. The inverse problem for a limited set of measurements has been studied by several researchers. Unique solutions can only be found if the topology of the system is restricted.

An often-made assumption is that the system consist of a series of lumped masses with springs in between, see figure 5.1(a). A system such as this has a diagonal mass matrix and a symmetric tri-diagonal (also called Jacobian) stiffness matrix. Gantmakher and Krein (1950) first solved the basic problem of reconstructing the mass and stiffness parameters of this system from its resonance frequencies $\omega^{[r]^2}$ and anti-resonance frequencies $\mu^{[r]^2}$. The anti-resonance frequencies $\mu^{[r]^2}$ are equal to the resonance frequencies of the constrained system. The constrained system is defined by fixing the last mass, see figure 5.1(b). As shown by Gladwell (1986) the resonance and anti-resonance frequencies can be used to compute the eigenvector coordinates $\nu^{[r]}_{N^{(q)}}$ for $r = 1, \cdots, N^{(q)}$ and vice versa.

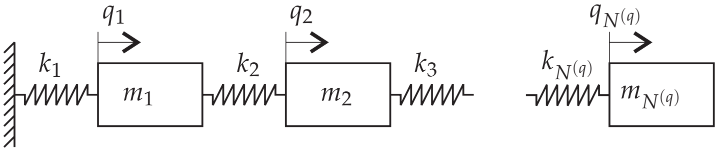

(a) System with eigenvalues $\omega^{[r]^2}$

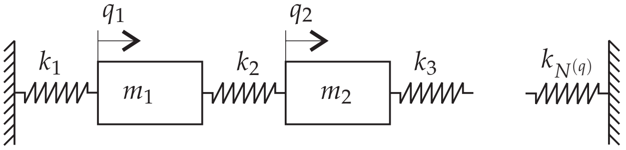

(b) Constrained system with eigenvalues $\mu^{[r]^2}$

Figure 5.1: System model, containing $N^{(q)}$ masses and springs. The anti-resonance frequencies of the system are equal to the resonance frequencies of its corresponding constrained system.

A vast amount of literature related to a series of lumped masses and its generalisation is available at the moment. An overview with regard to undamped systems can be found in Gladwell (1986, 2004). A pre- and post-multiplication of eigenvalue problem (5.5) with the square root of the mass matrix $\tilde{\mathbf{M}}^{1/2}$ (see Gladwell (1986)) yields the *standard eigenvalue problem*:

$$(\mathbf{J} - \omega^{[r]^2}\mathbf{I})\boldsymbol{u}^{[r]} = \mathbf{0}, \tag{5.7}$$

in which $\boldsymbol{u}^{[r]}$ is the eigenvector corresponding to the eigenvalue $\omega^{[r]^2}$ and

$$\mathbf{J} = \left(\tilde{\mathbf{M}}^{-1/2}\right)^T \tilde{\mathbf{K}}\tilde{\mathbf{M}}^{-1/2}. \tag{5.8}$$

The well-conditioned procedure for reconstructing Jacobian matrix $\mathbf{J}$ uniquely from $(\omega^{[r]^2}, u^{[r]}_{N^{(q)}})$ for $r = 1, \cdots, N^{(q)}$ is called the Lanczos algorithm; see Golub and Boley (1977); Boley and Golub (1988).

A lot of effort has been made to extend the Lanczos algorithm for different spring configurations, but still assuming a diagonal or a priory known mass matrix. Gladwell (1997, 1999) shows how an infinite family of tri-diagonal stiffness *and* mass matrices can be constructed, in such a way that each model has a specified set of resonance and anti-resonance frequencies. The tri-diagonal mass and stiffness matrices correspond to inline finite element models assembled of 2 DOF elements.

More recently, inverse eigenvalue problems have been studied for damped systems with complex eigenmodes and eigenvalues. Gladwell (1999) shows how to construct the inline finite element model with a damper at the free end, so that the system has specified (complex) eigenvalues.

Ram and Elhay (1996) analyse the problem of designing a system with a known diagonal mass matrix and a tri-diagonal stiffness and damping matrix, so that the spectrum of the original system and the constrained system has a specified set of complex eigenvalues. A system such as this corresponds to a serial train of known masses interconnected by springs and dampers as shown in figure 5.1. They show that a solution is always possible, but not unique.

Gladwell (2001) analyses the reconstruction of a damped parallel system, in which each parallel system is connected by a common mass at the free end. The reconstruction uses the eigenvalues of both the original and the constrained system. The analysis has two parts: the establishment of the conditions on the eigenvalues which ensure that they correspond to an actual system; and the derivation of the system parameters from its (constrained) eigenvalues.

Lancaster and Prells (2005) study the inverse problem for a general damped eigenvalue problem with positive definite mass and stiffness matrices and a positive semi-definite damping matrix. Assuming that all matrices are symmetric and a full set of eigenvalues and eigenvectors are provided, a solution is given to reconstruct the system matrices. Furthermore, conditions regarding the modal data are given for which a solution can be obtained. The mass matrix can only be computed uniquely if it is assumed that all matrices are symmetric.

A mathematical overview of general inverse eigenvalue techniques can be found in the book by Chu and Golub (2005).

Only a brief overview of the available literature on this subject is given above, but it shows that it is generally impossible to reconstruct the mass, stiffness and damping matrix of a mechanical system uniquely from only a partially described set of modal data. In our experimental setup the reduced data set arises from a lack of sensors, because only the driving torque and drive angle can be measured. In addition, the number of eigenvalues that can be identified is limited, because of the maximum sample rate of the robot controller.

As shown above, the number of sensors can be reduced if the topology of the system is restricted. For a system such as this the mass, stiffness and damping matrices have a sparse structure. The stiffness and damping matrices of the linearised robot model are diagonal. The mass matrix of the robot model has no sparse structure, except for the entries corresponding to the coordinates of the drive system. By using the joint rotations as degrees of freedom, as explained in section 3.3.3, a partly diagonal mass matrix and tri-diagonal structural stiffness and damping matrix are obtained. In section 5.8 this feature will be used to identify some of the dynamic parameters of the drive system. Before presenting the proposed identification method, it will be shown that an appropriate scaling of the eigenvectors can help solve the inverse eigenvalue problem.

5.3 Mass normalisation of the eigenvectors

The eigenmodes $\boldsymbol{\nu}^{[r]}$ are orthogonal with respect to the mass and stiffness matrix $\tilde{\mathbf{M}}$ and $\tilde{\mathbf{K}}$. However, as pointed out before the amplitude of an eigenmode is undefined, thus allowing us to choose it appropriately. A common choice is to apply a normalisation on the mass matrix (Gatti and Ferrari (1999); Meirovitch (1986)), yielding

$$\boldsymbol{\nu}^{[s]^T}\tilde{\mathbf{M}}\boldsymbol{\nu}^{[r]} = \delta_{rs}, \tag{5.9}$$

and

$$\boldsymbol{\nu}^{[s]^T}\tilde{\mathbf{K}}\boldsymbol{\nu}^{[r]} = \omega^{[r]^2}\delta_{rs}, \tag{5.10}$$

in which δ_{rs} is the Kronecker delta symbol.

The eigenvectors can be conveniently arranged in a square matrix of order $N^{(q)}$, known as the modal matrix and having the form

$$\mathbf{N} = [\boldsymbol{\nu}^{[1]}, \cdots, \boldsymbol{\nu}^{[N^{(q)}]}]. \tag{5.11}$$

In view of definition (5.11), all $N^{(q)}$ solutions of the eigenvalue problem, equation (5.5), can be written in a compact matrix equation

$$\tilde{\mathbf{K}}\mathbf{N} = \tilde{\mathbf{M}}\mathbf{N}\boldsymbol{\Omega}^2, \tag{5.12}$$

in which $\boldsymbol{\Omega}^2$ is a diagonal matrix containing the corresponding eigenvalues ω^2. If the modes are normalised to satisfy equation (5.9), we can write

$$\mathbf{N}^T\tilde{\mathbf{M}}\mathbf{N} = \mathbf{I} \tag{5.13}$$

and

$$\mathbf{N}^T\tilde{\mathbf{K}}\mathbf{N} = \boldsymbol{\Omega}^2. \tag{5.14}$$

Where this mass normalisation is well known from literature, below explicit relations will be derived for the mass and stiffness matrices of the inverse eigenvalue problem using this normalisation of the eigenvectors. Taking the inverse of equation (5.13) yields

$$(\mathbf{N}^T\tilde{\mathbf{M}}\mathbf{N})^{-1} = \mathbf{N}^{-1}\tilde{\mathbf{M}}^{-1}\mathbf{N}^{-T} = \mathbf{I}. \tag{5.15}$$

A pre- and post-multiplication by $\mathbf{N}$ and $\mathbf{N}^T$, respectively, gives

$$\tilde{\mathbf{M}}^{-1} = \mathbf{N}\mathbf{N}^T, \tag{5.16}$$

so

$$\tilde{\mathbf{M}} = (\mathbf{N}\mathbf{N}^T)^{-1}. \tag{5.17}$$

A pre- and post-multiplication of equation (5.14) by $\mathbf{N}$ and $\mathbf{N}^T$, respectively, gives

$$\mathbf{N}\mathbf{N}^T\tilde{\mathbf{K}}\mathbf{N}\mathbf{N}^T = \mathbf{N}\boldsymbol{\Omega}^2\mathbf{N}^T. \tag{5.18}$$

Substitution of relation (5.16) into this equation and pre- and post-multiplication by matrix $\tilde{\mathbf{M}}$ yields

$$\tilde{\mathbf{K}} = \tilde{\mathbf{M}}\mathbf{N}\boldsymbol{\Omega}^2\mathbf{N}^T\tilde{\mathbf{M}}. \tag{5.19}$$

Equations (5.17) and (5.19) give the explicit relations for the mass matrix $\tilde{\mathbf{M}}$ and the stiffness matrix $\tilde{\mathbf{K}}$ as a function of a given set of eigenvalues and eigenvectors, provided that the eigenvectors are normalised with respect to the mass matrix. Next, these equations will be used to derive a relationship between eigenvalues and the MFRF of a system.

5.4 Multivariable frequency response function of undamped system

Suppose that system (5.2) is excited by means of a set of sinusoidal forces with the same frequency ω but with various amplitudes and phases as specified by the vector $\boldsymbol{f}^{(0)} \in \mathcal{C}^{N^{(q)}}$. We have

$$\tilde{\mathbf{M}}\ddot{\boldsymbol{q}} + \tilde{\mathbf{K}}\boldsymbol{q} = \boldsymbol{f}^{(0)}e^{-j\omega t} \tag{5.20}$$

and assume that a solution exist in the form

$$\boldsymbol{q} = \boldsymbol{z}e^{-j\omega t}, \tag{5.21}$$

in which $\boldsymbol{f}^{(0)}$ and $\boldsymbol{z}$ are vectors of time-independent complex amplitudes. Substitution of equation (5.21) into equation (5.20) yields the algebraic system governing the amplitude of the response

$$(\tilde{\mathbf{K}} - \omega^2\tilde{\mathbf{M}})\boldsymbol{z} = \boldsymbol{f}^{(0)}. \tag{5.22}$$

The formal solution is

$$\boldsymbol{z} = (\tilde{\mathbf{K}} - \omega^2\tilde{\mathbf{M}})^{-1}\boldsymbol{f}^{(0)} \equiv \mathbf{H}(j\omega)\boldsymbol{f}^{(0)}, \tag{5.23}$$

in which $\mathbf{H}(j\omega)$ is the *Multivariable Frequency Response Function* (MFRF). Element $H_{j,k}(j\omega)$ of this matrix is the displacement response of the j^{th} degree of freedom when the excitation is applied at the k^{th} degree of freedom only.

Calculation of the response by means of equation (5.23) is highly inefficient because we need to invert a matrix for each frequency value. However, using the result of section 5.3, after pre- and post-multiplication of matrix $\mathbf{H}^{-1} = (\tilde{\mathbf{K}} - \omega^2\tilde{\mathbf{M}})$ by $\mathbf{N}^T$ and $\mathbf{N}$, we obtain

$$\mathbf{N}^T\mathbf{H}^{-1}\mathbf{N} = \mathbf{\Omega}^2 - \omega^2\mathbf{I}. \tag{5.24}$$

Furthermore $(\mathbf{N}^T\mathbf{H}^{-1}\mathbf{N})^{-1} = \mathbf{N}^{-1}\mathbf{H}\mathbf{N}^{-T}$ which, after pre- and post-multiplication of both sides by $\mathbf{N}$ and $\mathbf{N}^T$, respectively, leads to

$$\mathbf{H}(j\omega) = \mathbf{N}(\mathbf{\Omega}^2 - \omega^2\mathbf{I})^{-1}\mathbf{N}^T. \tag{5.25}$$

So the $(j,k)^{\text{th}}$ element of the MFRF matrix $\mathbf{H}$ can be explicitly written as

$$H_{j,k}(j\omega) = \sum_{r=1}^{N^{(q)}} \frac{\nu_j^{[r]}\nu_k^{[r]}}{\left({\omega^{[r]}}^2 - \omega^2\right)}. \tag{5.26}$$

Carrying out the summation in equation (5.26) and bringing all contributions under the same denominator yields (Gladwell (1999))

$$H_{j,k}(j\omega) = \alpha_{j,k}\frac{\prod_{r=1}^{N^{(q)}-1}({\mu^{[r]}}_{j,k}^2 - \omega^2)}{\prod_{r=1}^{N^{(q)}}({\omega^{[r]}}^2 - \omega^2)}, \tag{5.27}$$

in which ${\mu^{[r]}}_{j,k}$ are the anti-resonance frequencies of the MFRF $\mathbf{H}(j\omega)$ and $\alpha_{j,k}$ is an unknown scalar. Multiplying equation (5.26) and (5.27) by ω^2 and let ω go to infinity, yields

$$\lim_{\omega\to\infty} \omega^2 H_{j,k}(j\omega) = \sum_{r=1}^{N^{(q)}} \nu_j^{[r]}\nu_k^{[r]} = \alpha_{j,k}. \tag{5.28}$$

By using the result of equation (5.16), namely $\mathbf{N}\mathbf{N}^T = \tilde{\mathbf{M}}^{-1}$, we have $\sum_{r=1}^{N^{(q)}} \nu_j^{[r]}\nu_k^{[r]} = (\tilde{\mathbf{M}}^{-1})_{j,k} = \alpha_{j,k}$ and

$$H_{j,k}(j\omega) = (\tilde{\mathbf{M}}^{-1})_{j,k}\frac{\prod_{r=1}^{N^{(q)}-1}({\mu^{[r]}}_{j,k}^2 - \omega^2)}{\prod_{r=1}^{N^{(q)}}({\omega^{[r]}}^2 - \omega^2)}, \tag{5.29}$$

in which $(\tilde{\mathbf{M}}^{-1})_{j,k}$ means the $(j,k)^{\text{th}}$ element of the inverted mass matrix. As a result, the high frequency amplitude of $H_{j,k}(j\omega)$, see equation (5.28), is defined by

$$H_{j,k}^{(high)}(j\omega) = \frac{1}{\omega^2}(\tilde{\mathbf{M}}^{-1})_{j,k}, \tag{5.30}$$

for $\omega \gg \omega^{[N^{(q)}]}$. Equation (5.30) shows that for high frequencies the MFRF $\mathbf{H}(j\omega)$ is only a function of the mass matrix $\tilde{\mathbf{M}}$ and frequency ω.

The right hand side of equation (5.26) should be equal to the right hand side of equation (5.29). Multiplying both equations by $({\omega^{[m]}}^2 - \omega^2)$ and putting $\omega = \omega^{[m]}$ one finds

$$\nu_j^{[m]} \nu_k^{[m]} = (\tilde{\mathbf{M}}^{-1})_{j,k} \frac{\prod_{r=1}^{N^{(q)}-1} ({\mu^{[r]}}_{j,k}^2 - {\omega^{[m]}}^2)}{\prod_{r=1;r\neq m}^{N^{(q)}} ({\omega^{[r]}}^2 - {\omega^{[m]}}^2)}. \tag{5.31}$$

This relation shows that the (anti-)resonance frequencies and the eigenvectors corresponding to specific coordinates contain the same information.

In section 5.8 equations (5.28) and (5.31) will be used to estimate the drive parameters for the robot model. In the next section a special kind of eigenvectors will be presented, namely the rigid-body modes. The rigid-body modes describe the behaviour of MFRF $\mathbf{H}(j\omega)$ for low frequencies and will be used to identify the rigid mass matrix.

5.5 Rigid-body modes

According to Gatti and Ferrari (1999), the eigenvectors corresponding to the rigid-body modes satisfy the fundamental relation

$$\tilde{\mathbf{K}} \nu = \mathbf{0}. \tag{5.32}$$

A comparison of this equation with equation (5.5) shows that the rigid-body modes can be interpreted as eigenmodes of zero eigenfrequencies. The rigid-body modes are $\tilde{\mathbf{M}}$- and $\tilde{\mathbf{K}}$- orthogonal to the other (elastic) eigenmodes and the rigid-body modes are mutually $\tilde{\mathbf{M}}$-orthogonal.

Next, the low frequency behaviour of the MFRF $\mathbf{H}(j\omega)$ will be analysed for a system containing $N^{(r)}$ rigid-body modes. The corresponding MFRF $H_{j,k}^{(low)}(j\omega)$ is defined by letting ω go to zero in equation (5.26), yielding

$$H_{j,k}^{(low)}(j\omega) = \begin{cases} \frac{1}{\omega^2} \sum_{r=1}^{N^{(r)}} \nu_j^{[r]} \nu_k^{[r]} & \text{if} \quad \sum_{r=1}^{N^{(r)}} \nu_j^{[r]} \nu_k^{[r]} \neq 0 \\ 0 & \text{if} \quad \sum_{r=1}^{N^{(r)}} \nu_j^{[r]} \nu_k^{[r]} = 0 \end{cases}, \tag{5.33}$$

in which it is assumed that the first $N^{(r)}$ eigenvalues and vectors correspond to the rigid-body modes, so $\omega^{[r]} = 0$ for $r = 1, \cdots, N^{(r)}$. Equation (5.33) shows that the low frequency behaviour of $\mathbf{H}(j\omega)$ is fully defined by the rigid-body modes and the frequency ω.

5.6 Transfer function of damped system

In reality, a system will always contain a certain amount of damping. For damped systems, the eigenvalue decomposition is not as straightforward as in the undamped case, see Gatti and Ferrari (1999). Therefore, a so-called transfer function matrix will be introduced, from which the MFRF of the damped system can be easily extracted.

Let us consider again the linearised equation of motion presented in equation (5.1). Taking the Laplace transform of this equation, assuming that the initial conditions are zero ($\boldsymbol{q} = \mathbf{0}$ and $\dot{\boldsymbol{q}} = \mathbf{0}$), yields

$$\mathbf{G}(s)\boldsymbol{q}(s) = \boldsymbol{f}(s), \tag{5.34}$$

in which $\mathbf{G}(s) = (\tilde{\mathbf{M}}s^2 + \tilde{\mathbf{D}}s + \tilde{\mathbf{K}})$. A matrix inversion yields

$$\boldsymbol{q}(s) = \mathbf{H}(s)\boldsymbol{f}(s), \tag{5.35}$$

with $\mathbf{H}(s)$ the transfer function matrix, which can be expressed as

$$\mathbf{H}(s) = (\mathbf{G}(s))^{-1} = \frac{\mathbf{G}^{(adj)}(s)}{|\mathbf{G}(s)|}. \tag{5.36}$$

The numerator $\mathbf{G}^{(adj)}(s)$ is the $(N^{(q)} \times N^{(q)})$ adjoint matrix of $\mathbf{G}(s)$ containing polynomials in s of order $2(N^{(q)} - 1)$. The denominator is a polynomial in s of order $2N^{(q)}$. Therefore, equation (5.36) can also be written as

$$\mathbf{H}(s) = \frac{\mathbf{B}(s)}{A(s)} = \frac{\begin{bmatrix} B_{1,1}(s) & \cdots B_{1,N^{(q)}} \\ \vdots & \ddots & \vdots \\ B_{N^{(q)},1}(s) & \cdots B_{N^{(q)},N^{(q)}} \end{bmatrix}}{A(s)}, \tag{5.37}$$

which is called the common denominator transfer function model. Within this parametrisation the elements of matrix $\mathbf{H}(s)$ are described by

$$H(s)_{j,k} = \frac{B_{j,k}(s)}{A(s)} = \frac{\sum_{r=0}^{2(N^{(q)}-1)} b_{j,k,r}s^r}{\sum_{r=0}^{2N^{(q)}} a_r s^r}, \tag{5.38}$$

in which $b_{j,k,r}$ and a_r are the coefficients of the numerator and denominator polynomials.

An alternative parametrisation of equation (5.36) is

$$H(s)_{j,k} = K_{j,k}^{(H)} \frac{\prod_{r=1}^{2(N^{(q)}-1)} (s + z_{j,k,r})}{\prod_{r=1}^{2N^{(q)}} (s + p_r)}. \tag{5.39}$$

The coefficients p_r and $z_{j,k,r}$ are the complex poles and zeros of multivariable transfer function $\mathbf{H}(s)$, respectively. $K_{j,k}^{(H)}$ is a scalar, which will be defined later on.

A second alternative parametrisation of equation (5.36), with the advantage that all the coefficients are real valued, is

$$H(s)_{j,k} = K_{j,k}^{(H)} \frac{\prod_{r=1}^{(N^{(q)}-1)} (s^2 + 2\zeta_{j,k}^{[r](\mu)} \mu_{j,k}^{[r]} s + \mu_{j,k}^{[r]^2})}{\prod_{r=1}^{N^{(q)}} (s^2 + 2\zeta^{[r](\omega)} \omega^{[r]} s + \omega^{[r]^2})}, \tag{5.40}$$

provided that the poles and zeros show up in complex conjugated pairs. A comparison of the last two parameterisations yields

$$|p_{2r}| = |p_{2r+1}| = \omega^{[r]} \quad \text{and} \quad |z_{j,k,2r}| = |z_{j,k,2r+1}| = \mu_{j,k}^{[r]}. \tag{5.41}$$

The MFRF $\mathbf{H}(j\omega)$ of a transfer function $\mathbf{H}(s)$ is found by substitution of $s = j\omega$ into $\mathbf{H}(s)$. Note the similarity of equation (5.40), for $\zeta_{j,k}^{[r](\mu)} = \zeta^{[r](\omega)} = 0$, with MFRF of the undamped system presented in equation (5.29). A comparison of both equations for $s = j\omega$ goes to infinity yields

$$\mathbf{K}^{(H)} = \tilde{\mathbf{M}}^{-1}. \tag{5.42}$$

Thus far the theory is described for the general mechanical system as described by equation (5.1). In the next section, this theory will be applied to the robot model from chapter 3.

5.7 Transfer function matrix of robot system

Let us consider the linearised equations of motion of the robot manipulator, equation (3.90), in terms of the degrees of freedom

$$\boldsymbol{q} = \begin{bmatrix} \boldsymbol{e}^{(m)} \\ \boldsymbol{\epsilon}^{(m)} \end{bmatrix}. \tag{5.43}$$

Then we can write for equation (5.1)

$$\begin{bmatrix} \tilde{\mathbf{M}}_{ee} & \tilde{\mathbf{M}}_{e\epsilon} \\ \tilde{\mathbf{M}}_{\epsilon e} & \tilde{\mathbf{M}}_{\epsilon\epsilon} \end{bmatrix} \ddot{\boldsymbol{q}} + \begin{bmatrix} \tilde{\mathbf{D}}_{ee} & \tilde{\mathbf{D}}_{e\epsilon} \\ \tilde{\mathbf{D}}_{\epsilon e} & \tilde{\mathbf{D}}_{\epsilon\epsilon} \end{bmatrix} \dot{\boldsymbol{q}} + \begin{bmatrix} \tilde{\mathbf{K}}_{ee} & \tilde{\mathbf{K}}_{e\epsilon} \\ \tilde{\mathbf{K}}_{\epsilon e} & \tilde{\mathbf{K}}_{\epsilon\epsilon} \end{bmatrix} \boldsymbol{q} = \mathbf{B}^{(u)} \boldsymbol{\tau}^{(a)}, \tag{5.44}$$

in which

$$\begin{aligned} \tilde{\mathbf{M}} &= \bar{\mathbf{M}}_0, \\ \tilde{\mathbf{D}} &= \mathbf{D}_0 + \mathbf{C}_0 + \mathbf{F}_0, \\ \tilde{\mathbf{K}} &= \mathbf{K}_0 + \mathbf{G}_0 + \mathbf{N}_0 \end{aligned} \tag{5.45}$$

and $\mathbf{B}^{(u)}$ is defined as in equation (3.72). To facilitate notation the perturbation symbol δ of equation (3.90) has been omitted in equation (5.44).

Let $\boldsymbol{e}^{(m)}(s)$ and $\boldsymbol{\tau}^{(a)}(s)$ represent the Laplace transforms of the drive angle $\boldsymbol{e}^{(m)}(t_n)$ and the driving torques $\boldsymbol{\tau}^{(a)}(t_n)$. The relationship between $\boldsymbol{e}^{(m)}(s)$ and $\boldsymbol{\tau}^{(a)}(s)$ is given by

$$\boldsymbol{e}^{(m)}(s) = \mathbf{P}(s)\boldsymbol{\tau}^{(a)}(s), \tag{5.46}$$

in which

$$\mathbf{P}(s) = \mathbf{B}^{(u)^T}\mathbf{H}(s)\mathbf{B}^{(u)} \tag{5.47}$$

and $\mathbf{H}(s)$ is defined as in equation (5.36).

The computation of $\mathbf{H}(s)$ from $\mathbf{P}(s)$ is impossible, because matrix $\mathbf{B}^{(u)}$ is not a square matrix. As a result, the mass, damping and stiffness matrices of the robot model cannot be reconstructed from only measuring the drive angle and the driving torque. However, the next section presents a method to reconstruct parts of the mass and stiffness matrices using the presented inverse eigenvalue theory.

5.8 Parameter identification method for the robot model

An overview of the proposed identification method with regard to identifying the drive inertia $J^{[k](a)}$, the drive stiffness $k_1^{[k+1]}$ of joint j for $k = 2j - 1$ and the rigid mass matrix $\tilde{\mathbf{M}}_{ee}$ is summarised below.

1. Estimate transfer function $\mathbf{P}(s)$ from experimental data.
2. Compute the undamped MFRF $\mathbf{P}(j\omega)$, including the resonance $\omega^{[r]}$ and the anti-resonance frequencies $\mu_{j,k}^{[r]}$ from $\mathbf{P}(s)$.
3. Compute the drive inertias $J^{[k](a)}$ from the high frequency amplitude of MFRF $\mathbf{P}(j\omega)$.
4. Compute the rigid mass matrix $\tilde{\mathbf{M}}_{ee}$ from the low frequency amplitude of MFRF $\mathbf{P}(j\omega)$.
5. Compute the coordinates corresponding to the drive angles $\boldsymbol{e}^{(m)}$ of all eigenvectors $\boldsymbol{\nu}^{[r]}$ from the undamped resonance and anti-resonance frequencies and drive inertias $J^{[k](a)}$.
6. Compute the drive stiffness $k_1^{[k+1]}$ from the estimated eigenvectors $\boldsymbol{\nu}^{[r]}$ and drive inertias $J^{[k](a)}$.

A more detailed description of these steps is given below.

Step 1

In the first step, identification experiments should be performed to identify the transfer function matrix $\mathbf{P}(s)$, describing the drive angles $\boldsymbol{e}^{(m)}(s)$ as a function of the driving torques $\boldsymbol{\tau}^{(a)}(s)$. A detailed description of this identification process is presented in chapter 6.

Step 2

The next step involves the computation of the MFRF $\mathbf{P}(j\omega)$ for the corresponding undamped system from the transfer function $\mathbf{P}(s)$. It is assumed that all poles and zeros are complex conjugated pairs, except for the rigid-body modes. According to equation (5.41), the absolute values of the complex poles and zeros are equal to the resonance and anti-resonance frequencies $\omega^{[r]}$ and $\mu^{[r]}$, respectively, of the undamped system. Due to the relatively large joint friction and a small stiffness arising from the gravity compensating spring and the geometric and dynamic stiffness contributions, a rigid-body mode appears as two first order poles and zeros. To compute the MFRF for the undamped system, the first order poles and zeros are replaced by poles and zeros in the origin of the complex plane, which implies for the identified model

$$\begin{aligned}
&\tilde{\mathbf{K}}_{ee} = \tilde{\mathbf{D}}_{ee} = \mathbf{0},\\
&\tilde{\mathbf{K}}_{e\epsilon} = \tilde{\mathbf{D}}_{e\epsilon} = \mathbf{0},\\
&\tilde{\mathbf{K}}_{\epsilon e} = \tilde{\mathbf{D}}_{\epsilon e} = \mathbf{0}.
\end{aligned} \tag{5.48}$$

Note that the number of rigid-body modes $N^{(r)}$ is then equal to the number of drive angles $N^{(em)}$.

Step 3

Next, the high frequency amplitude of the MFRF is used to compute the drive inertias $J^{[k](a)}$. Equation (5.30) describes a relationship between the high frequency amplitude of $\mathbf{P}(j\omega)$ and the inverse mass matrix $\tilde{\mathbf{M}}^{-1}$. As a result of relationship (3.77), the rows and columns of the inverted mass matrix corresponding to the drive angles $\boldsymbol{e}^{(m)}$ have only entries on the main diagonal, namely $\frac{1}{J^{[k](a)}}$. This can be easily seen from the mass matrix presented in equation (3.79). So the drive inertias $\frac{1}{J^{[k](a)}}$ can be estimated using

$$P_{j,j}^{(high)}(j\omega) = \frac{1}{\omega^2 J^{[k](a)}}. \tag{5.49}$$

for $j = 1, \cdots, N^{(em)}$ and $k = 2j - 1$.

Step 4

Next, the low frequency amplitude of the identified MFRF is used to identify $\tilde{\mathbf{M}}_{ee}$. The rigid-body modes correspond to a motion in which all elastic degrees of freedom $\boldsymbol{\epsilon}^{(m)}$ are equal to zero, so $\nu_j^{[r]} = 0$ for $j > N^{(r)}$ and $r \leq N^{(r)}$. For the rigidified system ($\boldsymbol{\epsilon}^{(m)} = \mathbf{0}$) we can write

$$\tilde{\mathbf{M}}_{ee}\ddot{\boldsymbol{e}}^{(m)} = \boldsymbol{\tau}^{(a)}. \tag{5.50}$$

Therefore, the MFRF of this rigidified system is given by

$$H_{j,k}^{(rigid)}(j\omega) = \frac{1}{\omega^2}(\tilde{\mathbf{M}}_{ee}^{-1})_{j,k}. \tag{5.51}$$

A comparison of equation (5.33) with equation (5.51) yields

$$\sum_{r=1}^{N^{(r)}} \nu^{[r]}\nu^{[r]T} = \begin{bmatrix} \tilde{\mathbf{M}}_{ee}^{-1} & \mathbf{0} \\ \mathbf{0} & \mathbf{0} \end{bmatrix}, \tag{5.52}$$

from which we conclude that the low frequency amplitude of an identified MFRF gives an estimate of $\tilde{\mathbf{M}}_{ee}$. Furthermore, equation (5.52) shows a more fundamental relationship between the rigid-body modes and the rigid mass matrix.

Note that an alternative method to identify $\tilde{\mathbf{M}}_{ee}$ is the linear least squares robot identification technique described in section 2.2.1. By means of this technique, the rigid behaviour and the corresponding physical parameters can be identified very accurately. From this set of parameters, the rigid mass matrix $\tilde{\mathbf{M}}_{ee}$ can easily be computed.

Step 5

The next step involves the computation of the coordinates of the eigenvectors, which correspond to the measured drive angles $\boldsymbol{e}^{(m)}$. Equation (5.31) shows that these coordinates can be computed from the resonance and anti-resonance frequencies that were estimated in step two, and the corresponding entries of the inverted mass matrix. In step three it is shown that these entries equal the by equation (5.49) estimated inverted motor inertias.

Step 6

Finally, we exploit the diagonal structure of the first $N^{(em)}$ rows and columns of $\tilde{\mathbf{M}}$, to estimate the drive stiffness $k_1^{(k+1)}$. Writing the matrix multiplication of equation (5.19) for such a special mass matrix, yields

$$\tilde{K}_{j,j} = J^{[k](a)} \sum_{r=1}^{N^{(q)}} \nu_j^{[r]} \omega^{[r]^2} \nu_j^{[r]} J^{[k](a)}, \tag{5.53}$$

in which $k = 2j - 1$. It appears that the gravitational part of $\mathbf{G}_0$ and $\mathbf{N}_0$ is cancelled by the stiffness of the gravity compensating spring $\mathrm{D}\mathcal{F}^{(ec)T}k^{(c)}\mathrm{D}\mathcal{F}^{(ec)}$. If the nominal velocities and accelerations remain small, we have $\mathbf{K} \gg \mathbf{G}_0 + \mathbf{N}_0 + \mathrm{D}\mathcal{F}^{(ec)T}k^{(c)}\mathrm{D}\mathcal{F}^{(ec)}$, see equation (3.91). As a result we find that the drive stiffness $\tilde{K}_{j,j} \approx k_1^{(k+1)}$.

Thus, solely from drive angles and driving torque measurements we are able to estimate the drive inertias $J^{[k](a)}$, the rigid mass matrix $\tilde{\mathbf{M}}_{ee}$ and the drive stiffness $k_1^{[k+1]}$. Note that the theory presented in this chapter is based on the dynamic equations of motion of a robot manipulator, including joint flexibilities. Therefore, although only the drive flexibilities can be identified, this method is also applicable for robots including joint flexibilities. To illustrate the method a numerical example will be presented in the next section.

5.9 Numerical example

The robot model presented in section 4.2.2 is used for this simulation example. In this example, only the first 3 joints are considered. The mass, inertia and friction parameters are estimated from dedicated rigid robot identification experiments, see Waiboer (2007). For the stiffness parameters the estimates of table 4.1, page 48, are used. In comparison with section 4.2.2 the damping is increased, such that the relative damping of the poles is around 25%. The model is linearised while moving with a small velocity around a stretched horizontal configuration, see figure 5.2. The linearised mass, damping and stiffness matrices are used to compute the MFRF $\mathbf{H}(j\omega)$. The poles and zeros corresponding to the drive angles of the first three joints are presented in table 5.1. Next, the resonance and anti-resonance frequencies corresponding to the undamped system are computed from these poles and zeros. These are also presented in table 5.1.

In principle, a full set of resonance and anti-resonance frequencies and the frequency responses for low or high frequencies should be identified to reconstruct the drive system parameters. However, in practice only frequencies up to a certain frequency can be identified, because of the limited sample rate of

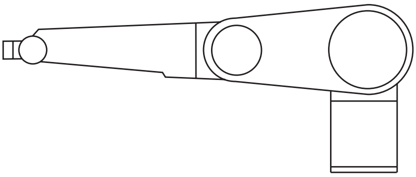

Figure 5.2: Nominal robot configuration during excitation

r	$p_{(2r-1)}$	$\omega^{[r]}$	$z_{1,1,(2r-1)}$	$\mu_{1,1}^{[r]}$	$z_{2,2,(2r-1)}$	$\mu_{2,2}^{[r]}$	$z_{3,3,(2r-1)}$	$\mu_{3,3}^{[r]}$
1	-2.1 - 0.0j	0.0	-2.1 - 0.0j	0.0	-1.3 - 0.0j	0.0	-0.7 - 0.0j	0.0
	-0.7 - 0.0j	0.0	-0.3 - 0.0j	0.0	-0.7 - 0.0j	0.0	-0.4 - 0.0j	0.0
2	-0.3 - 0.0j	0.0	-0.2 - 0.0j	0.0	-0.0 - 0.0j	0.0	-0.2 - 0.0j	0.0
	-0.2 - 0.0j	0.0	-0.0 - 0.0j	0.0	-0.0 - 0.0j	0.0	-0.0 - 0.0j	0.0
3	-0.0 - 0.0j	0.0	-0.2+ 14.8j	14.8	-0.5+ 20.3j	20.3	-1.5+ 31.3j	31.3
	-0.0 - 0.0j	0.0	-0.2 - 14.8j	14.8	-0.5 - 20.3j	20.3	-1.5 - 31.3j	31.3
4	-1.5+ 31.3j	31.3	-1.0+ 38.7j	38.7	-1.9+ 32.2j	32.3	-1.8+ 40.4j	40.4
	-1.5 - 31.3j	31.3	-1.0 - 38.7j	38.7	-1.9 - 32.2j	32.3	-1.8 - 40.4j	40.4
5	-1.6+ 40.9j	41.0	-0.6+ 51.7j	51.7	-0.6+ 49.9j	49.9	-3.2+ 49.4j	49.5
	-1.6 - 40.9j	41.0	-0.6 - 51.7j	51.7	-0.6 - 49.9j	49.9	-3.2 - 49.4j	49.5
6	-0.8+ 52.2j	52.2	-6.8+ 70.2j	70.5	-2.5+ 59.1j	59.2	-0.8+ 52.2j	52.2
	-0.8 - 52.2j	52.2	-6.8 - 70.2j	70.5	-2.5 - 59.1j	59.2	-0.8 - 52.2j	52.2
7	-7.1+ 71.0j	71.3	-7.2+ 81.5j	81.8	-8.6+ 78.0j	78.4	-5.8+ 79.6j	79.8
	-7.1 - 71.0j	71.3	-7.2 - 81.5j	81.8	-8.6 - 78.0j	78.4	-5.8 - 79.6j	79.8
8	-7.2+ 82.3j	82.6	-4.9+ 99.0j	99.1	-3.0+ 95.2j	95.3	-4.8+ 99.0j	99.1
	-7.2 - 82.3j	82.6	-4.9 - 99.0j	99.1	-3.0 - 95.2j	95.3	-4.8 - 99.0j	99.1
9	-4.9+ 99.0j	99.1	-12.4+144.0j	144.5	-11.9+143.1j	143.6	-12.3+144.0j	144.6
	-4.9 - 99.0j	99.1	-12.4 -144.0j	144.5	-11.9 -143.1j	143.6	-12.3 -144.0j	144.6
10	-12.4+144.1j	144.7	-47.5+243.4j	247.9	-48.8+244.3j	249.1	-49.1+245.0j	249.8
	-12.4 -144.1j	144.7	-47.5 -243.4j	247.9	-48.8 -244.3j	249.1	-49.1 -245.0j	249.8
11	-49.1+245.0j	249.8	-108.9+365.7j	381.5	-108.8+365.6j	381.5	-108.9+365.7j	381.5
	-49.1 -245.0j	249.8	-108.9 -365.7j	381.5	-108.8 -365.6j	381.5	-108.9 -365.7j	381.5
12	-108.9+365.7j	381.5						
	-108.9 -365.7j	381.5						

Table 5.1: The poles and zeros and corresponding resonance and anti-resonance frequencies of the simulation model in Hz.

the controller. This influences the estimation of both the drive inertia $J^{[k](a)}$ and the drive stiffness $k_1^{([k+1])}$. Table 5.2 shows the estimated drive parameters for a reduced set of (anti)-resonance frequencies. The reduction is done by neglecting the highest frequencies. This influences the frequency response for high frequencies and therefore the estimation of the drive inertia $J^{[k](a)}$ as well. The frequency response of the reduced model for low frequencies is kept constant. Table 5.2 shows that, for a reduced set of eigenvalues, the drive stiffness and drive inertia are underestimated. Therefore, the success of this estimation method depends on the number of eigenvalues that can be extracted from experimental data. This number should be in accordance with the number of degrees of freedom of the assumed model structure. The performance under experimental conditions will be addressed in the next chapter.

5.10 Discussion

In this work the normalisation of the eigenvectors with respect to the mass matrix is fully exploited. For such a set of eigenvectors, equation (5.16) presents a relationship for the mass matrix as a function of the eigenvectors. This relationship enables a physical interpretation of an up to now implicitly defined scaling factor $\alpha_{j,k}$ in the MFRF for a mechanical system, see equation (5.28). If the eigenvectors are normalised with respect to the mass matrix, this scal-

	Drive inertia (kg m^2)			Drive stiffness $\times 10^5$ (N m rad^{-1})		
N	$J^{[1](a)}$	$J^{[3](a)}$	$J^{[5](a)}$	$k_1^{[2]}$	$k_1^{[4]}$	$k_1^{[6]}$
true	3.10	1.31	0.79	2.80	2.70	1.00
10	3.10	1.31	0.79	2.80	2.70	1.00
9	3.10	1.31	0.79	2.80	2.68	1.00
8	3.05	1.31	0.79	1.53	2.47	1.00
7	3.04	1.29	0.79	1.46	2.23	0.98
6	3.04	1.18	0.79	1.46	1.53	0.97
5	2.99	1.07	0.73	1.27	1.03	0.71
4	2.92	0.74	0.39	1.08	0.23	0.02
3	2.86	0.67	0.35	0.98	0.16	0.00
2	2.55	0.42	0.34	0.63	0.03	0.00
1	0.57	0.18	0.34	0.00	0.00	0.00

Table 5.2: True and estimated drive parameters for a varying number of N (anti-)resonance frequencies. The system has 12 degrees of freedom, including 3 rigid-body modes. Two of them are redundant, so the maximum for $N = 10$.

ing factor $\alpha_{j,k}$ is proven to be the $(j,k)^{\text{th}}$ element of the inverted mass matrix. Based on this result, it is shown in equation (5.30) that the frequency response for high frequencies is solely a function of the mass matrix and the frequency. Furthermore, a relationship is derived between the rigid mass matrix and the rigid-body modes, see equation (5.52).

It is impossible to identify the full mass and stiffness matrix on the basis of driving torque and drive angle measurements only, but it is shown that the rigid mass matrix $\tilde{\mathbf{M}}_{ee}$, the drive stiffness $k_1^{[k+1]}$ and drive inertia $J^{[k](a)}$ can be identified uniquely. The sparse structure in the mass and stiffness matrix for entries that correspond to the drive system enables the identification of these parameters, without the need for additional sensors. This sparse structure is similar to the series of lumped masses model, presented in figure 5.1. Therefore, the Lanczos algorithm (see section 5.2) is proposed to identify the drive parameters for robots containing more than one drive flexibility per joint.

The success of the identification method depends on the number of (anti-)resonance frequencies that can be identified from experimental data. The identification of transfer functions, from which the resonance frequencies can be extracted, will be the topic of the next chapter. Conclusions about the actual number of (anti-)resonance frequencies that can be identified from experimental data will be postponed to the end of the next chapter.

Chapter 6

Identification of transfer functions

This chapter presents the identification of transfer functions from experimental data using frequency domain system identification techniques. The transfer functions describe the resonance and anti-resonance frequencies for the robot joints, which are used to identify the dynamic parameters of the drives as presented in the previous chapter.

An overview of available system identification methods can be found in textbooks e.g. Pintelon and Schoukens (2001); Ljung (1999). In this work, the frequency domain approach presented by Pintelon and Schoukens (2001) will be used. The frequency domain approach is more suitable for the identification of continuous transfer function models as presented in equation (5.46) than the time domain methods. Time domain methods are more common for the estimation of discrete models. An additional step is then required to convert the discrete poles and zeros to their continuous counterparts. Furthermore, for safety and stability reasons the robot model should be estimated from closed-loop experiments, leading to correlated input and output noise. The so-called frequency domain errors in variables model (EV), presented by Pintelon and Schoukens (2001), includes these type of noise sources and is therefore a very natural way to describe the identification of an open-loop model from noisy closed-loop measurement data. Finally, as shown by Schoukens et al. (2005), the frequency domain framework is also very suitable for describing the effects of nonlinear plant and controller dynamics on the estimated linear model. For these reasons the use of the frequency domain identification approach was decided.

The frequency domain system identification method is available as a MATLAB toolbox, namely the Frequency Domain System Identification Toolbox (FDIDENT), see Kollár (2001). Unfortunately, FDIDENT is restricted to SISO models. A pre-release for MIMO identification is provided by the authors.

However, this release does not contain all the functionality required for this work, such as the possibility to start the nonlinear optimisation with a user defined initial model, the use of the pole/zero parametrisation of transfer functions as presented in equation (5.39) and the estimation of symmetric transfer functions. Therefore, a new MIMO toolbox has been implemented which features this functionality, including model validation routines.

Furthermore, an extension of the errors in variables identification frame work will be given. Schoukens et al. (2005) describe the effects of nonlinear distortions for an output error identification framework only, thus without correlated input and output noise. The closed-loop robot system contains both nonlinear distortions and correlated input and output noise. Therefore, the nonlinear distortions are included in the errors in variables identification framework. Based on this formulation a new data averaging technique is proposed.

To outline the scope of this chapter, a short overview of the general system identification approach is presented below. System identification procedures consist of five basic steps.

1. Model structure selection

2. Experiment design

3. Collecting experimental data

4. Model estimation

5. Model validation

The first step is the selection of the desired model structure. The user must decide which dynamic behaviour the model should predict and to what extent. The selected model structure should correspond to this dynamic behaviour. As mentioned in the previous chapter, the linearised robot dynamics will be described by a transfer function matrix, see equation (5.46). The second step is the experiment design. A well-designed experiment is the best guarantee for building good models. It will be shown that the MIMO model structure and the closed-loop configuration restrict the allowable excitation signals. Therefore, a carefully designed experiment is required to obtain sufficiently high signal to noise ratios for the measurement signals. In the third step, experimental data is collected. The robot will be excited under the designed conditions and the robot response is measured. In step four, the parameters of the selected model structure are estimated. The model should be matched as closely as possible with the measured response of the system. This is mostly done by minimising a criterion that measures the accuracy of the fit. Finally, in step five the validity of the selected model should be tested: does the model describe the available data properly or are there still indicators that part of the robot dynamics is not well modelled?

Outline

In section 6.1 the errors in variables stochastic framework will be presented, which will be used to validate and quantify the estimated linear models. In section 6.2 the framework will be extended with a description of nonlinear distortions, arising from the nonlinear dynamics of the robot manipulator. In section 6.3 the estimation of the noise properties and the nonparametric multivariable frequency response function (MFRF) will be described. In section 6.4 the estimation and validation of a parametric MFRF will be presented. In section 6.5 the proposed experimental design will be discussed. In sections 6.6 and 6.7 , respectively, the results of simulation studies and experimental studies on the Stäubli RX90B will be presented. Finally, in section 6.8 some concluding remarks on the material presented in this chapter will be given.

6.1 Stochastic identification framework for linear systems

In the previous chapter, the linearised dynamic robot model was described by a transfer function matrix $\mathbf{P}^{(0)}(s)$ with $N^{(u)}$ inputs and $N^{(y)}$ outputs, see equation (5.46). Throughout this chapter the superscript 0 between round brackets is added to denote the true linearised model. The goal of this chapter is to estimate this function from experimental data. In this section, the stochastic identification framework as presented by Pintelon and Schoukens (2001) for SISO systems and Verboven et al. (2006) for MIMO systems will be applied to the Stäubli RX90B closed-loop robot system.

Figure 6.1 presents a schematic linearised model of the manipulator, operating in closed-loop with a linear feedback controller $\mathbf{C}(s)$. The signals $\boldsymbol{r}^{[m]}(t_n) \in \mathcal{R}^{N^{(u)}}$ and $\boldsymbol{\tau}^{[m](ff)}(t_n) \in \mathcal{R}^{N^{(u)}}$ represent deterministic periodic reference signals describing the joint position and the torque feed-forward, respectively. The superscript m between square brackets is introduced to denote the m^{th} measurement period, for $m = 1, \cdots, N^{(m)}$. Each period contains $N^{(t)}$ measurements, observed at time steps $t = t_n$, in which $t_n = nT^{(s)}$, $n = 0, 1, \cdots, N^{(t)} - 1$ and $T^{(s)}$ the sample time. The noise sources $\boldsymbol{v}^{[m](c)}(t_n)$ and $\boldsymbol{v}^{[m](p)}(t_n)$ represent the controller noise and process noise, respectively. The measurement noise is denoted by $\boldsymbol{m}^{[m](u)}(t_n)$ and $\boldsymbol{m}^{[m](y)}(t_n)$. Any deviation from the periodic behaviour is considered noise. The following time signals are observed during $N^{(m)}$ measured periods

$$\begin{aligned} \boldsymbol{u}^{[m]}(t_n) &= \boldsymbol{u}^{(0)}(t_n) + \boldsymbol{u}^{[m](v)}(t_n), \\ \boldsymbol{y}^{[m]}(t_n) &= \boldsymbol{y}^{(0)}(t_n) + \boldsymbol{y}^{[m](v)}(t_n). \end{aligned} \tag{6.1}$$

The vectors $\boldsymbol{u}^{[m]}(t_n) \in \mathcal{R}^{N^{(u)}}$ and $\boldsymbol{y}^{[m]}(t_n) \in \mathcal{R}^{N^{(y)}}$ stand for, respectively, the

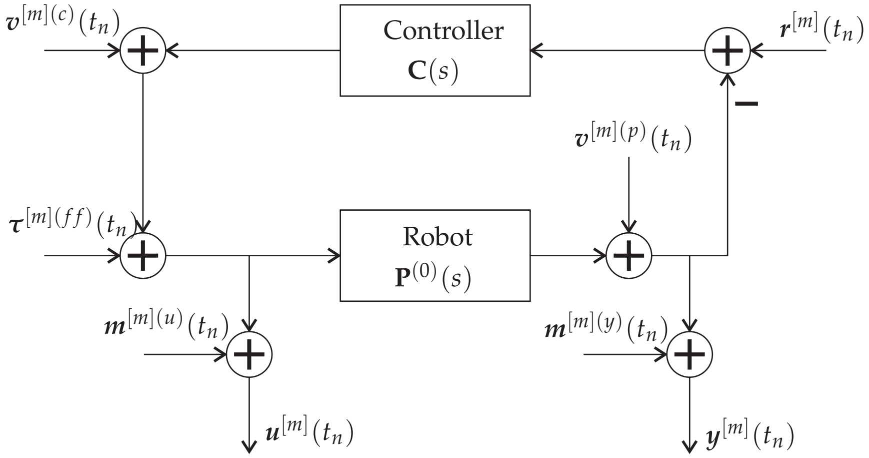

Figure 6.1: Closed-loop model of the linearised robot manipulator with $\boldsymbol{r}^{[m]}(t_n)$ *and* $\boldsymbol{\tau}^{[m](ff)}(t_n)$ *the reference signals,* $\boldsymbol{m}^{[m](u)}(t_n)$*,* $\boldsymbol{m}^{[m](y)}(t_n)$ *the measurement noise sources,* $\boldsymbol{v}^{[m](p)}(t_n)$ *the process noise,* $\boldsymbol{v}^{[m](c)}(t_n)$ *the controller noise and* $\boldsymbol{u}^{[m]}(t_n)$*,* $\boldsymbol{y}^{[m]}(t_n)$ *the measured input and output signals.*

measured motor torques $\boldsymbol{\tau}^{(a)}$ and the measured motor rotations $\boldsymbol{e}^{(m)}$. Vectors $\boldsymbol{u}^{(0)}(t_n)$ and $\boldsymbol{y}^{(0)}(t_n)$ are the corresponding true but unknown values, i.e. the input and output values in the absence of any noise disturbances. The noise sources $\boldsymbol{u}^{[m](v)}(t_n)$ and $\boldsymbol{y}^{[m](v)}(t_n)$ on the measurement signals consist of the disturbing noise sources $\boldsymbol{v}^{[m](c)}(t_n)$, $\boldsymbol{v}^{[m](p)}(t_n)$, $\boldsymbol{m}^{[m](u)}(t_n)$ and $\boldsymbol{m}^{[m](y)}(t_n)$.

Using the Discrete-time Fourier transform (DFT), the time-domain vector sequences $\boldsymbol{u}^{[m]}(t_n)$ and $\boldsymbol{y}^{[m]}(t_n)$, $n = 0, 1, \cdots, N^{(t)} - 1$ are transformed into the frequency domain

$$\begin{aligned} \boldsymbol{U}^{[m]}(\omega_f) &= \sum_{n=0}^{N^{(t)}-1} \boldsymbol{u}^{[m]}(t_n) e^{-j\omega_f T^{(s)} n}, \\ \boldsymbol{Y}^{[m]}(\omega_f) &= \sum_{n=0}^{N^{(t)}-1} \boldsymbol{y}^{[m]}(t_n) e^{-j\omega_f T^{(s)} n}, \end{aligned} \tag{6.2}$$

with $\omega_f = f \frac{2\pi}{N^{(t)} T^{(s)}}$, $f = 0, 1, \cdots, N^{(t)} - 1$ and j the imaginary unit.

According to Pintelon and Schoukens (2001); Verboven et al. (2006) the relationships within the frequency domain between the noisy input vector $\boldsymbol{U}^{[m]}(\omega_f) \in \mathcal{C}^{N^{(u)}}$ and noisy output vector $\boldsymbol{Y}^{[m]}(\omega_f) \in \mathcal{C}^{N^{(y)}}$, and the true ones $\boldsymbol{U}^{(0)}(\omega_f) \in \mathcal{C}^{N^{(u)}}$ and $\boldsymbol{Y}^{(0)}(\omega_f) \in \mathcal{C}^{N^{(y)}}$ are described by the frequency domain

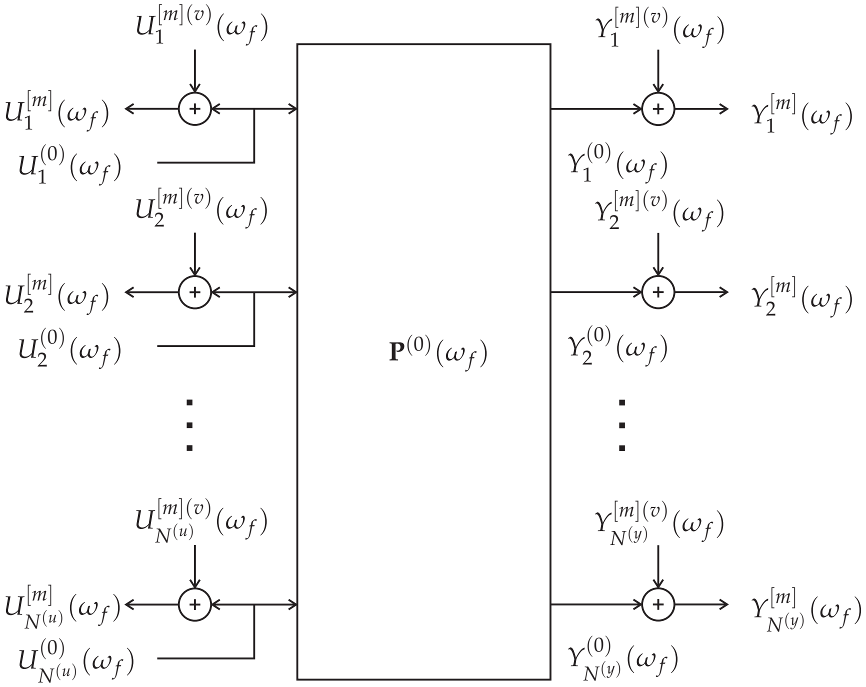

Figure 6.2: Frequency domain errors in variables model.

errors in variables (EV) stochastic model (figure 6.2),

$$\begin{aligned} \boldsymbol{U}^{[m]}(\omega_f) &= \boldsymbol{U}^{(0)}(\omega_f) + \boldsymbol{U}^{[m](v)}(\omega_f), \\ \boldsymbol{Y}^{[m]}(\omega_f) &= \boldsymbol{Y}^{(0)}(\omega_f) + \boldsymbol{Y}^{[m](v)}(\omega_f). \end{aligned} \tag{6.3}$$

The relationships between the true periodic input vector $\boldsymbol{U}^{(0)}(\omega_f)$ and output vector $\boldsymbol{Y}^{(0)}(\omega_f)$, is given by

$$\boldsymbol{Y}^{(0)}(\omega_f) = \mathbf{P}^{(0)}(\omega_f)\boldsymbol{U}^{(0)}(\omega_f), \tag{6.4}$$

in which $\mathbf{P}^{(0)}(\omega_f) \in \mathcal{C}^{N^{(y)} \times N^{(u)}}$ is the Multivariable Frequency Response Function associated with the linearised dynamic robot model. To facilitate notation, the MFRF of system $\mathbf{P}(s)$ will be denoted by $\mathbf{P}(\omega_f)$ instead of $\mathbf{P}(j\omega_f)$, which was used in chapter 5.

The vectors $\boldsymbol{U}^{[m](v)}(\omega_f) \in \mathcal{C}^{N^{(u)}}$ and $\boldsymbol{Y}^{[m](v)}(\omega_f) \in \mathcal{C}^{N^{(y)}}$ occurring in the frequency domain errors in variables model (6.3) are the Fourier transforms of vectors $\boldsymbol{u}^{[m](v)}(t_n)$ and $\boldsymbol{y}^{[m](v)}(t_n)$. Because of the feedback loop both the controller noise $\boldsymbol{V}^{[m](c)}(\omega_f)$ and the process noise $\boldsymbol{V}^{[m](p)}(\omega_f)$, corresponding to the time domain vectors $\boldsymbol{v}^{(c)}(t_n)$ and $\boldsymbol{v}^{(p)}(t_n)$, respectively, cause a correlation between the input and output errors. The errors $\boldsymbol{U}^{[m](v)}(\omega_f)$ and $\boldsymbol{Y}^{[m](v)}(\omega_f)$ are related to the disturbing noise sources as

$$\begin{aligned}
\boldsymbol{U}^{[m](v)}(\omega_f) =& \boldsymbol{M}^{[m](u)}(\omega_f) + (\mathbf{I} + \mathbf{C}(\omega_f)\mathbf{P}^{(0)}(\omega_f))^{-1} \\
& (-\mathbf{C}(\omega_f)\boldsymbol{V}^{[m](p)}(\omega_f) + \boldsymbol{V}^{[m](c)}(\omega_f)), \\
\boldsymbol{Y}^{[m](v)}(\omega_f) =& \boldsymbol{M}^{[m](y)}(\omega_f) + (\mathbf{I} + \mathbf{P}^{(0)}(\omega_f)\mathbf{C}(\omega_f))^{-1} \qquad (6.5) \\
& (\boldsymbol{V}^{[m](p)}(\omega_f) + \mathbf{P}^{(0)}(\omega_f)\boldsymbol{V}^{[m](c)}(\omega_f)), \\
& \qquad (6.6)
\end{aligned}$$

in which $\mathbf{I}$ is an identity matrix and $\mathbf{C}(\omega_f)$ is the MFRF of the controller model $\mathbf{C}(s)$. Vectors $\boldsymbol{M}^{[m](u)}(\omega_f)$ and $\boldsymbol{M}^{[m](y)}(\omega_f)$ are the Fourier transforms of the input and output measurement noise $\boldsymbol{m}^{[m](u)}(t_n)$ and $\boldsymbol{m}^{[m](y)}(t_n)$, respectively. Clearly, the disturbances $\boldsymbol{U}^{[m](v)}(\omega_f)$ and $\boldsymbol{Y}^{[m](v)}(\omega_f)$ are mutually correlated and are independent of the true input $\boldsymbol{U}^{(0)}(\omega_f)$.

Let the measurement vector, denoted by $\boldsymbol{Z}^{[m]}(\omega_f)$, be the stacked input and output vector of period m at frequency ω_f, so

$$\boldsymbol{Z}^{[m]}(\omega_f) = \begin{bmatrix} \boldsymbol{U}^{[m]}(\omega_f) \\ \boldsymbol{Y}^{[m]}(\omega_f) \end{bmatrix} \tag{6.7}$$

It is assumed that the random errors

$$\boldsymbol{Z}^{[m](v)}(\omega_f) = \begin{bmatrix} \boldsymbol{U}^{[m](v)}(\omega_f) \\ \boldsymbol{Y}^{[m](v)}(\omega_f) \end{bmatrix} \tag{6.8}$$

are complex normally distributed, with

$$\mathcal{E}(\boldsymbol{Z}^{[m](v)}(\omega_f)) = 0, \tag{6.9}$$

and

$$\operatorname{cov}(\boldsymbol{Z}^{[m](v)}(\omega_f), \boldsymbol{Z}^{[n](v)}(\omega_f)) = \mathbf{C}^{(Z^{(v)})}(\omega_f)\delta_{mn}, \quad m, n = 1, \cdots, N^{(m)} \tag{6.10}$$

in which δ_{mn} represents the Kronecker delta and $\mathcal{E}\{\}$ represents the expected value. $\mathbf{C}^{(Z^{(v)})}(\omega_f) \in \mathcal{C}^{(N^{(u)}+N^{(y)})\times(N^{(u)}+N^{(y)})}$ is a Hermitian symmetric noise covariance matrix. Hence, the noise disturbance is assumed to be (second-order) stationary and uncorrelated for different measured periods ($m \neq n$). Notice that $\mathbf{C}^{(Z^{(v)})}(\omega_f)$ accounts for the correlation among the input and output noise, $\boldsymbol{U}^{[m](v)}(\omega_f)$ and $\boldsymbol{Y}^{[m](v)}(\omega_f)$.

Thus far, the framework was described for a linear manipulator and controller model. In reality the controller and manipulator are both nonlinear systems. In the next section the influence of these nonlinearities on the identification of a linearised robot model will be described.

6.2 Stochastic identification framework for nonlinear systems

Schoukens et al. (2005) describe the influence of nonlinear distortions on the identification of linear SISO systems for an output error framework. Verboven et al. (2006) present a similar approach for MIMO systems. In this work, the nonlinear distortions will be included in the errors in variables framework, as this framework is more suitable to describe the closed-loop behaviour of the robot than the output error approach.

For nonlinear systems the MFRF depends on the excitation, therefore a class of input signals is defined first. It is assumed that the true input signals $\boldsymbol{u}^{(0)}(t_n)$ are described by random phase multi-sines, also called random multi-sines. A signal $u(t_n)$ is a random phase multi-sine if

$$u(t_n) = \frac{1}{N^{(t_n)}} \sum_{f=-N^{(t)}/2}^{N^{(t)}/2} |U(\omega_f)| e^{j(\frac{2\pi f n}{N^{(t)}} + \varphi_f)}, \tag{6.11}$$

with $\varphi_{-f} = -\varphi_f$, $|U(\omega_f)| = \sqrt{S_u(\omega_f)} \geq 0$ and $|U(\omega_f = 0)| = 0$. $S_u(\omega_f)$ is a user-defined uniformly bounded real function with a countable number of discontinuities representing the power spectrum of the excitation signal. The phases φ_f are the realisations of an independent (over f) uniformly distributed random process on $[0, 2\pi)$.

Besides the input, the class of nonlinear systems should be defined also. It is assumed that the nonlinear dynamics of the robot can be described by a Volterra model, see appendix F and Schetzen (1980). A formal proof is omitted, but it will be shown that the nonlinear phenomena of the Volterra model do correspond with the experimental data very well. According to Schoukens et al. (2005), the true output $\boldsymbol{Y}^{[o](NL)}(\omega_f)$ of a Volterra system excited by a random multi-sine consists of 2 parts

$$\boldsymbol{Y}^{[o](NL)}(\omega_f) = \mathbf{P}^{(R)}(\omega_f)\boldsymbol{U}^{[o](0)}(\omega_f) + \boldsymbol{Y}^{[o](s)}(\omega_f), \tag{6.12}$$

in which $\mathbf{P}^{(R)}(\omega_f)$ is called the related dynamic system and $\boldsymbol{Y}^{[o](s)}(\omega_f)$ is the stochastic nonlinear distortion. The superscript o between brackets denotes the o^{th} phase realisation of the random multi-sine. $\mathbf{P}^{(R)}(\omega_f)$ is the best linear approximation to the actual nonlinear system. It consists, in turn, of two parts

$$\mathbf{P}^{(R)}(\omega_f) = \mathbf{P}^{(0)}(\omega_f) + \mathbf{P}^{(B)}(\omega_f), \tag{6.13}$$

with $\mathbf{P}^{(0)}(\omega_f)$ the underlying linear system, as defined in equation (5.47), and $\mathbf{P}^{(B)}(\omega_f)$ the bias or symmetric errors due to the nonlinear distortions. $\mathbf{P}^{(B)}(\omega_f)$ and as a result also $\mathbf{P}^{(R)}(\omega_f)$ depend on the applied power spectrum, the nonlinear distortions and the number of components $N^{(t)}$. It does not depend on the actual realisation of the random excitation.

The stochastic nonlinear contribution $\boldsymbol{Y}^{[o](s)}$ depends on the actual realisation of the random excitation. However, the reader should be aware that it is not a random signal for a fixed excitation signal. Because of this contribution $\boldsymbol{Y}^{[o](s)}$ the MFRF measurements are not smooth as a function of the frequency, but scattered around their expected value (which equals $\mathbf{P}^{(R)}$). For a formal overview of the properties of $\boldsymbol{Y}^{[o](s)}$ and $\mathbf{P}^{(R)}$ the reader is referred to appendix F.

The nonlinearities will be included in the errors in variables framework by adding the nonlinear noise sources $\boldsymbol{Y}^{[o](s)}(\omega_f)$ to the outputs of the related linear system. The proposed relationships between the measured input and output vectors and the actual vectors are given by the following *nonlinear errors in variables* stochastic model that is presented in figure 6.3 and described by

$$\boldsymbol{U}^{[m,o]}(\omega_f) = \boldsymbol{U}^{[o](0)}(\omega_f) + \boldsymbol{U}^{[m,o](v)}(\omega_f) \tag{6.14a}$$

$$\boldsymbol{Y}^{[m,o]}(\omega_f) = \boldsymbol{Y}^{[o](0)}(\omega_f) + \boldsymbol{Y}^{[m,o](v)}(\omega_f) + \boldsymbol{Y}^{[o](s)}(\omega_f). \tag{6.14b}$$

The true output vector $\boldsymbol{Y}^{[o](0)}(\omega_f)$ is related to the true input vector $\boldsymbol{U}^{[o](0)}(\omega_f)$ by

$$\boldsymbol{Y}^{[o](0)}(\omega_f) = \mathbf{P}^{(R)}(\omega_f)\boldsymbol{U}^{[o](0)}(\omega_f), \tag{6.15}$$

with $\mathbf{P}^{(R)}(\omega_f)$ the earlier defined linear related system. For a Volterra system excited by a random multi-sine the stochastic nonlinearities $\boldsymbol{Y}^{[o](s)}(\omega_f)$ are asymptotically complex normally distributed, with mean

$$\mathcal{E}\{\boldsymbol{Y}^{[o](s)}(\omega_f)\} = \mathbf{0}, \tag{6.16}$$

and covariances

$$\mathcal{E}\{\boldsymbol{Y}^{[o](s)}(\omega_f)\boldsymbol{Y}^{[o](s)^H}(\omega_f)\} = \mathbf{C}^{(Y^{(s)})}(\omega_f) \tag{6.17}$$

and

$$\mathcal{E}\{\boldsymbol{Y}^{[o](s)}(\omega_f)\boldsymbol{Y}^{[o](s)^H}(\omega_l)\} = O(N^{(0)^{-1}}), \qquad k \neq l, \tag{6.18}$$

in which the expected value $\mathcal{E}\{\}$ has to be taken over different realisations of the multi-sine with equal power spectrum. Furthermore the $\boldsymbol{Y}^{[o](s)}(\omega_f)$ is uncorrelated with the true input $\boldsymbol{U}^{[o](0)}(\omega_f)$ and stochastic noise $\boldsymbol{Y}^{[m,o](v)}(\omega_f)$. The mathematical properties of $\boldsymbol{Y}^{[o](s)}(\omega_f)$ and $\mathbf{P}^{(R)}(\omega_f)$ are summarised in appendix F.

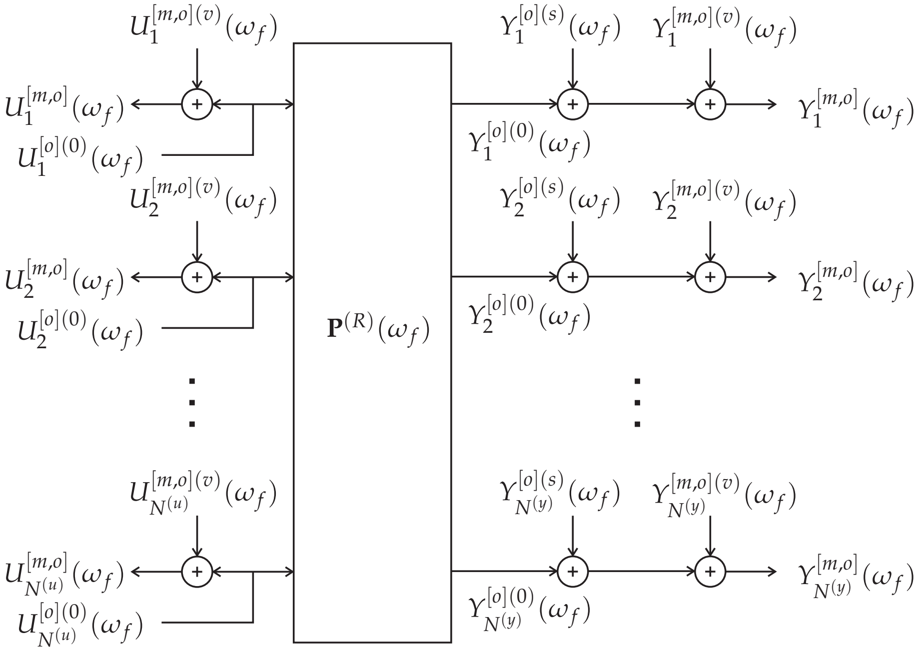

Figure 6.3: Nonlinear frequency domain errors in variables model.

Combining $\boldsymbol{U}^{[m,o]}(\omega_f)$ and $\boldsymbol{Y}^{[m,o]}(\omega_f)$ of equation (6.14) as in equation (6.7) gives

$$\boldsymbol{Z}^{[m,o]}(\omega_f) = \boldsymbol{Z}^{[o](0)}(\omega_f) + \boldsymbol{Z}^{[m,o](v)}(\omega_f) + \boldsymbol{Z}^{[o](s)}(\omega_f). \tag{6.19}$$

in which

$$\boldsymbol{Z}^{[o](0)}(\omega_f) = \begin{bmatrix} \boldsymbol{U}^{[o](0)}(\omega_f) \\ \boldsymbol{Y}^{[o](0)}(\omega_f) \end{bmatrix}, \tag{6.20a}$$

$$\boldsymbol{Z}^{[m,o](v)}(\omega_f) = \begin{bmatrix} \boldsymbol{U}^{[m,o](v)}(\omega_f) \\ \boldsymbol{Y}^{[m,o](v)}(\omega_f) \end{bmatrix}, \tag{6.20b}$$

$$\boldsymbol{Z}^{[o](s)}(\omega_f) = \begin{bmatrix} \mathbf{0} \\ \boldsymbol{Y}^{[o](s)}(\omega_f) \end{bmatrix}. \tag{6.20c}$$

The covariance of the stochastic noise $\mathbf{C}^{(Z^{(v)})}(\omega_f)$ is defined in equation (6.10). Combining the definitions of equations (6.17) and (6.20c) yields for the covariance of the stochastic nonlinear distortions

$$\mathbf{C}^{(Z^{(s)})}(\omega_f) = \mathcal{E}\{\boldsymbol{Z}^{[o](s)}(\omega_f)\boldsymbol{Z}^{[o](s)^H}(\omega_f)\} = \begin{bmatrix} \mathbf{0} & \mathbf{0} \\ \mathbf{0} & \mathbf{C}^{(Y^{(s)})}(\omega_f) \end{bmatrix}. \tag{6.21}$$

The next section presents a nonparametric identification method for estimating the multi-variable frequency response of the related linear system $\mathbf{P}^{(R)}(\omega_f)$ and the noise properties $\mathbf{C}^{(Z^{(v)})}(\omega_f)$ and $\mathbf{C}^{(Z^{(s)})}(\omega_f)$. Unless stated otherwise, from now on the related linear system will be denoted by $\mathbf{P}(\omega_f)$. Note that in general $\mathbf{P}(\omega_f) = \mathbf{P}^{(R)}(\omega_f) \neq \mathbf{P}^{(0)}(\omega_f)$.

6.3 Nonparametric identification

Estimation of the MFRF $\mathbf{P}(\omega_f)$ and its reliability requires the true input and output vectors and their covariances $\mathbf{C}^{(Z^{(v)})}(\omega_f)$ and $\mathbf{C}^{(Z^{(s)})}(\omega_f)$. They are a priori unknown but can be estimated from experimental data, using averaging techniques. Due to the different phase realisation between the experiments, the input and output vectors first need to be mapped to a common phase distribution before the signals may be averaged.

6.3.1 Mapping input and output signals to a common phase realisation

Pintelon and Schoukens (2001) present a SISO method to project the input and output signals for experiments with different inputs on a priori known deterministic input signal which is commonly available in open-loop experiments. A signal such as this is not available during closed-loop experiments. Therefore a new MIMO approach is presented for the nonlinear errors in variables framework discussed in the previous section.

In a closed-loop system not only the outputs $\boldsymbol{Y}^{[m,o]}(\omega_f)$, but also the inputs $\boldsymbol{U}^{[m,o]}(\omega_f)$ are disturbed by the nonlinear behaviour of both the robot manipulator and the feedback controller. To measure the nonlinear distortions of the robot separate from the nonlinear disturbances of the controller, a new mapping signal is proposed, namely the measured input signal $\boldsymbol{U}^{[m,o]}(\omega_f)$ averaged over different periods of the same multi-sine. As a result, all plant nonlinearities are projected onto the output and the nonlinearities of the controller are cancelled, which is in agreement with the nonlinear errors in variables model of figure 6.3.

In the proposed mapping for each phase realisation of the multi-sine, $N^{(u)}$ different (independent) experiments are performed, in which $N^{(u)}$ is the number of inputs. The design of these kinds of input signals is discussed in section 6.5. The measured input and output vectors $\boldsymbol{U}^{[m,o]}(\omega_f)$ and $\boldsymbol{Y}^{[m,o]}(\omega_f)$ are collected into matrices $\mathbf{U}^{[m,o]}(\omega_f)$ and $\mathbf{Y}^{[m,o]}(\omega_f)$, in which each column corresponds to one experiment. Let the averaged input and output spectra for each phase realisation o be defined by

$$\hat{\mathbf{U}}^{[o]}(\omega_f) = \frac{1}{N^{(m)}} \sum_{m=1}^{N^{(m)}} \mathbf{U}^{[m,o]}(\omega_f),$$
$$\hat{\mathbf{Y}}^{[o]}(\omega_f) = \frac{1}{N^{(m)}} \sum_{m=1}^{N^{(m)}} \mathbf{Y}^{[m,o]}(\omega_f) \tag{6.22}$$

and let the averaged absolute value of all inputs for different phase distributions be defined as

$$\bar{\mathbf{U}}(\omega_f) = \frac{1}{N^{(o)}} \sum_{o=1}^{N^{(o)}} \left| \hat{\mathbf{U}}^{[o]}(\omega_f) \right|. \tag{6.23}$$

Projection of the measured input and output spectra on $\hat{\mathbf{U}}^{[o]}(\omega_f)$ and multiplying the result by $\bar{\mathbf{U}}(\omega_f)$, yields

$$\tilde{\mathbf{U}}^{[m,o]}(\omega_f) = \mathbf{U}^{[m,o]}(\omega_f)(\hat{\mathbf{U}}^{[o]}(\omega_f))^{-1}\bar{\mathbf{U}}(\omega_f), \tag{6.24}$$
$$\tilde{\mathbf{Y}}^{[m,o]}(\omega_f) = \mathbf{Y}^{[m,o]}(\omega_f)(\hat{\mathbf{U}}^{[o]}(\omega_f))^{-1}\bar{\mathbf{U}}(\omega_f), \tag{6.25}$$

provided matrices $\hat{\mathbf{U}}^{[o]}(\omega_f)$ have full rank. This illustrates the requirement that $N^{(u)}$ independent experiments should be performed for each phase realisation. The columns of $\tilde{\mathbf{U}}^{[m,o]}(\omega_f)$ and $\tilde{\mathbf{Y}}^{[m,o]}(\omega_f)$ represent the transformed input and output vectors. To simplify notation, the tilde will be dropped from now on and it is assumed that all signals have been transformed to the same phase distribution using the procedure described above.

6.3.2 Noise covariance estimation

The variance of measurement vector $\mathbf{Z}^{[m,o]}$ has contributions to the stochastic noise $\mathbf{Z}^{[m,o](v)}$ and the nonlinear noise source $\mathbf{Z}^{[o](s)}$. According to D'Haene et al. (2004), the covariance of the stochastic contributions can be estimated by measuring several periods of the same multi-sine, yielding

$$\begin{aligned}\hat{\mathbf{C}}^{[o](Z^{(v)})}(\omega_f) =& \frac{1}{N^{(m)}-1} \sum_{m=1}^{N^{(m)}} \left(\mathbf{Z}^{[m,o]}(\omega_f) - \hat{\mathbf{Z}}^{[o]}(\omega_f)\right) \\ & \left(\mathbf{Z}^{[m,o]}(\omega_f) - \hat{\mathbf{Z}}^{[o]}(\omega_f)\right)^H,\end{aligned} \tag{6.26}$$

in which

$$\hat{\mathbf{Z}}^{[o]}(\omega_f) = \frac{1}{N^{(m)}} \sum_{m=1}^{N^{(m)}} \mathbf{Z}^{[m,o]}(\omega_f). \tag{6.27}$$

The sample covariance of the stochastic contributions $\hat{\mathbf{C}}^{(Z^{(v)})}(\omega_f)$ is defined as the average of the covariances presented in (6.26), yielding

$$\hat{\mathbf{C}}^{(Z^{(v)})}(\omega_f) = \frac{1}{N^{(o)}} \sum_{m=1}^{N^{(o)}} \hat{\mathbf{C}}^{[o](Z^{(v)})}(\omega_f). \tag{6.28}$$

The covariance of the nonlinear stochastic contributions can only be measured in combination with the stochastic contributions. Let the $\hat{\boldsymbol{Z}}(\omega_f)$ denote the sample mean of all measurements $\boldsymbol{Z}^{[m,o]}$ and be defined by

$$\hat{\boldsymbol{Z}}(\omega_f) = \frac{1}{N^{(o)}} \sum_{o=1}^{N^{(o)}} \hat{\boldsymbol{Z}}^{[o]}(\omega_f). \tag{6.29}$$

According to the noise assumptions presented in section 6.2, the covariance of the sample mean $\hat{\boldsymbol{Z}}(\omega_f)$ is defined by

$$\hat{\mathbf{C}}^{(\hat{Z})}(\omega_f) = \frac{\hat{\mathbf{C}}^{(Z^{(v)})}(\omega_f)}{N^{(o)}N^{(m)}} + \frac{\hat{\mathbf{C}}^{(Z^{(s)})}(\omega_f)}{N^{(o)}} \tag{6.30}$$

and can be estimated by (D'Haene et al. (2004))

$$\begin{aligned}\hat{\mathbf{C}}^{(\hat{Z})}(\omega_f) =& \frac{1}{N^{(o)}(N^{(o)}-1)} \sum_{o=1}^{N^{(o)}} \left(\hat{\boldsymbol{Z}}^{[o]}(\omega_f) - \hat{\boldsymbol{Z}}(\omega_f)\right) \\ & \left(\hat{\boldsymbol{Z}}^{[o]}(\omega_f) - \hat{\boldsymbol{Z}}(\omega_f)\right)^H. \end{aligned} \tag{6.31}$$

As a result of equation (6.30), the combination of estimators (6.28) and (6.31) yields the covariance $\hat{\mathbf{C}}^{(Z^{(s)})}(\omega_f)$ of the nonlinear contributions.

6.3.3 MFRF estimation

Let the estimated and averaged (see equation (6.29)) input and output vectors be collected in matrix $\hat{\mathbf{U}}$ and $\hat{\mathbf{Y}}$, respectively, in which each column corresponds to one experiment. According to Verboven et al. (2006), a maximum likelihood estimation for MFRF $\mathbf{P}(\omega_f)$ with regard to the errors in variables framework of equation (6.3) is given by

$$\hat{\mathbf{P}}(\omega_f) = \hat{\mathbf{Y}}(\omega_f)\hat{\mathbf{U}}^{-1}(\omega_f), \tag{6.32}$$

provided that matrix $\hat{\mathbf{U}}^{-1}(\omega_f)$ has full rank. The design of input signals assuring this condition is discussed in section 6.5. This estimator is also proposed for the nonlinear errors in variables model of equation (6.14), since the noise conditions are very similar. All noise sources are namely asymptotically described by a zero mean circular complex normal distribution. The estimate (6.32) belongs to the class of maximum likelihood estimators for which it has been proven that they are consistent and asymptotically efficient.

According to Verboven et al. (2006), the multivariable expression for the estimate of the noise covariance matrix for the MFRF is given by

$$\begin{aligned}\hat{\mathbf{C}}^{(\hat{\mathbf{P}})}(\omega_f) &= \operatorname{cov}(\hat{\mathbf{P}}(\omega_f)) \\ &= \left[\hat{\mathbf{U}}(\omega_f)^*\hat{\mathbf{U}}(\omega_f)^T\right]^{-1} \otimes \hat{\mathbf{B}}(\omega_f)\hat{\mathbf{C}}^{V^{(\hat{Z})}}(\omega_f)\hat{\mathbf{B}}(\omega_f)^H \end{aligned} \tag{6.33}$$

with

$$\hat{\mathbf{B}}(\omega_f) = \left[\hat{\mathbf{P}}(\omega_f), -\mathbf{I}\right]. \tag{6.34}$$

The symbol $\otimes$ denotes the Kronecker matrix product and the asterisk denotes the complex conjugate.

6.4 Parametric identification

6.4.1 Model estimation

The parametric system models are found by minimising a cost function that expresses the match between measurements and the model. Let the vector $\boldsymbol{p}$ contain the parameters of the nominator and denominator polynomials of true linear system $\mathbf{P}(s, \boldsymbol{p}) = \mathbf{B}(s, \boldsymbol{p})/A(s, \boldsymbol{p})$, as presented in equation (5.38) and (5.47). As a result of the nonlinearities in the system not $\mathbf{P}^{(0)}(s)$ will be estimated but the related linear system $\mathbf{P}^{(R)}(s)$. Given the stochastic framework of section 6.2, it is possible to derive a maximum likelihood estimator to identify the related linear system $\mathbf{P}^{(R)}(s)$, which will be denoted by $\mathbf{P}(s)$.

According to Pintelon and Schoukens (2001); Verboven (2002) and under the assumption that the input and output noise spectra are complex normally distributed the maximum likelihood (ML) cost function is defined by

$$V^{(ML)}(\boldsymbol{p}, \hat{\boldsymbol{Z}}) = \sum_{f=1}^{N^{(f)}} |\hat{\boldsymbol{\epsilon}}(\omega_f, \boldsymbol{p}, \hat{\boldsymbol{Z}})|^2, \tag{6.35}$$

in which $\hat{\boldsymbol{\epsilon}}(\omega_f, \boldsymbol{p}, \hat{\boldsymbol{Z}})$ are the weighted residuals,

$$\hat{\epsilon}_i(\omega_f, \boldsymbol{p}, \hat{\boldsymbol{Z}}) = \hat{e}_i(\omega_f, \boldsymbol{p}, \hat{\boldsymbol{Z}})/\hat{\sigma}_i^{(\hat{e})}(\omega_f, \boldsymbol{p}), \quad i = 1, \cdots, N^{(y)}. \tag{6.36}$$

The equation error $\hat{e}_i(\omega_f, \boldsymbol{p}, \hat{\boldsymbol{Z}})$ is defined by

$$\hat{\boldsymbol{e}}(\omega_f, \boldsymbol{p}, \hat{\boldsymbol{Z}}) = \hat{\boldsymbol{Y}}(\omega_f)A(s, \boldsymbol{p}) - \mathbf{B}(s, \boldsymbol{p})\hat{\boldsymbol{U}}(\omega_f) \tag{6.37}$$

and $\hat{\sigma}_i^{(\hat{e})}(\omega_f, \boldsymbol{p})$ represents the standard deviation of the equation error. The standard deviation is computed from the sample covariance matrix, which is given by

$$\hat{\mathbf{C}}^{(\hat{e})}(\omega_f, \boldsymbol{p}) = 2\mathrm{Re}\left(\mathbf{J}(\omega_f, \boldsymbol{p})\hat{\mathbf{C}}^{(\hat{Z})}(\omega_f)\mathbf{J}(\omega_f, \boldsymbol{p})^H\right) \tag{6.38}$$

in which

$$\mathbf{J}(\omega_f, \boldsymbol{p}) = \frac{\partial \boldsymbol{e}(\omega_f, \boldsymbol{p}, \boldsymbol{Z})}{\partial \boldsymbol{Z}} = \left[-\mathbf{B}(\omega_f, \boldsymbol{p}) \quad \mathbf{I}A(\omega_f, \boldsymbol{p})\right]. \tag{6.39}$$

The standard deviation of the equation error is given by $\hat{\sigma}_i^{(\hat{e})}(\omega_f, \boldsymbol{p}) = \sqrt{\hat{C}_{i,i}^{(\hat{e})}(\omega_f, \boldsymbol{p})}$.

Because $\hat{e}_i(\omega_f, \boldsymbol{p}, \hat{\boldsymbol{Z}})$ is a nonlinear function of $\boldsymbol{p}$, the cost function $V^{(ML)}$ is a nonquadratic function of $\boldsymbol{p}$. As with most nonlinear minimisation problems, the method may converge to a local minimum. Therefore, it is important to have starting values of sufficiently high accuracy. An (iterative) linear least squares solution, presented by Pintelon and Schoukens (2001), is proposed for this purpose. The linear least squares cost function is defined as

$$V^{(LS)}(\boldsymbol{p}, \hat{\boldsymbol{Z}}) = \sum_{f=1}^{N^{(f)}} |\hat{\boldsymbol{e}}(\omega_f, \boldsymbol{p}, \hat{\boldsymbol{Z}})|^2. \tag{6.40}$$

For the parametrisation of equation (5.38) this cost function is quadratic in the parameters $\boldsymbol{p}$. The linear least square cost function has two drawbacks when identifying continuous-time models: an overemphasising of high-frequency errors and a bad numerical condition. The numerical condition of the problem can be improved by scaling the frequency axis or parameterising the transfer functions with orthonormal polynominals (Barel and Bultheel (1995)).

To overcome the lack of sensitivity to low frequency errors of the linear least squares estimator, the equation error $\hat{\boldsymbol{e}}(\omega_f, \boldsymbol{p}, \hat{\boldsymbol{Z}})$ is divided by an initial estimate of the denominator polynomial $A(s, \boldsymbol{p})$. The obtained weighted linear least squares estimate $\boldsymbol{p}^{(1)}$ can be used to calculate a (hopefully) better estimate $\boldsymbol{p}^{(2)}$, and so on. The ith step of this iterative linear least squares procedure consists of minimising

$$V^{(IWLS)}(\boldsymbol{p}^{(i)}, \hat{\boldsymbol{Z}}) = \sum_{f=1}^{N^{(f)}} \frac{|\hat{\boldsymbol{e}}(\omega_f, \boldsymbol{p}^{(i)}, \hat{\boldsymbol{Z}})|^2}{|A(\omega_f, \boldsymbol{p}^{(i-1)})|^w}, \tag{6.41}$$

with respect to $\boldsymbol{p}^{(i)}$ for $w = 2$. The linear least squares estimate, denoted by $\hat{\boldsymbol{p}}^{(LS)}$, is used as starting value $\boldsymbol{p}^{(0)} = \hat{\boldsymbol{p}}^{(LS)}$. According to Pintelon and Schoukens (2001) setting the power of the denominator w smaller than 2 to improve the convergence of the iteration scheme may be required.

The maximum likelihood objective function with a parametrisation similar to equation (5.39) and the iterated linear least squares objective functions with parametrisation (5.38) are implemented in MATLAB. The nonlinear least squares problem of the maximum likelihood method is solved using the NONLSQ routine of the optimisation toolbox. Both the residual and the Jacobian matrix of the residual are provided to this optimisation routine.

6.4.2 Model validation

The estimated model should be validated to verify whether or not the model describes the measured data with sufficient accuracy. Several validation techniques that are applied in the remaining of this chapter will be discussed below.

Value objective function

Assuming that all dynamics are captured by the estimated model, the residual contains only contributions from the measurement noise and the stochastic nonlinearities. In the absence of model errors $V^{(ML)}(\hat{\boldsymbol{p}}, \hat{\boldsymbol{Z}})$ is asymptotically ($N^{(f)} \to \infty$) normally distributed with mean (Pintelon and Schoukens (2001), page 334)

$$\mathcal{E}\{V^{(ML)}(\hat{\boldsymbol{p}}, \hat{\boldsymbol{Z}})\} \approx \frac{N^{(o)} - 1}{N^{(o)} - 2}(N^{(f)}N^{(y)} - N^{(p)}/2) \tag{6.42}$$

and variance

$$\text{var}(V^{(ML)}(\hat{\boldsymbol{p}}, \hat{\boldsymbol{Z}})) \approx \frac{(N^{(o)} - 1)^3}{(N^{(o)} - 2)^2(N^{(o)} - 3)}(N^{(f)}N^{(y)} - N^{(p)}/2). \tag{6.43}$$

The factors $\frac{N^{(o)}-1}{N^{(o)}-2}$ and $\frac{(N^{(o)}-1)^3}{(N^{(o)}-2)^2(N^{(o)}-3)}$ in the equations above describe the loss of efficiency as a result of using estimated noise models instead of the true models. Note that an efficient estimator has the lowest possible parameter variance among all unbiased estimators. In this thesis the loss of efficiency is expressed in the number of different phase realisations of the random multi-sines $N^{(o)}$. For the nonlinear stochastic contributions the expressions as mentioned above are correct. However for the stochastic contributions the term $N^{(o)}N^{(m)}$ should be used, as can be seen from equation (6.30). Therefore, the presented mean and variance are upper estimates.

With equations (6.42) and (6.43) it is possible to compute uncertainty bounds for the cost function (6.35). A cost function that is outside these bounds indicates model errors, because the residual cannot be explained by the estimated noise levels. An alternative method to detect under-modelling is to check the correlation of the residuals.

Correlation test residuals

Pintelon and Schoukens (2001) present a correlation test for the FRF of SISO systems in an output error framework. A similar approach will be presented below for the residuals of the maximum likelihood estimator in an errors in variables approach.

According to equation (6.18), the nonlinearities $\boldsymbol{Z}^{[o](s)}$ should be uncorrelated if the true input $\boldsymbol{u}^{[o](0)}$ is a random multi-sine. The same holds true for the stochastic contributions $\boldsymbol{Z}^{[m,o](s)}$. As a result, the weighted residuals should be uncorrelated as well. Correlated residuals point to unmodelled dynamics, hence it makes sense to increase the model order.

The sample correlation of the residual is defined as

$$\hat{R}_j^{(\hat{\epsilon})}(l) = \frac{1}{(N^{(f)} - N^{(l)})} \sum_{f=1}^{(N^{(f)}-N^{(l)})} \hat{\epsilon}_j^H(\omega_f)\hat{\epsilon}_j(\omega_{f+l}), \tag{6.44}$$

for $l = 1, \cdots, N^{(l)}$ and $j = 1, \cdots, N^{(y)}$. Because the variance dominates the bias error in $\hat{\epsilon}_j(\omega_f)$, it follows that the sample correlation $\hat{R}_j^{(\hat{\epsilon})}(l)$ is asymptotically zero mean circular complex normally distributed (Pintelon and Schoukens (2001)), with sample variance

$$\hat{C}_j^{(\hat{R}^{(\hat{\epsilon})})}(l) = \left(\frac{(N^{(o)} - 1)}{(N^{(o)} - 2)}\right)^2 \frac{1}{(N^{(f)} - N^{(l)})}, \tag{6.45}$$

for $(N^{(f)} - N^{(l)}) \to \infty$. During the validation tests, graphical representations of the amplitude of $\hat{\boldsymbol{R}}^{(\hat{\epsilon})}(l)$ are used. Hence, the complex variance should be transferred into a bound on the amplitude. Since $\hat{\boldsymbol{R}}^{(\hat{\epsilon})}(l)$ is asymptotically zero mean circular complex normally distributed, the amplitude is chi-squared distributed with two degrees of freedom. For example the, 95% level is given by the bound: $\sqrt{3}\sqrt{\hat{C}_j^{(\hat{R}^{(\hat{\epsilon})})}(l)}$.

Variance of the parameters

The covariance of the estimated parameters $\hat{\boldsymbol{p}}$ can be computed with (Pintelon and Schoukens (2001), page 287)

$$\hat{\mathbf{C}}^{(\hat{\boldsymbol{p}})} = \frac{N^{(o)} - 1}{N^{(o)} - 3} \left(2\mathrm{Re}((\boldsymbol{\epsilon}'(\hat{\boldsymbol{p}}, \hat{\boldsymbol{Z}}))^H \boldsymbol{\epsilon}'(\hat{\boldsymbol{p}}, \hat{\boldsymbol{Z}}))\right)^{-1} \tag{6.46}$$

in which

$$\boldsymbol{\epsilon}'(\hat{\boldsymbol{p}}, \hat{\boldsymbol{Z}}) = \left.\frac{\partial \boldsymbol{\epsilon}(\boldsymbol{p}, \hat{\boldsymbol{Z}})}{\partial \boldsymbol{p}}\right|_{\boldsymbol{p}=\hat{\boldsymbol{p}}}. \tag{6.47}$$

Given the covariance of the model parameters, the covariance of other model characteristics can be computed. The variance of the estimated transfer function due to the noise sensitivity of the parameters is given by:

$$\hat{\mathbf{C}}^{(\hat{G})}(\omega_f, \hat{\boldsymbol{p}}) = \left.\frac{\partial \mathbf{P}(\omega_f, \boldsymbol{p})}{\partial \boldsymbol{p}}\right|_{p=\hat{p}} \hat{\mathbf{C}}^{(\hat{\boldsymbol{p}})} \left(\left.\frac{\partial \mathbf{P}(\omega_f, \boldsymbol{p})}{\partial \boldsymbol{p}}\right|_{p=\hat{p}} \right)^H . \tag{6.48}$$

For $\omega_f = 0$ and $\omega_f = \infty$, $|\mathbf{P}(\omega_f, \boldsymbol{p})|$ corresponds to the rigid mass matrix M_{ee} and the motor inertia $J^{[k](a)}$, see equation (5.51) and (5.30), respectively. Equation (6.48) is used to estimate their variances. Furthermore, this equation is used to compute the uncertainty bounds for the parametric transfer function.

In addition, the variance of the drive stiffness $k_1^{(m)[k]}$ can be estimated with matrix $\hat{\mathbf{C}}^{(\hat{\boldsymbol{p}})}$. Appendix E shows the inverse eigenvalue algorithm differentiated with respect to the parameters $\hat{\boldsymbol{p}}$. A pre- and post-multiplication of matrix $\hat{\mathbf{C}}^{(\hat{\boldsymbol{p}})}$ with this derivative yields an approximation of the variance of the drive parameters.

Comparison with nonparametric model

A simple validation test is to compare the differences between the measured nonparametric MFRF $\hat{\mathbf{P}}(\omega_f)$ and the parameteric MFRF $\mathbf{P}(\omega_f, \hat{\boldsymbol{p}})$. In order to decide if the residuals $\hat{\mathbf{P}}(\omega_f) - \mathbf{P}(\omega_f, \hat{\boldsymbol{p}})$ are significantly different from zero, their variance should be calculated. These residuals depend not only on $\hat{\boldsymbol{p}}$ but also on the raw data $\hat{\mathbf{P}}(\omega_f)$. Note that $\hat{\boldsymbol{p}}$ and $\hat{\mathbf{P}}(\omega_f)$ are correlated stochastic variables because they both depend on the same noise distortions $\mathbf{Z}^{(v)}(\omega_f)$. No estimator is known for the variance of the residuals in the multivariate situation. But in general $\mathbf{C}^{(P)}(\omega_f, \hat{\boldsymbol{p}}) \ll \mathbf{C}^{(\hat{P})}(\omega_f)$ so that we can use $\hat{\mathbf{C}}^{(\hat{P})}(\omega_f)$ as the uncertainty on the residuals. If $\hat{\mathbf{C}}^{(P)}(\omega_f, \hat{\boldsymbol{p}}) \approx \hat{\mathbf{C}}^{(\hat{P})}(\omega_f)$ we should accept that in that region we cannot detect the presence of model errors, because no reliable estimation of the residual uncertainty exists to decide whether or not they are significantly different from zero.

6.5 Experimental design

For stability and safety reasons, the experiments are carried out in closed-loop. The robot is excited with the feed-forward torques $\boldsymbol{\tau}^{(ff)}(t_n)$ which have a frequency spectrum that extends beyond the bandwidth of the closed-loop system. A velocity reversal excites the unwanted nonlinear behaviour originating from the asperity joint friction. To reduce the influence of velocity reversals, the robot is programmed to follow a well-designed trajectory $\boldsymbol{r}(t_n)$. First, the design of the feed-forward signal $\boldsymbol{\tau}^{(ff)}(t_n)$ is presented, and subsequently the design of the trajectory $\boldsymbol{r}(t_n)$.

6.5.1 Design of feed-forward signal

To fulfill the condition that matrix $\mathbf{U}(k)$ should have full rank, at least $N^{(u)}$ independent experiments should be carried out. Given a periodic signal $f(t_n)$ we restrict our selection of references to

$$\mathbf{O}^{(ff)}(t_n) = \mathbf{Y}f(t_n), \tag{6.49}$$

in which each column of $\mathbf{O}^{(ff)}(t_n)$ consist of the inputs $\boldsymbol{\tau}^{(ff)}(t_n)$ for one experiment. In Wernholt (2004) two options for matrix $\mathbf{Y}$ are compared, namely an identity matrix denoted by $\mathbf{Y}^{(1)}$ and matrix

$$\mathbf{Y}^{(2)} = \begin{bmatrix} 1 & 1 & 1 & & 1 \\ 1 & -1 & 1 & & 1 \\ 1 & 1 & -1 & & 1 \\ & & & \ddots & \\ 1 & 1 & 1 & & -1 \end{bmatrix}. \tag{6.50}$$

Depending on the type of disturbances, one is preferred over the other. In Verboven et al. (2006) it is shown that a so-called Hadamard matrix is optimal in the sense that it minimises the Cramer-Rao lower band (or, equivalently, maximises the Fisher information matrix). It can be shown that the same holds true for $\mathbf{Y}^{(2)}$.

The selection of an identity matrix $\mathbf{Y}^{(1)}$ implies single input experiments. Because of coupled dynamics between the different joints, excitation of a single joint will result in the movement of all joints. The reaction of the controller on this movement will be very closely correlated with the excitation signal. As a result, $N^{(y)}$ multiple input experiments with correlated inputs are performed, instead of the proposed single input measurements. The relatively low excitation level of the non-excited joints will result in low signal to noise ratios. As a result, the estimation of the true plant model is disturbed by the closed-loop dynamics of the controller. Therefore, matrix $\mathbf{Y}^{(2)}$ as defined in equation (6.50) appears to be the better choice. This choice will be validated with simulations in section 6.6.7.

The use of periodic excitation signals avoids leakage, reduces stochastic variance in nonparametric estimates for frequency response functions and can be used to estimate the noise variances for parametric estimates. For these reasons, a random multi-sine (equation (6.11)) is used as a feed-forward signal $\tau^{(ff)}(t_n)$. By using odd excitations, the influence of the nonlinear distortions can be decreased. Odd excitations are periodic signals that excite only the odd frequencies $(2k+1)\omega_1$ for $k = 0, 1, \ldots$ and ω_1 the base frequency and the amplitudes of the even frequencies are set at zero. According to Schoukens et al. (2005) each static or dynamic nonlinearity can be written as the sum of an even and odd nonlinear system. Even nonlinearities do not contribute to the best linear approximation $\mathbf{P}^{(R)}$. They only contribute to the nonlinear noise $\boldsymbol{Y}^{(s)}$ that acts as a disturbance during the measurement of $\mathbf{P}^{(R)}$. An even nonlinearity transfers all the power of an odd excitation to the even frequencies. Because $\mathbf{P}^{(R)}$ is only measured at the excited odd frequencies the measurements will no longer be disturbed by the even nonlinearity, and the uncertainty on $\mathbf{P}^{(R)}$ is reduced.

Equation (6.33) shows that for nonparametric frequency response measurements, the uncertainty is inversely proportional to the power of the excitation signal. For signals that have a specified maximum peak value, it is convenient to use the so-called crest factor as a measure of the signal quality. The crest factor for a signal is given by the ratio between the peak value of the signal and its effective root mean square (rms) value, whereby effective means that only power in the frequency band of interest is included in the rms calculation. To maximise the crest factor of a random multi-sine, an iterative optimisation procedure is used, which is referred to in literature as the clipping algorithm (Pintelon and Schoukens (2001)). Starting from a random phase distribution and a given amplitude spectrum this algorithm computes a more optimal phase distribution, which minimises the Crest factor. By using this method, the outcome is not necessarily a random multi-sine anymore. Note that the properties of $\boldsymbol{Y}^{[o](s)}$ presented in section 6.2 only hold true for excitation with a random multi-sine. Fortunately, it appears that the optimised multi-sines are actually less correlated than the initial ones.

6.5.2 Design of joint trajectory

The reference trajectory $\dot{\boldsymbol{r}}$ for the joint velocity is a (smoothed) square wave. The square wave should reduce the number of unwanted velocity reversals that lead to nonlinear friction behaviour (Wernholt (2004)). A smoothed square wave is required, because the reference generator of the controller requires a smooth trajectory. A true square wave will lead to infinite acceleration commands. An extension of the method is proposed to further reduce the unwanted effects of the friction behaviour. By extracting the measurement vectors $\boldsymbol{u}(t_n), \boldsymbol{y}(t_n)$ of two experiments with an identical reference trajectory $\boldsymbol{r}(t_n)$ but opposite sign of the feed-forward input $\boldsymbol{f}(t_n)$ some of the nonlinear terms will cancel. The effectiveness of this approach will be demonstrated in section 6.7.

The amplitude of the square wave is a trade-off between the number of velocity reversals, the total joint movement of the robot, and the applied input power of the feed-forward. For a fixed number of velocity reversals and a fixed measurement time a higher amplitude of the square wave will result in larger movements of the robot joints. Because the dynamics of the robot are pose dependent, it is hard to find a linear model that describes these large joint rotations. If the amplitude of the square wave is too small compared to the level of the feed-forward torques, the square wave is not able to prevent velocity reversals introduced by the feed-forward torques.

The base frequency of the square wave should always be an integer multiple of the base frequency of the multi-sine (ω_1), because the proposed identification techniques require periodic excitation. To ensure that only odd frequencies are excited as proposed in section 6.5.1, the reference trajectory is filtered to remove all frequencies other than $(2k+1)\omega_1, \quad k = 0, 1, \cdots$.

6.6 Simulation results

In this section, the identification techniques presented in this chapter will be demonstrated on the simulated responses of a robot manipulator. Experimental results will be presented in the next section.

6.6.1 Simulation model

The used simulation model is based on the Stäubli RX90B industrial robot and is similar to the model presented in section 5.9. This time all 6 joints of the manipulator are included. The first 3 joints are flexible, the other 3 are modelled rigid. To reduce the computation time the perturbation method has been used, see Jonker and Aarts (2001) and section 3.4. Using this method, the dynamic model is split into two parts. A rigidified nonlinear system describes the nominal rigid link motion of the manipulator and a linear time varying (LTV) system describes the vibrational motion of the manipulator. Henceforth this simulation model will be referred to as the nonlinear model.

A model of the true digital CS8 robot controller generates the feedback torques to drive the robot along an excitation trajectory. The zero order hold in the current loop of the digital feedback controller operates at a much higher sample rate than the data capturing. As a result, the torque measurements are corrupted by aliasing effects. To prevent aliasing during sampling, a digital low pass filter with a cut off frequency of 90 Hz has been placed in the simulation model before the data is captured at 250 Hz.

The measurement noise is modelled by adding uncorrelated Gaussian noise to the measured motor current, the motor position and motor velocity. An additional noise source can be found in the controller model, because the controller includes noise generating operations like quantisation effects.

6.6.2 Experiment design

All simulations are computed around one nominal configuration, namely a stretched horizontal position, see figure 5.2, page 75. The velocity profile for the joints $\dot{r}(t_n)$ is a smoothed square wave with an amplitude of 0.11 rad/s and a base frequency of $\omega_1 = \frac{1}{4.096}$ Hz. The smoothing has been done by using a skewed sine as upset function. The feed-forward signal $f(t_n)$ is a multi-sine with the same base frequency, an amplitude of 45 Nm and a frequency grid

$(2k+1)\omega_1$ for $k = 5, \cdots, 160$. Note that the harmonics $k = 0, \cdots, 4$ are omitted. This has been done to prevent velocity reversals. Furthermore, Crest-factor optimisation has been performed using the Clipping algorithm (section 6.5.1). As a result, the Crest factor has been decreased from 3.1 to 1.3. For reasons of noise characterisation and data averaging, the signals are repeated during $N^{(m)} = 8$ periods. The input matrix $\mathbf{Y}^{(2)}$ defined in equation (6.50) describes the feed-forward signals $\boldsymbol{\tau}^{(ff)}(t_n)$ for 3 independent experiments, as presented in equation (6.49). Each experiment is performed twice. The second time, the sign of all feed-forward inputs was reversed for reasons explained in paragraph 6.5.2. Furthermore, all experiments are repeated for 16 different phase realisations of the multi-sine. Therefore 96 experiments in total are simulated. During each simulation the signals $\boldsymbol{u}(t_n)$ and $\boldsymbol{y}(t_n)$ corresponding to the driving torques $\boldsymbol{\tau}^{(a)}$ and the drive angles $\boldsymbol{e}^{(m)}$, respectively, are sampled.

The identification technique used is based on the response of the system to periodic inputs. The model includes only a small amount of structural damping. Therefore it will take some time before the transients are damped out. For this reason, each simulation starts with an additional period, which is deleted from the data afterwards.

6.6.3 Identification of the nonparametric MFRF

After data processing in the time domain, namely the subtraction of two identical experiments with only an opposite sign of the feed-forward, the resulting signals are Fourier transformed. To improve the visibility of the (anti-)resonance frequencies in FRF plots, the Fourier spectra of the drive angles $\boldsymbol{e}^{(m)}$ are multiplied by $(j\omega_f)^2$, which are the corresponding imaginary frequencies squared. This is equivalent to differentiating the time domain signals twice with respect to time. As a result the outputs $\boldsymbol{y}$ represent the drive accelerations $\ddot{\boldsymbol{e}}^{(m)}$ instead of the drive angle $\boldsymbol{e}^{(m)}$ and $\mathbf{P}$ represents the relation between force and acceleration.

Next the input and output spectra of all experiments are mapped to a common phase realisation of the input spectra and the noise covariances of the stochastic noise and the stochastic nonlinearities are estimated.

The nonparametric estimation technique described in section 6.3 is used to estimate the MFRF of the robot model. Figure 6.4 shows the MFRF of the true open-loop model, linearised around the nominal configuration during motion, and the estimated model. Furthermore, the standard deviation for the estimated MFRF is presented. Figure 6.4 shows that the differences between the actual and estimated MFRF in the region around 40 Hz are relative large. Furthermore, these differences are larger than predicted by the standard deviation of the noise. So the bias error $\mathbf{P}^{(B)}(\omega_f)$ is larger than the errors originating from stochastic noise $\boldsymbol{Z}^{[m,o](v)}(\omega_f)$ and stochastic plant nonlinearities $\boldsymbol{Z}^{[o](s)}(\omega_f)$. In this simulation example an estimation of the bias error can easily be made, because the true plant model is known. In reality it is much more difficult to estimate the size of the bias error and only the stochastic errors are known. The figure shows that the stochastic errors do not always give a good indication of the actual accuracy of the estimated model.

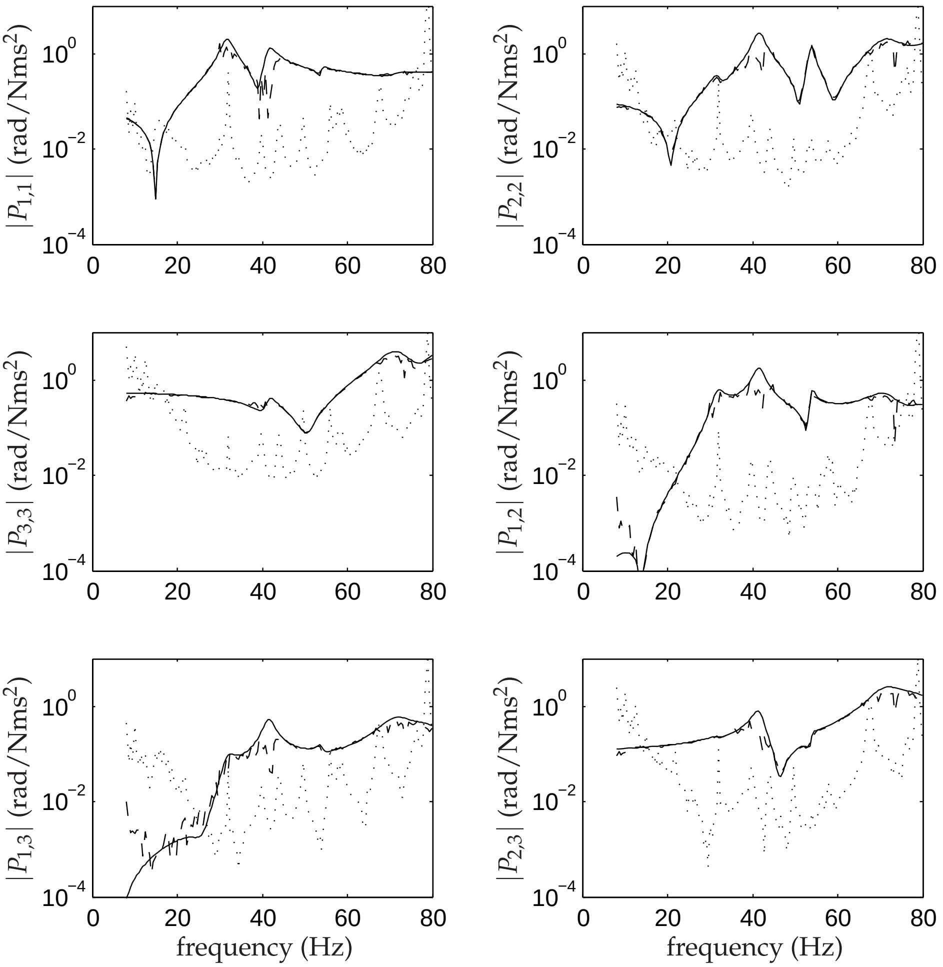

Figure 6.4: Estimated nonparametric MFRF of the simulation example. The figures show the true model (—), the estimated nonparametric model (- -) and the standard deviation $\sqrt{\hat{C}^{(\hat{G})}(\omega_f)}$ *of the estimated MFRF (· · ·).*

6.6.4 Identification of the parametric transfer functions

Next, parametric transfer functions are estimated using the maximum likelihood estimator described in section 6.3. The optimisation is performed on the excited frequency grid between 8 and 80 Hz. For lower frequencies, the signal to noise ratio is very low. The first interesting (anti-)resonance frequency is around 15 Hz. The estimated parametric model contains 12 common poles and 12 zeros for each joint separate. Furthermore, a symmetric model structure is estimated, so $P_{j,k}(s) = P_{k,j}(s)$. Note that 2 poles in $s \approx 0$, arising from rigid-body modes, are cancelled by the time differentiation of the outputs.

The iterated linear least square cost function with parametrisation (5.38) is used to obtain starting values for the maximum likelihood estimator. This parametrisation in particular results in a bad numerical condition for the estimation problem. Note that this parametrisation is required to obtain a linear estimator. As a result, the outcome of this estimation is very sensitive to the coefficient w in equation (6.41). The maximum likelihood estimator is a nonlinear optimisation problem, which requires sufficiently accurate initial values. Therefore, the coefficient w was varied between 0.2 and 2 and the best solution, according to the maximum likelihood cost function, has been used for the nonlinear optimisation.

The left-side plots of figure 6.5 show the true and estimated parametric MFRF for the simulation model. The figures on the right show the differences between the estimated parametric MFRF and the true MFRF, including its 95% confidence intervals. Although only the diagonal terms of the MFRF are presented, the off-diagonal terms are also included in the estimation. Because of bias errors, the differences between the estimated parametric MFRF and the MFRF for the true model are not within its 95% confidence interval. A comparison between the parametric and nonparametric MFRF shows that the parameterised MFRF has a slightly smaller bias error than the nonparametric MFRF.

The value of the objective function (6.35) is 1647. Based on the 95% uncertainty bounds of the objective function a value between 1404 and 1599 is expected. This indicates that some under-modelling is present and that the model order should be increased. The sample correlation of the residual, see equation (6.44), including the 95% confidence bounds are presented in figure 6.6. A significant peak for lag $l = 0$ can be seen, indicating that the residuals are uncorrelated. A closer look at the 95% confidence bounds of $\hat{\boldsymbol{R}}^{(\hat{\epsilon})}$ demonstrates that two of the residuals satisfy these bound. For output 1, 2 and 3 the percentages of samples within these bounds are are 95%, 85% and 97%, respectively. Therefore, the model does not pass this correlation test, although the differences are small. This also indicates that model errors remain and that the model order should be increased. However, the number of poles and zeros of the estimated model is already 2 more than that of the actual model in the estimated frequency range. The highest frequency of these two additional poles

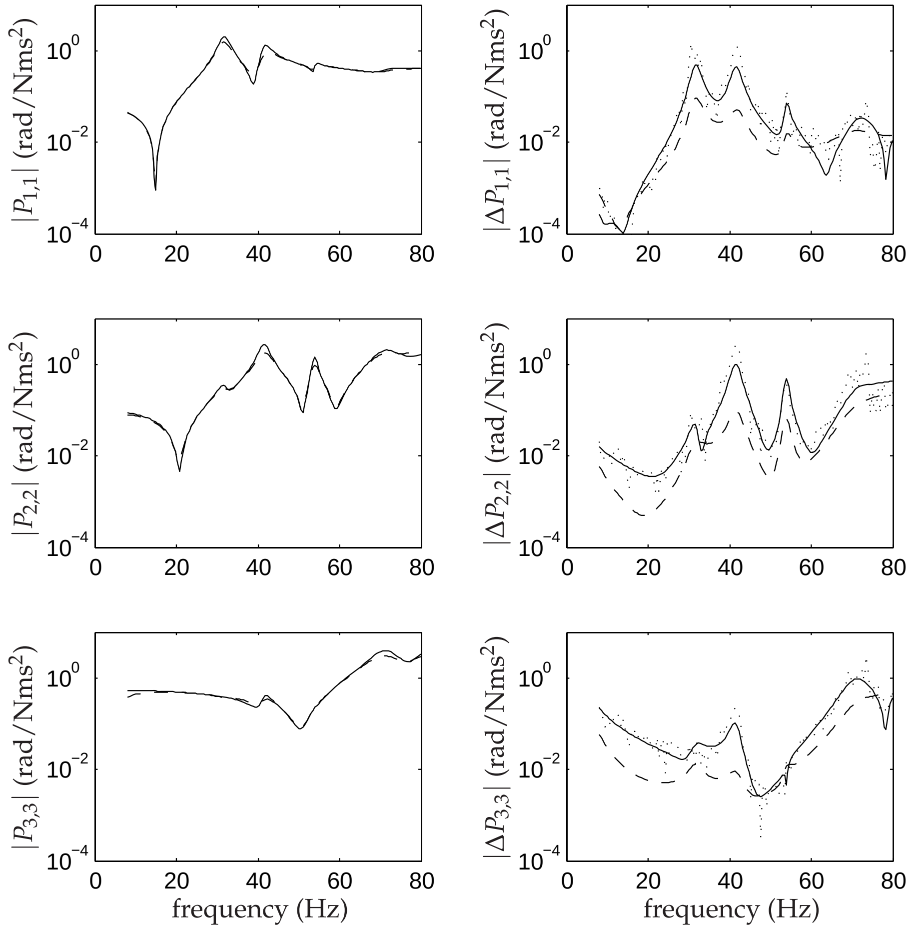

Figure 6.5: The figures on the left show the parametric estimate (- -) and the true model (—) of the simulation example. The figures on the right show the differences between the estimated nonparametric MFRF and the true model (· · ·) and the parametric MFRF and the true model (—). The 95% confidence interval of the parametric estimation is denoted by (- -).

and zeros is 5.1 Hz. Thus, these poles and zeros only affect the low frequency behaviour, where the data is very noisy.

The reasons for not passing the validation tests are the nonlinearities in the closed-loop system, leading to a bias term in the estimated models. Although in general the correlation test should not be sensitive to nonlinearities, this only applies if the true input $\boldsymbol{U}^{[o](0)}$ is an uncorrelated random multi-sine and

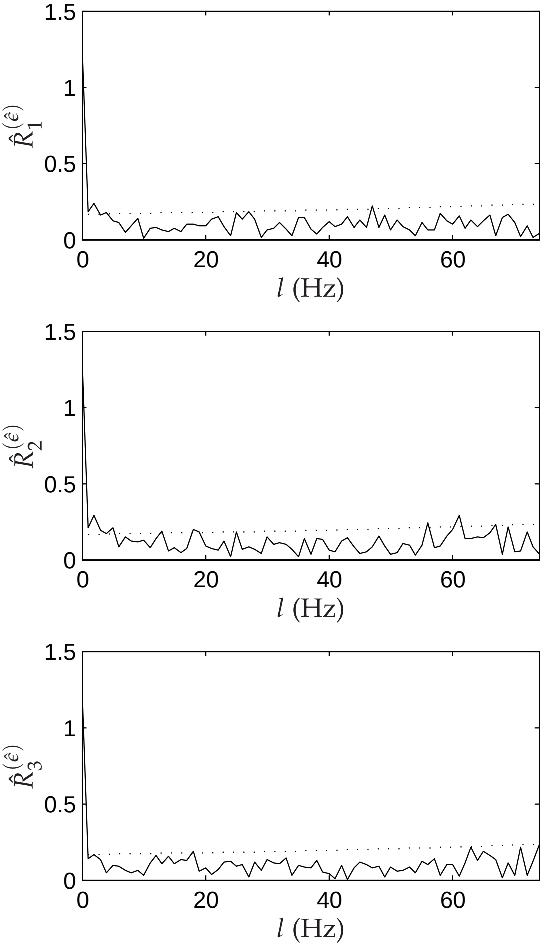

Figure 6.6: Correlation residuals of the simulation example. The 95% confidence bound is denoted by $(\cdots)$.

the number of frequencies $N^{(f)}$ go to infinity. An uncorrelated input signal is almost impossible, because the robot is a closed-loop system. As a result, the random multi-sine that is used as torque feed-forward $\boldsymbol{\tau}^{(ff)}$, is coloured by the sensitivity function before it is applied as input signal $\boldsymbol{U}^{[o](0)}$. Simulations showed that the averaging over different phase realisations of the multi-sine improves the random character of the nonlinearities in the averaged input and output signals.

Another reason for not passing the validation tests could be that only a local minimum has been found by the optimisation algorithm and not the global one. However, starting the nonlinear optimisation with the true model yields the same results as presented above. Therefore it is very likely that the global optimum is found.

The absolute value of the estimated poles $\hat{p}_r$ and zeros $\hat{z}_{j,k,r}$ of the multivariable transfer function $\hat{\mathbf{P}}(s)$ define the resonance frequencies ω and anti-resonance frequencies μ of the robot model, respectively. A comparison between the true values and estimated values is presented in table 6.1. The table shows only the flexible modes, the rigid-body modes of the true model and the two additional low frequency poles and zeros of the estimated model are omitted. The table shows that the maximum difference between the estimated and actual frequencies is 1.54 Hz. Furthermore, the lower (anti-)resonance frequencies are estimated more accurately than the highest. The reason for this is the limited number of data points for the highest (anti-)resonance frequencies.

6.6.5 Identification of the physical parameters

The identification procedure presented in section 5.8 in combination with the frequencies of table 6.1 yields an estimation of the drive parameters. Table 6.2 shows the estimated and true drive parameters of the simulation model and the difference between both. It can be seen that the order of magnitude is correct but that there are some considerable differences, especially for $k_1^{[2]}$, which is the drive stiffness of joint 1. One of the reasons for the estimation errors in table 6.2 is the errors in the estimated (anti-)resonance frequencies, as has been shown in table 6.1. Another reason is that the amount of estimated poles and zeros is too low, compared to the degrees of freedom of the robot model. A larger frequency spectrum, that covers all (anti-)resonance frequencies, should be used for the identification. However, the maximum frequency is limited by the sample rate of the data acquisition system. In section 5.9, table 5.2 it was found that a reduced number of (anti-)resonance frequencies leads to an underestimation of the parameters. Table 6.2 shows an overestimation of the drive inertias. This is caused by an underestimation of the low frequency amplitude for the estimated transfer functions, while in table 5.2 it is assumed that the low frequency amplitude is known exactly.

As a result the rigid mass matrix $\mathbf{M}_{ee}$, which is inverse proportional to the low frequency amplitude according to equation (5.51), has been overestimated as well. The entries of the estimated and true mass matrices $\mathbf{M}_{ee}$ are presented in table 6.3.

From the simulation results presented thus far, it must be concluded that the accuracy of the method is relatively low. Any conclusions about the amount of eigenfrequencies that can be identified will be addressed later in section 6.7, because this is only meaningful for experimental data.

r	$p_{(2r-1)}$	$\hat{p}_{(2r-1)}$	$\omega^{[r]}$	$\hat{\omega}^{[r]}$	$\lvert\omega^{[r]} - \hat{\omega}^{[r]}\rvert$	$\sqrt{\hat{C}^{(\omega)}}$
1	$-1.3 \pm 31.7j$	$-1.7 \pm 31.6j$	31.7	31.6	0.08	0.04
2	$-1.2 \pm 41.5j$	$-1.9 \pm 41.7j$	41.5	41.7	0.22	0.05
3	$-0.6 \pm 53.8j$	$-1.0 \pm 53.8j$	53.8	53.8	0.03	0.03
4	$-3.7 \pm 71.1j$	$-4.8 \pm 70.8j$	71.2	70.9	0.22	0.09
5	$-4.0 \pm 80.4j$	$-5.7 \pm 79.8j$	80.5	80.0	0.52	0.36

r	$z_{1,1,(2r-1)}$	$\hat{z}_{1,1,(2r-1)}$	$\mu_{1,1}^{[r]}$	$\hat{\mu}_{1,1}^{[r]}$	$\lvert\mu_{1,1}^{[r]} - \hat{\mu}_{1,1}^{[r]}\rvert$	$\sqrt{\hat{C}_{1,1}^{(\mu)}}$
1	$-0.1 \pm 14.9j$	$-0.1 \pm 14.9j$	14.9	14.9	0.00	0.01
2	$-0.7 \pm 39.0j$	$-1.5 \pm 39.1j$	39.0	39.1	0.12	0.07
3	$-0.5 \pm 53.6j$	$-0.9 \pm 53.6j$	53.6	53.6	0.02	0.03
4	$-3.5 \pm 70.1j$	$-4.3 \pm 70.1j$	70.2	70.2	0.02	0.15
5	$-4.1 \pm 79.9j$	$-6.1 \pm 79.4j$	80.0	79.7	0.39	0.43

r	$z_{2,2,(2r-1)}$	$\hat{z}_{2,2,(2r-1)}$	$\mu_{2,2}^{[r]}$	$\hat{\mu}_{2,2}^{[r]}$	$\lvert\mu_{2,2}^{[r]} - \hat{\mu}_{2,2}^{[r]}\rvert$	$\sqrt{\hat{C}_{2,2}^{(\mu)}}$
1	$-0.4 \pm 20.8j$	$-0.6 \pm 20.6j$	20.8	20.6	0.11	0.02
2	$-1.5 \pm 32.6j$	$-1.9 \pm 32.4j$	32.6	32.5	0.15	0.07
3	$-0.5 \pm 51.0j$	$-0.6 \pm 50.8j$	51.0	50.8	0.14	0.01
4	$-1.1 \pm 59.1j$	$-1.2 \pm 59.2j$	59.1	59.2	0.07	0.03
5	$-4.8 \pm 77.9j$	$-5.6 \pm 76.3j$	78.0	76.5	1.54	0.41

r	$z_{3,3,(2r-1)}$	$\hat{z}_{3,3,(2r-1)}$	$\mu_{3,3}^{[r]}$	$\hat{\mu}_{3,3}^{[r]}$	$\lvert\mu_{3,3}^{[r]} - \hat{\mu}_{3,3}^{[r]}\rvert$	$\sqrt{\hat{C}_{3,3}^{(\mu)}}$
1	$-1.3 \pm 31.7j$	$-1.6 \pm 31.5j$	31.7	31.5	0.17	0.05
2	$-1.4 \pm 40.4j$	$-2.2 \pm 40.8j$	40.5	40.8	0.39	0.06
3	$-1.6 \pm 50.4j$	$-1.7 \pm 50.4j$	50.4	50.4	0.01	0.04
4	$-0.6 \pm 53.9j$	$-1.1 \pm 53.8j$	53.9	53.8	0.05	0.04
5	$-2.9 \pm 77.2j$	$-3.9 \pm 76.3j$	77.2	76.4	0.78	0.42

Table 6.1: The estimated and true (anti-)resonance frequencies of the simulation model in Hz.

6.6.6 Analysis of the dominant nonlinearities

Simulations with a linearised time invariant manipulator and/or joint friction model have provided insight into the dominant nonlinearities of the closed-loop robot system. Two types of nonlinearities are considered separately: the nonlinearities introduced by the joint friction model, and the nonlinearities introduced by the manipulator model. Figure 6.7 shows the differences between the true MFRF and the MFRFs estimated from the simulated responses of partly linear time invariant (LTI) models. The MFRFs in figure 6.7 are estimated based on the simulated responses of one phase realisation of the multisine. The figure shows that for low frequencies, up to 40 Hz, joint friction is the most dominant nonlinear distortion. For higher frequencies the nonlinearities introduced by the manipulator also have an important influence on the accu-

	Drive inertia (kg m^2)			Drive stiffness $\times 10^5$ (N m rad^{-1})		
	$J^{[1](a)}$	$J^{[3](a)}$	$J^{[5](a)}$	$k_1^{[2]}$	$k_1^{[4]}$	$k_1^{[6]}$
true	3.10	1.31	0.79	2.80	2.70	1.00
estimated	3.25	1.50	0.79	1.49	2.16	0.98
difference	-0.15	-0.18	-0.01	1.31	0.54	0.02

Table 6.2: The estimated and true drive parameters of the simulation model.

	M_{e_1,e_1}	M_{e_2,e_2}	M_{e_3,e_3}	M_{e_1,e_2}	M_{e_1,e_3}	M_{e_2,e_3}
true	17.02	13.87	2.55	0.01	0.01	3.20
estimated	17.24	14.56	2.58	-0.00	-0.05	3.35
difference	-0.21	-0.69	-0.03	0.01	0.05	-0.15

Table 6.3: The estimated and true entries of mass matrix $\mathbf{M}_{ee}$ in kg m^2.

racy of the estimated MFRF. The differences between the estimated MFRF of the full linearised model and the true model are much smaller than the difference between the MFRF of the partly linearised model and the true model. This illustrates that the nonlinearities have a large influence on the accuracy of the obtained MFRF. The remaining error in figure 6.7 between the MFRF of the full linearised model and the MFRF of the true model is caused by the stochastic noise, nonlinearities in the feedback controller and the data sampling process.

6.6.7 Selection of the input matrix

The selection of input matrix $\mathbf{Y}^{(2)}$ over $\mathbf{Y}^{(1)}$ is illustrated with a simulation example. Based on simulated responses using both $\mathbf{Y}^{(1)}$ and $\mathbf{Y}^{(2)}$ a nonparametric identification has been done, based on one phase realisation of the multi-sine. The differences between the estimated and true model are presented in figure 6.8. The figure shows that input matrix $\mathbf{Y}^{(2)}$ gives more accurate results than $\mathbf{Y}^{(1)}$. However, the differences are very small.

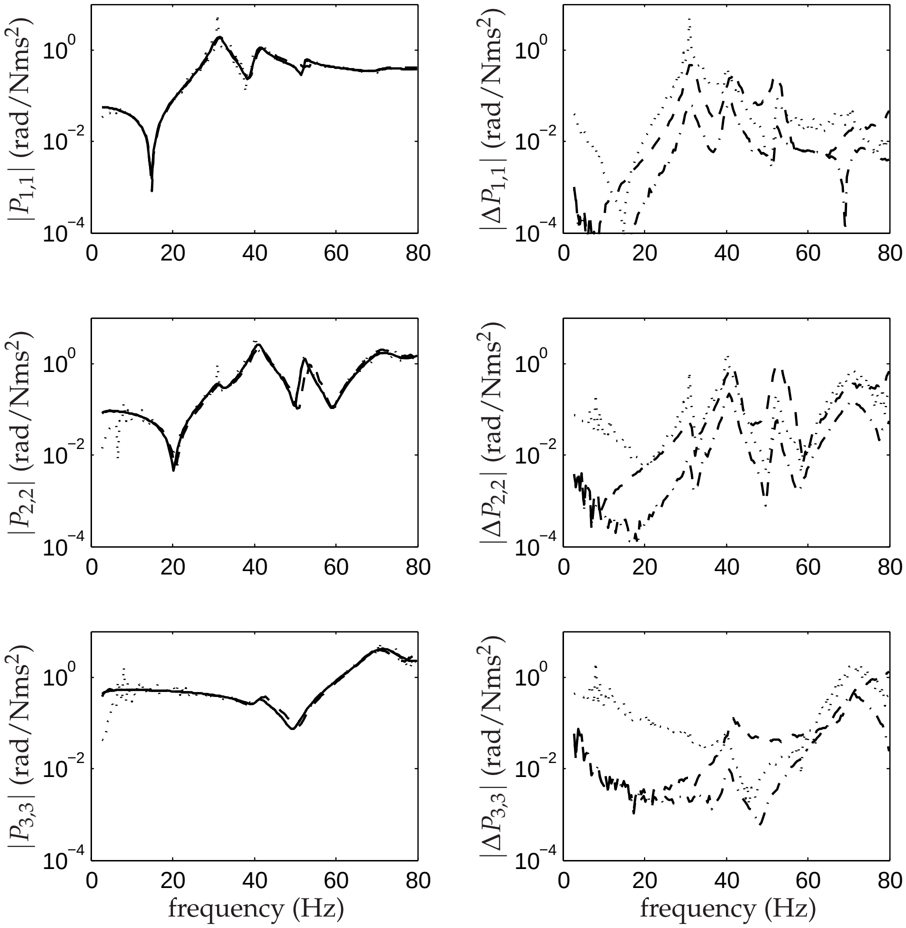

Figure 6.7: The figures on the left show the nonparametric MFRF of the robot model that is estimated on the simulated responses of an LTI manipulator and joint friction model (- · -). The MFRF of the true LTI model is represented by (—). The MFRF that is estimated on the responses of an LTI manipulator model and a nonlinear joint friction model is represented by (· · ·). The MFRF that is estimated on the responses of a nonlinear manipulator and an LTI joint friction model is represented by (- -). The differences between the estimated models and the true model are presented on the right.

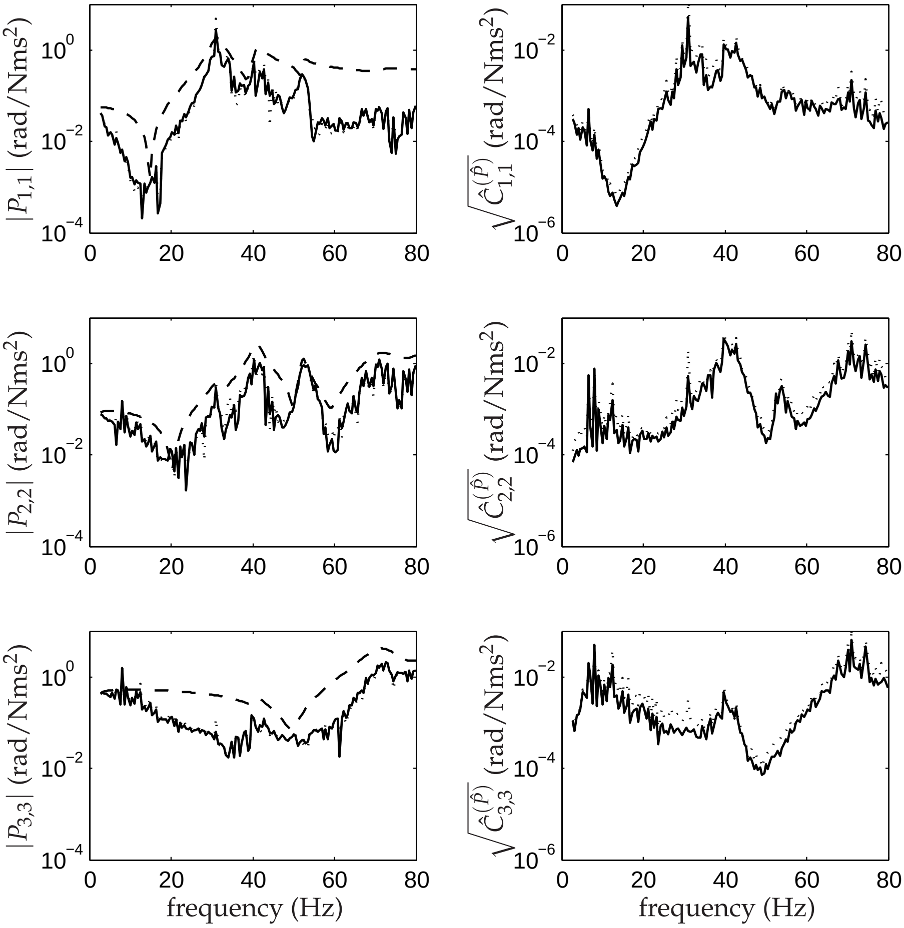

Figure 6.8: The figures on the left show the MFRF estimate for the true model (- -) and the difference between this model and the estimated model for an excitation specified by $\mathbf{Y}^{(1)}$ *(· · ·) and* $\mathbf{Y}^{(2)}$ *(—). The figures on the right show the standard deviation of the MFRF for both estimates.*

6.7 Experimental results

This section presents the experimental results of the Stäubli RX90B robot.

6.7.1 Experiment design

The experiments described with regard to the simulation example in section 6.6 have also been performed on the Stäubli RX90B, which resulted in a data set containing the input and output signals for 96 experiments.

The signals are normally sampled at 250 Hz. To check the presence of aliasing effects on the actual robot, one data set is captured at a higher sample rate of 2 kHz. Unfortunately, only a small set of data can be captured at this sample rate, making it unsuitable for identification. Fortunately, this data set showed that the amount of power above 125 Hz is very low. So aliasing is, in reality, not an issue and the data sampled at 250 Hz can be used for identification.

6.7.2 Data analysis

The input and output signals of two experiments with equal reference but opposite feed-forward are subtracted. The resulting signals are projected onto the same phase distribution (see section 6.2) and averaged afterwards. Next, the outputs are differentiated twice with respect to time and the covariances of the stochastic input and output noise including the nonlinear contributions is estimated. Figure 6.9 shows the average signal to noise ratios of the measurements for each joint. The signal to noise ratio is defined by the amplitude of the frequency spectrum divided by the standard deviation of the corresponding measurement noise. The figure shows that the signal to noise ratios are relative low, especially for the lower frequencies. In the output, the noise due to nonlinearities is dominant. However, the stochastic input noise is considerable as well.

Usually, the influence of nonlinearities can be reduced by decreasing the excitation level. Therefore, all experiments are repeated with a smaller multi-sine amplitude, namely 30 Nm instead of 45 Nm. The obtained signal to noise ratios are also presented in figure 6.9. A comparison between the signal to noise ratios of both excitation levels demonstrates that a decrease of excitation level does not decrease the influence of the nonlinearities. Actually, the overall signal to noise ratio is a bit decreased. This takes place because the stochastic signal to noise ratio is decreased. An improvement of the signal to noise ratio by taking the mean of experiments with different phase realisations of the multi-sine is possible. Therefore, a large set of experiments have been performed.

The averaging of two experiments with a switched sign of the feed-forward signal should reduce the influence of the nonlinearities. The signal to noise ratios of the data set with high excitation is compared to a data set without switching. The results are presented in figure 6.10. The switching should

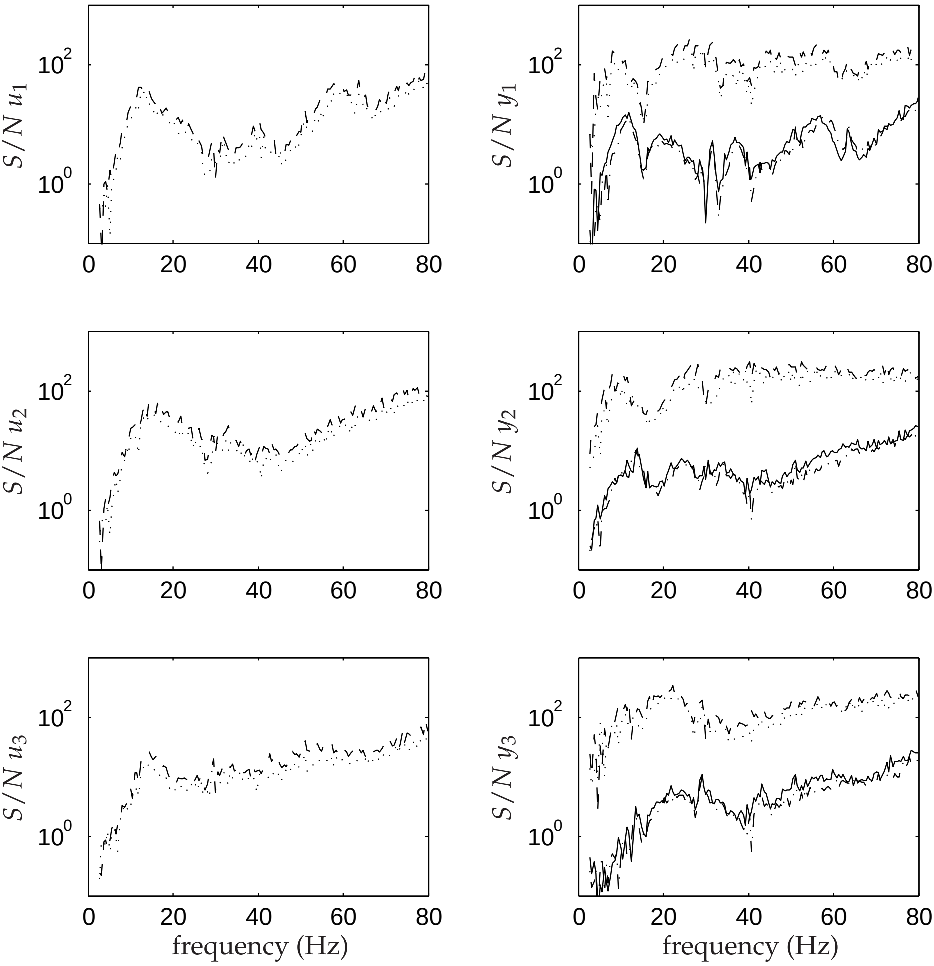

Figure 6.9: The left-hand and right-hand figures show the signal to noise ratios of the input and output signals, respectively. For the high excitation level the signal to noise ratio corresponding to the stochastic noise $\boldsymbol{Z}^{(v)}$ is denoted by (- -) and the nonlinear output noise $\boldsymbol{Y}^{(s)}$ is denoted by (—). For the low excitation level the signal to noise ratio corresponding to the stochastic noise $\boldsymbol{Z}^{(v)}$ is denoted by $(\cdots)$ and the nonlinear output noise $\boldsymbol{Y}^{(s)}$ is denoted by $(- \cdot -)$.

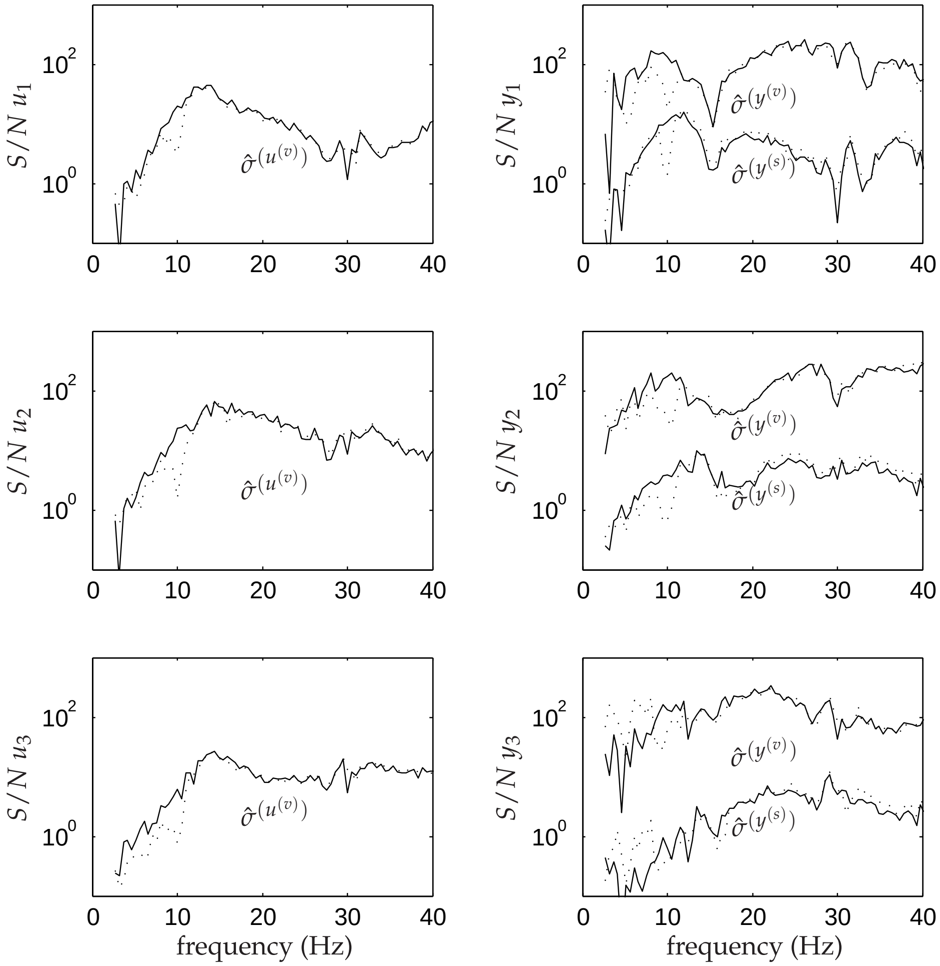

Figure 6.10: The left-hand and right-hand figures show the signal to noise ratios of the input and output signals, respectively. For the data set in which switching has been applied the signal to noise ratios are denoted by (—). For the non-switched data set the signal to noise ratios are denoted by $(\cdots)$.

cancel the low frequency nonlinear dynamics excited by the smoothed square wave. Consequently, the figure is zoomed in on the lower frequency range. The switched data set contains twice as many experiments, therefore the signal to noise ratios of the non-switched set are multiplied by $\sqrt{2}$. For joints 1 and 2 the switching does indeed improve the signal to noise ratios. However, for joint 3 the switching has a negative influence on the signal to noise ratios for the output signals. This makes sense because the switching aims to reduce the effect of the nonlinearities. However, the total input power is also reduced by the switching. As a result, the relative influence of the stochastic noise is increased.

6.7.3 Identification of the nonparametric MFRF

Next, the nonparametric MFRF $\mathbf{P}(\omega_f)$ and its 95% confidence intervals are estimated. The results are presented in figure 6.11. The confidence intervals of the MFRF introduced by the stochastic noise are given separately from the overall covariance intervals, which include stochastic and nonlinear contributions. The figure clearly shows that the variance due to nonlinearities is much larger than the stochastic contributions.

6.7.4 Identification of the parametric transfer functions

Using the averaged data sets, parameterised transfer functions are estimated. Initial models are estimated with the iterated least squares method, for varying values of weighting power w and varying model orders. The transfer functions are assumed to be symmetric, so $P_{j,k}(\omega_f) = P_{k,j}(\omega_f)$. Unfortunately, none of the estimated initial models could be used directly for the maximum likelihood estimation. All the estimated initial models contain one of more poles and zeros around 50 Hz. Because only the off-diagonal terms of the estimated MFRFs ($P_{j,k}(\omega_f)$ for $j \neq k$) show a high but narrow spike at this frequency, this is probably not a mechanical resonance frequency but is caused by the electronics. Furthermore, for high frequencies the estimated models also have poles and zeros with a real part larger than zero. It appears that these poles and zeros affect mainly the phase and not the amplitude of the estimated MFRF. Therefore it is expected that these high frequency poles are caused by the sampling process. For these reasons, the frequency range of the data set is restricted from 8 to 75 Hz and also data points around 50 Hz are removed. Next, one of the initial models is adapted by removing poles and zeros around 50 Hz and above 75 Hz. This resulted in an initial model containing 20 poles and zeros and an adapted data set for the nonlinear maximum likelihood optimisation.

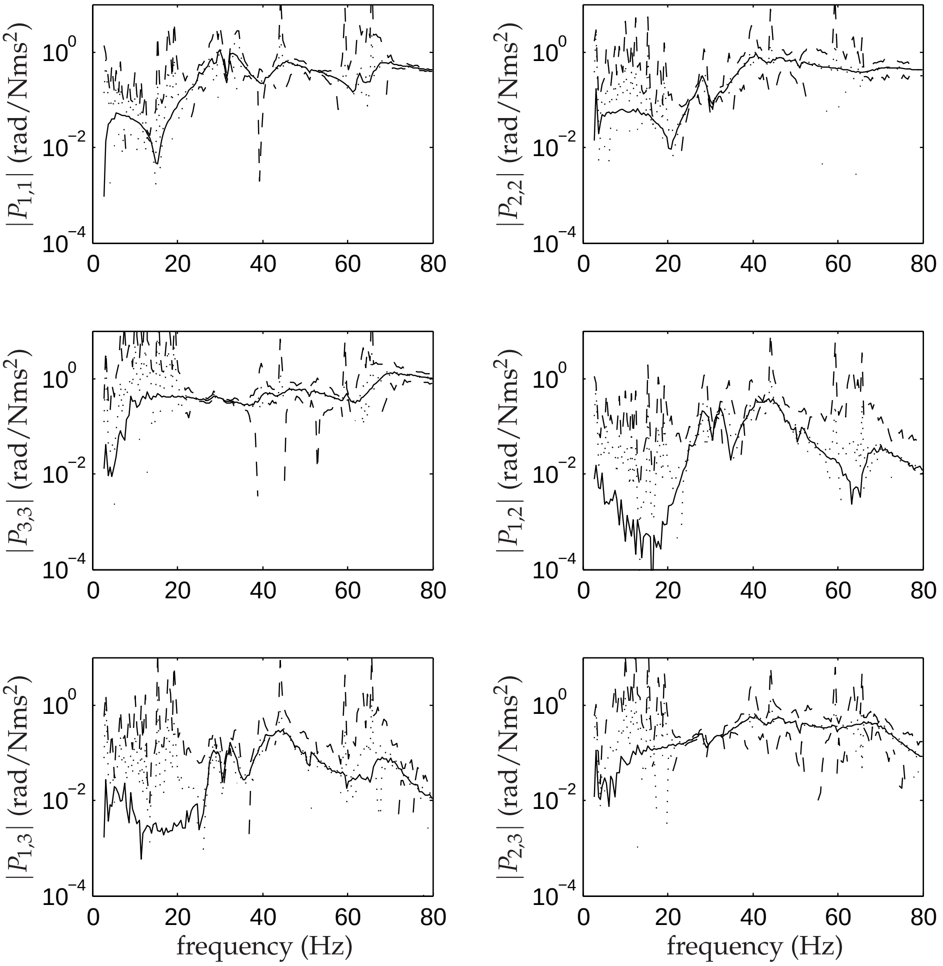

Figure 6.11: The figures show the MFRF (—) of the Stäubli RX90B estimated from experimental data. Also the 95% confidence levels, arising from only stochastic noise $\mathbf{Z}^{(v)}$ *(· · ·) and from stochastic and nonlinear noise* $\mathbf{Z}^{(v)} + \mathbf{Z}^{(s)}$ *are presented (- -).*

The estimated parametric and nonparametric MFRFs are presented in figure 6.12, including their 95% confidence intervals. The figure shows that the parametric MFRF is generally within the 95% confidence intervals of the nonparametric MFRF, except for $P_{1,1}(\omega_f)$ and $P_{2,2}(\omega_f)$ between the 35 and 50 Hz.

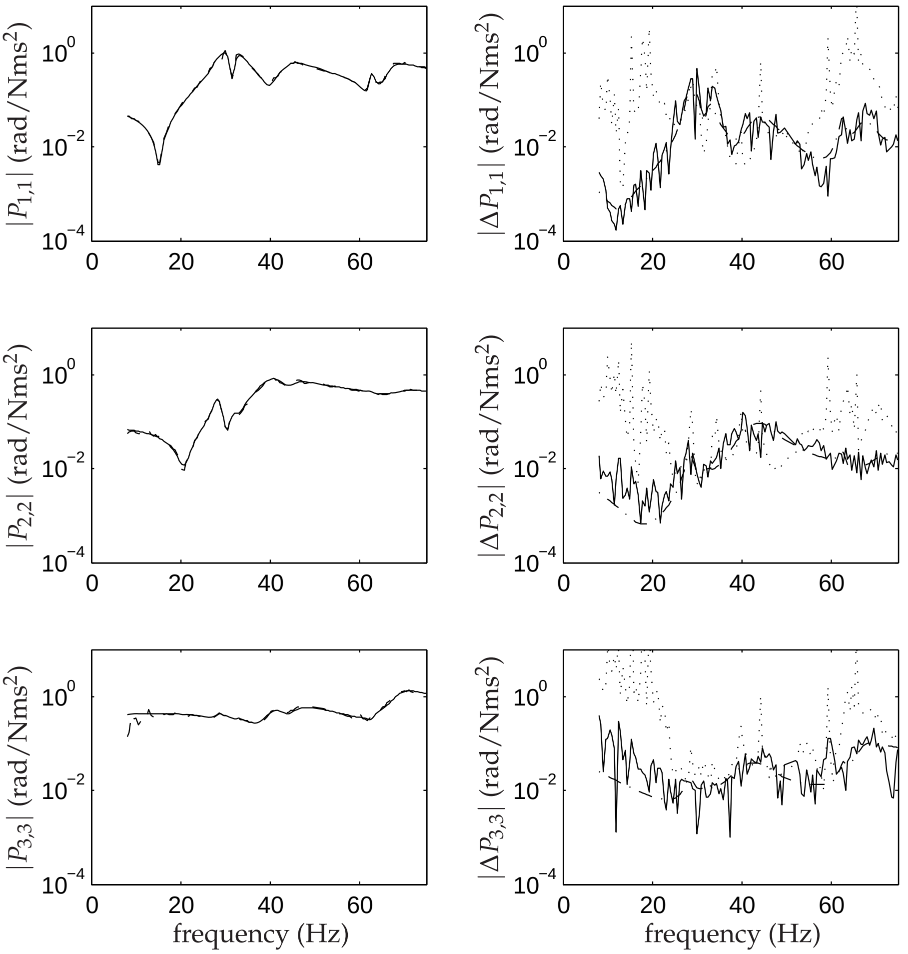

Figure 6.12: The figures on the left show the estimated nonparametric MFRF (- -) and the parametric MFRF (—) of the experimental data set. The figures on the right show the difference between the estimated parametric and nonparametric MFRF. The 95% confidence interval of the nonparametric and parametric estimation is denoted by $(\cdots)$ and $(- \cdot -)$, respectively.

The objective function (6.35) for the maximum likelihood estimation is 1649, which is outside the 95% confidence region given by 1231 - 1413. This indicates that the model order is too low. Figure 6.13 shows the correlation test for the residuals. A closer look shows that two of the outputs satisfy the 95% bound. For outputs 1, 2 and 3 the percentages of samples within this bound are 97%, 96% and 90%, respectively. The number of lags l of $R_3^{(\hat{\varepsilon})}(l)$ which exceeds the 95% bound is more than expected from the noise levels. However, the differences between the bound and the exceeding points is only small. A model containing 22 poles and zeros gives a slightly lower objective function, namely 1601. However, the correlation test gives the same values. Based on the results presented thus far, it is concluded that all the dynamics present in the measurement data are described by the model. Furthermore, it appears to be impossible to remove any poles or zeros without further violating the validation tests. For an 18 order model the correlation test gives 96%, 94% and 88%. Therefore it is concluded that 20 is the correct number of poles and zeros for this data set.

The estimated model contains two real poles: one at -7 Hz and one at 75.4 Hz. For $P_{1,1}(\omega_f)$, $P_{2,2}(\omega_f)$, $P_{3,3}(\omega_f)$ and $P_{2,3}(\omega_f) = P_{3,2}(\omega_f)$, these poles are more or less cancelled by two real zeros at the same frequencies. For the other off-diagonal terms $P_{1,2}(\omega_f) = P_{2,1}(\omega_f)$ and $P_{1,3}(\omega_f) = P_{3,1}(\omega_f)$ these poles are not cancelled. Furthermore, these transfer functions have zeros in the right half plane. These zeros cannot be explained by the model structure presented in chapter 3. Due to the low signal to noise ratio for these off-diagonal terms, these poles are probably originating from noise. Furthermore, there could be a small delay between the different joints, as all the joints have their own digital motion controller synchronised by a Sercos communication bus. This delay could force the model estimation to approximate this delay by introducing zeros into the right half plane. It is expected that all the complex poles and zeros in $P_{1,1}(\omega_f)$, $P_{2,2}(\omega_f)$, $P_{3,3}(\omega_f)$ and $P_{2,3}(\omega_f)$ correspond to actual vibration modes because none of the poles and zeros cancel and all have a negative real part. The complex poles and zeros and corresponding (anti-)resonance frequencies are presented in table 6.4, including their standard deviation.

6.7.5 Identification of the physical parameters

Using the parameter identification method presented in chapter 5 and the (anti-)resonance frequencies presented in table 6.4, the drive parameters and their standard deviation are estimated. Because 9 vibration modes are estimated, the identified parameters correspond to the model presented in chapter 3, which also has 9 vibration modes, namely 3 for each joint. The estimated parameters are presented in table 6.5. The standard deviation of the drive stiffness is considerably. Furthermore the table shows that the estimated drive stiffnesses are lower than the estimates presented in table 4.1, page 48. However, there might be some differences between both estimations, because the

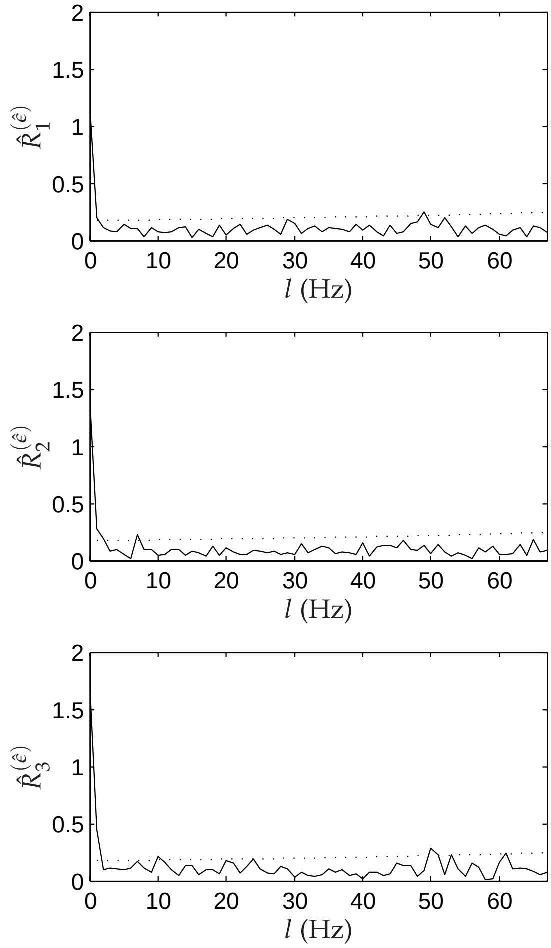

Figure 6.13: Correlation of the residuals for the experimental data set. The 95% confidence bound is denoted by ($\cdots$).

loading conditions are different and both estimates have considerable accuracy margins. The drive inertias are comparable with the values identified from the rigid identification experiments done by Waiboer (2007), see the 'true' values in table 6.2, page 106. Note that part of the transmission inertia, which in the rigid model is added to the drive inertia, in the flexible model is added to the link inertia, depending on the exact location of the drive stiffness. Therefore, the estimated drive inertias of the flexible model are lower than of the rigid model.

r	$\hat{p}_{(2r-1)}$	$\hat{\omega}^{[r]}$	$\sqrt{\hat{C}^{(\omega)}}$
1	$-0.8 \pm 28.3j$	28.4	0.02
2	$-1.3 \pm 30.2j$	30.3	0.10
3	$-1.3 \pm 32.5j$	32.5	0.08
4	$-3.5 \pm 40.8j$	41.0	0.10
5	$-3.2 \pm 44.6j$	44.7	0.08
6	$-0.6 \pm 62.5j$	62.6	0.04
7	$-18.5 \pm 61.4j$	64.1	1.55
8	$-2.3 \pm 67.1j$	67.1	0.17
9	$-3.9 \pm 69.2j$	69.3	0.42

r	$\hat{z}_{1,1,(2r-1)}$	$\hat{\mu}^{[r]}_{1,1}$	$\sqrt{\hat{C}^{(\mu)}_{1,1}}$
1	$-0.3 \pm 15.1j$	15.1	0.03
2	$-0.9 \pm 28.5j$	28.5	0.10
3	$-0.4 \pm 31.6j$	31.6	0.03
4	$-1.5 \pm 39.8j$	39.8	0.09
5	$-3.9 \pm 42.6j$	42.8	0.23
6	$-0.8 \pm 61.8j$	61.8	0.07
7	$-1.6 \pm 64.6j$	64.6	0.14
8	$-3.5 \pm 68.2j$	68.3	0.51
9	$-19.5 \pm 65.6j$	68.4	2.02

r	$\hat{z}_{2,2,(2r-1)}$	$\hat{\mu}^{[r]}_{2,2}$	$\sqrt{\hat{C}^{(\mu)}_{2,2}}$
1	$-1.0 \pm 20.7j$	20.8	0.03
2	$-1.6 \pm 29.5j$	29.5	0.12
3	$-0.5 \pm 30.4j$	30.4	0.04
4	$-1.0 \pm 32.9j$	33.0	0.06
5	$-1.9 \pm 43.9j$	44.0	0.15
6	$-0.6 \pm 62.6j$	62.6	0.04
7	$-22.9 \pm 61.5j$	65.7	2.01
8	$-2.5 \pm 66.9j$	66.9	0.23
9	$-3.5 \pm 68.2j$	68.3	0.48

r	$\hat{z}_{3,3,(2r-1)}$	$\hat{\mu}^{[r]}_{3,3}$	$\sqrt{\hat{C}^{(\mu)}_{3,3}}$
1	$-0.9 \pm 28.2j$	28.2	0.04
2	$-1.3 \pm 30.1j$	30.2	0.12
3	$-1.3 \pm 32.3j$	32.4	0.10
4	$-2.9 \pm 37.6j$	37.7	0.15
5	$-1.9 \pm 44.0j$	44.1	0.10
6	$-0.5 \pm 62.5j$	62.5	0.05
7	$-4.6 \pm 63.0j$	63.1	0.53
8	$-16.6 \pm 62.7j$	64.9	2.11
9	$-2.0 \pm 67.0j$	67.0	0.31

Table 6.4: The complex poles and zeros and corresponding (anti-)resonance frequencies in Hz, estimated using the experimental data set.

	Drive inertia (kg m^2)			Drive stiffness $\times 10^5$ (N m rad^{-1})		
	$J^{[1](a)}$	$J^{[3](a)}$	$J^{[5](a)}$	$k^{[2]}_1$	$k^{[4]}_1$	$k^{[6]}_1$
estimate	3.54	3.63	1.47	1.39	1.68	0.62
st. dev.	0.00	0.00	0.07	0.49	0.48	0.21

Table 6.5: The estimated drive parameters of the Stäubli RX90B robot manipulator, including their standard deviations.

According to equation (5.51) the identified transfer functions yields a prediction of the rigid mass matrix. In table 6.6 this estimate is compared to the results of Waiboer (2007). The latter are expected to be more accurate, since these results are based on dedicated low frequency identification experiments. However, no quantitative accuracy level is known for this estimate. Fortunately, the differences between both estimates are small, except for the coupling term M_{e_2,e_3}. Overall, the new frequency domain identification method gives reasonable results for the rigid mass matrix.

	M_{e_1,e_1}	M_{e_2,e_2}	M_{e_3,e_3}	M_{e_1,e_2}	M_{e_1,e_3}	M_{e_2,e_3}
flexible identification	17.16	15.03	2.54	-0.09	0.04	2.36
st. dev.	4.14	3.88	1.59	0.00	0.20	1.54
rigid identification	17.02	13.87	2.55	0.01	0.01	3.20
difference	-0.14	-1.16	0.00	0.10	-0.03	0.84

Table 6.6: The estimated entries of mass matrix $\mathbf{M}_{ee}$ *in kg* m^2*, including their standard deviation. Furthermore, the results of a rigid identification performed by Waiboer (2007) and the difference between both estimates are presented.*

6.8 Discussion

This chapter presented a MIMO errors in variables framework to identify Multivariable Frequency Response Functions of the Stäubli RX90B. The MFRF are parameterised by common denominator rational transfer functions, from which the robots resonance and anti-resonance can easily be extracted. Next, the inverse eigenvalue theory of chapter 5 is used to identify the drive parameters. To validate the identified transfer functions nonparametric identification methods have been presented as well. A lot of effort was put into including the nonlinearities in the errors in variables stochastic framework and the experimental design strategy. Both the simulation example and the experimental analysis have shown that this is indeed an important issue for the Stäubli RX90B.

The uncertainty of the results is mainly caused by the nonlinear distortions of the model. The validation of the models is also much more difficult because of these nonlinear distortions. Because the identification is applied to a closed-loop MIMO system, for which it is difficult to perform several random excitations with a constant power spectrum, the 'standard' validation techniques, such as the residual correlation test and the value of the objective function, do not give reliable results. A finer frequency grid than that has been used thus far, would simplify the validation. For a fine frequency grid it is easier to distinguish between the smooth behaviour of the true model and the noisy behaviour of the stochastic noise and the stochastic nonlinear distortions. At the moment, the frequency grid is limited by the buffer size of the data acquisition system and the total measurement time.

Simulations showed that the predicted accuracy of the estimated transfer functions is overestimated because of bias errors. However, the predicted accuracy margins give at least an indication of the accuracy level of the estimated transfer functions and drive parameters.

If the number of (anti-)resonance frequencies that can be extracted from the experimental setup is too low compared to the assumed model structure, like in the simulation example, a reduction of the number of lumped stiffnesses would be a logical step. Although this may be possible for linear models, it is hard to decrease the order of the nonlinear system without affecting the static behaviour. Therefore, it is important to estimate all the (anti-)resonance frequencies for the nonlinear model.

In general, the frequency domain parameter identification approach presented in this and the previous chapter gives much more insight into the behaviour of the manipulator than the linear least squares method from section 4.2. Instead of one large fit that is either correct or incorrect, the frequency domain approach estimates transfer functions describing the dynamic behaviour for each drive separately. The proposed method is much more involved than the linear least squares method, but the intermediate results, like the transfer functions, are also very useful for analysing the dynamic behaviour.

The experimental analysis showed that the number of modes that can be extracted from the data set is in agreement with the number of modes of the linearised robot model. The estimated accuracy as a result of measurement noise and stochastic nonlinear distortions is rather low for the drive stiffness $k_1^{[k+1]}$ and rigid mass matrix $\mathbf{M}_{ee}$. A comparison of the estimated stiffness parameters with the estimates from the static identification does not give any reason to reject the parameter estimates, as the estimated accuracy intervals for both estimates are substantial. The identification method gives reasonable estimates for the rigid mass matrix $\mathbf{M}_{ee}$, although dedicated rigid identification experiments probably give more accurate results. The accuracy of the drive inertias $J^{[k](a)}$ is much better. Furthermore, for the estimated drive inertias no representative other values are available. Overall, the results demonstrate the abilities of the proposed method.

Chapter 7

Conclusions and discussion

In this chapter, the conclusions from the preceding chapters will be summarised. Next, recommendations for further research will be presented.

7.1 Conclusions

This thesis presented modelling and identification techniques that have been developed for the realistic dynamic simulation of industrial robots. The key to accurate dynamic simulation lies in the availability of a model structure with a set of appropriate dynamic parameters that model the relevant physical phenomena of the robot correctly. It has been shown that for the Stäubli RX90B the joint and drive flexibilities are of the same order of magnitude. The modelling of robots with both joint and drive flexibilities has not received much attention in literature so far.

- In this thesis a robot model is presented, which includes both joint and drive flexibilities. The equations of motion are derived using a nonlinear finite element method. Dynamic behaviour arising from inertia and gravitational forces, flexibilities, structural damping, joint friction and a gravity compensating spring, which are all present in the Stäubli RX90B, are included in the model. Furthermore, closed-loop simulations can be carried out with a model of the actual CS8 motion controller.

- A new lumped mass formulation is presented, which includes a vector to describe the centre of mass of an element with respect to one of the element nodes. The introduction of this vector enables a parameter linear formulation of the equations of motion, which facilitates the parameter identification procedure. Furthermore the number of elements and, as a result, the computation time can be reduced, because no additional element is required to describe the centre of mass of a link.

The identification of rigid robot models is a research area that is mostly covered and for which standard techniques are available. The identification of flexible robot models is less common and no standard techniques are available.

- The model structure presented in his work is appropriate for a linear least squares identification technique. Simulations showed that this technique is capable of estimating the dynamic parameters for the flexible robot model, provided that all degrees of freedom can be measured, i.e. drive angles and flexible deformations.
- The main issue when identifying flexible models is the lack of sensors, because with regard to industrial robots usually only the motor rotations are measured. In this work it has been attempted to compute the elastic deformations of the Stäubli RX90B from the relative displacement between two links. This displacement is measured with a Krypton Rodym 6D camera system. Unfortunately, it appeared that this measurement system is unsuitable for measuring the small elastic deformations, because the absolute accuracy is too low. The joint and drive deformations are expressed in a local coordinate frame attached to one of the corresponding links. The specification of these local frames with respect to the base frame of the measurement system is too inaccurate as well. The specification of local frames to express the joint deformations with respect to a global coordinate frame is always an issue when measuring the joint deformations. This applies not only to camera systems, but for other external sensors as well. This is the case especially if the small joint deformations are computed from large and absolute link measurements.

Because the time domain linear least squares method did not succeed for our application, a frequency domain inverse eigenvalue identification method is proposed.

- Simulations showed that the drive inertia and drive stiffness parameters of the nonlinear robot model can be identified with this identification method, provided that all resonance and anti-resonance frequencies for the drives are accurately known.
- Although only drive parameters can be identified, the identification method can be applied to robots with both drive and joint flexibilities.
- It is shown that a normalisation of the eigenvectors with respect to the mass matrix leads to explicit relationships for the mass and stiffness matrix as function of the eigenvalues and eigenvectors. These relationships enable a physical interpretation of a thus far implicitly defined scaling factor in the MFRF of a undamped mechanical system. As a result, it can be shown that the low and high frequency amplitudes of the MFRF converge to the inverse of the rigid mass matrix $\tilde{\mathbf{M}}_{ee}$ and the full mass matrix $\tilde{\mathbf{M}}$, respectively.

The identification method requires a full set of (anti-)resonance frequencies for each joint. The use of frequency domain system identification techniques to extract the (anti-)resonance frequencies from experimental data has been proposed.

- The errors in variables framework is an appropriate description of the measurement conditions for the Stäubli RX90B robot. Firstly, because of the occurrence of a considerable amount of stochastic noise on the input. Secondly, because of correlated stochastic input and output noise as a result of closed-loop experiments. Thirdly, because of the large stochastic nonlinear distortions.

- The robot nonlinearities appear to have a large influence on the reliability of the estimated linear model. Therefore, to include the stochastic nonlinear distortions in the noise model and apply data averaging techniques, sufficient different random phase realisations should be measured.

- In general, the iterated weighted least squares method does not provide a sufficiently accurate initial value for the maximum likelihood estimator. Therefore, different weighting factors and some manual pole and zero manipulation are required.

- The maximum likelihood estimator enables quantitative validation methods to evaluate the accuracy of the estimated MFRF, the (anti-)resonance frequencies and the drive parameters.

- The inverse eigenvalue identification method is rather complex and the model computation very time consuming. However, this frequency domain method gives much more insight into the robot dynamics than the linear least squares method. Instead of one large fit, the frequency domain approach estimates transfer functions describing the dynamic behaviour for each drive separately. These transfer functions are already very useful for analysing the dynamic behaviour.

- The number of modes that can be identified from experimental data is in agreement with the number of modes of the proposed model structure. The estimated accuracy as a result of measurement noise and stochastic nonlinear distortions is rather low for the rigid mass matrix $\mathbf{M}_{ee}$ and the drive stiffness $k_1^{[k+1]}$. The estimated accuracy for the drive inertia $J^{[k](a)}$ is very reasonable. In addition, a comparison with other estimates does not give any reason to reject the parameter estimates or the model structure. These results prove the ability of the proposed method.

7.2 Discussion and recommendations

This thesis was focussed on the joint and drive flexibilities of the Stäubli RX90B. To further improve the accuracy of the simulation model, more aspects should be included. The floor and the mounting of the robot on the floor are not infinitely stiff. An appropriate model extension to describe this flexibility could be two orthogonal bending stiffnesses between the floor and the pillar on which the robot is mounted. Static measurements have shown that the corresponding stiffnesses are in the order of 1.2×10^7 N m rad^{-1}. This is much larger than the measured joint and drive stiffnesses and therefore not included in the model thus far. However, for higher frequency ranges or an increase in the total mass due to an additional payload, this stiffness may influence the dynamic behaviour of the robot and should be included in the model.

Another model extension would be the inclusion of drive nonlinearities, leading to a drive angle dependent gear ratio. Scheringa (2006) showed that these drive nonlinearities are present in the Stäubli RX90B. However, more research is required to measure and model the kinematic relations and include these in the nonlinear finite element model. It would be very interesting to investigate the effects of these nonlinearities on the tip motion of the robot, as the drive nonlinearities will excite the flexibilities in the robot model.

The model of the CS8 motion controller introduces and excites a lot of high frequency dynamics in closed-loop simulations of the robot. This gives aliasing problems during sampling and leads to a very small integration time step during simulation. It appears that these aliasing problems are not present in reality. Therefore it is worthwhile to check the correctness and implementation of the controller model.

Further research is also required with regard to parameter identification techniques for flexible robots. Thus far the inverse eigenvalue technique only provides the drive inertia and drive stiffness. The real parts of the estimated poles and zeros contain information about the damping of the system. It would be useful to exploit this information for an inverse eigenvalue problem including damping.

In order to estimate the remaining parameters of the model, other identification experiments should be performed. A unique estimate of all the parameters can only be obtained using external measurements, from which the elastic joint and drive deformations can be reconstructed. Orientating measurements have shown that acceleration sensors are able to measure the small vibrations of the robot. Research should be done to extract the physical coordinates of the nonlinear model from several acceleration measurements. A frequency domain version of the linear least squares method presented in section 4.2 is suggested to identify the parameters. As it is very hard to obtain accurate absolute position measurements from acceleration sensors, a frequency domain method is more appropriate than the time domain method.

To improve the signal to noise ratios of the measurement signals, more research should be done on the design of the excitation signals. In first instance, an increase of the amplitude of the feed-forward signal $\boldsymbol{\tau}^{(ff)}$ could be an option. Second, the designed feed-forward signal could be compensated by the closed-loop sensitivity function, so that the actual input $\boldsymbol{u}$ is white instead of the feed-forward signal $\boldsymbol{\tau}^{(ff)}$. Third, the maximum amplitudes could be varied for each joint, depending on its maximum driving torque. As already mentioned, a finer frequency grid is also advisable in order to simplify the validation of parametric models.

Appendix A

Spatial finite elements

A.1 Spatial truss element

The position of the slider truss element is determined by the position vectors $\boldsymbol{x}^{(p)}$ and $\boldsymbol{x}^{(q)}$ of the end nodes p and q, see figure A.1. The vector of nodal coordinates for the truss element is then expressed by $\boldsymbol{x}^{(k)} = (\boldsymbol{x}^{(p)}, \boldsymbol{x}^{(q)})$. These six Cartesian coordinates describe the position of the truss element relative to the fixed inertial coordinate axes (x, y, z). A possible rotation of the element around the axis pq is not involved in the description of the element position. The element thus has five degrees of freedom, which give rise to a single deformation mode, associated with the elongation of the element. This elongation can be expressed as a function of the instantaneous values of the position coordinates $(x_i^{(p)}, x_i^{(q)})$ and the reference length $l_0^{[k]}$ of the element. The elongation of the truss element is defined by

$$e_1^{[k]} = \mathcal{D}_1^{[k]}(\boldsymbol{x}^{[k]}) = l^{[k]} - l_0^{[k]}, \tag{A.1}$$

in which $l^{[k]}$ is the actual length of the element, which is determined by the instantaneous distance between the nodes p and q, that is:

$$l^{[k]} = ||\boldsymbol{x}^{(p)} - \boldsymbol{x}^{(q)}||. \tag{A.2}$$

A.2 Lambda element

Although the λ-element is not a real structural element, the way in which it is used in the theory justifies its presentation as an element. According to Euler, an arbitrary rotation can always be described as a rotation around a certain axis

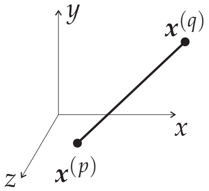

Figure A.1: The spatial truss element

$\boldsymbol{n}_\phi$ at certain angle ϕ. The set of Euler parameters that describes this rotation forms the unit quaternion

$$\begin{bmatrix} \lambda_0 \\ \boldsymbol{\lambda}_\phi \end{bmatrix}, \tag{A.3}$$

which is defined as:

$$\lambda_0 = \cos\left(\frac{\phi}{2}\right), \tag{A.4a}$$

$$\boldsymbol{\lambda}_\phi = \begin{bmatrix} \lambda_1 \\ \lambda_2 \\ \lambda_3 \end{bmatrix} = \boldsymbol{n}_\phi \sin\left(\frac{\phi}{2}\right). \tag{A.4b}$$

Rotations described in terms of Euler parameters are only real rotations if they satisfy the constraint equation

$$\lambda_0^2 + \lambda_1^2 + \lambda_2^2 + \lambda_3^2 = 1, \quad \text{or} \quad \boldsymbol{\lambda}^T \boldsymbol{\lambda} = 1. \tag{A.5}$$

Let the deformation function for the λ-element be defined as

$$e^{[k]} = \mathcal{D}^{[k]} = \boldsymbol{\lambda}^T \boldsymbol{\lambda} - 1. \tag{A.6}$$

Consequently the constraint condition for the Euler parameters is of a similar form as the un-deformability condition $e^{[k]} = 0$ for the λ-element. For each set of Euler parameters used in the robot model a λ-element is added to the list of elements with the condition that the deformation modes belonging to the λ-elements must be zero.

A.3 Spatial hinge element

The spatial hinge element illustrated in figure A.2 describes the relative rotation between nodes p and q. The hinge element was introduced by Werff (1983). Later on, Geradin et al. (1986) presented the expressions for the deformations

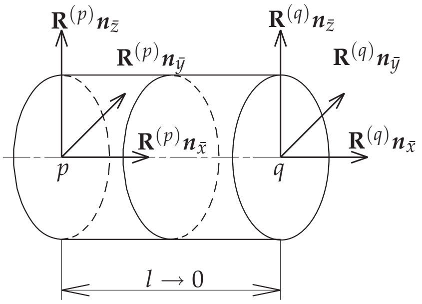

Figure A.2: Spatial hinge element

in their present form. The formulation presented below is taken from Waiboer (2007).

Using the Euler parameters, the vector of nodal coordinates for the hinge element is expressed as

$$\boldsymbol{x}^{[k]} = \begin{bmatrix} \boldsymbol{\lambda}^{(p)} \\ \boldsymbol{\lambda}^{(q)} \end{bmatrix} = \begin{bmatrix} \lambda_0^{(p)} & \lambda_1^{(p)} & \lambda_2^{(p)} & \lambda_3^{(p)} & | & \lambda_0^{(q)} & \lambda_1^{(q)} & \lambda_2^{(q)} & \lambda_3^{(q)} \end{bmatrix}^T. \tag{A.7}$$

The configuration of the hinge element is then described by the two sets of Euler parameters $\boldsymbol{\lambda}^{(p)}$ and $\boldsymbol{\lambda}^{(q)}$ describing the orientation of the orthogonal triads $(\boldsymbol{n}_{\bar{x}}^{(p)}, \boldsymbol{n}_{\bar{y}}^{(p)}, \boldsymbol{n}_{\bar{z}}^{(p)})$ and $(\boldsymbol{n}_{\bar{x}}^{(q)}, \boldsymbol{n}_{\bar{y}}^{(q)}, \boldsymbol{n}_{\bar{z}}^{(q)})$ rigidly attached to nodes p and q. Note that nodes p and q coincide and that initially their orientation is identical. The relative rotation of the triad $(\boldsymbol{n}_{\bar{x}}^{(q)}, \boldsymbol{n}_{\bar{y}}^{(q)}, \boldsymbol{n}_{\bar{z}}^{(q)})$ with respect to the triad $(\boldsymbol{n}_{\bar{x}}^{(p)}, \boldsymbol{n}_{\bar{y}}^{(p)}, \boldsymbol{n}_{\bar{z}}^{(p)})$ is described by the set of Euler parameters $\boldsymbol{\lambda}^{(r)}$ which is obtained from the quaternion product (Geradin et al. (1986))

$$\boldsymbol{\lambda}^{(p)} \circ \boldsymbol{\lambda}^{(r)} = \boldsymbol{\lambda}^{(q)}, \tag{A.8}$$

in which

$$\boldsymbol{\lambda}^{(p)} \circ \boldsymbol{\lambda}^{(r)} = (\lambda_0^{(p)}\lambda_0^{(r)}, -\boldsymbol{\lambda}_{\phi}^{(p)} \cdot \boldsymbol{\lambda}_{\phi}^{(r)}, \lambda_0^{(p)}\boldsymbol{\lambda}_{\phi}^{(r)} + \lambda_0^{(r)}\boldsymbol{\lambda}_{\phi}^{(p)} + \boldsymbol{\lambda}_{\phi}^{(p)} \times \boldsymbol{\lambda}_{\phi}^{(r)}). \tag{A.9}$$

Multiplying both sides of equation (A.9) with the adjoint quaternion $\bar{\boldsymbol{\lambda}}^{(p)}$, which is defined as

$$\bar{\boldsymbol{\lambda}}^{(p)} = \begin{bmatrix} \lambda_0^{(p)} \\ -\boldsymbol{\lambda\phi}^{(p)} \end{bmatrix}, \tag{A.10}$$

yields the expression for the relative rotation r of node q with respect to node p

$$\boldsymbol{\lambda}^{(r)} = \bar{\boldsymbol{\lambda}}^{(p)} \circ \boldsymbol{\lambda}^{(q)}. \tag{A.11}$$

This is a relative rotation expressed in the global reference frame. Usually the hinge is initially oriented according to the local reference frame $(\boldsymbol{n}_{\bar{x}}^{(p)}, \boldsymbol{n}_{\bar{y}}^{(p)}, \boldsymbol{n}_{\bar{z}}^{(p)})$. Expressing the relative rotation $\boldsymbol{\lambda}^{(r)}$ in this local reference frame yields

$$\boldsymbol{\lambda}'^{(r)} = (\lambda_0^{(r)}, \boldsymbol{\lambda}_\phi^{(r)} \cdot \boldsymbol{n}_{\bar{x}}^{(p)}, \boldsymbol{\lambda}_\phi^{(r)} \cdot \boldsymbol{n}_{\bar{y}}^{(p)}, \boldsymbol{\lambda}_\phi^{(r)} \cdot \boldsymbol{n}_{\bar{z}}^{(p)}). \tag{A.12}$$

The hinge element has a total of eight nodal coordinates. As a rigid body the element has three degrees of freedom and with two constraint deformation modes for the Euler parameters (equation (A.6)) this leaves a total of three deformation modes. The deformation modes of the hinge element are expressed as

$$\text{relative rotation}: e_1^{[k]} = \mathcal{D}_1^{[k]}(\boldsymbol{x}^{[k]}) = 2\arctan\left(\frac{\lambda_1'^{(r)}}{\lambda_0'^{(r)}}\right), \tag{A.13a}$$

$$\text{bending}: \epsilon_2^{[k]} = \mathcal{D}_2^{[k]}(\boldsymbol{x}^{[k]}) = 2(\lambda_0'^{(r)}\lambda_2'^{(r)} - \lambda_1'^{(r)}\lambda_3'^{(r)}), \tag{A.13b}$$

$$\epsilon_3^{[k]} = \mathcal{D}_3^{[k]}(\boldsymbol{x}^{[k]}) = 2(\lambda_1'^{(r)}\lambda_2'^{(r)} + \lambda_0'^{(r)}\lambda_3'^{(r)}). \tag{A.13c}$$

The first torsional deformation mode $e_1^{[k]}$ represents a large relative rotation around the joint axis $\boldsymbol{n}_{\bar{x}}$. Bending mode $\epsilon_2^{[k]}$ represents a bending deformation of the main axis $\boldsymbol{n}_{\bar{x}}^{(q)}$, into the negative $\boldsymbol{n}_{\bar{z}}^{(p)}$ direction. Bending mode $\epsilon_3^{[k]}$ represents a deformation of the main axis into the positive $\boldsymbol{n}_{\bar{y}}^{(p)}$ direction.

A.4 Spatial beam element

Figure A.3 shows the spatial beam element in an (x, y, z) inertial coordinate system. The configuration of the element is determined by the vectors $\boldsymbol{x}^{(p)}$ and $\boldsymbol{x}^{(q)}$ of the end nodes and the angular orientation of orthogonal triads $(\boldsymbol{n}_{\bar{x}}, \boldsymbol{n}_{\bar{y}}, \boldsymbol{n}_{\bar{z}})$ rigidly attached to each end point. In the undeflected state, the triads coincide with the axis pq and the principle axes of its cross-section. The angular orientation of the triads at either end point with respect to their initial (undeflected) orientation is specified by rotation matrices $\mathbf{R}^{(p)}$ and $\mathbf{R}^{(q)}$. If the beam is rigid then the rotation matrices are identical and in the initial undeflected state they are equal to the identity matrix.

Therefore, the vector of nodal coordinates for the beam element using Euler parameters is given by $\boldsymbol{x}^{[k]} = (\boldsymbol{x}^{(p)}, \boldsymbol{\lambda}^{(p)}, \boldsymbol{x}^{(q)}, \boldsymbol{\lambda}^{(q)})$. With the vector $\boldsymbol{l}^{[k]} = \boldsymbol{x}^{(q)} - \boldsymbol{x}^{(p)}$, the deformation functions of the beam element can now be

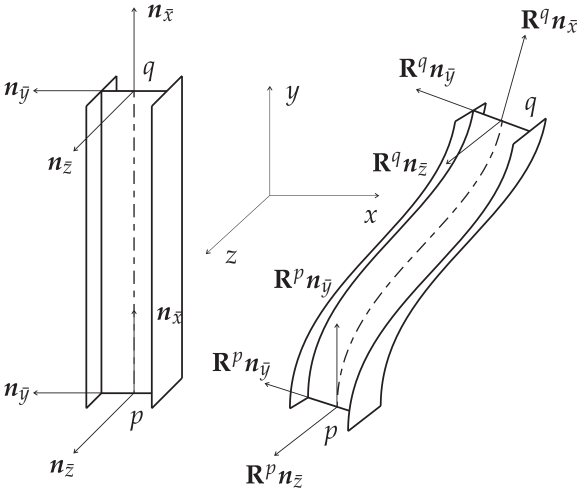

Figure A.3: The spatial beam element

written as follows (Besseling (1982)):

$$\text{elongation}: \epsilon_1^{[k]} = \mathcal{D}_1^{[k]} = \|\boldsymbol{l}^{[k]}\| - l_0^{[k]}, \tag{A.14a}$$

$$\text{torsion}: \epsilon_2^{[k]} = \mathcal{D}_2^{[k]} = [(\mathbf{R}^{(p)}\boldsymbol{n}_{\bar{z}}, \mathbf{R}^{(q)}\boldsymbol{n}_{\bar{y}}) - (\mathbf{R}^{(p)}\boldsymbol{n}_{\bar{y}}, \mathbf{R}^{(q)}\boldsymbol{n}_{\bar{z}})]l_0^{[k]}/2, \tag{A.14b}$$

$$\text{bending}: \epsilon_3^{[k]} = \mathcal{D}_3^{[k]} = -(\mathbf{R}^{(p)}\boldsymbol{n}_{\bar{z}}, \boldsymbol{l}^{[k]}), \tag{A.14c}$$

$$\epsilon_4^{[k]} = \mathcal{D}_4^{[k]} = (\mathbf{R}^{(q)}\boldsymbol{n}_{\bar{z}}, \boldsymbol{l}^{[k]}), \tag{A.14d}$$

$$\epsilon_5^{[k]} = \mathcal{D}_5^{[k]} = (\mathbf{R}^{(p)}\boldsymbol{n}_{\bar{y}}, \boldsymbol{l}^{[k]}), \tag{A.14e}$$

$$\epsilon_6^{[k]} = \mathcal{D}_6^{[k]} = -(\mathbf{R}^{(q)}\boldsymbol{n}_{\bar{y}}, \boldsymbol{l}^{[k]}). \tag{A.14f}$$

Here, $\|\boldsymbol{l}^{[k]}\|$ and $l_0^{[k]}$ represent the actual length and the reference length of the element; $(\,,\,)$ stands for the inner product of two vectors. The deformation mode coordinates in equation (A.14) possess the proper invariance with respect to rigid body motions of the beam element.

Appendix B

Differentiation equation (3.43) with respect to time

With the identities $\boldsymbol{\Lambda}^T\boldsymbol{\Lambda} = (\mathbf{I} - \boldsymbol{\lambda}\boldsymbol{\lambda}^T)$, in which $\mathbf{I}$ is a 4×4 identity matrix, and $\boldsymbol{\Lambda}'\boldsymbol{\lambda} = 0$ (Nikravesh (1988)) the second term of equation (3.43) may be simplified to

$$4\boldsymbol{\Lambda}^T \frac{d}{dt}(\boldsymbol{\Lambda}\boldsymbol{\Lambda}'^T\mathbf{J}'^{[k](p)}\boldsymbol{\Lambda}'\boldsymbol{\Lambda}^T\boldsymbol{\Lambda}\dot{\boldsymbol{\lambda}}) = 4\boldsymbol{\Lambda}^T \frac{d}{dt}(\boldsymbol{\Lambda}\boldsymbol{\Lambda}'^T\mathbf{J}'^{[k](p)}\boldsymbol{\Lambda}'\dot{\boldsymbol{\lambda}}). \tag{B.1}$$

Carrying out the differentiation with respect to time yields

$$\begin{aligned} 4\boldsymbol{\Lambda}^T \frac{d}{dt}(\boldsymbol{\Lambda}\boldsymbol{\Lambda}'^T\mathbf{J}'^{[k](p)}\boldsymbol{\Lambda}'\dot{\boldsymbol{\lambda}}) =& 4\boldsymbol{\Lambda}^T\dot{\boldsymbol{\Lambda}}\boldsymbol{\Lambda}'^T\mathbf{J}'^{[k](p)}\boldsymbol{\Lambda}'\dot{\boldsymbol{\lambda}} \\ &+ 4\boldsymbol{\Lambda}^T\boldsymbol{\Lambda}\dot{\boldsymbol{\Lambda}}'^T\mathbf{J}'^{[k](p)}\boldsymbol{\Lambda}'\dot{\boldsymbol{\lambda}} \\ &+ 4\boldsymbol{\Lambda}^T\boldsymbol{\Lambda}\boldsymbol{\Lambda}'^T\mathbf{J}'^{[k](p)}\dot{\boldsymbol{\Lambda}}'\dot{\boldsymbol{\lambda}} \\ &+ 4\boldsymbol{\Lambda}^T\boldsymbol{\Lambda}\boldsymbol{\Lambda}'^T\mathbf{J}'^{[k](p)}\boldsymbol{\Lambda}'\ddot{\boldsymbol{\lambda}}. \end{aligned} \tag{B.2}$$

With the identity $\dot{\boldsymbol{\Lambda}}\boldsymbol{\Lambda}'^T = \boldsymbol{\Lambda}\dot{\boldsymbol{\Lambda}}'^T$ the fist two parts of the right hand side of equation (B.2) can be combined to

$$4\boldsymbol{\Lambda}^T\dot{\boldsymbol{\Lambda}}\boldsymbol{\Lambda}'^T\mathbf{J}'^{[k](p)}\boldsymbol{\Lambda}'\dot{\boldsymbol{\lambda}} + 4\boldsymbol{\Lambda}^T\boldsymbol{\Lambda}\dot{\boldsymbol{\Lambda}}'^T\mathbf{J}'^{[k](p)}\boldsymbol{\Lambda}'\dot{\boldsymbol{\lambda}} = 8\dot{\boldsymbol{\Lambda}}'^T\mathbf{J}'^{[k](p)}\boldsymbol{\Lambda}'\dot{\boldsymbol{\lambda}}. \tag{B.3}$$

Since $\dot{\boldsymbol{\Lambda}}'\dot{\boldsymbol{\lambda}} = 0$, the third part of the right hand side of equation (B.2) is zero. With the identities $\boldsymbol{\Lambda}^T\boldsymbol{\Lambda} = (\mathbf{I} - \boldsymbol{\lambda}\boldsymbol{\lambda}^T)$ and $\boldsymbol{\Lambda}'\boldsymbol{\lambda} = 0$ the fourth part can be simplified to

$$4\boldsymbol{\Lambda}^T\boldsymbol{\Lambda}\boldsymbol{\Lambda}'^T\mathbf{J}'^{[k](p)}\boldsymbol{\Lambda}'\ddot{\boldsymbol{\lambda}} = 4\boldsymbol{\Lambda}'^T\mathbf{J}'^{[k](p)}\boldsymbol{\Lambda}'\ddot{\boldsymbol{\lambda}}. \tag{B.4}$$

Substitution of equations (B.2-B.4) into equation (B.1) gives

$$4\boldsymbol{\Lambda}^T \frac{d}{dt}(\boldsymbol{\Lambda}\boldsymbol{\Lambda}'^T\mathbf{J}'^{[k](p)}\boldsymbol{\Lambda}'\boldsymbol{\Lambda}^T\boldsymbol{\Lambda}\dot{\boldsymbol{\lambda}}) = 8\dot{\boldsymbol{\Lambda}}'^T\mathbf{J}'^{[k](p)}\boldsymbol{\Lambda}'\dot{\boldsymbol{\lambda}} + 4\boldsymbol{\Lambda}'^T\mathbf{J}'^{[k](p)}\boldsymbol{\Lambda}'\ddot{\boldsymbol{\lambda}}. \tag{B.5}$$

Appendix C

Specifications Krypton Rodym 6D camera system

The Krypton Rodym 6D system is a camera-based position measurement system. Using three linear CCD cameras, the system computes real time the three dimensional coordinates of individual markers attached to an object to be measured. The markers are infrared light emitting diodes that are activated in sequence to provide real-time marker discrimination. The use of multiple markers allows calculating the orientation of the object they are attached to.

Figure C.1 shows the measurement system and its working volume. Raw measurements of a marker position are expressed with respect to the camera's coordinate system. This (x, y, z) frame has its origin in the middle of the sensitive surface of the central camera. The z-coordinate of the camera frame represents the distance between the camera and the marker along the optical axis of the camera system. The coordinates x and y are situated in a plane, that is orthogonal to the optical axis. The camera system has a resolution of 0.002 mm.

To increase the absolute accuracy of the camera system, software compensates the raw data with an estimated model that predicts the true measurement value for each raw measurement value. The camera calibration and its verification is done by the manufacturer. The results are presented in the calibration certificate (Nysen (2001)) and summarised in table C.1. The table shows the 3D measurement errors, measured over a measurement volume of 1 m^3. The measurement error for the z-coordinate is much larger than for the x and y-direction. Histograms presented in the calibration certificate, visualising the errors in the x, y and z direction separately, show that the measurement accuracy in the x and y direction is a factor 5 higher than for the z coordinate. Theredore if measurements are performed in the x-y frame of the camera system a higher accuracy can be obtained than presented in table C.1. Table C.2 shows the measurement accuracy for each coordinate separately. The values

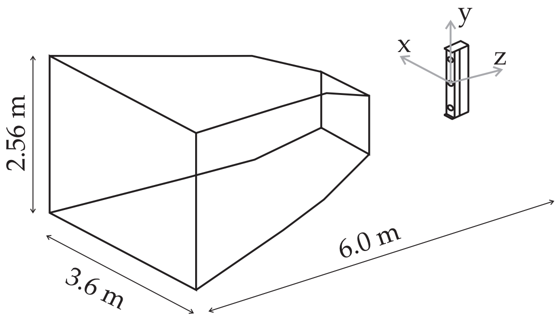

Figure C.1: Measurement setup Rodym 6D camera system

are estimated from table C.1 assuming the 5 times higher accuracy of the x,y-coordinate.

Region	z-coordinates	max. (mm)	std. dev. (mm)
I	2-3 m	0.119	0.034
II	3-4 m	0.209	0.052
III	4-5 m	0.283	0.114
IV	5-6 m	0.520	0.167

Table C.1: 3D measurement errors over a measurement volume of 1 m^3 of the Krypton 6D measurement system, according to Nysen (2001).

Region	x,y-coodinates		z-coodinates	
	max. (mm)	std. dev. (mm)	max.(mm)	std. dev. (mm)
I	0.023	0.007	0.115	0.033
II	0.040	0.010	0.201	0.050
III	0.054	0.022	0.272	0.110
IV	0.100	0.032	0.500	0.161

Table C.2: Estimated measurement errors of a calibrated Krypton 6D measurement system.

The camera system is equipped with a so-called 'space probe', which is a tool consisting of multiple markers and a pointer. The space probe is used to validate the camera system by measuring calibrated distances between several points in 3D space, see Bielen (2001). The accuracy of the camera system for measuring the distance between two points is specified in table C.3

The last camera calibration was done in 2001, see Bielen (2001); Nysen (2001). During the last few years, various people have validated the accuracy of the calibrated system for use in the laboratory, see De Roo (2003); Scheringa (2006). De Roo (2003) validated the accuracy for small marker displacements, namely for steps around 0.1 mm, and only a very limited number of points. She found out that at that moment the camera was within its specification for these types of measurements. Furthermore, she showed that the system is sensitive to temperature fluctuations. After switching on the power, it takes around 5 hours before the system is stabilised and during this time the coordinates drift away 0.3 mm. The camera calibration by the manufacturer is performed for a stabilised ambient temperature of 20°. These conditions cannot be met at the laboratory.

More recently, Scheringa (2006) validated the calibration using measurements from multiple markers. He showed that the camera performs at least 2.5 times worse than is indicated by the specification given in the calibration report of the manufacturer (Bielen (2001)) that is presented in table C.3. This factor is a rough estimation because the measurements are not exactly the same. Because uncalibrated reference lengths are used, this value is a lower bound. The actual accuracy is could be much worse than this.

	distance to the camera (m)	3D measurement uncertainty (μm)
zone I	1.5-3	$90 + 10 \cdot L$
zone II	3-5	$90 + 25 \cdot L$
zone III	5-6	$190 + 25 \cdot L$

Table C.3: The measurement uncertainty expressed as the maximum measured length deviation for 95% of the measurements, L = measured length (m), from Bielen (2001).

Appendix D

Model parameters

Nr	Symbol	p	$p^{(E)}$	$\hat{p}^{(E)}$	Unit	$\frac{\lvert p^{(E)}-\hat{p}^{(E)}\rvert}{p^{(E)}}$
1	$m'^{[1]}$	4.32e+001	1.00e-010	0.00e+000	kg	1.000
2	$m'^{[1]}s_x^{[1]}$	4.36e-002	2.65e-004	1.25e-004	kg m	0.528
3	$m'^{[1]}s_y^{[1]}$	1.68e+000	9.78e-001	9.66e-001	kg m	0.012
4	$m'^{[1]}s_z^{[1]}$	4.23e+000	-7.99e-004	-7.97e-004	kg m	0.002
5	$J'^{[1](p)}_{xx}$	8.26e-001	1.98e-001	2.01e-001	kg m^2	0.018
6	$J'^{[1](p)}_{yy}$	5.81e-001	2.44e-002	2.13e-002	kg m^2	0.127
7	$J'^{[1](p)}_{zz}$	2.45e-001	1.75e-001	1.56e-001	kg m^2	0.106
8	$J'^{[1](p)}_{xy}$	5.14e-002	5.17e-002	5.62e-002	kg m^2	0.086
9	$J'^{[1](p)}_{xz}$	-4.17e-003	-4.96e-005	-3.84e-005	kg m^2	0.226
10	$J'^{[1](p)}_{yz}$	-1.65e-001	3.29e-002	2.94e-002	kg m^2	0.106

Table D.1: Physical parameters p, essential parameters $p^{(E)}$, estimated essential parameter $\hat{p}^{(E)}$ and relative parameter error $|p^{(E)} - \hat{p}^{(E)}|/p^{(E)}$ of the 4DOF model of the Stäubli RX90B.

Nr	Symbol	p	$p^{(E)}$	$\hat{p}^{(E)}$	Unit	$\frac{\lvert p^{(E)}-\hat{p}^{(E)}\rvert}{p^{(E)}}$
11	$m'^{[2]}$	1.80e+001	1.99e+001	1.98e+001	kg	0.003
12	$m'^{[2]}s_x^{[2]}$	1.80e-004	4.83e-008	4.02e-008	kg m	0.167
13	$m'^{[2]}s_y^{[2]}$	1.41e+000	1.41e+000	1.36e+000	kg m	0.031
14	$m'^{[2]}s_z^{[2]}$	3.50e+000	1.17e+000	1.23e+000	kg m	0.055
15	$J'^{[2](p)}_{xx}$	1.09e+000	3.04e-002	9.77e-003	kg m^2	0.678
16	$J'^{[2](p)}_{yy}$	9.46e-001	-1.13e-001	-1.21e-001	kg m^2	0.064
17	$J'^{[2](p)}_{zz}$	1.40e-001	1.39e-001	1.25e-001	kg m^2	0.106
18	$J'^{[2](p)}_{xy}$	8.59e-005	-5.59e-008	-5.38e-008	kg m^2	0.037
19	$J'^{[2](p)}_{xz}$	6.50e-005	-3.65e-008	-3.16e-008	kg m^2	0.134
20	$J'^{[2](p)}_{yz}$	-2.40e-001	-2.38e-001	-2.28e-001	kg m^2	0.043
21	$m'^{[3]}$	1.64e+001	2.24e+001	2.16e+001	kg	0.036
22	$m'^{[3]}s_x^{[3]}$	1.64e-004	2.24e-007	7.26e-008	kg m	0.675
23	$m'^{[3]}s_y^{[3]}$	-1.47e+000	-1.56e+000	-1.46e+000	kg m	0.063
24	$m'^{[3]}s_z^{[3]}$	-1.14e-001	-5.46e-002	-8.18e-002	kg m	0.499
25	$J'^{[3](p)}_{xx}$	1.83e-001	1.96e-001	1.84e-001	kg m^2	0.059
26	$J'^{[3](p)}_{yy}$	4.29e-002	4.71e-002	4.37e-002	kg m^2	0.073
27	$J'^{[3](p)}_{zz}$	1.80e-001	1.88e-001	1.93e-001	kg m^2	0.029
28	$J'^{[3](p)}_{xy}$	1.15e-004	-3.06e-007	-2.77e-007	kg m^2	0.096
29	$J'^{[3](p)}_{xz}$	1.01e-004	-2.92e-007	-3.23e-007	kg m^2	0.109
30	$J'^{[3](p)}_{yz}$	-6.20e-003	-2.88e-004	6.49e-004	kg m^2	3.252
31	$m'^{[4]}$	1.14e+001	1.05e+001	1.12e+001	kg	0.063
32	$m'^{[4]}s_x^{[4]}$	1.15e-002	1.15e-002	3.43e-003	kg m	0.701
33	$m'^{[4]}s_y^{[4]}$	1.14e-004	-2.52e-007	-1.27e-007	kg m	0.496
34	$m'^{[4]}s_z^{[4]}$	2.90e+000	2.90e+000	2.88e+000	kg m	0.007
35	$J'^{[4](p)}_{xx}$	9.15e-001	9.15e-001	9.10e-001	kg m^2	0.006
36	$J'^{[4](p)}_{yy}$	9.14e-001	9.14e-001	9.05e-001	kg m^2	0.009
37	$J'^{[4](p)}_{zz}$	5.61e-002	5.61e-002	4.43e-002	kg m^2	0.210
38	$J'^{[4](p)}_{xy}$	-9.90e-003	-9.90e-003	-1.01e-002	kg m^2	0.025
39	$J'^{[4](p)}_{xz}$	-2.83e-003	-2.81e-003	-3.11e-003	kg m^2	0.106
40	$J'^{[4](p)}_{yz}$	7.10e-005	-1.53e-007	2.37e-008	kg m^2	1.155
41	$J^{[1](a)}$	1.36e+000	1.36e+000	1.41e+000	kg m^2	0.038
42	$J^{[2](a)}$	1.36e+000	1.36e+000	1.40e+000	kg m^2	0.028
43	$J^{[3](a)}$	6.92e-001	6.92e-001	7.09e-001	kg m^2	0.025
44	$J^{[4](a)}$	3.10e-001	3.10e-001	3.24e-001	kg m^2	0.047

Continuation table D.1

Nr	Symbol	p	$p^{(E)}$	$\hat{p}^{(E)}$	Unit	$\frac{\lvert p^{(E)}-\hat{p}^{(E)}\rvert}{p^{(E)}}$
45	$k^{(c)}$	2.03e+004	2.03e+004	2.01e+004	N m^{-1}	0.010
46	$\sigma^{(c,0)}$	1.66e+003	1.66e+003	1.66e+003	N	0.002
47	$\tau_1^{(a,0)}$	1.86e+001	5.37e-003	-1.07e-003	N m	1.199
48	$c_1^{(v)}$	6.63e+001	6.63e+001	6.62e+001	N m (s/rad)$^{(1-\delta_j^{(v)})}$	0.002
49	$\tau_2^{(a,0)}$	3.26e+001	-3.91e-003	9.24e-003	N m	3.364
50	$c_2^{(v)}$	6.21e+001	6.21e+001	6.18e+001	N m (s/rad)$^{(1-\delta_j^{(v)})}$	0.005
51	$\tau_3^{(a,0)}$	8.12e+000	1.48e-004	-9.40e-003	N m	64.384
52	$c_3^{(v)}$	2.11e+001	2.11e+001	2.10e+001	N m (s/rad)$^{(1-\delta_j^{(v)})}$	0.003
53	$\tau_4^{(a,0)}$	8.84e+000	-1.31e-001	-1.08e-001	N m	0.178
54	$c_4^{(v)}$	1.72e+001	1.72e+001	1.71e+001	N m (s/rad)$^{(1-\delta_j^{(v)})}$	0.007
55	$k_1^{[1]}$	2.80e+005	2.80e+005	2.78e+005	N m rad^{-1}	0.007
56	$k_2^{[1]}$	4.40e+005	4.40e+005	4.39e+005	N m rad^{-1}	0.002
57	$k_3^{[1]}$	4.40e+005	4.40e+005	4.39e+005	N m rad^{-1}	0.003
58	$k_1^{[2]}$	2.70e+005	2.70e+005	2.69e+005	N m rad^{-1}	0.004
59	$k_2^{[2]}$	2.40e+005	2.40e+005	2.39e+005	N m rad^{-1}	0.005
60	$k_3^{[2]}$	2.40e+005	2.40e+005	2.39e+005	N m rad^{-1}	0.006
61	$k_1^{[3]}$	1.00e+005	1.00e+005	9.95e+004	N m rad^{-1}	0.005
62	$k_2^{[3]}$	2.10e+005	2.10e+005	2.09e+005	N m rad^{-1}	0.006
63	$k_3^{[3]}$	2.10e+005	2.10e+005	2.07e+005	N m rad^{-1}	0.016
64	$k_1^{[4]}$	9.00e+004	9.00e+004	7.13e+004	N m rad^{-1}	0.207
65	$k_2^{[4]}$	1.60e+005	1.60e+005	1.59e+005	N m rad^{-1}	0.005
66	$k_3^{[4]}$	1.60e+005	1.60e+005	1.59e+005	N m rad^{-1}	0.008
67	$d_1^{[1]}$	2.80e+002	2.80e+002	2.63e+002	N m s rad^{-1}	0.061
68	$d_2^{[1]}$	4.40e+002	4.41e+002	4.45e+002	N m s rad^{-1}	0.009
69	$d_3^{[1]}$	4.40e+002	4.40e+002	4.39e+002	N m s rad^{-1}	0.003
70	$d_1^{[2]}$	2.70e+002	2.69e+002	2.65e+002	N m s rad^{-1}	0.014
71	$d_2^{[2]}$	2.40e+002	2.40e+002	2.33e+002	N m s rad^{-1}	0.029
72	$d_3^{[2]}$	2.40e+002	2.40e+002	2.19e+002	N m s rad^{-1}	0.087
73	$d_1^{[3]}$	1.00e+002	1.00e+002	9.86e+001	N m s rad^{-1}	0.014
74	$d_2^{[3]}$	2.10e+002	2.10e+002	2.09e+002	N m s rad^{-1}	0.007
75	$d_3^{[3]}$	2.10e+002	2.10e+002	1.80e+002	N m s rad^{-1}	0.142
76	$d_1^{[4]}$	9.00e+001	9.00e+001	7.10e+001	N m s rad^{-1}	0.211
77	$d_2^{[4]}$	1.60e+002	1.60e+002	1.59e+002	N m s rad^{-1}	0.006
78	$d_3^{[4]}$	1.60e+002	1.60e+002	1.58e+002	N m s rad^{-1}	0.010

Continuation table D.1

Appendix E

Noise sensitivity of inverse eigenvalue algorithm

It is assumed that the resonance frequencies $\omega^{[r]}$, the anti-resonance frequencies $\mu_{j,j}^{[r]}$ and the gain $\mathbf{K}^{(H)}$ (see equation (5.40)), including their covariance, are estimated from experimental data using the techniques described in chapter 6. Then the drive stiffness $k_1^{[k+1]}$ of joint j is estimated by substitution of equation (5.31) into equation (5.53), yielding

$$k_1^{[k+1]} \approx \tilde{K}_{j,j} = J^{[k](a)} \sum_{m=1}^{N^{(q)}} \frac{\prod_{r=1}^{N^{(q)}-1} \left({\mu_{j,j}^{[r]}}^2 - {\omega^{[m]}}^2\right)}{\prod_{r=1;r\neq m}^{N^{(q)}} \left({\omega^{[r]}}^2 - {\omega^{[m]}}^2\right)} {\omega^{[m]}}^2. \tag{E.1}$$

The drive inertia $J^{[k](a)}$ is estimated using equation (5.42), which shows that

$$J^{[k](a)} = \left({\mathbf{K}^{(H)}}^{-1}\right)_{j,j} \tag{E.2}$$

for $k = 2j - 1$ and $j = 1, \cdots, N^{(em)}$.

To estimate the influence of measurement noise on the estimated drive parameters, equation (E.1) should be differentiated with respect to its parameters

$\omega^{[r]}$, $\mu_{j,j}^{[r]}$ and $J^{[k](a)}$. Differentiating equation (E.1) with respect to $\omega^{[r]}$ yields

$$\begin{aligned}
J_{j,m}^{(1)} =& -2J^{[k](a)^{-1}} \frac{\sum_{n=1}^{N^{(q)}-1} \prod_{r=1;r\neq n}^{N^{(q)}-1} (\mu_{j,j}^{[r]^2} - \omega^{[m]^2})}{\prod_{r=1;r\neq m}^{N^{(q)}} (\omega^{[r]^2} - \omega^{[m]^2})} \omega^{[m]^3} \\
&+ 2J^{[k](a)^{-1}} \sum_{m=1}^{N^{(q)}} \frac{\prod_{r=1}^{N^{(q)}-1} (\mu_{j,j}^{[r]^2} - \omega^{[m]^2})}{\prod_{r=1;r\neq m}^{N^{(q)}} (\omega^{[r]^2} - \omega^{[m]^2})} \omega^{[m]} \\
&- 2J^{[k](a)^{-1}} \sum_{n=1;n\neq m}^{N^{(q)}} \left(\frac{\prod_{r=1}^{N^{(q)}-1} (\mu_{j,j}^{[r]^2} - \omega^{[n]^2})}{\left(\prod_{r=1;r\neq m}^{N^{(q)}} (\omega^{[r]^2} - \omega^{[n]^2})\right)^2} \omega^{[n]^2} \right. \\
&\times \left. \prod_{r=1;r\neq m,r\neq n}^{N^{(q)}} (\omega^{[r]^2} - \omega^{[n]^2}) \omega^{[m]} \right) \\
&+ 2J^{[k](a)^{-1}} \left(\frac{\prod_{r=1}^{N^{(q)}-1} (\mu_{j,j}^{[r]^2} - \omega^{[m]^2})}{\left(\prod_{r=1;r\neq m}^{N^{(q)}} (\omega^{[r]^2} - \omega^{[n]^2})\right)^2} \omega^{[m]^2} \right. \\
&\times \left. \sum_{n=1;p\neq m}^{N^{(q)}} \prod_{r=1;r\neq m,r\neq n}^{N^{(q)}} (\omega^{[r]^2} - \omega^{[m]^2}) \omega^{[m]} \right).
\end{aligned} \tag{E.3}$$

Differentiating equation (E.1) with respect to $\mu_{j,j}^{[r]}$ yields

$$J_{j,n}^{(2)} = 2J^{[k](a)} \sum_{m=1}^{N^{(q)}} \frac{\prod_{r=1;r\neq n}^{N^{(q)}-1} (\mu_{j,j}^{[r]^2} - \omega^{[m]^2})}{\prod_{r=1;r\neq m}^{N^{(q)}} (\omega^{[r]^2} - \omega^{[m]^2})} \omega^{[m]^2} \mu_{j,j}^{[r]}. \tag{E.4}$$

Differentiation of equation (E.1) with respect to $J^{[k](a)}$ yields

$$J_{j,n}^{(3)} = \sum_{m=1}^{N^{(q)}} \frac{\prod_{r=1}^{N^{(q)}-1} (\mu_{j,j}^{[r]^2} - \omega^{[m]^2})}{\prod_{r=1;r\neq m}^{N^{(q)}} (\omega^{[r]^2} - \omega^{[m]^2})} \omega^{[m]^2}. \tag{E.5}$$

Let $\mathbf{J}$ be the combined derivative of the drive stiffnesses, defined by

$$\mathbf{J} = [\mathbf{J}^{(1)} \mathbf{J}^{(2)} \mathbf{J}^{(3)}]. \tag{E.6}$$

The covariance of the drive stiffnesses, denoted by $\hat{\mathbf{C}}^{(k)}$, is approximated by

$$\hat{\mathbf{C}}^{(k)} \approx \mathbf{J} \mathrm{diag}(\hat{C}^{(w)}) \mathbf{J}^T, \tag{E.7}$$

in which $\hat{C}^{(w)}$ is a vector containing the estimated covariances of the resonance frequencies $\omega^{[r]}$, the anti-resonance frequencies $\mu_{j,j}^{[r]}$ and the drive inertias $J^{[k](a)}$.

These covariances are closely related to the covariances of the transfer function parameters $\hat{\mathbf{C}}^{(\hat{p})}$, presented in equation (6.46).

Appendix F

Properties of nonlinear distortions

The class of nonlinear systems analysed in this appendix is the continuous time SISO Volterra model, defined by Schetzen (1980) as:

$$y(t) = \sum_{n=1}^{Q} y_n(t) \tag{F.1}$$

in which

$$y_n(t) = \int_0^\infty \cdots \int_0^\infty g_n(\tau_1, \cdots, \tau_n) u(t - \tau_1) \cdots u(t - \tau_n) d\tau_1 \cdots d\tau_n, \tag{F.2}$$

$u(t)$ is the input, $y(t)$ is the output and the $g_n(\tau_1, \cdots, \tau_n)$ are called the Volterra kernels of the system.

Schoukens et al. (2005) have shown that for this class of systems excited by a random multi-sine equation (6.12) is an exact representation of the underlying nonlinear system. With regard to these conditions, the related linear system is defined by

$$P^{(R)}(\omega_f) = \underset{P}{\arg}\ \min \mathcal{E}\{|Y^{[m,o]}(\omega_f) - PU^{[m,o]}(\omega_f)|^2\}, \tag{F.3}$$

in which the expected value $\mathcal{E}\{\}$ has to be taken over different realisations of the multi-sine with equal power spectrum. Furthermore, the nonlinear noise source has the following properties:

1. Zero mean: $\mathcal{E}\{Y^{[o](s)}(\omega_f)\} = 0$.
2. Uncorrelated with the input: $\mathcal{E}\{Y^{[o](s)}(\omega_f) {U^{[m,o](0)}}^H(\omega_f)\} = 0$.

3. $Y^{[o](s)}(\omega_f)$ is asymptotically independent of $U^{[m,o](0)}(\omega_l)$, for all f, l.
4. $Y^{[o](s)}(\omega_f)$ is asymptotically circular complex normally distributed and mixing of arbitrary order.
5. The even moments do not disappear:

$$\mathcal{E}\{Y^{[o](s)}(\omega_f){Y^{[o](s)}}^H(\omega_f)\} = C^{(Y^{(s)})}(\omega_f) = O({N^{(o)}}^0).$$

6. The odd moments converge to zero $(f \neq l)$:

$$\mathcal{E}\{Y^{[o](s)}(\omega_f)Y^{[o](s)}(\omega_l)^H\} = O({N^{(o)}}^{-1}).$$

Bibliography

Albu-Schäffer, A. and Hirzinger, G. (2001). Parameter identification and passivity based joint control for a 7dof torque controlled light weight robot. In *IEEE International Conference on Robotics and Automation*, pages 2852–2858.

Alici, G. and Shirinzadeh, B. (2005). Enhanced stiffness modeling, identification and characterization for robot manipulators. *IEEE Transactions on Robotics*, 21(4):554–564.

Armstrong, B. (1989). On finding exciting trajectories for identification experiments involving systems with nonlinear dynamics. *International Journal of Robotics Research*, 8(6):28–48.

Armstrong-Hélouvry, B. (1991). *Control of Machines with Friction*. Kluwer Academic Publishers.

Armstrong-Hélouvry, B. , Dupont, P. , and Canudas de Wit, C. (1994). A survey of models, analysis tools and compensation methods for the control of machines with friction. *Automatica*, 30(7):1083–1138.

Barel, M. v. and Bultheel, A. (1995). Orthonormal polynomial vectors and least squares approximation for a discrete inner product. *Electronic Transactions on Numerical Analysis*, 3:1–23.

Berglund, E. and Hovland, G. (2000). Automatic elasticity tuning of industrial robot manipulators. In *IEEE Conference on Decision and Control*, volume 5, pages 5091–5096, Sydney, Australia.

Besseling, J. (1982). Non-linear theory for elastic beams and rods and its finite element representation. *Computer Methods in Applied Mechanics and Engineering*, 31:205–220.

Bielen, S. (2001). Camera verification report. Technical report, Krypton.

Boley, D. and Golub, G. (1988). Survey of matrix inverse eigenvalue problems. *Inverse Problems*, 3:595–622.

Canudas De Wit, C. , Olsson, P. , Aström, K. , and Lischinsky, P. (1995). A new model for control of systems with friction. *IEEE Transactions on Automatic Control*, 40(3):419–425.

Chen, K. and Beale, D. (2003). A linear approach for experimental dynamic parameter estimation of planar mechanisms. *Multibody System Dynamics*, 9:165–184.

Chu, M. and Golub, G. (2005). *Inverse Eigenvalue Problems*. Numerical Mathematics and Scientific Computation. Oxford University Press.

Dahl, P. (1977). Measurement of solid friction parameters of ball bearings. In *Proceedings of 6th Annual Symposium on Incremental Motion, Control Systems and Devices*.

De Angelis, M. , Lus, H. , Betti, R. , and Longman, R. (2002). Extracting physical parameters of mechanical models from identified state-space represenatations. *Journal of Applied Mechanics*, 69:617–625.

D'Haene, T. , Pintelon, R. , Schoukens, J. , and Van Gheem, E. (2004). Variance analysis of frequency response function measurements using periodic excitations. In *Instrumentation and Measurement Technology Conference*, pages 1595–1600.

Ewins, D. (2000). *Modal Testing: theory, practice and application*. Mechanical Engineering Research Studies 10. Engineering Dynamics Series. Research Studies Press Ltd.

Friswell, M. and Mottershead, J. (1995). *Finite Element Updating in Structural Dynamics*, volume 38 of *Solid Mechanics and its Applications*. Kluwer Academic Publishers.

Gantmakher, F. and Krein, M. (1950). Oscillation matrices and kernels and small vibrations of mechanical systems. *Moscow Leningrad: State Publishing House for Technical-Theoretical Litrature. English Translation by U.S. Atomic Energy Commision, Wahington, DC, 1961*.

Gatti, P. and Ferrari, V. (1999). *Applied Structural and Mechanical Vibrations: theory, methods and measuring instrumentation*. E & FN Spon, 29 West 35th Street, New York.

Gautier, M. and Khalil, W. (1990). Direct calculation of minimum set of inertial parameters of serial robots. *IEEE Transactions on Robotics and Automation*, 6(3):373–377.

Gautier, M. and Khalil, W. (1992). Exciting trajectories for the identification of base inertial parameters of robots. *International Journal of Robotics Research*, 11(4):362–375.

Geradin, M. , Robert, G. , and Buchet, P. (1986). *Finite Element Methods for Nonlinear Problems*, chapter Kinematic and Dynamic Analysis of Mechanisms a Fininite Element Approach Based on Euler Parameters. Springer-Verlag, Berlin.

Gerat, V. (1994). Speed reducer of the cycloidal type for robots and other industrial manipulators. US patent 5286235.

Gladwell, G. (1986). *Inverse Problems in Vibration*, volume 9 of *Mechanics: Dynamical Systems*. Martinus Nijhoff.

Gladwell, G. (1997). Inverse vibration problems for finite element models. *Inverse Problems*, 13:311–322.

Gladwell, G. (1999). Inverse finite element vibration problems. *Journal of Sound and Vibration*, 211(2):309–324.

Gladwell, G. (2001). On the reconstruction of a damped vibrating sytem from two complex spectra, part 1: Theory. *Journal of Sound and Vibration*, 240(2):203–217.

Gladwell, G. (2004). *Inverse Problems in Vibration*. Solid Mechanics and its Applications. Kluwer Academic Publishers, The Netherlands, 2 edition.

Golub, G. and Boley, D. (1977). Inverse eigenvalue problems for band matrices. In Watson, G. , editor, *Invited paper presented at the Dundee conference on numerical analysis*.

Hakvoort, W. (2004). Identification of inertia and stiffness parameters of the Stäubli RX90 robot. Master's thesis, University of Twente, Department of Mechanical Engineering, Laboratory of Mechanical Automation, The Netherlands.

Hardeman, T. , Aarts, R. , and Jonker, J. (2005). Modelling and identification of robots with joint and drive flexibilities. In Ulbrich, H. and Günthner, W. , editors, *IUTAM Symposium on Vibration Control of Nonlinear Mechanisms and Structures*, volume 130 of *Solid Mechanics and its Applications*, pages 173–182, Munich, Gemany. Springer.

Hardeman, T. , Aarts, R. , and Jonker, J. (2006). A finite element formulation for dynamic parameter identification of robot manipulators. *Multibody System Dynamics*, 16:21–35.

Haug, E. (1992). *Intermediate Dynamics*. London: Prentice Hall.

Hovland, G. , Berglund, E. , and Hanssen, S. (2001). Identification of coupled elastic dynamics using inverse eigenvalue theory. In *Proceedings of the 32nd International Symposium on Robotics*, pages 1392–1397.

Hovland, G. , Berglund, E. , and Sordalen, O. (1999). Identification of joint elasticity of industrial robots. In *Proceedings of the 6th International Symposium on Experimental Robotics*, pages 455–464, Sydney, Australia.

Huang, J. (2003). A new approach to parametric identification of a single-link flexible joint manipulator. *Journal of Intelligent and Robotic Systems*, 37:273–284.

Imregun, M. , Sanliturk, K. , and Ewins, D. (1995a). Finite element model updating using frequency response function data - ii. case study on a medium-size finite element model. *Mechanical Systems and Signal Processing*, 9(2):203–213.

Imregun, M. , Visser, W. , and Ewins, D. (1995b). Finite element model updating using frequency response function data - i. theory and initial investigation. *Mechanical Systems and Signal Processing*, 9(2):187–202.

Jain, A. and Rodriguez, G. (1993). An analysis of the kinematics and dynamics of under-actuated manipulators. *IEEE Transactions on Robotics and Automation*, 9:411–422.

Jonker, J. (1989). A finite element dynamic analysis of spatial mechanisms with flexible links. *Computer Methods in Applied Mechanics and Engineering*, 76:17–40.

Jonker, J. (1990). A finite element dynamic analysis of flexible manipulators. *International Journal of Robotic Research*, 9:59–74.

Jonker, J. (1991). Linearisation of dynamic equations of flexible mechanisms - a finite element approach. *International Journal for Numerical Methods in Engineering*, 31:1375–1392.

Jonker, J. and Aarts, R. (1998). Modelling of flexible mechanisms and manipulators for control purpose. In *Proceedings of the Fourth International Conference on Motion and Vibration Control*, pages 291–297. ETH-Zurich, Institute of Robotics, MoViC.

Jonker, J. and Aarts, R. (2001). A perturbation method for dynamic analysis and simulation of flexible manipulators. *Multibody System Dynamics*, 6:245–266.

Jonker, J. and Meijaard, J. (1990). *Multibody Systems Handbook*, chapter SPACAR-Computer Program for Dynamic Analysis of Flexible Spatial Mechanisms and Manipulators, pages 123–143. Springer-Verlag, Berlin, Germany.

Khalil, W. Gautier, M. (2000). Modeling of mechanical systems with lumped elasticity. In *IEEE International Conference on Robotics and Automation*, pages 3964–3969.

Khalil, W. and Dombre, E. (2002). *Modeling, Identification and Control of Robots*. Hermes Penton Science.

Khan, I. and Ohba, R. (2003). Taylor series based finite difference approximations of higher-degree derivatives. *Journal of Computational and Applied Mathematics*, 154:115–124.

Kollár, I. (2001). *Frequency Domain System Identification Toolbox*. Vrije Universiteit Brussel.

Kozlowski, K. (1998). *Modelling and Identification in Robotics*. Springer-Verlag.

Lancaster, P. and Prells, U. (2005). Inverse problems for damped vibrating systems. *Journal of Sound and Vibration*, 283:891–914.

Lanczos, C. (1970). *The variational principles of mechanics*. University of Toronto Press, 4th edition.

Lawson, C. and Hanson, R. (1974). *Solving Least Squares Problems*. Prentice-Hall. Englewood Cliffs, New Jersey.

Ljung, L. (1999). *System Identification: Theory for the user*. Prentice Hall, 2nd edition.

Lus, H. , De Angelis, M. , and Betti, R. (2003). A new approach for reduced order modeling of mechanical systems using vibration measurements. *Journal of Applied Mechanics*, 70:715–723.

Mata, V. , Benimele, F. , Farhat, N. , and Valera, A. (2005). Dynamic parameter identification in industrial robots considering physical feasibility. *Advanced Robotics*, 19(1):101–119.

Mayeda, H. , Yoshida, K. , and Osuka, K. (1990). Base parameters of manipulator dynamic models. *IEEE Transactions on Robotics and Automations*, 6(3):312–321.

Meijaard, J. (1991). Direct determination of periodic solutions of the dynamical equations of flexible mechanisms and manipulators. *Numerical Methods in Engineering*, 32:1691–1710.

Meirovitch, L. (1986). *Elements of Vibration Analysis*. McGraw-Hell, 2 edition.

Miro, J. and White, A. (2002). Modelling an industrial manipulator, a case study. *Simulation Practice and Theory*, 9:293–319.

Modak, S. , Kundra, T. , and Nakra, B. (2002). Comparative study of model updating methods using simulated experimental data. *Computers and Structures*, 80:437–447.

Nikravesh, P. (1988). *Computer-aided Analysis of Mechanical Systems*. Englewood Cliffs, N.J: Prentice-Hall.

Nysen, R. (2001). Calibration certificate. Technical report, Krypton.

Ochier, J. , Mladenova, C. , and Müller, P. (1995). An approach to automatic generation of dynamic equations of elastic joint manipulators in symbolic language. *Journal of Intelligent and Robotic Systems*, 14:199–218.

Olsen, H. , Åström, K. , Canudas de Wit, C. , Gäfvert, M. , and Lischinsky, P. (1998). Friction models and friction compensation. 4:176–195.

Olsen, M. and Petersen, H. (2001). A new method for estimating parameters of a dynamic robot model. *IEEE Transactions on Robotics and Automation*, 17(1):95–100.

Östring, M. and Gunnarsson, S. (2004). Recursive identification of physical parameters in a flexible robot arm. *Asian Journal of Control*, 6:407–414.

Östring, M. , Gunnarsson, S. , and Norrlöf, M. (2003). Closed-loop identification of an industrial robot containing flexibilities. *Control Engineering Practice*, 11:291–300.

Pham, M. , Gautier, M. , and Poignet, P. (2001). Identification of joint stiffness with bandpass filtering. In *IEEE International Conference on Robotics and Automation*, pages 2867–2872.

Pham, M. , Gautier, M. , and Poignet, P. (2002). Accelerometer based identification of mechanical systems. In *IEEE International Conference on Robotics and Automation*, pages 4293–4298.

Pintelon, R. and Schoukens, J. (2001). *System Identification, A Frequency Domain Approach*. IEEE Press, New York.

Ram, Y. and Elhay, S. (1996). An inverse eigenvalue problem for the symmetric tridiagonal pencil with application to damped oscillatory systems. *SIAM Journal on Applied Mathematics*, 56(1):232–244.

Rodriguez, G. , Kreuz-Delgado, K. , and A., J. (1991). A spatial operator algebra for manipulator modelling and control. *The International Journal of Robotic Research*, 10:371–381.

Roo, S. de (2003). Testing the trajectory performance of the Stäubli RX90 robot for laser welding. Master's thesis, University of Twente, Department of Mechanical Engineering, Laboratory of Mechanical Automation, The Netherlands.

Scheringa, I. (2006). Modeling and analysis of geometric drive train nonlinearities in the stäaubli rx90 robot. Master's thesis, University of Twente, Department of Mechanical Engineering, Laboratory of Mechanical Automation, The Netherlands.

Schetzen, M. (1980). *The Volterra and Wiener Theories of Nonlinear Systems*. Wiley, New York.

Schoukens, J. , Pintelon, R. , Dobrowiecki, T. , and Rolain, Y. (2005). Identification of linear systems with nonlinear distortions. *Automatica*, 41:491–504.

Shome, S. , Beale, D. G. , and Wang, D. (1998). A general method for estimating dynamic parameters of spatial mechanisms. *Nonlinear Dynamics*, 16:349–368.

Spong, M. (1987). Modeling and control of elastic joint robots. *Journal of Dynamic Systems, Measurement, and Control*, 109:310–319.

Strang, G. (1976). *Linear Algebra and its Applications*. Academic Press, New York.

Swain, A. and Morris, A. (2003). A unified dynamic model formulation for robotic manipulation systems. *Journal of Robotic Systems*, 20(10):601–620.

Swevers, J. , Ganseman, C. , Schutter, J. d. , and Brussel, H. v. (1996). Experimental robot identification using optimised periodic trajectories. *Mechanical Systems and Signal Processing*, 10(5):561–577.

Tsaprounis, C. and Aspragathos, N. (2000). Adaptive tracking controller for rigid-link elastic-joint robots with link acceleration estimation. *Journal of Intelligent and Robotic Systems*, 27:68–83.

Verboven, P. (2002). *Frequency-Domain System Identification for Modal Analysis*. PhD thesis, Vrije Universiteit Brussel, Belgium.

Verboven, P. , Guillaume, P. , Vanlanduit, S. , and Cauberghe, B. (2006). Assesment of nonlinear distortions in modal testing and analysis of vibrating automotive structures. *Journal of Sound and Vibration*, 293:299–319.

Waiboer, R. (2007). *Dynamic Modelling, Identification and Simulation of Industrial Robots for Off-line Programming of Robotised Laser Welding*. PhD thesis, NIMR, University of Twente, The Netherlands.

Waiboer, R. , Aarts, R. , and Jonker, J. (2005a). Modelling and identification of a six axes industrial robot. In *Proceedings of IDETC/CIE*, Long Beach, USA. ASME.

Waiboer, R. , Aarts, R. , and Jonker, J. (2005b). Velocity dependence of joint friction in robotic manipulators with gear transmissions. In J.M., G. , Cuadrado, J. , and García Orden, J. , editors, *ECCOMAS Thematic Conference Multibody Dynamics*, Advances in Computational Multibody Dynamics, pages 1–19, Madrid, Spain.

Werff, K. v. d. (1983). Spacar, a program system for the analysis of the motion of spatial mechanisms (tm 739). Technical report, Delft University of Technology, Laboratory for Engineering Mechanics.

Wernholt, E. (2004). *On Multivariable and Nonlinear Identification of Industrial Robots*. PhD thesis, Linköping University, Sweden.

Wernholt, E. and Gunnarsson, S. (2005). Nonlinear grey-box identifcation of industrial robots containing flexibilities. In *IFAC World Congress*, volume 16.